A Loss Resilient Entanglement Swapping Protocol using Non-Classical States of Light

RYAN CHARLES PARKER

PHD

UNIVERSITY OF YORK

Physics

October 2018

"I think I can safely say that nobody understands quantum mechanics."

Richard Feynman

"In fact, the mere act of opening the box will determine the state of the cat, although in this case there were three determinate states the cat could be in: these being Alive, Dead, and Bloody Furious."

Terry Pratchett

UNIVERSITY OF YORK

Abstract

York Centre for Quantum Technologies
Physics

Doctor of Philosophy

A Loss Resilient Entanglement Swapping Protocol using Non-Classical States of Light

by Ryan Charles Parker

Distributing and sharing entanglement at a distance is a key ingredient in many future quantum communication protocols, however entanglement is a fragile resource and can break down upon interacting with the environment. Within this thesis we present two possible entanglement swapping protocols, and show that these protocols are resilient to small levels of photonic losses. We propose the use of these protocols in quantum communication schemes that require shared entangled qubits, in the form of a Bell state.

The input states to our proposed protocols are hybrid entangled states, which are discrete-variable and continuous-variable entangled states. We use the vacuum and single photon Fock state as our discrete half, which is stationary in our entanglement swapping protocol, whereas the continuous variable half is modelled as travelling through lossy optical fibre before being measured. The first protocol uses coherent states in a superposition as propagating modes in our entanglement swapping set-up, whereas the second, more complicated, protocol uses superposed cat states.

We model photonic losses by applying a beam-splitter of transmission T to our propagating continuous variable modes, along with an input vacuum state. We also model the more realistic circumstance in which the losses in these two continuous variable modes are not equal. We then detect these continuous variable modes using a vacuum projective measurement and balanced homodyne detection. We also investigate homodyne measurement imperfections and non-ideal outcomes, as well as success probabilities of these measurement schemes. We calculate the entanglement negativity and linear entropy of our final two qubit state, as well as fidelity against the $|\Phi^+\rangle$ Bell state in the coherent state protocol, and a phase-rotated $|\Phi^+(\alpha)\rangle$ Bell state in the cat state regime.

We demonstrate that a small amount of loss mismatch does not destroy the overall entanglement, thus demonstrating the physical practicality of this protocol.

Contents

List of Tables

List of Figures

Acknowledgements

I acknowledge support from my funding-body EPSRC (EP/M013472/1).

First and foremost, I am eternally grateful for the patience and support of my academic supervisor, Prof. Tim Spiller - transitioning from the wonderful world of Chemistry, to the seemingly impossible field of quantum physics has been challenging to say the least. I cannot thank you enough for offering me this brilliant project in the first place, but also keeping me on track throughout my studies.

On this note I also thank Dr Jaewoo Joo for teaching me how to code (another new concept to me at the start of my PhD) and for being my ever-supportive collaborator throughout my degree.

I thank Jan-Ole Risske for being my mathematical encyclopaedia throughout my PhD, as well as my fellow desk-room partner, and for supplying me with endless bags of German Haribo when it was needed most. Good luck with the rest of your studies, it's your turn next!

Next is Dr Marta Estarellas (note that I acknowledge you with the Dr you so graciously deserve). Your ever-positive attitude has taught me that we do indeed deserve to call ourselves physicists (despite being secret Chemistry undergraduates), and we really did overcome our "imposter syndrome" after all.

Nichola Shannon, I think it's fair to say that I wouldn't have even made it this far in the first place had we not have helped each other through the monstrous final year of our undergraduate degrees. Thank you for visiting me up north throughout my PhD, thank you for recognising that (despite what I have always said) I really *could* do it all along, and thank you for always being my fabulous best friend.

I thank my family for their continuous love and support, and to my parents for visiting me for plentiful museum trips and fancy dinners in York (and for being my free removal service).

Lastly, I thank my partner Joe James - I quite honestly cannot imagine how impossible living with me over the past two years has been, through all the constant tears and tantrums when "I just could not do it". You may not understand quantum mechanics, but as I have always told you, no-one does.

Declaration of Authorship

I, Ryan Charles Parker, declare that this thesis titled “A Loss Resilient Entanglement Swapping Protocol using Non-Classical States of Light”, is a presentation of original work and I am the sole author. This has not previously been presented for an award at this, or any other, University. All sources are acknowledged as References.
Part of this work has been published, in which I was first author of [1].

Chapter 1

Introduction

1.1 General Overview

Quantum information, one of the newest and arguably most exciting fields of quantum physics, relies on the use of quantum entanglement and the superposition principle for practical use in numerous technological applications, such as quantum metrology, quantum communication and quantum cryptography. Communication and cryptography (the art of encoding information) are undeniably the two most developed and relevant to the world we currently live in and are aiming for in the future.

Quantum information theory is becoming both more widely researched, and more relevant to current technological demand. Certain aims are clear in this field, and were discussed by M. Neilsen and I. Chuang; identifying new elementary classes of resources (such as the classical bit or the qubit); investigating dynamical processes in quantum mechanics (such as quantum memory); quantifying resource trade-offs as a result of dynamical processes (i.e. the minimum resources to transfer information between two parties) [2].

Most public (classical) communication schemes that are used currently rely on the difficulty of computationally calculating certain mathematical problems, such as finding the two prime factors p and q of a 1000-digit number $N = pq$ - in fact this scheme was devised by Rivest, Shamir and Adleman in 1977, in which they proposed the first *known* public-key cryptography protocol (known as the RSA protocol) [3] [4]. The simple concept behind asymmetric public-key cryptosystems, such as the RSA protocol, is that any user can access the public encryption key (consider a random string of bits, i.e. 00101011...) which they use to encode their message, however only the receiver can access the decryption key - this is entirely secure, reliant on the fact that this key is completely unavailable to anyone but the receiver [5].

In reality, this is of course not the case, and with the expansion of computer networks, the cryptography research community were tasked with devising new methods of sharing secret keys; in a public-key cryptosystem the encryption key is publicly available (i.e. accessible to anyone in the network), whereas the decryption key is available only to the two users that wish to communicate [6]. In performing public-key cryptography practically, one therefore uses the RSA protocol, relying

on hard-to-solve factorisation problems, to provide security in this key distribution scheme.

Although this factorisation problem is currently impossible to solve with modern-day technologies, cryptography protocols that rely on this security process are potentially vulnerable in the future if quantum computers are manufactured [7]. In fact, it was the derivation of a quantum algorithm by P. Shor in 1994, which introduced a method in which one could theoretically break this factorisation problem, exponentially faster than any classical computer could [8]. This fundamental lack of security poses a huge flaw for security systems reliant on hard-to-solve factorisation problems, and as such it falls to quantum (and indeed classical) cryptographers to improve these schemes to ensure unconditional security.

With this fundamental flaw in the future security of cryptosystems, one of the main challenges in quantum technologies is the prevention of information that is sent between two parties (often named Alice and Bob) being extracted by an eavesdropper (named Eve). Quantum Key Distribution (QKD) is one of the most significant elements in quantum communication, and is among the most developed quantum technologies, which promises *information-theoretic* security, guaranteed by the fundamental laws of quantum mechanics [9]. QKD can exploit quantum entanglement (discussed in Subsec. 1.2.10), although this is not a requirement, to ensure that any information that is sent between Alice and Bob that is intercepted by Eve will be detected by either Alice or Bob - if this is the case, the intercepted key that Alice and Bob have shared can simply be thrown away and they can attempt another exchange without Eve discovering any information on their shared system. In simple terms, quantum entanglement is the most non-classical manifestation of the quantum formalism, and occurs when two quantum states are combined in such a way that the states cannot be described independently [10].

For the purposes of QKD, should Eve happen to intercept and measure one of the quantum states sent between Alice and Bob, this will then alter the state of the remaining entangled qubit (in possession by Alice or Bob), which they will be able to detect [2]. Therefore, QKD offers the promise of unconditionally secure communications. QKD has possible implementations for enhanced information security for military, financial and also diplomatic causes. It is for this reason quantum communication and its counter-parts are so important for the world we live in, and emphasises the need for extensive research within this field, so as to improve security proofs further.

The BB84 (so named after C. Bennett and G. Brassard in 1984 when the protocol was developed) [11] and the E91 (developed by A. Ekert in 1991) [12] are fundamental QKD protocols, and were the first notable ones in this field to be produced. The BB84 is the original QKD scheme and is recognised as the first quantum cryptography protocol and was proven using photon polarisation states (polarisation is discussed further in Subsec. 1.2.4) for the transmission of information; this protocol also uses the one-time pad, a device which produces a completely random secret

key that is used to encrypt and decrypt information that is transmitted between Alice and Bob, and this technique is known to be secure against Eve on the condition that the key is not reused and is truly random [13].

In the BB84 scheme the photons are polarised with respect to the bit values (0 or 1) that the one-time pad generates, and are also polarised according to a randomly generated basis, rectilinear (+) and diagonal ($\times$), hence Alice has the ability to send four differently polarised photons to Bob, each of which she takes a record of. Bob then chooses a basis to perform an orthonormal measurement in, either rectilinear or diagonal, and according to quantum measurement theory all information on the initial polarisation is lost and so the photon is subsequently polarised in the direction of the basis that was used in the measurement. Finally, Bob communicates with Alice via a public channel (at this stage the security of the protocol is not impacted if Eve intercepts this channel) the basis used for his measurements. Alice responds with the basis she sent the photons in, and the results are kept if both of the bases match, or discarded, and the resultant bit string (which will probabilistically be 50% the length of the bits sent) is the shared key that is required by the protocol [14]. Furthermore, as a result of quantum measurements altering the state that is measured, Alice and Bob are only required to publicly check then discard a portion of their bit string to see how many of their results match, and if it is less than a pre-set threshold then it is indicative of an eavesdropper being present attempting to gain knowledge via measurement, which introduces detectable errors [15].

The E91 protocol manipulates quantum entanglement (note that the BB84 scheme does not) between pairs of photons shared between Alice and Bob; unlike the BB84 scheme, in the E91 photons are not sent from Alice to Bob, they are instead distributed from an entanglement source, and are then sent to Alice and Bob [16]. This is particularly useful from a practical perspective: in a real-life situation the two parties would realistically be far separated, and so distribution of photons from a central source (such as a satellite) would be required. In the E91 protocol, A. Ekert proposed the use of entanglement to share the secret random key between Alice and Bob as a result of the state correlations that arise from entangled systems [17]. The security proof of this protocol relies on violation of Bell's Inequality [18], which states, in the simplest terms, that some correlations that are actually predicted by the rules of quantum mechanics cannot be reproduced by any local theorem [19].

These two protocols perfectly describe the implementation of QKD for secure communication and since their development many schemes have been produced that manipulate the rules of quantum mechanics and information theory in various ways, such as; the SARG04 protocol, which is similar to the BB84 protocol, but instead uses attenuated laser pulses as opposed to single-photon sources, thus developing a more robust protocol [20]; the B92 protocol, derived from the BB84 scheme, the difference arising from the use of non-orthogonal states as opposed to a rectilinear and diagonal basis for polarisation [21]; decoy state QKD, the most commonly

implemented QKD protocol, in which weak coherent pulses are used for unconditionally secure information transfer [22]. H. Singh, A. Singh and D. Gupta provide a more extensive overview of QKD protocols in their review "Quantum Key Distribution: A Review" [23].

Continuous variables (CVs, as discussed in Subsec. 1.2.4) are of particular use in QKD and communication protocols, and a number of cryptographic schemes that manipulate coherent states have been produced [24, 25], and recently the most long-distance QKD protocol so far, of 100 km, has been successfully performed experimentally using CVs [26]. The practicality of using CVs is also worth noting; they are compatible with current standard optical telecommunication technologies, and so could be suitable for large-scale communication protocols [27, 28].

Overcoming detector side-channel attacks from an eavesdropper is yet another notoriously difficult problem within QKD, and other quantum communication protocols, to avoid. One solution for this is to use Measurement Device Independent QKD (MDI-QKD) schemes. In MDI-QKD, Alice and Bob prepare their states as per usual, but instead send these states to an untrusted relay (Eve), who then performs a measurement on these. This is the key point to why MDI-QKD is so attractive; in MDI-QKD it is actually *desired* for Eve to intercept the signal and measure, as it is this process that causes the wave-function collapse in the measured modes to then complete the QKD protocol, and much work has been carried out concerning this, using CVs, DVs, and hybrid schemes using both [29, 30].

Using an Entanglement Swapping (ES) protocol for QKD can resolve the issue of a third-party eavesdropping and intercepting any useful information [31]. ES is discussed further in Subsec. 1.2.11, however, simplistically ES is a scheme in which Alice and Bob, who wish to share an entangled pair of qubits, begin with separately entangled states, and by sending half of each of these pairs to a detection scheme elsewhere this causes entanglement to be subsequently shared between Alice and Bob. This is perhaps even more bizarre conceptually than entanglement itself, which usually originates via a direct interaction between two quantum states [10]; entanglement swapping requires no such interaction (aside from the initial separate entanglement generation by Alice and Bob), yet they can still share entanglement after performing ES.

As already stated, ES protocols require a joint measurement to be performed on the two halves of the quantum states sent by both Alice and Bob (see Fig. 1.8), and so if these states are the ones that are sent to Eve, which she then subsequently measures (as she will be under the impression that she is gaining useful information) then she has actually *assisted* Alice and Bob in achieving entanglement for their remaining qubits, as required in their communication protocol. This is an integral point which should be emphasised, as it is one of the most intricate and sophisticated uses of quantum entanglement, and as such ES protocols are the basis for considerable research within quantum technology.

ES is an especially advantageous approach to distributing entanglement at a distance so as to achieve long-distance quantum communication; this is as a result of the joint measurement that is performed actually guaranteeing successful entanglement [32]. This therefore highlights further the importance of this project. Establishing what may be achieved with an ES protocol, such as the one proposed in this report, is of particular use as it means the protocol can be adapted and used in multiple ways.

ES was first demonstrated experimentally in 1993 by M. Zukowski *et al.* [32], and has since been performed with discrete variables (DVs, discussed in Subsec. 1.2.4) in various cases [33–35], and also for CVs [36, 37]. CV systems typically pose the advantage of high success probability, whereas DVs are often robust against lossy channels; hence, an advantage could be gained from using both CV and DV states in what is referred to as a hybrid entanglement scheme [38], and will be investigated in this work. Both, DVs and CVs, have been extensively researched when used in entanglement swapping protocols together and have also been demonstrated experimentally [39].

One of the most fundamental, adversely impacting factors of quantum technologies to research is decoherence, and how to overcome "noisy" communication channels - in the practical quantum world we must consider the system we are observing to be open, that is to say that the environment interacts with the system, thus causing decoherence, noise and losses [40].

Throughout this thesis we propose two entanglement swapping protocols (see Chapter 2, Sec. 2.1) with the aim to produce a highly entangled pair of qubits, which could potentially be sold to a customer (or customers) for further uses within quantum communication protocols (such as QKD, as discussed). Unfortunately, it is well recognised that entanglement is a fragile resource, and breaks down in the presence of environmental noise [41], even when the quantum state is described as a photon travelling through optical fibre. Within this work we investigate photonic losses in our propagating modes (see Fig. 2.2) to demonstrate that we can still distribute a shared entangled pair of qubits between Alice and Bob, whilst tolerating a small amount of loss. Overcoming losses in optical fibres is a huge challenge within the quantum technology community, and one particularly compelling method to overcome these losses is in quantum repeater networks.

The general concept of a quantum repeater network is as follows: Alice and Bob wish to share an entangled pair of qubits, to do so they first distribute entanglement over each elementary link (node), in which quantum memories are required to ensure that these nodes store the entangled state, and then entanglement swapping experiments (as described throughout this thesis) are performed between the middle nodes in the repeater network [42]. The result is that Alice and Bob then share entanglement, despite never having directly interacted. The following schematic of Fig. 1.1 shows the straightforward concept behind quantum repeaters:

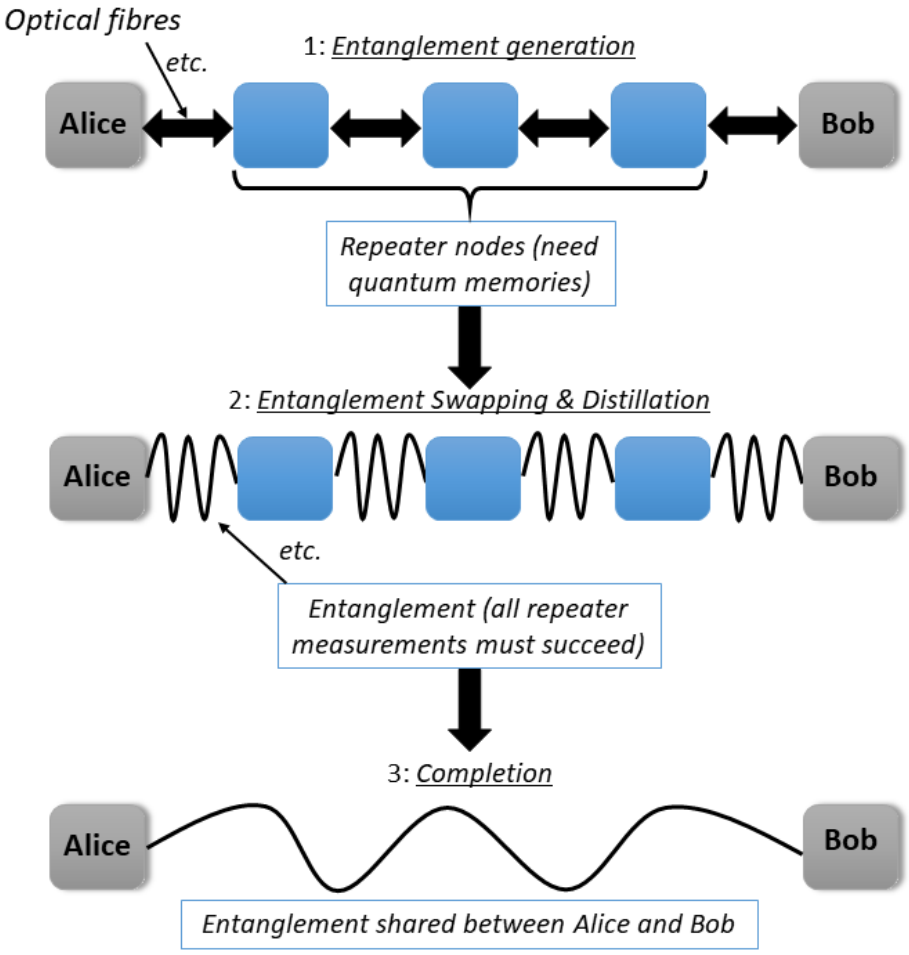

FIGURE 1.1: A schematic diagram of the general concept of a quantum repeater network. The first step is generating initial entanglement at each node (and Alice and Bob), before performing entanglement swapping (and subsequent entanglement distillation) methods between nodes, to distribute entanglement between Alice and Bob.

Note that this method also requires an entanglement distillation step (as shown in Fig. 1.1, and as discussed in detail in Chapter 6), which increases the level of entanglement shared between two qubits, at the expense of requiring multiple *lower-entanglement* pairs of qubits to do so [43]. This in turn ensures that the final entanglement shared between Alice and Bob does not break down, and of course should a single entanglement swapping experiment fail at any of these nodes then the quantum repeater process fails. Furthermore, quantum repeater networks also require quantum memories (the storage, and subsequent retrival of, quantum states [44]) to store the quantum states at each node between entanglement swapping experiments, which are currently difficult to devise at the time of writing [45]. Nonetheless, this process of dividing a lossy channel between Alice and Bob into smaller, more manageable lengths, means that quantum repeater networks are a real possibility in the future for truly long-distance quantum communication schemes in distributing entanglement [46], thus further proving the importance of entanglement swapping protocols, such as these proposed in this work.

Finally, we note here that despite the promising nature of many of these quantum cryptographic concepts, in the hopes of being able to communicate with absolute security in the near future, before many of these concepts (such as QKD, or repeater networks) can be widely adopted for commercial use, there are a number of important challenges still to address. Inherently, the actual integration of these communication networks into our current infrastructure is a challenge in itself, although we do recognise that there are indeed many protocols which work with currently built infrastructure [27]. Moreover, many of these quantum technologies are cutting-edge research, and so to keep the implementation of these at low-costs is also a huge challenge for this community [47]. Lastly, and of most importance to the work in this thesis, is overcoming photon losses when sending quantum signals through optical fibres (and indeed free-space too, although this is not considered in this work) [48]. There are many challenges left in integrating quantum technology-based architecture into our daily lives, but the possibilities of the security it brings, impacting everyone across the world, makes it an undeniably appealing and vital field of study.

We now discuss a few key concepts and definitions, required for the intricate mathematical and conceptual detail of this thesis, before presenting our proposed entanglement swapping protocols in more detail in Chapter 2.

1.2 Basic Definitions

1.2.1 The Qubit

In classical physics, and conventional digital data approaches, the bit is used as the basic unit of measure of information, and takes the values of 0 and 1. When we move into the quantum world, the most simple system in information theory is the quantum bit (qubit), and this is described by the two orthogonal states $|0\rangle$ and $|1\rangle$, thus forming an orthonormal basis for two-dimensional state space. It is important to note, however, that the qubit does not just exist in the states of $|0\rangle$ or $|1\rangle$, and this is the key difference between classical and quantum information. Using qubits it is possible to form a linear combination of states, known as a quantum *superposition*:

$$|\psi\rangle = c_0 |0\rangle + c_1 |1\rangle , \tag{1.1}$$

where c_0 and c_1 are complex numbers such that $|c_0|^2 + |c_1|^2 = 1$, since the probability of finding that qubit in either state must sum to unity. Following quantum measurement theory, upon measuring the bit value of this qubit the result is 0, with probability $|c_0|^2$, or 1, with probability $|c_1|^2$ [2], hence the state of the qubit can be described geometrically as a unit vector in a two-dimensional complex vector space. Typically, $|0\rangle$ is the vacuum state, and $|1\rangle$ is the single photon state. Alternatively, $|0\rangle$ and $|1\rangle$ could represent two orthogonal polarisation states. In this work, it will be assumed that the state $|0\rangle$ indicates a vacuum state (the quantum state with the lowest possible energy), as opposed to 'logical 0' which is the state as described above.

Qubits can also be expressed geometrically in terms of the Bloch sphere. The surface of the Bloch sphere represents the pure state space of the two-level system (the qubit), as follows:

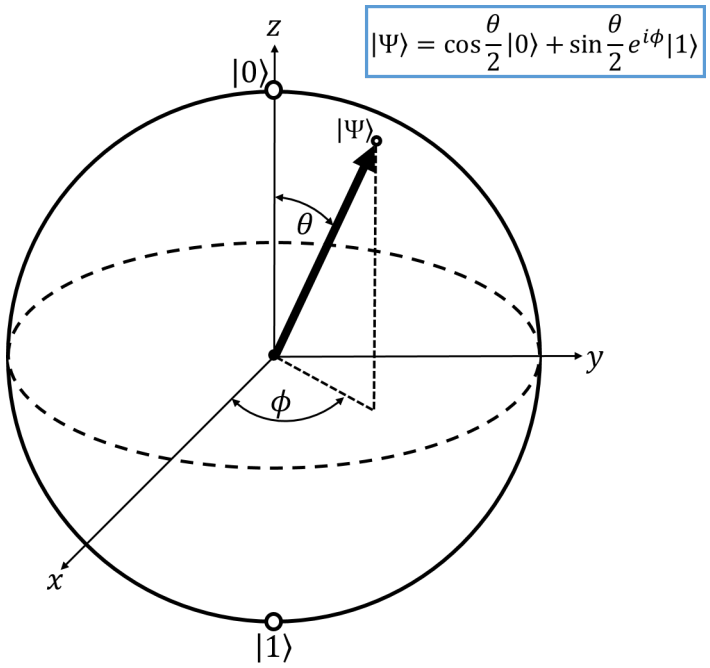

FIGURE 1.2: Bloch sphere representation of the two-level qubit state space.

(Note the equivalence of the state described by $|\Psi\rangle$ in Fig. 1.2 and the state described in Eq. 1.1). The antipodal points of the Bloch sphere correspond to the mutually orthogonal states $|0\rangle$ and $|1\rangle$ (orthogonal here meaning that the inner product of these two states is 0, such that $\langle 0|1\rangle = 0$), and so any point on the surface of the Bloch sphere denotes a pure quantum state. The Bloch sphere also parametrises mixed quantum state, hence it follows that any point that is inside the sphere (i.e. not on the surface) is described as a mixed quantum state, and can only be expressed as a density matrix, which is discussed in the following subsection.

1.2.2 A Note on Notation

In this short subsection we will briefly review our notation for Dirac brakets. Notation for such brakets can differ between authors and so it is important that we define this early on this work, particularly when we have complicated mathematical formulae, relying heavily on Dirac brakets, later in this thesis.

To indicate the mode in which a quantum state (or indeed density matrix) is in, we will use a subscript mode label. For example, if we have a single qubit superposition quantum state (i.e. as per Eq. 1.1) in mode A, then this is denoted as $|\psi\rangle_A = c_0 |0\rangle_A + c_1 |1\rangle_A$, and the complex conjugate of this state is then expressed as ${}_A\langle\psi| = c_{0A}^* \langle 0| + c_{1A}^* \langle 1|$.

Similarly, for a two qubit superposition state, each mode label refers to each respective qubit in that state, such that, for example, $|\psi\rangle_{AB} = c_0 |00\rangle_{AB} + c_1 |11\rangle_{AB}$, and again the complex conjugate is denoted as ${}_{AB}\langle\psi| = c_0^*{}_{AB}\langle 00| + c_1^*{}_{AB}\langle 11|$.

Finally, for density matrices we denote the modes in the same way as we do for quantum states, such that ρ_{AB} denotes a density matrix describing modes A and B. Notation of mode labels of a density matrix in terms of its quantum state counterparts (see Subsec. 1.2.3) is then expressed as, for example, $\rho_{AB} = |\psi\rangle_{AB}\langle\psi|$. We note that we refer to this as the "outer product" of two quantum states. The *inner* product of two quantum states in modes A and B is then expressed as ${}_{AB}\langle\psi|\psi\rangle_{AB}$ ${}_{AB}\langle\psi|\psi\rangle_{AB}$.

For clarification, in general we denote which mode we are referring to in the Dirac bra or ket by using a subscript mode label on the angled side bracket of the bra or ket.

1.2.3 Pure and Mixed Quantum States

In the most basic description, one can say that a quantum system whose state $|\Psi\rangle$ is known exactly is a pure quantum state, hence the density matrix representation of this pure state would simply be $\rho = |\Psi\rangle\langle\Psi|$, where ρ is the standard symbol for a density matrix. A superposition of pure states is also a pure state. Mathematically, we can calculate if a quantum state is pure by taking the trace of the density matrix and checking that $\mathrm{Tr}\left[\rho^2\right] = 1$ (or equivalently $\rho = \rho^2$).

It is important to note that *any* quantum state can be represented in terms of the density matrix (up to an arbitrary global phase), such that

$$\rho = \sum_i p_i |\psi_i\rangle\langle\psi_i| , \tag{1.2}$$

where p_i is the probability of the system being in the state $|\psi_i\rangle$. Note that inherently these probabilities are always non-negative, and that the normalisation condition is fulfilled by this density matrix representation such that the sum of all the probabilities is equal to unity, or $\sum_i p_i = 1$. Consider the (pure) quantum state given in Eq. 1.1 - we may express this as a density matrix as:

$$\begin{aligned} \rho = |\psi\rangle\langle\psi| &= (c_0|0\rangle + c_1|1\rangle)(c_0^*\langle 0| + c_1^*\langle 1|) \\ &= \begin{pmatrix} |c_0|^2 & c_0 c_1^* \\ c_1 c_0^* & |c_1|^2 \end{pmatrix}, \end{aligned} \tag{1.3}$$

where the superscript $*$ denotes complex conjugate, and the normalisation (trace) condition still holds in the density matrix representation, such that $|c_0|^2 + |c_1|^2 = 1$.

For a quantum state to be described as a mixed state, one can then consider this to be a probabilistic mixture (or ensemble) of the pure states of the density matrix ρ. To clarify, for ρ to be described as mixed we cannot write this as a density matrix describing a pure state. Again, it is relatively facile to determine if a density matrix

is mixed: in this case, for a mixed state the trace of the squared density matrix would never be unity, hence one would find that $\mathrm{Tr}\left[\rho^2\right] < 1$ and therefore $\rho^2 \neq \rho$.

Referring back to the Bloch sphere diagram, depicted in Fig. 1.2, the mixed state at the centre of the Bloch sphere would be described Mathematically as $\rho = \frac{1}{2}(|0\rangle\langle 0| + |1\rangle\langle 1|)$. This in fact is a maximally mixed state, hence why we depict it as being at the centre of the Bloch sphere; for a state to not be maximally mixed, only partially mixed, it would therefore be shown as not being at the centre of the Bloch sphere, nor being at the surface. Such a state could be, for example, $\rho = \frac{1}{4}|0\rangle\langle 0| + \frac{3}{4}|1\rangle\langle 1|$, or any combination of probabilities that are not equal (i.e. $p_0 \neq p_1$).

The assessment of whether ρ describes a quantum state that is pure or mixed via determining the trace of ρ^2 gives rise to another (analogous) criterion for establishing the level of purity of a state: entropy. This will be covered in more detail later on in this thesis (Sec. 2.7), as we calculate the entropy of the quantum state produced via our protocol to determine its purity.

1.2.4 Discrete vs Continuous Quantum Information

A discrete variable (DV) is one that can be characterised by a finite number of possible values.

Electromagnetic waves, viewed in terms of photons, are coupled oscillating electric and magnetic fields. The electric and magnetic fields always oscillate perpendicularly, and the polarisation of such a wave indicates the direction of the electric field [49]. The polarisation is characterised by a discrete basis of just two orthogonal states. There is an infinite number of different choices of discrete basis that one could make to describe the system (which are all related by rotations on the Bloch sphere, given in Fig. 1.2). However, the polarisation of a photon is a DV because in any of these bases you only have two states; the possible outcomes for a linear polarisation measurement are either horizontal or vertical, and for circular polarisation are left or right polarised, and cannot be anything else [50]. In fact, quite often in the field of quantum communications and computation, horizontally and vertically polarised photons (denoted $|H\rangle$ and $|V\rangle$ respectively) are utilised as DV states.

Other physical examples of DVs are angular momentum, or a spin-$\frac{1}{2}$ qubit in a magnetic field (such as an electron, with spin "up" or "down"), and these are intrinsic properties of these physical systems. In fact, spin-$\frac{1}{2}$ electrons are great applicants in a host of quantum computational applications, as they have exceptionally long coherence times (seconds) [51, 52]. In quantum information, an example of a DV system is the two-level system qubit, which may only exist as $|0\rangle$, $|1\rangle$ or a superposition of both (as described in Subsec. 1.2.1).

By contrast, a continuous variable (CV) is one that has an infinite number of possible values - that is to say that CVs are degrees of freedom associated to observables

with a continuous spectrum (but may also have observables with a discrete spectrum, but with an infinite number of levels), such as the strength of an electromagnetic field. Further examples are the position $\hat{x}$ and momentum $\hat{p}$ of a free particle, or the one-dimensional simple harmonic oscillator [53] - the one-dimensional simple harmonic oscillator requires an infinite number of basis states to fully describe it, hence why this is continuous.

To reiterate, it is the number of basis states needed that determines whether a variable is discrete (finite) or continuous (infinite). As a simple comparison of discrete and continuous variables, in terms of quantum computing one could consider a DV as *digital* data (binary) and a CV as *analog* data. In fact, there is a vast array of research that has taken place over the last few years regarding discrete and continuous hybrid systems, such as coupling a qubit (DV) to a harmonic oscillator (CV) [54], exploiting the useful nature of both DV and CV quantum states, and these hybrid systems are what we concern ourselves with in this thesis.

1.2.5 Fock States

Now that we have a clear description of discrete and continuous variables, we can consider the quantum states that will be used in this work. Fock states represent a well-defined number of particles (or "quanta"), or in the case of this work, photons, in an eigenmode of a field (such as the quantum harmonic oscillator for bosons, see Fig. 1.3) [55].

In this sense it is simple to see that Fock states are photon number eigenstates [56]; the electromagnetic field comprises an infinite number of different modes, and as such it comprises an infinite number of CV systems. Each of these modes is described by an infinite basis of Fock states for that mode, see Fig. 1.3. These separate modes can be accessed and manipulated independently, and it is possible to use some of these as approximate DV systems, and others as CV systems. This is vital when it comes to the Fock states we wish to use in this thesis, namely the zero photon and single photon states (as described later in this section).

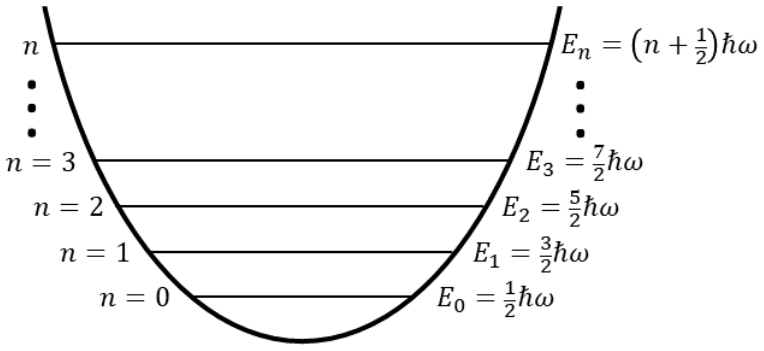

FIGURE 1.3: Diagram to represent the discrete energy levels of a quantum harmonic oscillator, of frequency ω, where E_i are the energy eigenstates of energy level $n = i$, and $\hbar = \frac{h}{2\pi}$ with h denoting Planck's Constant [57]

Fock states are a complete infinite basis of orthogonal states, and these states are used to compose/decompose CV systems. However, it is commonly accepted that (in certain cases) one can approximate that the only relevant Fock states are the vacuum and the one-photon state (corresponding to the $n = 0$ and $n = 1$ energy levels in Fig. 1.3 respectively); it then follows that the vacuum and single-photon Fock states may be considered as *approximately well-defined* DV states [58]. This approximation depends on conditions that the relevant system/setting needs to satisfy, and so for a discussion of how one could obtain a vacuum and single-photon Fock state see Subsec. 1.2.6.

Fock states are also known as number states for the simple reason that they can be mathematically expressed in Dirac notation as a single number $|n\rangle$, describing the number of quanta present in that state. For example, if we have a no photon Fock state (i.e. the vacuum state) then this would be expressed as $|0\rangle$, and for a single photon state $|1\rangle$ - in fact, these are the two specific Fock states that will be used throughout this work, as an approximate DV qubit, indicating the presence or absence of a photon. As previously stated, the number states form a complete basis, meaning $\sum_{n=0}^{\infty} |n\rangle \langle n| = \hat{I}$ [59] (where $\hat{I}$ is the identity matrix), and are also orthonormal (such that $\langle n|n'\rangle \, \delta_{nn'}$, where $\delta_{nn'}$ is the Kronecker delta), and therefore one can use this as a basis to expand any arbitrary quantum state $|\psi\rangle = \sum_n C_n |n\rangle$ of a single mode.

One can effect the addition or subtraction of a photon from a Fock state using the creation operator ($\hat{a}^\dagger$) and annihilation operator ($\hat{a}$) respectively [60]. The application of these two operators simply acts by raising the number of particles in the Fock state by 1 (for each single application of the creation operator), or vice versa, by lowering the number of particles by 1 for the annihilation operator:

$$\hat{a}^\dagger |n\rangle = \sqrt{n+1} \, |n+1\rangle \, , \quad \hat{a} \, |n\rangle = \sqrt{n} \, |n-1\rangle \, , \tag{1.4}$$

where, the creation and annihilation operator do not commute, and obey the commutation relation of $\left[\hat{a}, \hat{a}^\dagger\right] = 1$ [57]. Referring back to the discrete quantised energy level diagram of a harmonic oscillator, of Fig. 1.3, it is evident that applying the creation or annihilation operator simply causes us to move up or down an energy level - it is for this exact reason that these operators are sometimes referred to as the "ladder" operators.

1.2.6 Generating the Vacuum and Single Photon Fock State

Fock states are proving to be invaluable within the field of quantum computing and communications - a superposition of the vacuum and single photon Fock state can be used to implement a qubit, and as such we focus primarily on these Fock states within this work. We therefore move our discussion of Fock states into the practical world, and consider experimental generation of these fundamentally important quantum states.

In an ideal world, some sort of *photon gun* would be the most desirable single-photon source - a photon "gun" would work such that upon pressing a button, a single photon is produced, with zero probability of multiple photons being emitted, and with arbitrarily fast repition rates [61]. Of course, in reality the quantum world is not so simple, and so much work has been carried out in recent years in building a simple single photon source [62, 63].

In fact, experimental research into creating single photons has been carried out long before the turn of the 21st century, and the first single photon source was developed as early as 1976, in which J. F. Clauser experimentally demonstrated excitation of a calcium atom to cause emission of two photons, in which the observation of one of these emitted photons heralds the other photon [64]. This notion of using an atomic source undergoing an *atomic cascade* to produce single photons was investigated rigorously following this work, and was also performed by P. Grangier *et al.* in 1986 [65]. The process of an atomic cascade can be described simplistically by considering an atom (calcium, in the case of [65]) which is irradiated by a laser, which therefore excites the atom (via two-photon absorption). The atom then rapidly decays (referred to as the atomic cascade) into a lower energy state, emitting a photon, before decaying once more to the ground state, emitting another photon.

Weak coherent pulses (see Subsec. 1.2.7) are produced by attenuating a coherent laser beam such that the coherent state has amplitude $|\alpha| << 1$, and therefore contains, on average, significantly less than one photon per pulse [61]. These were initially investigated in research as potential approximations for a single photon source for quantum cryptography purposes [66, 67]. However, the probability that the weak coherent pulse contains two (or more) photons cannot be decreased without also lowering the probability of having a single photon present, thus inhibiting the security of any protocols relying on the presence and usage of single photons [68]. Consider an eavesdropper (Eve), who may be able to intercept this weak coherent signal between Alice and Bob - upon interception, Eve may be able to split the coherent signal into two (or more) photons, before sending the signal on to Bob. Hence, Eve is then able to constantly learn a small amount of the bits shared between Alice and Bob, which is evidently a significant flaw from a security perspective [66].

A more useful mechanism to produce single photons is spontaneous parametric down conversion (SPDC): SPDC is the process in which a non-linear crystal is pumped by a strong laser source, such that high energy photons from the pump beam are converted into two lower energy photons (known as the signal and the idler outputs) [69]. SPDC can be illustrated as follows:

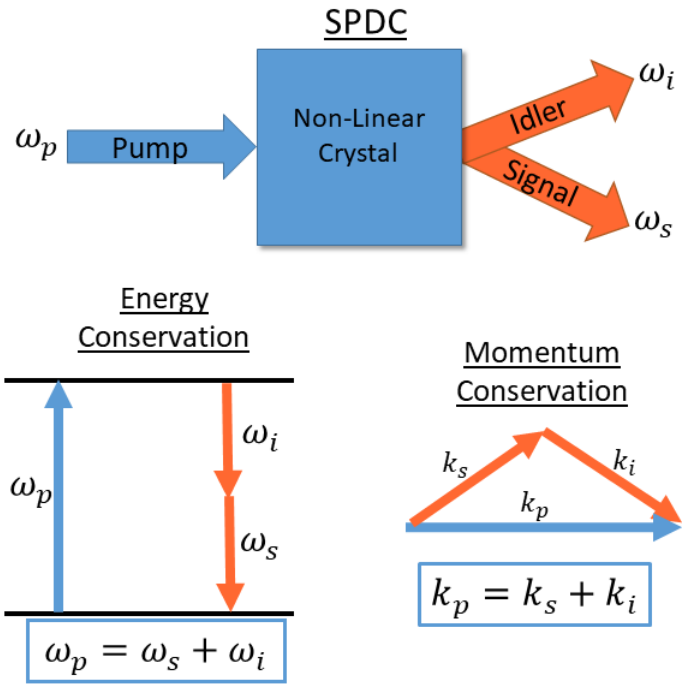

FIGURE 1.4: Diagram to illustrate the general mechanism of generating two photons (the signal and the idler) from an input photon (the pump), via use of a non-linear crystal, where ω is the frequency and k is the momentum of the photons. We also present simple diagrams to show how energy and momentum are conserved throughout this SPDC process.

Of course, as can be seen in Fig. 1.4, we are not producing a single photon via SPDC, however the detection of the idler photon heralds the presence of the signal photon. SPDC can be described mathematically using the annihilation and creation operators of Eq. 1.4 as:

$$|1\rangle_p |0\rangle_s |0\rangle_i \rightarrow \hat{a}_p \hat{a}_s^\dagger \hat{a}_i^\dagger |1\rangle_p |0\rangle_s |0\rangle_i = |0\rangle_p |1\rangle_s |1\rangle_i \,, \tag{1.5}$$

where, the subscripts p, s and i denote the pump, signal and idler beams respectively. The above equation also informs us why this process is referred to as *spontaneous* - the initial signal and idler modes are in vacuum states and as such "spontaneously" gain a single photon in each mode. As this process is also described as *parametric* the total energy and momentum of the field is conserved [70].

SPDC was first presented theoretically in 1970 by D. N. Klyshko *et al.* [71] (and later by C. Hong and L. Mandel [72, 73]), and as early as 1970, D. Burnham and D. Weinberg experimentally verified that the optical fields produced via SPDC are correlated both temporally and spatially [74]. By temporal correlations, we mean that the two photons that are emitted do so at the same time (refer to Eq. 1.5), and spatial correlations refer to the fact that the output photons are emitted from the same point.

More recently, collecting single (or two) fluorescence photons from nanoemitters (i.e. semi-conducting quantum dots and defect centres in solid state materials such

as diamond) have been studied as sources of single photons, as this process is typically more efficient than SPDC in generating single photons [75–77]. The first work demonstrating experimentally the two-photon emission from a semi-conductor quantum dot was performed in 2008 by A. Hayat *et al.* [78], and since then has sparked a huge amount of research output in this field, and as such semi-conductors are the current likely candidates for a true single-photon generating device [79].

Ultimately, it should be evident by now that there are many challenges that have been faced in generating single photons "on demand", and the limitations strongly depend on the target applications; however, the most general problem faced by this community right now is in developing a highly efficient, compact and robust device, able to produce either one or two photons at the press of a button.

1.2.7 Coherent States and Schrödinger Cat States

A coherent state of a harmonic oscillator, or a single bosonic field mode, such as a mode of the electromagnetic field, is the unique eigenstate of the annihilation operator $\hat{a}$, with eigenvalue α:

$$\hat{a}\,|\alpha\rangle = \alpha\,|\alpha\rangle\,, \tag{1.6}$$

where $|\alpha\rangle$ represents the coherent state of amplitude α (where α is a complex number [50]). Coherent states are CV states, and as such α can in principle take any value. It is vital here to note that the coherent state can be represented in the basis of Fock states, and as such is a summation of discrete variable states as follows:

$$|\alpha\rangle = e^{-\frac{|\alpha|^2}{2}} \sum_{n=0}^{\infty} \frac{\alpha^n}{\sqrt{n!}}\,|n\rangle\,, \tag{1.7}$$

where $|n\rangle$ is the Fock number state [60] (this description of a coherent state is invaluable within this work and will be covered in detail throughout the calculations).

Coherent states are not orthogonal [80]: consider two coherent states of different amplitude, described as $|\alpha\rangle$ and $|\beta\rangle$, if one uses the Fock state basis representation (as per Eq. 1.7) it then follows that:

$$\begin{aligned}
\langle\beta|\alpha\rangle &= e^{-\frac{|\alpha|^2}{2}-\frac{|\beta|^2}{2}} \sum_{n=0}^{\infty}\sum_{m=0}^{\infty} \frac{(\beta^*)^n\alpha^m}{\sqrt{n!m!}}\,\langle n|m\rangle \\
&= e^{-\frac{|\alpha|^2}{2}-\frac{|\beta|^2}{2}} \sum_{n=0}^{\infty} \frac{(\beta^*\alpha)^n}{n!} \\
&= e^{-\frac{|\alpha|^2}{2}-\frac{|\beta|^2}{2}+\beta^*\alpha} = e^{\frac{\beta^*\alpha-\beta\alpha^*}{2}}\, e^{\frac{-|\beta-\alpha|^2}{2}}
\end{aligned} \tag{1.8}$$

hence coherent states are not orthogonal. Of course, in the limit of large differences between the amplitudes of α and β the coherent states become *nearly* orthogonal - essentially, for two coherent states to be effectively orthogonal we require that the last exponential, $e^{\frac{-|\beta-\alpha|^2}{2}}$, in Eq. 1.8 be vanishingly small.

As discussed in the previous section, the number states form an orthonormal and complete basis, and as such may be used to expand any arbitrary quantum state. Conversely, coherent states form an *overcomplete* basis, satisfying the completeness relation $\frac{1}{\pi}\int \mathrm{d}^2\alpha\,|\alpha\rangle\langle\alpha| = \hat{I}$, where $\mathrm{d}^2\alpha = \mathrm{dRe}(\alpha)\mathrm{dIm}(\alpha)$ [81]. An overcomplete basis is one that has more states than are required to express any other arbitrary quantum state in terms of the coherent state basis [82]. Relating back to Eq. 1.8, $\langle\alpha|\beta\rangle \neq 0$ for $\alpha \neq \beta$, we can then say that the set $\{|\alpha\rangle\}$ is overcomplete. For a proof of the completeness relation here, refer to Appendix A.

The coherent state is a *Poissonian distribution* (a discrete probability distribution) of Fock states [83], and so if we have a single photon Fock state $|1\rangle$, this is not equivalent to a coherent state of amplitude $|\alpha| = 1$. Instead, the coherent state of amplitude $|\alpha| = 1$ is a quantum state with *mean photon number* of 1 (and thus would be expressed in terms of photon number probability as a distribution with the maximum probability at $n = 1$). In fact, $|\alpha|$ denotes the amplitude of the coherent state, with the mean photon number $\langle\hat{n}\rangle$ given by:

$$\langle\hat{n}\rangle = \langle\hat{a}^\dagger\hat{a}\rangle = |\alpha|^2, \tag{1.9}$$

hence, for a coherent state of amplitude $|\alpha| = 1.5$ then the average photon number is $\langle\hat{n}\rangle = 1.5^2 = 2.25$.

The coherent state can be created from a vacuum state via use of the displacement operator $\hat{D}(\alpha)$ [55]:

$$|\alpha\rangle = e^{\alpha\hat{a}^\dagger - \alpha^*\hat{a}}\,|0\rangle = \hat{D}(\alpha)\,|0\rangle\,, \tag{1.10}$$

where, $\hat{a} = \hat{x} + i\hat{p}$ and $\hat{a}^\dagger = \hat{x} - i\hat{p}$. Here, $\hat{x}$ and $\hat{p}$ are the dimensionless field quadratures (see Fig. 1.5 and Eq. 1.11). These quadrature operators represent continuous-variable observables that are able to be measured via homodyne detection [84], which will be discussed in the next chapter (Chapter 2, Sec. 2.6) as one of the measurements we apply to our system. We remark here that some authors define these quadrature operators as $\hat{X} = \frac{1}{\sqrt{2}}(\hat{a} + \hat{a}^\dagger)$ and $\hat{P} = \frac{i}{\sqrt{2}}(\hat{a}^\dagger - \hat{a})$, however, we define the quadrature operators in this work as:

$$\hat{x} = \frac{1}{2}(\hat{a} + \hat{a}^\dagger), \quad \text{and} \quad \hat{p} = \frac{\mathrm{i}}{2}(\hat{a}^\dagger - \hat{a}). \tag{1.11}$$

It is also important to note that the canonical coherent state is a state of minimum uncertainty, such that

$$\Delta x = \Delta p = \frac{1}{2}, \tag{1.12}$$

where Δx and Δp are the standard deviations of the position and momentum respectively.

A coherent state can be represented in terms of position and momentum phase space as:

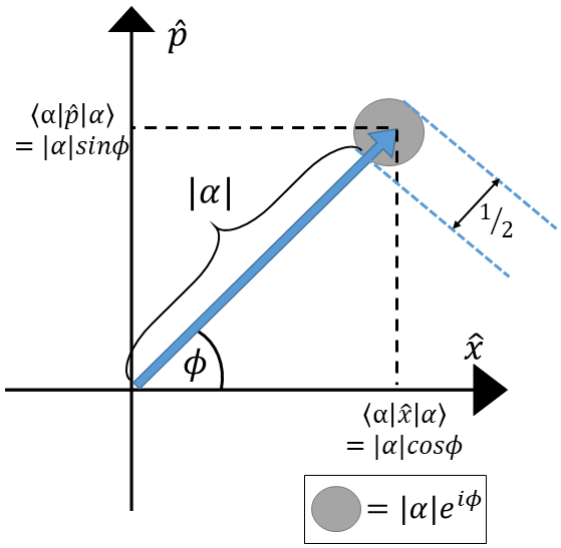

FIGURE 1.5: Diagram to represent the state space occupied by the coherent state $|\alpha\rangle$, where $\hat{x}$ and $\hat{p}$ are the field quadratures (dimensionless operators), ϕ is the phase angle of the coherent state, $|\alpha|$ is the amplitude of the state, and the value of $\frac{1}{2}$ is the uncertainty (see Eq. 1.12).

Note that in Fig. 1.5 the expectation value of the variables, $\hat{x}$ and $\hat{p}$, given the state $|\alpha\rangle$, is equal to the amplitude ($|\alpha|$) of the coherent state, multiplied by the cosine or sine of the phase angle. To derive the field quadratures $\hat{x}$ and $\hat{p}$ let us first consider an arbitrary quadrature as a function of a phase angle θ:

$$\hat{x}_\theta = \frac{1}{2}\left(\hat{a}e^{-\mathrm{i}\theta} + \hat{a}^\dagger e^{\mathrm{i}\theta}\right), \tag{1.13}$$

and so we can now adjust the phase angle θ to give us the specific quadratures we desire. In this manner, we then set $\hat{x}_{\theta\to 0} = \hat{x}$ and $\hat{x}_{\theta\to\frac{\pi}{2}} = \hat{p}$, which then returns the expressions for position and momentum as defined in Eq. 1.11, where clearly $\hat{p}$ is equivalent to $\hat{x}$ but rotated by $\frac{\pi}{2}$ in phase space. Following this, the coherent state expectation values are then:

$$\langle\hat{x}\rangle = \frac{1}{2}(\alpha + \alpha^*) = \mathrm{Re}\,\alpha, \quad \langle\hat{p}\rangle = \frac{1}{2\mathrm{i}}(\alpha - \alpha^*) = \mathrm{Im}\,\alpha, \tag{1.14}$$

where we have made use of $\alpha = \alpha_x + \mathrm{i}\alpha_y$ and $\alpha^* = \alpha_x - \mathrm{i}\alpha_y$.

Intrinsically, the uncertainty in $\hat{x}$ and $\hat{p}$ of any coherent state is equally distributed in all directions (see Fig. 1.5, and also Eq. 1.12). This is unlike the squeezed state, which is represented as an ellipse in phase space (thus the name "squeezed") [85], and therefore the uncertainty is not equally distributed in all directions - however there is still no violation of the Heisenberg uncertainty principle limit of $\Delta x \Delta p \geq \frac{1}{4}$, where Δx and Δp are the standard deviations of the position and momentum, as defined in Eq. 1.12 [86].

Coherent states possess the ability of existing in a superposition state, and are known as Schrödinger Cat States, or Coherent Superposition States (CSSs) and will

be used throughout this work. These non-classical states of light were first introduced by V. V. Dodonov *et al.* in 1974 [87]. These states can be simplistically shown in the following diagrams of the cat superposition phase space:

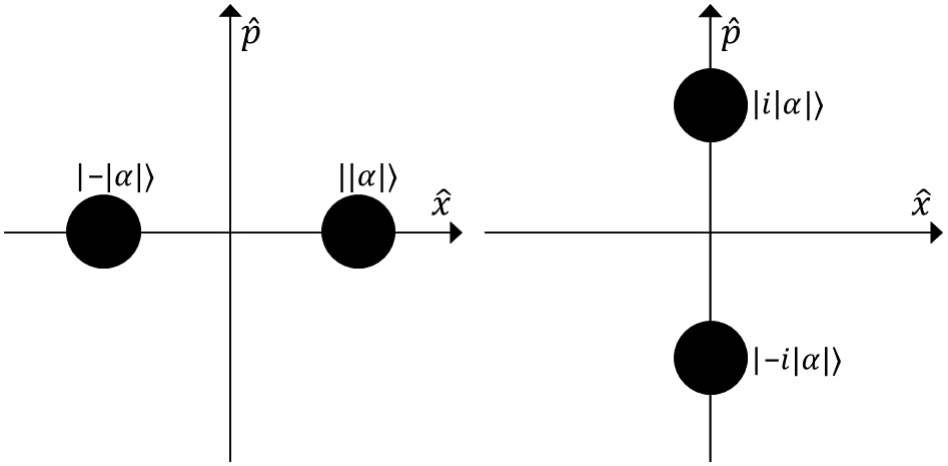

FIGURE 1.6: Diagram to represent the cat state $|CSS^{\pm}_{\alpha}\rangle = N^{\pm}_{\alpha}(||\alpha|\rangle \pm |-|\alpha|\rangle)$ and the *phase-rotated* cat state $|CSS^{\pm}_{\mathrm{i}\alpha}\rangle = N^{\pm}_{\alpha}(|\mathrm{i}|\alpha|\rangle \pm |-\mathrm{i}|\alpha|\rangle)$ (given in Eq. 1.15, where $\hat{x}$ and $\hat{p}$ are the field quadratures (dimensionless operators), as given in Eq. 1.11.

Two-component cat states are superpositions of coherent states with opposite phase. For example, the ones that will be used in this work are:

$$\begin{aligned} |CSS^{\pm}_{\alpha}\rangle &= N^{\pm}_{\alpha}(||\alpha|\rangle \pm |-|\alpha\rangle\,|), \\ |CSS^{\pm}_{\mathrm{i}\alpha}\rangle &= N^{\pm}_{\alpha}(|\mathrm{i}|\alpha|\rangle \pm |-\mathrm{i}|\alpha\rangle\,|), \end{aligned} \tag{1.15}$$

where, $N^{\pm}_{\alpha}$ is the normalisation factor, and $N^{\pm}_{\alpha} = \frac{1}{\sqrt{2(1\pm e^{-2|\alpha|^2})}}$. It is clear, observing Fig. 1.6, where each of the coherent states have arisen from. Also note that the "phase-rotated cat state" ($|CSS^{\pm}_{i\alpha}\rangle$) is simply the "standard" cat state ($|CSS^{\pm}_{\alpha}\rangle$) that has been rotated by a factor of $\phi = \frac{\pi}{2}$ in the complex α plane (see the phase-space representation of a coherent state in Fig. 1.5).

Importantly we should point out that cat states are referred to as either "even" or "odd", dependent on the choice of the relative phase that exists between the superposed states. For example, consider the cat state to be written as:

$$|\psi_{cat}\rangle = \mathcal{N}(|\alpha\rangle + e^{\mathrm{i}\Phi}\,|-\alpha\rangle), \tag{1.16}$$

where the normalisation factor is given as $\mathcal{N}$. Clearly, the state shown above in Eq. 1.16 is still a superposition of two coherent states, and are still separated in phase by a factor $\frac{\pi}{2}$. However, if we now set the *relative* phase Φ in Eq. 1.16 to $\Phi = 0$ we obtain an even cat state given as $|CSS^{+}_{\alpha}\rangle = N^{+}_{\alpha}(||\alpha|\rangle + |-|\alpha|\rangle)$, and if we set $\Phi = \pi$ we create the odd cat state, given as $|CSS^{-}_{\alpha}\rangle = N^{-}_{\alpha}(||\alpha|\rangle - |-|\alpha|\rangle)$ [80]. However, as previously stated, within this work we are concerned only with using even cat states.

Also note that there is another widely accepted form of the cat state, which is namely the Yurke-Stoler cat state (as introduced by B. Yurke and D. Stoler in 1986 [88]), which takes the form:

$$|\psi_{YS}\rangle = \frac{1}{\sqrt{2}}(|\alpha\rangle + \mathrm{i}\,|\alpha\rangle). \tag{1.17}$$

This form of the cat state clearly stems from the generalised form given in Eq. 1.16, but for $\Phi = \frac{\pi}{2}$, and will be discussed further in the next section, Subsec. 1.2.8.

Lastly, we should discuss what happens to cat states if we take the large amplitude ($|\alpha|$) limit: by taking $|\alpha|$ large enough two coherent states in superposition become *quasi-orthogonal* [89]. The suffix "quasi" here referencing the fact that these states are not *truly* orthogonal, however in the limit of $|\alpha| = 2.0$ the overlap of two coherent states, given as $\langle\alpha|{-\alpha}\rangle = e^{-2|\alpha|^2} < 10^{-3}$. Evidently, this overlap is minimal, and so it is clear why these can be considered as effectively orthogonal, provided that the amplitude $|\alpha|$ is large enough, such that the coherent states in superposition do not overlap. In fact, this overlap (or lack thereof) dependent on the amplitude of the coherent states in superpositions is vital when it comes to our proposed entanglement swapping protocol throughout this work, and this will be discussed later once results have been presented.

Conversely, even and odd cat states are orthogonal to each other, for all α. This is easily calculated as the overlap between an even and an odd cat state as:

$$\begin{aligned}\langle CSS^{+}_{\alpha}|CSS^{-}_{\alpha}\rangle &= N^{+}_{\alpha}N^{-}_{\alpha}(\langle\alpha| + \langle-\alpha|)(|\alpha\rangle - |-\alpha\rangle) \\ &= N^{+}_{\alpha}N^{-}_{\alpha}(1 - e^{-|\alpha|^2} + e^{-|\alpha|^2} - 1) = 0.\end{aligned} \tag{1.18}$$

Hence, even and odd cat states are orthogonal for all α, and as such can be distinguished by a photon number measurement, as even cat states contain only even numbers of photons, and odd cat states contain only odd [56].

1.2.8 Generating Coherent State Superpositions

Within this thesis, we will discuss extensively the use of coherent state superpositions (so-called Schrödinger cat states). It is therefore essential that we have some appreciation of how these states are generated experimentally. Since the realisation that coherent states were widely applicable for usage in continuous variable quantum cryptography [90], there has been a vast number of theoretical and experimental research papers on how to generate these non-classical states of light, and so in this section we give only a brief overview of how one could feasibly prepare a cat state with current technology.

Firstly we note here that, depending on the intended purpose of the cat state, these states of light can be made in various ways - within the work in this thesis we are only concerned with cat states which occupy freely propagating optical modes. As such, we are not interested on the generation of cat states in stationary modes,

such as optical states confined to an optical cavity via quantum electrodynamics experiments as per the methods given in [91, 92].

Cat states occupying freely propagating optical modes have been able to be produced experimentally since the last few decades of research began on this topic. Via use of the optical Kerr effect, in 1986 B. Yurke and D. Stoler successfully demonstrated how one could create a cat state (of the form Eq. 1.17) from the unitary evolution of a single coherent state [88]. The optical Kerr effect, in simple terms, causes the refractive index of a material to change when one applies an external electric field [93], and many experimental methods to produce coherent state superpositions have exploited the Kerr effect and are still commonly used at the time of writing [94, 95]. In fact, the reason cat states can be made via exploitation of the Kerr Effect is due to another phenomenon which arises here, known as "self-phase modulation" - when light passes through a Kerr-like medium (material or liquid) exhibiting the optical Kerr effect, there is a change in the phase of the light pulse (dependent on the intensity of the light) [96].

To mathematically model how the Yurke-Stoler cat state of Eq. 1.17 was made, we first begin with a coherent state (as defined in Eq. 1.7), but apply an interaction Hamiltonian of the form $\hat{H}_I = \hbar K(\hat{a}^\dagger \hat{a})^2 = \hbar K \hat{n}^2$, in which $\hbar$ is Planck's constant, $\hat{n}$ is the photon number operator, and K is proportional to a third-order non-linear susceptibility $\chi^{(3)}$. Note here that by "non-linear susceptibility" we refer to the property of non-linear optical media in which the polarisation of the media does not respond linearly to an applied electrical field [97] - the field of non-linear optics is not relevant to the work carried out in this thesis and so we do not discuss this concept in any further detail. Applying the interaction Hamiltonian $\hat{H}_I$ to the coherent state of Eq. 1.7, for time t, gives:

$$|\psi_{YS}(t)\rangle = e^{-\frac{\mathrm{i}\hat{H}_I t}{\hbar}} |\alpha\rangle = e^{-\frac{|\alpha|^2}{2}} \sum_{n=0}^{\infty} \frac{\alpha^n}{\sqrt{n!}} e^{-\mathrm{i}Kn^2 t} |n\rangle . \tag{1.19}$$

Finally, if we set $t = \frac{\pi}{2K}$, then $e^{-\mathrm{i}Kn^2 t} = e^{-\frac{\mathrm{i}\pi n^2}{2}}$, and so for $e^{-\frac{\mathrm{i}\pi n^2}{2}} = 1$ then n must be even, and for $e^{-\frac{\mathrm{i}\pi n^2}{2}} = \mathrm{i}$, then n must be odd. It therefore follows that we have:

$$\left|\psi_{YS}\left(\frac{\pi}{2K}\right)\right\rangle = \frac{1}{\sqrt{2}} e^{-\frac{\mathrm{i}\pi}{4}} (|\alpha\rangle + \mathrm{i}\,|-\alpha\rangle), \tag{1.20}$$

which is in fact identical (ignoring the overall phase factor of $e^{-\frac{\mathrm{i}\pi}{4}}$) to the standard Yurke-Stoler cat state as defined in Eq. 1.17 [98].

Unfortunately, it is widely known now that the optical Kerr effect is usually very weak at the single-photon level [99], and light attenuation is not negligible at the level required to generate a coherent state superposition [100]. As such, there has been a lot of research governing various alternate methods of generating photonic cat states, that do not rely on this non-linear optical phenomenon.

One such method is via photon subtraction, due to its simplistic implementation [101]; by subtracting a single photon from a squeezed vacuum, transmitting the vacuum through a weakly reflecting beam-splitter and finally, via heralded photon detection in the reflected beam, low-amplitude cat states can be generated [102]. Note here that a squeezed vacuum state is a coherent state of very low amplitude, but with $|\alpha| > 0$ (hence is no longer a true vacuum state), with unequal uncertainties in the position and momentum phase-space [103].

The initial notion of photon subtraction to produce low-amplitude cat states was proposed by M. Dakna *et al.* in 1996 [104], in which they recognised that squeezed vacuum states are strong approximations to a cat state of low-amplitude [105]. Interestingly, the limit of low-amplitude cat states is particularly useful in this thesis, as will be shown later that we in fact prefer to have cat states of amplitude $1.0 \leq |\alpha| \leq 2.5$ for use in our proposed entanglement swapping protocols. We also reference here that this method of producing cat states is also possible via subtraction of two or three photons, which results in a slightly higher amplitude cat state [106, 107]. In fact, there are an enormous number of various experimental methods used to produce cat states via photon subtraction and heralded photon detection.

Although we have only discussed brief possible techniques to produce optical cat states here, we do recognise that there are many more potential methods, such as optical back-action evasion schemes [108] (a similar, but more complicated, scheme than photon subtraction that relies on the use of two-mode squeezed vacuum states and photon counting detectors). For a highly comprehensive literature review on the generation of freely propagating cat states, refer to [56].

1.2.9 Beam-Splitters

A beam-splitter (BS) is an optical device that mixes two incident beams (or channels/modes), with the possibility of making these entangled for certain inputs [109]. The BS device itself consists of a semi-reflective mirror, which is able to reflect or transmit a beam of input light depending on the mirror's reflectivity [110]. Beam-splitters are invaluable within the field of quantum technology, and will be used in this work to theoretically model the loss that may occur in a channel [111], and also to entangle the lossy propagating modes prior to measuring them.

Schematically, a generalised BS (of transmission coefficient T) can be represented as follows:

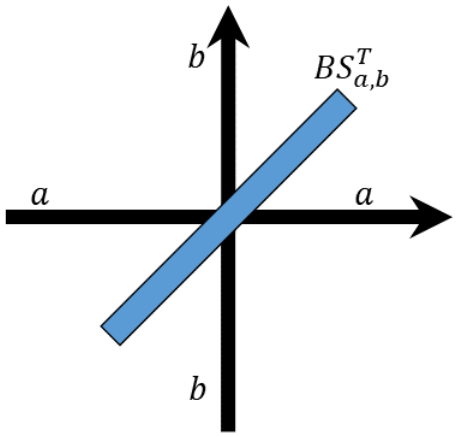

FIGURE 1.7: A diagram to represent a generalised beam-splitter (BS^T), of transmission coefficient T, acting on two modes described by the annihilation operators $\hat{a}$ and $\hat{b}$.

Mathematically there are various conventions for applying a BS operation to a quantum state, however, here we present a derivation which is adapted from P. Kok *et al.* [112].

We define the reflection and transmission coefficients (the probability amplitudes) of the BS, as $R = \sin^2\xi$ and $T = 1 - R = \cos^2\xi$, respectively (for $R = |r|^2$ and $T = |t|^2$, where r is the reflection amplitude and t is the transmission amplitude). Note that within the theoretical calculations using beam-splitters in this work, it shall be assumed that the beam-splitter itself is entirely lossless - this means that 100% of the beam is transmitted and reflected [113–115]; that is to say that $R+T = 1$. We model photon loss using a beam-splitter implementation in this work by assuming that we do not know the exact values for R and T, and so the mathematical interpretation of the operator will be denoted BS^T (hence, if a beam-splitter equally splits two incident beams then the operator would be $BS^{1/2}$).

The action of the BS depicted in Fig. 1.7 on any initial quantum state is then given by a unitary operator ($\hat{U}_{BS}$):

$$\hat{U}_{BS} = \exp\Big[-\mathrm{i}\xi\left(e^{\mathrm{i}\kappa}\hat{a}^\dagger\hat{b} + e^{-\mathrm{i}\kappa}\hat{b}^\dagger\hat{a}\right)\Big], \tag{1.21}$$

where ξ and κ are phase angles, and the unitary relation $\hat{U}^\dagger_{BS}\hat{U}_{BS} = \hat{I}$ applies to this BS operator, for identity operator $\hat{I}$. Intrinsically, the action of this unitary operator on a vacuum state acts as the identity, such that $\hat{U}_{BS}\,|0\rangle = |0\rangle$.

Using the BS schematic of Fig. 1.7, we denote our photonic modes as a and b (with annihilation operators $\hat{a}$ and $\hat{b}$ respectively), where the probability amplitudes for the output modes are then denoted $\cos\xi$ and $\sin\xi$ respectively, and so in operator form this gives [116]:

$$\hat{U}_{BS}\hat{a}^\dagger\hat{U}^\dagger_{BS} = \cos(\xi)\hat{a}^\dagger - \mathrm{i}e^{-\mathrm{i}\kappa}\sin(\xi)\hat{b}^\dagger, \tag{1.22}$$

$$\hat{U}_{BS}\hat{b}^\dagger\hat{U}^\dagger_{BS} = -\mathrm{i}e^{\mathrm{i}\kappa}\sin(\xi)\hat{a}^\dagger + \cos(\xi)\hat{b}^\dagger. \tag{1.23}$$

Within this work we set the phase angle as $\kappa = -\pi/2$, thus the output modes become:

$$\hat{U}_{BS}\hat{a}^\dagger\hat{U}_{BS}^\dagger = \cos(\xi)\hat{a}^\dagger + \sin(\xi)\hat{b}^\dagger, \tag{1.24}$$

$$\hat{U}_{BS}\hat{b}^\dagger\hat{U}_{BS}^\dagger = -\sin(\xi)\hat{a}^\dagger + \cos(\xi)\hat{b}^\dagger, \tag{1.25}$$

using $e^{\frac{\pm i\pi}{2}} = \pm i$. We note that phase shifts for the reflected and transmitted beam-splitter outputs are dependent on the material (the coating) of the beam-slitter [117].

As an example to show how this model for a BS works, consider a single photon input in mode a and a vacuum (no photon) state in mode b. The single photon in mode a is mathematically given by the action of the creation operator on this mode: $\hat{a}^\dagger |0\rangle_a = |1\rangle_a$. We now wish to model a 50:50 BS effect on these input modes, and so we apply the unitary operator given in Eq. 1.21 to the input states (as well as the relations in Eq. 1.25), as follows:

$$\begin{aligned}\hat{U}_{BS}\hat{a}^\dagger |0\rangle_a |0\rangle_b &= \hat{U}_{BS}\hat{a}^\dagger\hat{U}_{BS}^\dagger\hat{U}_{BS} |0\rangle_a |0\rangle_b \\ &= (\cos(\xi)\hat{a}^\dagger + \sin(\xi)\hat{b}^\dagger) |0\rangle_a |0\rangle_b \\ &= \frac{1}{\sqrt{2}}(\hat{a}^\dagger + \hat{b}^\dagger) |0\rangle_a |0\rangle_b = \frac{1}{\sqrt{2}}(|0\rangle_a |1\rangle_b + |1\rangle_a |0\rangle_b),\end{aligned} \tag{1.26}$$

where we have set $\cos\xi = \sin\xi = \frac{1}{\sqrt{2}}$ (for $\xi = \frac{\pi}{4}$), as we are considering a 50:50 BS here, and used the unitary relation $\hat{U}_{BS}^\dagger\hat{U}_{BS} = \hat{I}$ in the first step; this unitary operator is what we define and use as the BS operator throughout the rest of this thesis. It is simple to see that the output state given above is in fact the $|\Psi^+\rangle = \frac{1}{\sqrt{2}}(|0\rangle |1\rangle + |1\rangle |0\rangle)$ Bell state, which will be discussed in the next section.

In fact, the process described above is a purely quantum manifestation that arises when one injects a single photon and a vacuum state as inputs into a 50:50 BS; we have no way of knowing exactly which mode the single photon will be output to, as the probabilities of that single photon being transmitted or reflected via the BS are equal, hence the output state is entangled.

In the next chapter, we further this notion of beam-splitting to model photon losses that occur in a coherent state as it propagates through lossy optical fibre, and also apply the 50:50 BS method described above to two input coherent states.

1.2.10 Entanglement

Quantum entanglement is one of the most striking phenomena in quantum mechanics, and is an invaluable resource in the world of quantum information, technology, communication, computation and more. Entanglement occurs when two or more particles (such as qubits, photons or even ions) are combined in such a way that the quantum states of the particles cannot be described independently - that is to say that the resultant state cannot be factorised (or written as a product state). A product state describing two systems, $|\psi\rangle_A$ and $|\psi\rangle_B$, can be factorised such that

$|\psi\rangle = |\psi\rangle_A \otimes |\psi\rangle_B$ and, as opposed to what occurs with states that are entangled, system A can be measured without losing any of the information about system B.

The most notable two-qubit entangled states that are used in the field of quantum information and technology are the Bell states, and can be represented as follows:

$$\left|\Phi^{\pm}\right\rangle_{AB} = \frac{1}{\sqrt{2}}(|00\rangle_{AB} \pm |11\rangle_{AB}), \tag{1.27}$$

$$\left|\Psi^{\pm}\right\rangle_{AB} = \frac{1}{\sqrt{2}}(|01\rangle_{AB} \pm |10\rangle_{AB}). \tag{1.28}$$

It is clear that the A and B channels cannot be factorised mathematically in the above Bell states, and so these are described as entangled states. Moreover, we can specifically refer to the Bell states as *maximally* entangled states; "maximally" because the entropy of the mixed state of B is at its maximum when A is traced out (and vice versa). This notion of entropy will be addressed throughout this thesis, and the explicit formula is given in Sec. 2.7. As an example, if we trace out state B in the $|\Phi^+\rangle_{AB} = \frac{1}{\sqrt{2}}(|00\rangle_{AB} + |11\rangle_{AB})$ Bell state, then state A is described by:

$$\begin{aligned}
\mathrm{Tr}_B\left[\rho_{AB}\right] &= \mathrm{Tr}_B\left[\left|\Phi^+\right\rangle_{AB}\left\langle\Phi^+\right|\right] = \mathrm{Tr}_B\left[\frac{1}{2}(|00\rangle_{AB} + |11\rangle_{AB})(\langle 00|_{AB} + \langle 11|_{AB})\right] \\
&= \mathrm{Tr}_B\left[\frac{1}{2}(|00\rangle_{AB}\langle 00| + |00\rangle_{AB}\langle 11| + |11\rangle_{AB}\langle 00| + |11\rangle_{AB}\langle 11|)\right] \\
&= \frac{1}{2}(|0\rangle_A\langle 0|_B\langle 0|0\rangle_B + |0\rangle_A\langle 1|_B\langle 0|1\rangle_B + |1\rangle_A\langle 0|_B\langle 1|0\rangle_B + |1\rangle_A\langle 1|_B\langle 1|1\rangle_B) \\
&= \frac{1}{2}(|0\rangle_A\langle 0| + |1\rangle_A\langle 1|),
\end{aligned} \tag{1.29}$$

which is a maximally mixed single qubit state.

When states are entangled, classically-counter-intuitive features arise, such that the entangled states can be separated over arbitrarily large distances and upon quantum measurement (such as position or momentum) of one of the states, the result of the other state will be perfectly correlated. For example, consider the Bell state detailed in Eq. 1.27: this two-particle entangled state possesses the characteristics that each particle exists in a superposition of $|0\rangle$ and $|1\rangle$, and so if one of the particles is measured and found to be in the state $|0\rangle$, then it follows that the remaining particle must also be $|0\rangle$. Note that in Eq. 1.27 the $|\Phi^{\pm}\rangle_{AB}$ state measurement outcomes give perfect correlations, and the $|\Psi^{\pm}\rangle_{AB}$ state in Eq. 1.28 give perfect anti-correlations of measurements on A and B in this basis.

Although this may give the superficial impression of superluminal (faster than the speed of light) information transfer between very distant parties, it is not possible to communicate or send information faster than the speed of light [118]. The reason for this is because intrinsically one still needs to consider classical communications for this to work. Let us assume that a party named Alice is in possession of mode A and a party named Bob is in possession of B: if Alice measures her particle and finds that the state was $|0\rangle_A$, then we know, following the laws of quantum entanglement,

that Bob's state therefore must be in state $|0\rangle_B$. However, Bob cannot possibly know that his state is in fact $|0\rangle_B$ without Alice communicating her result to him, which inherently requires a classical communication link (such as a telephone call) between Alice and Bob.

This phenomenon was described in 1935 in a renowned paper by Einstein, Podolsky and Rosen and became part of their so-called EPR Paradox, in which they stated that the wave-function of a quantum state does not provide a complete description of physical reality [119]. It was claimed that for entangled measurement correlations to be possible then there must be a violation of local realism, the theory that limits cause-and-effect to the speed of light ("locality") and also states that any particle must have a real, pre-existing value for any measurement ("realism"). This is counter-intuitive to how we now know entanglement works, and has since been proven experimentally, proving that the local realist view of the world is not compatible in quantum theory as it is a classical theory.

1.2.11 Entanglement Swapping

Entanglement swapping is the process in which two halves of two entangled pairs of particles become entangled and are then measured. As a result of this, the measured entangled pair collapses and so entanglement is then passed on to the remaining two particles [120]. Consider: two entangled pairs, AB and CD, where particles B and D are then entangled, and subsequently measured. The result is that particles A and C are then entangled, to produce a state AC, hence the terminology "entanglement swapping". The general scheme of entanglement swapping can be easily elucidated in the following diagram:

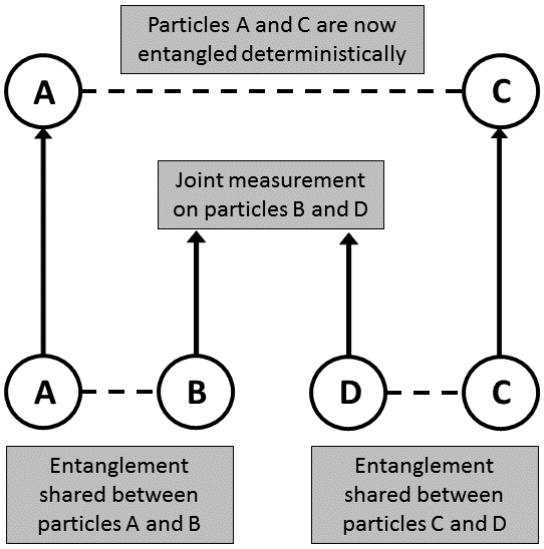

FIGURE 1.8: Diagram to represent how the initial entanglement shared between particles (qubits) $A-B$ and $C-D$ can be swapped to particles $A-C$.

This is yet another truly striking phenomenon of quantum physics, as particles A and C are not required to have ever interacted, and in fact this entanglement swapping scheme could be possible if A and C have never even *existed* at the same time. In this work it was shown that if the measurement of particle A occurs before creation of the second initially entangled pair CD then there are still correlations between measurements of particles A and C, which are actually considered entangled despite never coexisting [121].

We also note here that entanglement swapping is effectively a form of quantum teleportation, as the transfer of one half of an entangled state, either from mode B to D or from C to A [39]. Quantum teleportation is the process in which Alice can transport an unknown state of a spin-half particle to Bob by conveying only two bits of classical information [122, 123]. Entanglement swapping produces entanglement between two (distant) independent qubits (that are not required to have interacted), which is in contrast to teleportation, in which a single quantum state is teleported from one qubit to another [124].

1.3 Thesis Outline

In addition to this Introduction, this thesis is divided into five more chapters. In Chapter 2 a brief introduction of our proposed entangled swapping protocol is discussed, with each stage of this protocol being addressed regarding the general Mathematical formalisms, as well as some experimental considerations. Chapter 3 involves in depth Mathematical analysis of this proposed protocol, using coherent states and also cat states, with results and discussion regarding entanglement negativity, fidelity and linear entropy of these two protocol examples, considering small levels of photon losses. This notion of photon losses is extended in Chapter 4, to the case where we investigate unequal photon losses in the two lossy modes and establish the level of impact this has on the protocol outcomes. In Chapter 5 we then discuss homodyne detection non-idealities and imperfections, with an outlook to the practical and realistic experimental implementations of this protocol. Following this, Chapter 6 then brings the previous chapters together for an analysis of this scheme in terms of protocol optimisation, where we deliberate the most effective combination of variables (such as coherent state amplitude, level of photon loss, resolution bandwidth of homodyne detection, success probabilities of measurements and more), with further consideration of entanglement purification to further increase the level of entanglement produced via our ES protocol. Finally, we give an outlook to the future of this field in the conclusive Chapter 7, and review the relevant applications of our proposed ES protocol to the real-world, as well as bringing together all of the key results of our entanglement swapping protocol.

Chapter 2

Methods

In this section we present and discuss our proposed entanglement swapping (ES) protocol. Each element of the protocol will be discussed individually, and in chronological order.

2.1 The Entanglement Swapping Protocol

In this work, we present an ES protocol with which one can use to theoretically distribute entanglement over distance, via use of projective measurements and the principle of entanglement, when allowing for small levels of photon losses. We propose two circumstances, in which the proposed ES protocol is the same in each case, but the initial hybrid entangled states differ; *hybrid* here meaning that the entanglement is shared between a discrete variable state and a continuous variable one. In the first protocol we consider an initial quantum state with a coherent state as the continuous variable state, and in the second (more complex) protocol we begin with a cat state as the continuous part.

The initial hybrid entangled states (denoted as $|\psi_{HE}\rangle_{AB}$ and $|\psi_{HE}\rangle_{CD}$), for hybrid entanglement shared between modes A-B and C-D respectively), for the coherent state and cat state protocols, are described mathematically as follows:

$$|\psi_{HE}^{Coh.}\rangle_{AB} = \frac{1}{\sqrt{2}}(\,|0\rangle_A\,||\alpha|\rangle_B + |1\rangle_A\,|-|\alpha|\rangle_B) \tag{2.1}$$

$$|\psi_{HE}^{Cat}\rangle_{AB} = \frac{N_\alpha^+}{\sqrt{2}}\Big(\,|0\rangle_A\,(\,||\alpha|\rangle_B + |-|\alpha|\rangle_B) + |1\rangle_A\,(\,|\mathrm{i}|\alpha|\rangle_B + |-\mathrm{i}|\alpha|\rangle_B)\Big), \tag{2.2}$$

where, the subscript HE denotes a hybrid entangled quantum state and $N_\alpha^\pm = 1/\sqrt{2 \pm 2e^{-2|\alpha|^2}}$ is the normalisation of a cat state. Note that the hybrid entanglement shared between modes A and B (described by Eqs. 2.1 and 2.2) is identical to that of modes C and D ($|\psi_{HE}^{Coh.}\rangle_{CD}$ and $|\psi_{HE}^{Cat}\rangle_{CD}$).

Clearly, in our ES protocol modes A and C are the discrete variable states and B and D are continuous variables. We construct our ES protocol such that the continuous variable halves of the hybrid entangled states are the ones that propagate, as these are considered to be somewhat resilient to photon losses - in Sec. 2.3 we show how photon loss is modelled with the coherent state, and we show that photon losses in fact only reduce the amplitude of the coherent states. Referring back to Fig. 1.5,

if we allow for photon losses it merely causes the coherent state to move towards the origin of the phase space diagram. The discrete variable halves of the hybrid entangled states in our protocol (which we set to be Fock states) are stationary and are what we wish to share entanglement between, should our protocol succeed.

We now present a schematic describing our proposed ES protocol, for the ideal case where we have no photon losses in the propagating modes (B and D), to illustrate the principle of this protocol:

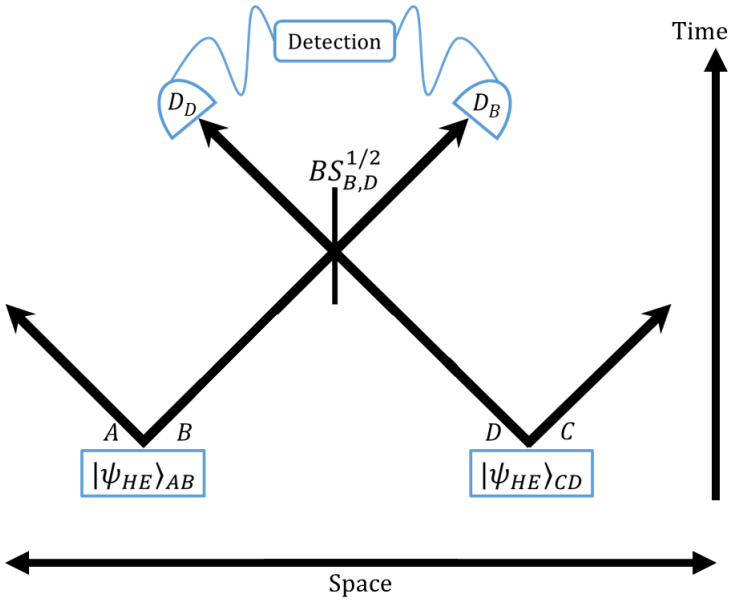

FIGURE 2.1: Diagram to represent the four channel system (where $|\psi_{HE}\rangle_{AB}$ and $|\psi_{HE}\rangle_{CD}$ are entangled hybrid states) undergoing entanglement swapping with no lossy channels. Modes B and D are mixed at a 50:50 beam-splitter ($BS^{1/2}_{B,D}$) and subsequently measured (D_B and D_D) to complete the protocol.

Fig. 2.1 describes simplistically the entire process to our entanglement swapping protocol. With space as the horizontal axis and time as the vertical axis, it is clear that our two initial hybrid entangled states $|\psi_{HE}\rangle_{AB}$ and $|\psi_{HE}\rangle_{CD}$ are initially separated by an arbitrary distance - this distance can vary, however, as will be explained later for the practicality of this theoretical approach, we need only assume that they are separated. Note that although modes A and C are "stationary" the arrows in Fig. 2.2 indicate a movement in space; this is to represent that modes A and C are then able to be sent on for further uses in communications, perhaps to a potential customer (or indeed separated customers) that require an entangled pair of qubits.

In the first step in the ideal no loss protocol, modes B and D propagate towards each other and meet at a 50:50 beam-splitter $BS^{1/2}_{B,D}$ (which will be detailed in Sec. 2.4) and then subsequently measured (this will also be explained further in Secs. 2.5 and 2.6). This beam-splitter operation, followed by a measurement, is key to this protocol, as it is this process which swaps the entanglement shared between modes A-B and C-D to A-C. This is due to the collapse of the wavefunctions of modes B

and D as a result of being measured (a direct consequence of one of the postulates of quantum mechanics).

In this protocol we detect mode B with a vacuum measurement (see Sec. 2.5); more specifically, this could be a vacuum-one-photon measurement, where if we do not hear the detector "click", then we know that a vacuum was successfully measured. We detect mode D with a homodyne measurement (see Sec. 2.6). Note that there is no particular reason why we measure these modes in such a way, if we were to perform a vacuum measurement in mode D and a homodyne measurement in mode B then the results would be identical to Fig. 2.1's output. What is integral, however, is that we perform a vacuum measurement on one mode and a homodyne measurement on the other, as will be explained later (Sec. 3.2.1).

Finally, once we have measured modes B and D, in the most ideal case (as will be explained later) our final state will be a maximally entangled Bell state in modes A and C, described mathematically as $|\Phi^+\rangle_{AC} = \frac{1}{\sqrt{2}}(|00\rangle_{AC} + |11\rangle_{AC})$. In the case where we use Schrödinger cat states in modes B and D our final state shared between modes A and C in the most ideal case will be a "phase-rotated" maximally entangled Bell state, $|\Phi^+(\alpha)\rangle_{AC} = \frac{1}{\sqrt{2}}\left(|00\rangle_{AC}\, e^{-\mathrm{i}|\alpha|^2} + |11\rangle_{AC}\, e^{\mathrm{i}|\alpha|^2}\right)$.

So far we have considered only a very idealistic case, in which the propagating modes are subject to no form of decoherence which would cause the quantum state to lose photons. Realistically, and practically, this is impossible, even over very short distances and when sent through optical fibres (as discussed in Sec. 2.3). We therefore introduce two extra beam-splitters of transmission T into our protocol, so as to model the effects of photon losses in modes B and D; our *lossy* proposed entanglement swapping protocol can now be described using the following schematic:

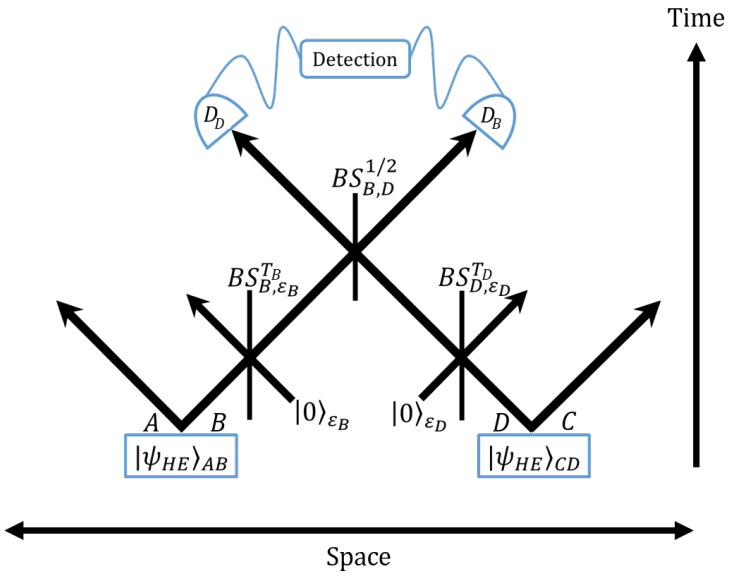

FIGURE 2.2: Diagram to represent the four channel system (where $|\psi_{HE}\rangle_{AB}$ and $|\psi_{HE}\rangle_{CD}$ are entangled hybrid states) undergoing entanglement swapping with two lossy channels (B and D), modelled by mixing a vacuum state ($|0\rangle_{\varepsilon_B}$ and $|0\rangle_{\varepsilon_D}$ respectively) using a beam-splitter of transmission T (BS^{T}_{B,ε_B} and BS^{T}_{D,ε_D}). The lossy modes B and D then meet at a 50:50 beam-splitter ($BS^{1/2}_{B,D}$) and are subsequently measured (D_B and D_D).

(Note the equivalence of the above figure with that of the no loss case, Fig. 2.1). In Fig. 2.2, as time progresses modes B and D are individually subjected to beam-splitters BS^{T}_{B,ε_B} and BS^{T}_{D,ε_D}, of transmission T, with a vacuum state $|0\rangle_{\varepsilon_B}$ and $|0\rangle_{\varepsilon_D}$ to simulate loss (this will be derived in Sec. 2.3). After these beam-splitters the rest of the protocol is identical to that of the no loss case (Fig. 2.1).

We will now discuss each element of the lossy protocol given in Fig. 2.2, beginning with the generation of our initial hybrid entangled states.

2.2 Generating the hybrid entangled states $|\psi_{HE}\rangle_{AB}$ $|\psi_{HE}\rangle_{CD}$

The first step of this protocol is generating the initial hybrid entangled states. The term "hybrid" is used here to describe entanglement shared between a discrete variable (DV) quantum state and a continuous variable (CV) one. In our protocol we use the Fock state as our DV half, and a coherent state (or cat state) as the CV half. For overviews of potential methods to produce single photon Fock states and cat states, see Chapter 1, Subsecs. 1.2.6 and 1.2.8 respectively.

Hybrid entangled states are of great importance in the field of quantum communication and computation, as they exploit the usefulness of the DV state and CV state, whilst countering the intrinsic problems with using these states on their own. For example, DV qubits often require heralded approaches, and as such have low success probabilities in their preparation and implementation, however the fidelities against the desired state to be produced (see Sec. 2.9 for a discussion of fidelity) often approach unity [125]. Contrastingly, in the CV regime, the actual preparation

and implementation of quantum states is deterministic and unconditional, however these states can be sensitive to photonic losses and so produce desired quantum states with lower fidelities. Thus, preparing an initial system that is a hybrid state of both helps to overcome the intrinsic problems when using DV states or CV states on their own.

The bipartite hybrid entangled states we want to generate, which have a DV qubit in a spatial mode (that is to say, it is stationary) and a CV qubit in the propagating mode, for our proposed coherent state entanglement swapping protocol, can be described mathematically as follows:

$$|\psi_{HE}^{Coh.}\rangle_{AB} = \frac{1}{\sqrt{2}}(|0\rangle_A\,||\alpha|\rangle_B + |1\rangle_A\,|-|\alpha|\rangle_B),$$
$$|\psi_{HE}^{Coh.}\rangle_{CD} = \frac{1}{\sqrt{2}}(|0\rangle_C\,||\alpha|\rangle_D + |1\rangle_C\,|-|\alpha|\rangle_D), \tag{2.3}$$

Mode B (or D) is assumed to be a photonic coherent state propagating through a photon-lossy channel, whereas the stationary mode A (or C) can be represented by a variety of physical systems. In this section we briefly discuss possible methods to produce this hybrid entangled state.

A hybrid photonic state has been recently demonstrated experimentally using polarisation photons in [126] - in this work O. Morin *et al.* produce the exact state given in Eqs. 2.3, without relying on difficult-to-implement Kerr non-linearities (as discussed in Chapter 1, Subsec. 1.2.8). Instead, this work utilises probabilistic heralded single photon measurements to prepare a hybrid entangled state given as $|\Psi\rangle_{AB} = \mathcal{N}((|0\rangle_A + |1\rangle_A)\,||\alpha|\rangle_B + e^{-i\phi}(|0\rangle_A - |1\rangle_A)\,|-|\alpha|\rangle_B)$, where ϕ is a relative phase. Upon finally performing a Hadamard gate $\hat{H}$ (which transforms $\hat{H}(|0\rangle + |1\rangle) \rightarrowtail |0\rangle$ and $\hat{H}(|0\rangle - |1\rangle) \rightarrowtail |1\rangle$), this then gives the states described in Eqs. 2.3.

Alternatively, hybrid states may be produced using a vacuum and a single-photon state for mode A (or C), as per the method given by H. Jeong *et al.* in 2014 [38]. The method for this applies a superposition of photon addition operators ($r\hat{a}_A^\dagger + t\hat{a}_B^\dagger$), implemented using a beam-splitter of reflection and transmission amplitudes r and t respectively. This can be shown mathematically as follows:

$$|\Psi\rangle_{AB} = |0\rangle_A\,||\alpha_i|\rangle_B \xrightarrow{r\hat{a}_A^\dagger + t\hat{a}_B^\dagger} \approx \frac{1}{\sqrt{2}}\left(|1\rangle_A\,||\alpha_i|\rangle_B + |0\rangle_A\,\frac{\hat{a}_B^\dagger\,||\alpha_i|\rangle_B}{\sqrt{|\alpha_i|^2+1}}\right), \tag{2.4}$$

in which the subscript i on the coherent states denotes that these are initial amplitudes, and the transmission amplitude has been set to $t = (|\alpha_i|^2 + 2)^{-\frac{1}{2}}$, to balance the probabilities of the superposition of photon addition operators occurring on either mode. Application of a photon addition operator onto a coherent state simply gives a coherent state of greater amplitude, given as $\hat{a}_B^\dagger\,||\alpha_i|\rangle_B \approx |g|\alpha_i|\rangle$, where g denotes the gain in the amplitude. Using this photon addition operator, along with a displacement operator on mode B (to give us the state described in Eq. 2.3), is

described by:

$$|\Psi\rangle_{AB} \approx \frac{1}{\sqrt{2}}(|1\rangle_A\,||\alpha_i|\rangle_B + |0\rangle_A\,|g|\alpha_i|\rangle_B) \xrightarrow{\text{Displacement operator}} \frac{1}{\sqrt{2}}(|0\rangle_A\,||\alpha_f|\rangle_B + |1\rangle_A\,|-|\alpha_f|\rangle_B), \tag{2.5}$$

where the subscript f on the coherent states denotes that these are the final coherent state amplitudes, given as $|\alpha_f| = (g|\alpha_i| - |\alpha_i|)/2$, due to application of the displacement operator. Clearly, using this method, one can produce an equivalent state to our desired initial hybrid entangled state (Eq. 2.3), but in a very different method used by O. Morin *et al.* in [126].

One further experimentally-feasible method to produce the hybrid states given in Eqs. 2.3 is by using entangled polarisation qubits (i.e. $|H\rangle_A$ and $|V\rangle_A$, where H and V denote horizontal and vertical polarisation respectively) in an initial state of $\frac{1}{\sqrt{2}}(|H\rangle_A\,|V\rangle_B + |V\rangle_A\,|H\rangle_B)$, along with a coherent superposition state in mode C [127]. Upon applying a series of beam-splitter operations and auxiliary modes (to erase path information), the resultant state is given by $\frac{1}{\sqrt{2}}(|H\rangle_A\,||\alpha|\rangle_B + |V\rangle_A\,|-|\alpha|\rangle_B)$, which is clearly the state given in Eqs. 2.3.

Another possible route to produce hybrid entanglement is by relying on Kerr non-linearities [128–131] however these are hard to realise practically (as discussed in Chapter 1, Subsec. 1.2.8). Finally, we note that there are many other possible techniques that could be used to generate hybrid entangled states [132–135], as a result of the usefulness of these states for a range of quantum communication and computation purposes being realised over the last few years.

We also propose a second entanglement swapping protocol in this work, which we refer to as the "cat state protocol". In our second, more complicated, protocol we instead begin with initial hybrid entangled states given as:

$$|\psi_{HE}^{Cat}\rangle_{AB} = \frac{N_\alpha^+}{\sqrt{2}}\Big(\,|0\rangle_A\,(\,||\alpha|\rangle_B + \,|-|\alpha|\rangle_B) + \,|1\rangle_A\,(\,|\mathrm{i}|\alpha|\rangle_B + \,|-\mathrm{i}|\alpha|\rangle_B)\Big), \tag{2.6}$$

where $N_\alpha^\pm = 1/\sqrt{2 \pm 2e^{-2|\alpha|^2}}$ is the normalisation of a cat state, and the hybrid state as described above is the same for modes C and D. For the position and momentum phase-space representation of the cat states given in mode B in Eq. 2.6, see Fig. 1.6.

We note here that, although clearly much work has been carried out experimentally in research with regards to preparing the hybrid states given in Eqs. 2.3, the hybrid states given above in Eq. 2.6 are far more complicated to prepare experimentally. In fact, this is cutting edge research, however one potential method could be: begin with a qubit $|0\rangle_A$ which is prepared in a product state with a cat state $||\alpha|\rangle_B + \,|-|\alpha|\rangle_B$, and apply a Hadamard gate to the qubit. This will then yield a

state given as:

$$\hat{H}\,|\Psi\rangle_{AB} = \mathcal{N}\hat{H}\,|0\rangle_A\,(\,||\alpha|\rangle_B + \,|-|\alpha|\rangle_B) \\ \rightarrowtail \mathcal{N}(|0\rangle_A\,(\,||\alpha|\rangle_B + \,|-|\alpha|\rangle_B) + |1\rangle_A\,(\,||\alpha|\rangle_B + \,|-|\alpha|\rangle_B)). \tag{2.7}$$

If one then performs a conditional rotation of $\frac{\pi}{2}$ (conditional on the qubit state, i.e. only when the qubit state in mode A is $|1\rangle_A$) to the cat components, this will give the hybrid state given in Eq. 2.6. We note here that although this may not be precisely how this hybrid entangled state would be generated in practice, this is a perfectly viable gate sequence, so there is no issue of principle in creating hybrid states with cats.

2.3 Modelling Loss

One of the biggest obstacles in photonic quantum technologies and communications is photon losses. This is an unavoidable and intrinsic consequence of how photons act in optical fibre - when travelling through optical fibre a fraction of the propagating photons will be absorbed into the fibre, causing photon losses.

Loss of photons by absorption in the lossy optical fibre will be modelled by sending the beam mode of interest through a beam-splitter, and then discarding the reflected output mode as being lost to the environment. This means mathematically tracing over the reflected output mode (this will be covered in a later section, see Chapter 3, Subsec. 3.2.4). To theoretically model loss we use the standard method of mixing our lossy propagating modes (B and D) with a vacuum mode at a beam-splitter, as follows:

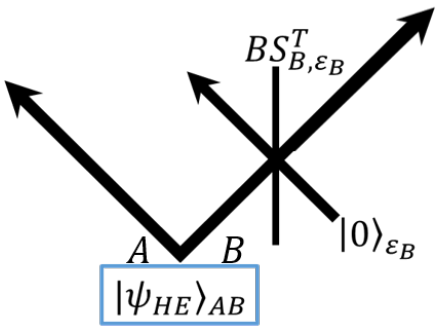

FIGURE 2.3: Diagram to show how loss can be modelled theoretically - note that this is equivalent to modelling loss in mode D using a beam-splitter BS^{T}_{D,ε_D} with a vacuum state in mode ε_D.

Mathematically, to model the loss that occurs as shown schematically in Fig. 2.3, we use a similar method used to model a 50:50 BS acting on a vacuum and single photon state (as per Eq. 1.26). Using the BS diagram of Fig. 1.7, our input states are a coherent state in mode a and a vacuum state in mode b (note the equivalence here to Fig. 2.3). We then apply our unitary operator (defined in Eq. 1.21) to model

the effect of the BS; this time however, we must perform a unitary transformation on the displacement operator $|\alpha\rangle = \hat{D}(\alpha)\exp\left[\alpha\hat{a}^\dagger - \alpha^*\hat{a}\right]|0\rangle$. To do so, we first need to expand the displacement operator, using the Taylor series expansion ($e^x = 1 + \frac{x^1}{1!} + \frac{x^2}{2!} + (\ldots)$) as follows:

$$\begin{aligned}\hat{D}(\alpha) &= \hat{I} + (\alpha\hat{a}^\dagger - \alpha^*\hat{a}) + \frac{(\alpha\hat{a}^\dagger - \alpha^*\hat{a})(\alpha\hat{a}^\dagger - \alpha^*\hat{a})}{2!} + (\ldots) \\ &= \hat{I} + (\alpha\hat{a}^\dagger - \alpha^*\hat{a}) + \frac{\alpha^2\hat{a}^{\dagger 2} + (\alpha^*)^2\hat{a}^2 - |\alpha|^2(\hat{a}^\dagger\hat{a} + \hat{a}\hat{a}^\dagger)}{2!} + (\ldots). \end{aligned} \tag{2.8}$$

Now, we apply the unitary operator for the BS to the above, giving:

$$\begin{aligned}\hat{U}_{BS}\hat{D}(\alpha)\hat{U}_{BS}^\dagger = \hat{U}_{BS}\hat{I}\hat{U}_{BS}^\dagger &+ (\alpha\hat{U}_{BS}\hat{a}^\dagger\hat{U}_{BS}^\dagger - \alpha^*\hat{U}_{BS}\hat{a}\hat{U}_{BS}^\dagger) \\ &+ \frac{\alpha^2\hat{U}_{BS}\hat{a}^\dagger\hat{U}_{BS}^\dagger\hat{U}_{BS}\hat{a}^\dagger\hat{U}_{BS}^\dagger + (\alpha^*)^2\hat{U}_{BS}\hat{a}\hat{U}_{BS}^\dagger\hat{U}_{BS}\hat{a}\hat{U}_{BS}^\dagger}{2!} \\ &- \frac{|\alpha|^2(\hat{U}_{BS}\hat{a}^\dagger\hat{U}_{BS}^\dagger\hat{U}_{BS}\hat{a}\hat{U}_{BS}^\dagger + \hat{U}_{BS}\hat{a}\hat{U}_{BS}^\dagger\hat{U}_{BS}\hat{a}^\dagger\hat{U}_{BS}^\dagger)}{2!} + (\ldots), \end{aligned} \tag{2.9}$$

and so now we have an expression for how the BS unitary operator acts on the displacement operator:

$$\therefore \hat{U}_{BS}\hat{D}(\alpha)\hat{U}_{BS}^\dagger\hat{U}_{BS}|0\rangle = \exp\left[\alpha\hat{U}_{BS}\hat{a}^\dagger\hat{U}_{BS}^\dagger - \alpha^*\hat{U}_{BS}\hat{a}\hat{U}_{BS}^\dagger\right]|0\rangle. \tag{2.10}$$

Using this form of the displacement operator we can now model the effect of a BS on a coherent state in mode a and a vacuum in mode b, with a BS of transmission T, such that:

$$\begin{aligned}\hat{U}_{BS}|\alpha\rangle_a|0\rangle_b &= \hat{U}_{BS}\hat{D}(\alpha)\hat{U}_{BS}^\dagger\hat{U}_{BS}|0\rangle_a|0\rangle_b \\ &= \exp\left[\alpha\hat{U}_{BS}\hat{a}^\dagger\hat{U}_{BS}^\dagger - \alpha^*\hat{U}_{BS}\hat{a}\hat{U}_{BS}^\dagger\right]|0\rangle_a|0\rangle_b, \end{aligned} \tag{2.11}$$

where we then apply the relations given in Eq. 1.25, which then gives:

$$\hat{U}_{BS}|\alpha\rangle_a|0\rangle_b = \exp\left[\alpha(\cos(\xi)\hat{a}^\dagger + \sin(\xi)\hat{b}^\dagger) - \alpha^*(\cos(\xi)\hat{a} + \sin(\xi)\hat{b})\right]|0\rangle_a|0\rangle_b, \tag{2.12}$$

We can then re-express the above equation as separate exponentials, which gives:

$$\hat{U}_{BS}|\alpha\rangle_a|0\rangle_b = \exp\left[\alpha\cos(\xi)\hat{a}^\dagger - \alpha^*\cos(\xi)\hat{a}\right]\exp\left[\alpha\sin(\xi)\hat{b}^\dagger - \alpha^*\sin(\xi)\hat{b}\right]|0\rangle_a|0\rangle_b, \tag{2.13}$$

where we are able to separate the exponential into two terms, as above, due to the commutative nature of the annihilation and creation operators acting on different modes (i.e. for two modes i and j, $\left[\hat{a}_i^\dagger, \hat{a}_j^\dagger\right] = 0$ and $[\hat{a}_i, \hat{a}_j] = 0$) via use of a corollary of the Baker-Campbell-Hausdorff Formula, given as: $e^{\hat{X}+\hat{Y}} = e^{\hat{X}}e^{\hat{Y}}e^{-\frac{[\hat{X},\hat{Y}]}{2}}$ [136]. We note here that this degenerate form of the Baker-Campbell-Hausdorff Formula is only true when the operators $\hat{X}$ and $\hat{Y}$ commute with their commutator ($[\hat{X}, \hat{Y}]$).

Finally, we define the reflection and transmission coefficients (the probability amplitudes) as $R = \sin^2 \xi$ and $T = 1 - R = \cos^2 \xi$, respectively, hence the final output from the unitary BS $\hat{U}_{BS}$ is:

$$\begin{aligned}\hat{U}_{BS} \left|\alpha\right\rangle_a \left|0\right\rangle_b &= \exp\left[\sqrt{T}\,\alpha\hat{a}^\dagger - \sqrt{T}\,\alpha^*\hat{a}\right] \exp\left[\sqrt{1-T}\,\alpha\hat{b}^\dagger - \sqrt{1-T}\,\alpha^*\hat{b}\right] \left|0\right\rangle_a \left|0\right\rangle_b \\ &= \left|\sqrt{T}\,\alpha\right\rangle_a \left|\sqrt{1-T}\,\alpha\right\rangle_b . \end{aligned} \tag{2.14}$$

where the level of loss in the system is parametrised by T, and so for no loss we set $T = 1$, which would result in no change to the input state. That is to say there is no mixing of our propagating coherent state in mode B with the vacuum state of mode ε_B (as per Fig. 2.3) as 100% of the information in mode B passes through the beam-splitter. However, realistically this is not the case, and so a variety of losses will be accounted for in our proposed entanglement swapping protocol.

Importantly, it should be pointed out that the outcome from the BS process described above is absolutely *not* an entangled state. Compare the final state given by Eq. 2.14, but for $T = 0.50$ (denoting a 50:50 BS), with the state given by two input states of a vacuum in one mode and a single photon in the other, incident upon a 50:50 BS, Eq. 1.26. The state given in Eq. 1.26 is clearly maximally entangled, and is a direct consequence of the probabilities of the photon being either reflected or transmitted by the BS being equal, thus creating an entangled output. This is not the case when coherent states are considered, as in Eq. 2.14, where the coherent state input is actually *split* into both output modes, thus giving a product state. In fact, this is due to the more classical-like nature of coherent states, where the BS effectively splits a coherent light beam into two modes of equal intensity. Inherently, even in the very low $|\alpha|$ limit, we still would not return the entangled state described by Eq. 1.26, as entanglement cannot arise as a limiting case of a product state [80].

2.4 50:50 Beam-Splitter

Following the first beam-splitters, which are used to model photon losses within optical fibre, we then mix the two lossy propagating modes B and D at a 50:50 beam-splitter ($BS^{\frac{1}{2}}_{B,D}$). This is an integral part of an entanglement swapping protocol, as this is the operation that swaps the initial entanglement shared between modes A and B, and C and D, to shared entanglement between modes A and C. For this operation to be successful clearly both propagating coherent states in modes B and D must meet at this 50:50 beam-splitter at the same time, and we make this assumption in our work.

Consider the beam-splitter schematic of Fig. 1.7. We now wish to have the two input states as coherent states, $\left|\alpha\right\rangle_a$ and $\left|\beta\right\rangle_b$, where α and β denote the amplitude of each respective coherent state. We mathematically model this mixing via a 50:50 BS using the same method outlined in Sec. 2.3 to model loss via a BS.

As before, we then apply our unitary operator (defined in Eq. 1.21) to model the effect of the BS, again using the same method for calculating the effect of $\hat{U}_{BS}$ on the displacement operator. This time we instead have two input coherent states, and so we need to also use a displacement operator on, both, modes a and b. We therefore define the displacement operator that acts on mode a as per Eq. 2.10, and for mode b we then define $\hat{U}_{BS}\hat{D}(\beta)\hat{U}_{BS}^{\dagger}\hat{U}_{BS}\left|0\right\rangle = \exp\left[\beta\hat{U}_{BS}\hat{b}^{\dagger}\hat{U}_{BS}^{\dagger} - \beta^{*}\hat{U}_{BS}\hat{b}\hat{U}_{BS}^{\dagger}\right]\left|0\right\rangle$. The action of the BS operator $\hat{U}_{BS}$ on these two input coherent states (recall that we define and apply the unitary operator $\hat{U}_{BS}$ as the BS operator in this work) is then calculated as:

$$\begin{aligned}
&\hat{U}_{BS}\left|\alpha\right\rangle_{a}\left|\beta\right\rangle_{b} \\
&\quad= \hat{U}_{BS}\hat{D}(\alpha)\hat{U}_{BS}^{\dagger}\hat{U}_{BS}\hat{D}(\beta)\hat{U}_{BS}^{\dagger}\hat{U}_{BS}\left|0\right\rangle_{a}\left|0\right\rangle_{b} \\
&\quad= \exp\left[\alpha\hat{U}_{BS}\hat{a}^{\dagger}\hat{U}_{BS}^{\dagger} - \alpha^{*}\hat{U}_{BS}\hat{a}\hat{U}_{BS}^{\dagger}\right]\exp\left[\beta\hat{U}_{BS}\hat{b}^{\dagger}\hat{U}_{BS}^{\dagger} - \beta^{*}\hat{U}_{BS}\hat{b}\hat{U}_{BS}^{\dagger}\right]\left|0\right\rangle_{a}\left|0\right\rangle_{b} \\
&\quad= \exp\left[\alpha(\cos(\xi)\hat{a}^{\dagger} + \sin(\xi)\hat{b}^{\dagger}) - \alpha^{*}(\cos(\xi)\hat{a} + \sin(\xi)\hat{b})\right] \\
&\quad.\exp\left[\beta(-\sin(\xi)\hat{a}^{\dagger} + \cos(\xi)\hat{b}^{\dagger}) - \beta^{*}(-\sin(\xi)\hat{a} + \cos(\xi)\hat{b})\right]\left|0\right\rangle_{a}\left|0\right\rangle_{b}, \qquad (2.15)
\end{aligned}$$

where we have applied the creation and annihilation operators relations given in Eq. 1.25. Next, we separate the exponentials as a result of the commutative nature of the creation and annihilation operators (via use of the Baker-Campbell-Hausdorff Formula [136]) as before, giving:

$$\begin{aligned}
\hat{U}_{BS}\left|\alpha\right\rangle_{a}\left|\beta\right\rangle_{b} = &\exp\left[\alpha\cos(\xi)\hat{a}^{\dagger} - \alpha^{*}\cos(\xi)\hat{a}\right]\exp\left[\alpha\sin(\xi)\hat{b}^{\dagger} - \alpha^{*}\sin(\xi)\hat{b}\right] \\
&\exp\left[-\beta\sin(\xi)\hat{a}^{\dagger} + \beta^{*}\sin(\xi)\hat{a}\right]\exp\left[\beta\cos(\xi)\hat{b}^{\dagger} - \beta^{*}\cos(\xi)\hat{b}\right]\left|0\right\rangle_{a}\left|0\right\rangle_{b}. \qquad (2.16)
\end{aligned}$$

Once again, we set the transmission and reflection amplitudes such that $\cos\xi = \sqrt{T}$ and $\sin\xi = \sqrt{1-T}$. This then gives the final output state from the BS^{T} operation as:

$$\begin{aligned}
\hat{U}_{BS}\left|\alpha\right\rangle_{a}\left|\beta\right\rangle_{b} = &\exp\left[\sqrt{T}\,\alpha\hat{a}^{\dagger} - \sqrt{T}\,\alpha^{*}\hat{a}\right]\exp\left[\sqrt{1-T}\,\alpha\hat{b}^{\dagger} - \sqrt{1-T}\,\alpha^{*}\hat{b}\right] \\
&\exp\left[-\sqrt{1-T}\,\beta\hat{a}^{\dagger} + \sqrt{1-T}\,\beta^{*}\hat{a}\right]\exp\left[\sqrt{T}\,\beta\hat{b}^{\dagger} - \sqrt{T}\,\beta^{*}\hat{b}\right]\left|0\right\rangle_{a}\left|0\right\rangle_{b} \\
= &\left|\sqrt{T}\,\alpha - \sqrt{1-T}\,\beta\right\rangle_{a}\left|\sqrt{1-T}\,\alpha + \sqrt{T}\,\beta\right\rangle_{b}. \qquad (2.17)
\end{aligned}$$

Finally, as the above is a model of a BS of transmission T, we now set $T = \frac{1}{2}$, which then gives us our final output states from applying a 50:50 BS operator to two coherent states:

$$\hat{U}_{BS}\left|\alpha\right\rangle_{a}\left|\beta\right\rangle_{b} = \left|\frac{\alpha-\beta}{\sqrt{2}}\right\rangle_{a}\left|\frac{\alpha+\beta}{\sqrt{2}}\right\rangle_{b}. \qquad (2.18)$$

This again shows the classical nature of coherent states; the above output state is clearly not entangled, it is another product state like in Eq. 2.14, as the 50:50 BS

splits the intensities of both input beams equally into both output modes.

2.5 Vacuum Measurement, D_B

Following the application of a 50:50 beam-splitter to mix modes B and D, we must then subsequently measure modes B and D to project their respective wavefunctions, thus creating entanglement between modes A and C. Our proposed entanglement swapping protocol requires a vacuum measurement in mode B, however, physically the measurement of a vacuum state is not straightforward [137].

One such way to reveal the presence or absence of a photon is to use a *perfect* photodetector, and upon not hearing the characteristic *click* of the detector, indicating the presence of one or more photons, it can be assumed that there is not a photon present [138]. In practice this is not quite as simple; the quantum efficiency of such photodetectors is not unity, and as such only a small fraction of photons that arrive at the detector lead to an electric pulse [139]. Typically, as is also the case for photons travelling through optical fibre, most photons will also be reflected upon arriving at the detector.

A further limitation of photodetectors, demonstrated in so-called *avalanche* photodetectors (which use a highly-sensitive photodiode which is able to convert light to electricity via the photoelectric effect [140]), is that it is very difficult to discriminate between individual photons or multiple photons being present [141]. This, however, does not matter within our protocol, as we merely care about there being no photons, a null detection, (indicated by no detector click) or one or more photons. We should point out that, although we do not need to know the photon number in a click, we do have an error if there is no click but there were one or more photons present - this can be quantified in terms of quantum efficiency, which is the fraction of photon flux which contributes to the photocurrent in a photodetector [142]. If the quantum efficiency is less than 100% then evidently not all photons that arrive at a photon detector are counted.

More recently, there have been advances in photodetection methods and one way to detect the presence of a vacuum state, even without destroying the quantum state, is to apply a cavity quantum electrodynamic technique [143]. In this work, an optical field is confined to a cavity, in which the optical field may have zero photons (a vacuum) or one or more photons. This cavity is then coupled to a three level atomic field with two ground states, in which an atom is driven by a laser to the excited state, and the presence or absence of photons in the optical cavity mode is indicated by which of the two ground states the atomic field returns to.

On the other hand, to mathematically represent a vacuum state detection is more simple. To measure the presence of a vacuum, or lack thereof, we apply a positive-operator valued measure (POVM) described by the operator [144]:

$$\hat{P}_i^0 = |0\rangle_i \langle 0| , \tag{2.19}$$

where, $|0\rangle_i$ represents a vacuum state in mode i. This POVM measurement can be calculated relatively straightforwardly, by application of this vacuum projector $\hat{P}_i^0$ onto a coherent state (as is required in our proposed entanglement swapping protocol), as follows:

$$|0\rangle_i \langle 0|\alpha\rangle_i = |0\rangle_i e^{-\frac{|\alpha|^2}{2}} \sum_{n=0}^{\infty} \frac{\alpha^n}{\sqrt{n!}} {}_i\langle 0|n\rangle_i = |0\rangle_i e^{-\frac{|\alpha|^2}{2}} \sum_{n=0}^{\infty} \frac{\alpha^n}{\sqrt{n!}} \delta_{n,0} = |0\rangle_i e^{-\frac{|\alpha|^2}{2}}, \tag{2.20}$$

in which we have applied the Fock basis representation of the coherent state (as per Eq. 1.7), and we have made use of the Kronecker delta function, in which $\delta_{n,0} = 0$ for $n \neq 0$ and $\delta_{n,0} = 1$ for $n = 0$.

2.6 Homodyne Measurement, D_D

For successful entanglement swapping, we measure mode D via balanced homodyne detection, and mode B by a vacuum measurement. A generalised scheme of balanced homodyne detection consists of one 50:50 beam-splitter, a strong coherent field $\big||\beta|e^{i\theta}\big\rangle$ of amplitude $|\beta|$, and two photodetectors; the probe mode (mode D) is combined at a beam-spliter with the strong coherent field ("local oscillator") of equal frequency, and photodetection is then used to measure the outputs (see Fig. 2.4) [145–147].

If we perform homodyne detection on an input signal in mode B_1 and the coherent field is injected in mode B_2, then the operator $BS^{\frac{1}{2}}_{B_1,B_2}$ mixes the input state and the coherent field, as follows [55]:

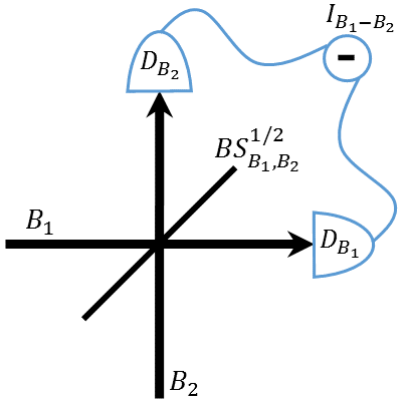

FIGURE 2.4: Diagram to represent the two channel system undergoing balanced homodyne detection, where B_1 is the input signal (mode D in ES protocols) and B_2 is the local oscillator. $I_{B_1-B_2}$ is the intensity difference between the photodetectors D_{B_1} and D_{B_2}.

The intensity difference (photon number difference) between the two photodetectors (D_{B_1} and D_{B_2}) can be calculated using the two mode operator $\hat{I}_{\hat{B}_1-\hat{B}_2}$, which we shall now derive. Following our beam-splitter method and notation (as derived in Chapter 1, Subsec. 1.2.9), let the outputs of the 50:50 beam-splitter in each mode

be:

$$\hat{B}_1 = \frac{1}{\sqrt{2}}(\hat{b}_1 + \hat{b}_2) \quad \text{and} \quad \hat{B}_2 = \frac{1}{\sqrt{2}}(\hat{b}_2 - \hat{b}_1) \tag{2.21}$$

in which we have used the unitary beam-splitter transformations as per Eq. 1.25, but set $\cos\xi = \sin\xi = \frac{1}{\sqrt{2}}$ (for $\xi = \frac{\pi}{4}$), as we are considering a 50:50 BS here. This then gives our photodetector intensity difference operator as:

$$\hat{I}_{\hat{B}_1 - \hat{B}_2} = \langle \hat{B}_1^\dagger \hat{B}_1 - \hat{B}_2^\dagger \hat{B}_2 \rangle = \langle \hat{b}_1^\dagger \hat{b}_2 + \hat{b}_2^\dagger \hat{b}_1 \rangle \,. \tag{2.22}$$

Now, setting the local oscillator mode to $\hat{B}_2 = |\beta| e^{i\theta}$, it follows that:

$$\hat{I}_{\hat{B}_1 - \hat{B}_2} = 2|\beta| \langle \hat{x}_\theta \rangle \,, \tag{2.23}$$

where, $\hat{x}_\theta = \frac{1}{2}\left(\hat{b}_1 e^{-i\theta} + \hat{b}_1^\dagger e^{i\theta}\right)$ [80] (see Eq. 1.13), $|\beta|$ is the amplitude of the strong coherent field injected in mode B_2, and the phase of the quadrature $\hat{x}_\theta$ to be measured is given by the phase θ of this local oscillator [148]. Finally, we note here that as the signal (mode B_1) and the local oscillator (mode B_2) beams are generated from a common source in all experiments that use homodyne detectors, we can assume that the phases of the signal and local oscillator are fixed in relation [84]. Hence, we identify the phase of the local oscillator as the phase difference between modes B_1 and B_2.

The probability amplitude of a homodyne measurement on an arbitrary coherent state $\left||\alpha|e^{i\varphi}\right\rangle$ can be described by projecting with an $\hat{x}_\theta$ eigenstate, where $\hat{x}_\theta |x_\theta\rangle = x_\theta |x_\theta\rangle$ [40]:

$$\left\langle x_\theta \middle| |\alpha| e^{\mathrm{i}\varphi} \right\rangle = \frac{1}{2^{-\frac{1}{4}} \pi^{\frac{1}{4}}} \exp\left[-(x_\theta)^2 + 2e^{\mathrm{i}(\varphi-\theta)} |\alpha| x_\theta - \frac{1}{2} e^{2\mathrm{i}(\varphi-\theta)} |\alpha|^2 - \frac{1}{2}|\alpha|^2 \right], \tag{2.24}$$

where the subscript on x_θ is indicative of the angle in which the homodyne measurement is performed, and as previously stated, importantly this angle can be chosen through the phase of the local oscillator. For a full derivation of this wave-function please see Appendix B. The homodyne measurement projector is thus described mathematically as:

$$\hat{\Pi}_{HD}(x_\theta) = |x_\theta\rangle \langle x_\theta| \,, \tag{2.25}$$

where, the subscript HD indicates "homodyne detection", and θ gives the phase angle in which the measurement takes place. We note here that homodyne measurement is a routine and very accurate measurement technique used widely in optics, for many years, as a means of measuring phase-dependent quantum phenomena [149–152].

As will be shown to be vital in our calculations later in this thesis, the outcome of a homodyne measurement is a value x_θ of the continuous quadrature variable

$\hat{x}_\theta$, and the resultant homodyne measurement value is given by a probability distribution that comes from the modulus squared of the wave-function (as given in Eq. 2.24). We therefore define an *ideal* homodyne measurement as the case when the resultant homodyne measurement value is at the maximum of the probability distribution, as will be assessed in Chapter 3.

In Chapter 5, we also consider two circumstances in which this homodyne measurement is not the ideal/perfect case; 'non-ideal' homodyne measurement outcomes, in which we assess the impact caused by the homodyne measurement outcome not being precisely where we ideally expect it to be (i.e. the measurement outcome is not at the maximum point of the probability distribution); 'imperfect' homodyne detection, where we quantify the homodyne detection outcome to have a given resolution bandwidth around the ideal (or non-ideal) measured value.

2.7 Linear Entropy

Establishing quantum entropies is absolutely vital in quantum statistical mechanics and information theory. Within information theory, entropy is a measure of the lack of information about a system [153]; intrinsically, the entropy of a pure quantum state would be 0, as we have complete information about this system, and so the more mixed a state becomes, the more the entropy then increases. Shannon first derived classical information entropy as $H(X) = -\sum_i p_i \ln p_i$ [153], (where $H(X)$ is the Shannon information entropy of random variable X, and p_i are the probabilities of the different possible values X may take [2]).

The Shannon entropy can be considered as a measure of the uncertainty associated with a classical probability distribution. Shannon's measure of entropy is easily extended to the quantum world, by replacing the classical probability distribution with quantum density matrices [154]; Von Neumann entropy was first introduced in J. V. Neumann's groundbreaking book *Mathematical Foundations of Quantum Mechanics* in 1932 (English translation published in 1955 [155]). Von Neumann entropy is calculated as $S_{VN} = -\operatorname{Tr}[\rho \ln \rho]$, where the subscript VN denotes Von Neumann entropy, and ρ is a density matrix (note the equivalence of the Von Neumann entropy measure with that of Shannon's classical entropy measure).

Linear entropy is an approximation to the Von Neumann entropy, and is often employed as a measure of entropy of a density matrix, as it is more straight-forward to compute; Von Neumann entropy requires one to diagonalise a density matrix, which becomes more complex for non-pure density matrices [156].

Although linear entropy is an approximation to Von Neumann entropy, it is nonetheless still an accurate assessment for 2-qubit density matrices [157], and still monotonically increases as a function of any variables which cause the mixture of our final density matrix to increase. Monotonically increasing here means that the linear entropy is entirely non-decreasing [158] (as will be shown in practice once we plot linear entropy in Chapter 3). For example, if we have decoherence in our system

in terms of photon losses, the linear entropy should reflect this by being monotonic as a function of photon losses.

Linear entropy is calculated using the formula:

$$S_L(\rho) = 1 - \mathrm{Tr}\left[\rho^2\right], \tag{2.26}$$

where S_L is the linear entropy of the density matrix ρ, and can take any value between 0 (corresponding to a pure state), to $S_L^{max.} = 1 - \frac{1}{d}$, where d is the dimension of the system [159, 160]. In the case of a two qubit system (with dimension value 4, as it is a 4x4 matrix) the maximum value the linear entropy can take will therefore be 0.75. The normalisation can also be adjusted such that $0 \geq S_L \geq 1$, by instead calculating linear entropy as $S_L = \frac{d}{d-1}(1 - \mathrm{Tr}\left[\rho^2\right])$ [161]. However, in this work we will instead use the definition given in Eq. 2.26.

For an example of how the linear entropy of our final density matrix is calculated, refer to Appendix E.

2.8 Entanglement Negativity

Entanglement negativity is one of many ways to compute and measure the entanglement of quantum systems [162], and was first introduced by G. Vidal and R. Werner in 2002 [163]. For entangled pure systems, determining the entropy of the subsystems is enough to quantify bipartite entanglement, however in the case of mixed states (which we are concerned with in this work) the entropy no longer suffices as an accurate measure of entanglement. For a measure of entanglement ($E(\rho)$) to be considered acceptable it should satisfy certain postulates [164–166]; separability, such that $E(\rho) = 0$ if, and only if, ρ is separable; non-negativity, i.e. $E(\rho) \geq 0$; monotonicity, such that any LOCC (local operations and classical communication) cannot increase the entanglement; convexity, such that the entanglement measure is monotonic under discarding information.

Entanglement negativity satisfies the above postulates, and is related to the Peres-Horodecki criterion for entanglement; the Peres-Horodecki criterion assess the separability of a quantum state, such that if the partial transpose of the density matrix is also a valid quantum state (that is to say that it can be expressed as only Dirac kets) then this quantum state is described as separable, and therefore not entangled [167, 168]. It then follows that if the partial transpose of a density matrix is non-separable (and therefore somewhat entangled) it may therefore have negative eigenvalues [169]. To calculate entanglement negativity we use the equation

$$\mathcal{N}(\rho) = -2\sum_i \lambda_i^-, \tag{2.27}$$

where $\mathcal{N}(\rho)$ denotes the entanglement negativity value of the density matrix ρ, and

$\sum_i \lambda_i^-$ represents the negative eigenvalues of the partial transpose of ρ. Entanglement negativity may take any value between 0 and 1, describing a state of no entanglement, and of maximal entanglement, respectively. Following on from our above discussion of the Peres-Horodecki criterion, the entanglement negativity of a quantum state therefore does not violate these criterion.

As an example of how this calculation is performed, consider the maximally entangled $|\Phi^+\rangle = \frac{1}{\sqrt{2}}(|00\rangle + |11\rangle)$ Bell state. Firstly, we need to calculate the partial transpose of the density matrix of $|\phi^+\rangle$, by:

$$\begin{aligned} \rho_{\Phi^+} = \left|\Phi^+\right\rangle \left\langle\Phi^+\right| &= \frac{1}{2}(|00\rangle\langle 00| + |00\rangle\langle 11| + |11\rangle\langle 00| + |11\rangle\langle 11|) \\ \therefore \quad \rho_{\Phi^+}^{PT} &= \frac{1}{2}(|00\rangle\langle 00| + |01\rangle\langle 10| + |10\rangle\langle 01| + |11\rangle\langle 11|), \end{aligned} \tag{2.28}$$

where the superscript PT denotes the partial transpose of the density matrix ρ. Next, we then need to calculate the determinant of $\rho_{\Phi^+}^{PT} - \lambda\hat{I}$ (where λ are the eigenvalues, and $\hat{I}$ is the identity matrix, and $\det\left(\rho_{\Phi^+}^{PT} - \lambda\hat{I}\right) = 0$), so as to then be able to find the eigenvalues of ρ_{Φ^+}, as follows:

$$\begin{aligned} \det\left(\rho_{\Phi^+}^{PT} - \lambda\hat{I}\right) &= \begin{vmatrix} \frac{1}{2}-\lambda & 0 & 0 & 0 \\ 0 & -\lambda & \frac{1}{2} & 0 \\ 0 & \frac{1}{2} & -\lambda & 0 \\ 0 & 0 & 0 & \frac{1}{2}-\lambda \end{vmatrix} \\ &= \left(\frac{1}{2}-\lambda\right) \begin{vmatrix} -\lambda & \frac{1}{2} & 0 \\ \frac{1}{2} & -\lambda & 0 \\ 0 & 0 & \frac{1}{2}-\lambda \end{vmatrix} \\ &= \left(\frac{1}{2}-\lambda\right) \left(\lambda \begin{vmatrix} -\lambda & 0 \\ 0 & \frac{1}{2}-\lambda \end{vmatrix} - \frac{1}{2} \begin{vmatrix} \frac{1}{2} & 0 \\ 0 & \frac{1}{2}-\lambda \end{vmatrix} + 0 \begin{vmatrix} \frac{1}{2} & -\lambda \\ 0 & 0 \end{vmatrix}\right) \\ &= \left(\frac{1}{2}-\lambda\right) \left((-\lambda)(-\lambda)\left(\frac{1}{2}-\lambda\right) - \left(\frac{1}{2}\right)\left(\frac{1}{2}\right)\left(\frac{1}{2}-\lambda\right)\right) \\ &= \left(\frac{1}{2}-\lambda\right)^2 \left(\lambda^2 - \frac{1}{4}\right) = \lambda^4 - \lambda^3 + \frac{\lambda}{4} - \frac{1}{16} = 0, \end{aligned} \tag{2.29}$$

where the determinant has been computed using the Laplace expansion formula [170]. Now, we must solve the last equation given above to determine the eigenvalues of the density matrix, which are then:

$$\lambda = \begin{cases} -\frac{1}{2} \\ \frac{1}{2} \\ \frac{1}{2} \\ \frac{1}{2} \end{cases} \tag{2.30}$$

As we now have the four eigenvalues of ρ_{Φ^+} we can calculate the entanglement negativity of this density matrix using the formula given in Eq. 2.27, which is done

by simply multiplying the sum of all of the negative eigenvalues by 2. In the case of ρ_{Φ^+} we have only one eigenvalue that is negative, therefore the entanglement negativity is calculated as $\mathcal{N}(\rho) = -2(-\frac{1}{2}) = 1$. Indeed, we expect the entanglement negativity of ρ_{Φ^+} to be unity as the Bell states are maximally entangled two qubit states.

It is important to note here that in general entanglement negativity is calculated using $\mathcal{N}(\rho) = -\sum_i \frac{|\lambda_i^-| - \lambda_i^-}{2}$ [171], where the maximum value for the entanglement negativity is then $\frac{1}{2}$ (this is straight-forward to check given the eigenvalues determined in the above method). Within this work we have merely normalised the entanglement negativity so that the maximum is unity and the minimum is 0 [169]. Lastly, we point out that entanglement negativity is sometimes considered in literature as *logarithmic* negativity $E_{\mathcal{N}}(\rho)$, which is defined as $E_{\mathcal{N}}(\rho) = \log_2 ||\rho^{PT}||$, where $||.||$ is the trace norm, and the superscript PT again denotes partial transpose [172]. The logarithmic negativity is related to negativity by $E_{\mathcal{N}}(\rho) = \log_2(2\mathcal{N}(\rho) + 1)$.

For an example of how the entanglement negativity of our final density matrix is calculated, refer to Appendix E.

2.9 Fidelity

Fidelity is a measure of the distance of two quantum states, or density matrices [173]. In this respect, the distance here refers to the closeness or overlap of these quantum states. The fidelity of a density matrix ρ can be calculated as:

$$F(\left|\psi\right\rangle, \rho) = \left\langle\psi\right| \rho \left|\psi\right\rangle, \tag{2.31}$$

where $\left|\psi\right\rangle$ is the ideal state, and ρ is the density matrix being analysed. This definition of fidelity was first introduced by B. Schumacher in 1995 [174]. Calculating the closeness (fidelity) of ρ with respect to $\left|\psi\right\rangle$ will return a value of 1 if the matrix is identical to that of this particular quantum state $\left|\psi\right\rangle$, and 0 if these two states are orthogonal (that is to say that they are as physically distinct as possible). However, this definition of fidelity applies only in the special case that $\left|\psi\right\rangle$ is a pure quantum state.

As an example of how this definition of fidelity may be applied to a pure quantum system, consider the Bell states. Let us calculate the fidelity of the $\left|\Phi^+\right\rangle = \frac{1}{\sqrt{2}}(\left|00\right\rangle + \left|11\right\rangle)$ Bell state, with respect to $\left|\Phi^-\right\rangle = \frac{1}{\sqrt{2}}(\left|00\right\rangle - \left|11\right\rangle)$. Fidelity is then determined as:

$$F(\left|\Phi^-\right\rangle, \rho_{\Phi^+}) = \frac{1}{4}(\left\langle 00\right| - \left\langle 11\right|)(\left|00\right\rangle\left\langle 00\right| + \left|00\right\rangle\left\langle 11\right| + \left|11\right\rangle\left\langle 00\right| + \left|11\right\rangle\left\langle 11\right|)(\left|00\right\rangle - \left|11\right\rangle), \tag{2.32}$$

where, $\rho_{\Phi^+} = \left|\Phi^+\right\rangle\left\langle\Phi^+\right|$. Using the inner products $\langle 0|0\rangle = \langle 1|1\rangle = 1$ and $\langle 0|1\rangle = \langle 1|0\rangle = 0$, the expression for fidelity then reduces to $F(\left|\Phi^-\right\rangle, \rho_{\Phi^+}) = 0$. Of course, this result is not at all surprising, as the Bell states are known for all being pure, and

also orthogonal with respect to each other. Following the same method as above, but instead calculating the fidelity of the $|\phi^+\rangle$ Bell state with respect to itself, yields a fidelity of $F(|\Phi^+\rangle, \rho_{\Phi^+}) = 1$. Again, this result is as expected, because two identical quantum states would indeed have a maximal overlap of unity.

As we will be concerned primarily with mixed matrices within this work, it is more insightful to instead consider a more generalised definition of fidelity in terms of two density matrices ρ and σ, as introduced by R. Jozsa [175]:

$$F = \left| \mathrm{Tr} \left[\sqrt{\sqrt{\sigma}\,\rho\sqrt{\sigma}} \right] \right|^2 . \tag{2.33}$$

The above formula again works such that 0 corresponds to two orthogonal density matrices, and unity if, and only if, ρ and σ are identical.

We note here that there are in fact two accepted forms of Eq. 2.33, in that it can also be defined as $F = \mathrm{Tr} \left[\sqrt{\sqrt{\sigma}\,\rho\sqrt{\sigma}} \right]$ [2], and is often referred to as *square root* fidelity. The same applies to the less general definition of fidelity given in Eq. 2.31, which can also be computed as $F(|\psi\rangle, \rho) = \sqrt{\langle\psi|\,\rho\,|\psi\rangle}$. In either case this calculation still holds such that $F = 0$ for two orthogonal states, and $F = 1$ for two identical states. In this work we stick to the original definition of fidelity as per Eq. 2.33.

For an example of how the fidelity of our final density matrix is calculated, refer to Appendix E.

2.10 Success Probabilities

Success probability determines the likelihood of a particular process successfully taking place. In the case of our protocol we want to calculate the success probabilities for the vacuum and homodyne measurements. Due to the nature of success probability calculations these will be discussed later in this report (Sec. 6.1) once a more formal discussion of the protocol has been carried out.

Chapter 3

Coherent State and Cat State ES

Part of the work detailed in this section was published in [1]: R. C. Parker, J. Joo, M. Razavi and T. P. Spiller, *J. Opt*, **19**, 10 (2017).

3.1 Coherent State ES

Now that we are equipped with all of the necessary tools to investigate our proposed entanglement swapping protocol, we will first demonstrate the case where we use a coherent states as the propagating modes, before moving onto the more complicated case where we consider cat states instead.

3.1.1 No Loss

Firstly, we will discuss the case for no losses to show the ideal principle of our proposed protocol. We illustrate our protocol in terms of a schematic (as per Fig. 2.2) but for no loss, as:

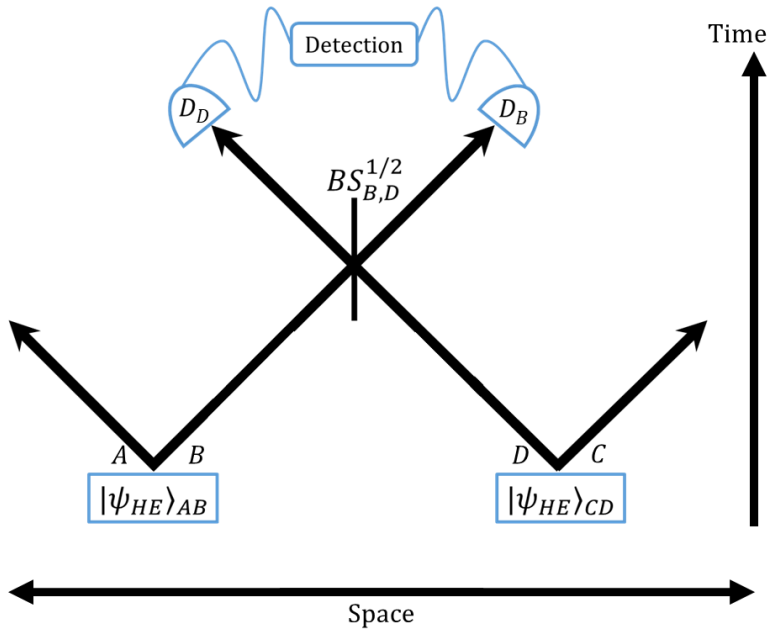

FIGURE 3.1: Diagram to represent the four channel system (where $|\psi_{HE}\rangle_{AB}$ and $|\psi_{HE}\rangle_{CD}$ are entangled hybrid states) undergoing entanglement swapping with no lossy channels. Modes B and D are mixed at a 50:50 beam-splitter ($BS_{B,D}^{1/2}$) and subsequently measured (D_B and D_D) to complete the protocol.

The initial hybrid entangled state of our coherent state entanglement swapping protocol, for no loss, is given mathematically as:

$$|\Psi^{Coh.}\rangle_{ABCD} = BS_{B,D}^{1/2}\,|\psi_{HE}^{Coh.}\rangle_{AB}\,|\psi_{HE}^{Coh.}\rangle_{CD}\,, \tag{3.1}$$

where, the subscript HE denotes a hybrid entangled quantum state. These hybrid entangled states are described as $|\psi_{HE}^{Coh.}\rangle_{AB} = \frac{1}{\sqrt{2}}(\,|0\rangle_A\,||\alpha|\rangle_B + |1\rangle_A\,|-|\alpha|\rangle_B)$ (and the same for the hybrid entangled state of modes C and D - see Eq. 2.3). Hence we can express our total initial hybrid entangled state as:

$$|\Psi_{HE}^{Coh.}\rangle_{ABCD} = \frac{1}{2}\Big[\Big(\,|0\rangle_A\,||\alpha|\rangle_B + |1\rangle_A\,|-|\alpha|\rangle_B\Big) \otimes \Big(\,|0\rangle_C\,||\alpha|\rangle_D + |1\rangle_C\,|-|\alpha|\rangle_D\Big)\Big] \tag{3.2}$$

$$= \frac{1}{2}\Big[\,|00\rangle_{AC}\,||\alpha|\rangle_B\,||\alpha|\rangle_D + |01\rangle_{AC}\,||\alpha|\rangle_B\,|-|\alpha|\rangle_D + |10\rangle_{AC}\,|-|\alpha|\rangle_B\,||\alpha|\rangle_D + |11\rangle_{AC}\,|-|\alpha|\rangle_B\,|-|\alpha|\rangle_D\Big]. \tag{3.3}$$

We then apply the 50:50 beam-splitter operator shown in Eq. 3.1 to mix modes B and D, using the following beam-splitter transformation outputs:

$$BS_{i,j}^{1/2}\,|\alpha\rangle_i\,|\beta\rangle_j = \left|\frac{\alpha-\beta}{\sqrt{2}}\right\rangle_i \left|\frac{\alpha+\beta}{\sqrt{2}}\right\rangle_j, \tag{3.4}$$

where the above unitary transformation was derived in Chapter 2, Sec. 2.4, Eq. 2.18. The derivation was for the general case of a 50:50 BS operation on two coherent states

of different amplitudes, however, in this protocol our coherent states that meet at the 50:50 BS are of the same amplitude, therefore the BS outputs are given as:

$$\begin{aligned} BS^{1/2}_{B,D}\,||\alpha|\rangle_B\,||\alpha|\rangle_D &= |0\rangle_B\,|\sqrt{2}\,|\alpha|\rangle_D \\ BS^{1/2}_{B,D}\,||\alpha|\rangle_B\,|-|\alpha|\rangle_D &= |\sqrt{2}\,|\alpha|\rangle_B\,|0\rangle_D \\ BS^{1/2}_{B,D}\,|-|\alpha|\rangle_B\,||\alpha|\rangle_D &= |-\sqrt{2}\,|\alpha|\rangle_B\,|0\rangle_D \\ BS^{1/2}_{B,D}\,|-|\alpha|\rangle_B\,|-|\alpha|\rangle_D &= |0\rangle_B\,|-\sqrt{2}\,|\alpha|\rangle_D\,, \end{aligned} \tag{3.5}$$

such that,

$$\begin{aligned} |\Psi^{Coh.}\rangle_{ABCD} &= \frac{1}{2}\Big[\,|00\rangle_{AC}\,|0\rangle_B\,|\sqrt{2}\,|\alpha|\rangle_D + |01\rangle_{AC}\,|\sqrt{2}\,|\alpha|\rangle_B\,|0\rangle_D \\ &\quad + |10\rangle_{AC}\,|-\sqrt{2}\,|\alpha|\rangle_B\,|0\rangle_D + |11\rangle_{AC}\,|0\rangle_B\,|-\sqrt{2}\,|\alpha|\rangle_D\,\Big] \\ &= \frac{1}{2}\Big[\,|0\rangle_B\,\Big(\,|00\rangle_{AC}\,|\sqrt{2}\,|\alpha|\rangle_D + |11\rangle_{AC}\,|-\sqrt{2}\,|\alpha|\rangle_D\,\Big) \\ &\quad + |0\rangle_D\,\Big(\,|01\rangle_{AC}\,|\sqrt{2}\,|\alpha|\rangle_B + |10\rangle_{AC}\,|-\sqrt{2}\,|\alpha|\rangle_B\,\Big)\Big]. \end{aligned} \tag{3.6}$$

If one measures a vacuum state in mode B, applying the vacuum projector $\hat{P}^0_B = |0\rangle_B\,\langle 0|$ (given in Eq. 2.19) to Eq. 3.4 gives:

$$\begin{aligned} \hat{P}^0_B\,|\Psi^{Coh.}\rangle_{ABCD} &= |0\rangle_B\,\langle 0|\Psi^{Coh.}\rangle_{ABCD} = \sqrt{\mathcal{P}_0^{Coh.}}\,|0\rangle_B\,|\Psi^{Coh.}\rangle_{ACD} \\ &= \sqrt{\mathcal{P}_0^{Coh.}}\,|0\rangle_B\,\Big[\,{}_B\langle 0|0\rangle_B\Big(\,|00\rangle_{AC}\,|\sqrt{2}\,|\alpha|\rangle_D + |11\rangle_{AC}\,|-\sqrt{2}\,|\alpha|\rangle_D\,\Big) \\ &\quad + |0\rangle_D\,\Big(\,|01\rangle_{AC\,B}\langle 0|\sqrt{2}\,|\alpha|\rangle_B + |10\rangle_{AC\,B}\langle 0|-\sqrt{2}\,|\alpha|\rangle_B\Big)\Big], \end{aligned} \tag{3.7}$$

where the output states from the vacuum measurement projector are calculated as the overlap with a vacuum state, such that:

$$|0\rangle_B\,\langle 0|0\rangle_B = |0\rangle_B \tag{3.8}$$

$$|0\rangle_B\,\langle 0|\sqrt{2}\,|\alpha|\rangle_B = e^{-|\alpha|^2}\,|0\rangle_B \tag{3.9}$$

$$|0\rangle_B\,\langle 0|-\sqrt{2}\,|\alpha|\rangle_B = e^{-|\alpha|^2}\,|0\rangle_B\,, \tag{3.10}$$

and the remaining $|0\rangle_B$ term in the above outputs will be used to calculate the conjugate outputs when we form the final density matrix, ρ_{ABCD} of the total quantum state $|\Psi^{Coh.}\rangle_{ABCD}$. In Eq. 3.7 the normalisation is taken as $\mathcal{P}_0^{Coh.}$ to account for the fact that this projective measurement has a success probability associated with it; we therefore will now briefly discuss the success probability of the projective vacuum measurement for the no loss protocol.

3.1.2 Success Probability of Vacuum Measurement

We consider now the success probability of performing a projective vacuum measurement to the state given by Eq. 3.6. To do so, we use the identity operator $\hat{I}_B$

written in the Fock state basis for mode B:

$$\hat{I}_B = |0\rangle_B \langle 0| + \sum_{n=1}^{\infty} |n\rangle_B \langle n|, \tag{3.11}$$

where, $\langle n|0\rangle = 0$ for $n \geq 1$. We choose this form of the identity operator as we wish to model the success of projecting with a vacuum state, and so we also must consider the cases where we do not project with a vacuum. We therefore allow for a summation of $\sum_{n=1}^{\infty} |n\rangle_B \langle n|$ to account for any states we may potentially project with that are not a vacuum state. If we then apply this identity ("do-nothing") operator to our input state $|\Psi^{Coh.}\rangle_{ABCD}$ we get:

$$\begin{aligned}\hat{I}_B |\Psi^{Coh.}\rangle_{ABCD} &= |0\rangle_B \langle 0|\Psi^{Coh.}\rangle_{ABCD} + \sum_{n=1}^{\infty} |n\rangle_B \langle n|\Psi^{Coh.}\rangle_{ABCD}, \\ &\equiv \sqrt{\mathcal{P}_0^{Coh.}}\, |0\rangle_B |\Psi_0^{Coh.}\rangle_{ACD} + \sum_{n=1}^{\infty} \sqrt{\mathcal{P}_n^{Coh.}}\, |n\rangle_B |\Psi_n^{Coh.}\rangle_{ACD},\end{aligned} \tag{3.12}$$

where, $\mathcal{P}_0^{Coh.}$ is the success probability for successful vacuum projection, for ${}_{ACD}\langle\Psi_0^{Coh.}|\Psi_0^{Coh.}\rangle_{ACD} = 1$ and ${}_{ACD}\langle\Psi_0^{Coh.}|\Psi_n^{Coh.}\rangle_{ACD} = 0$, where $|\Psi_0^{Coh.}\rangle_{ACD}$ is the state in which the vacuum has successfully projected with, and $|\Psi_n^{Coh.}\rangle_{ACD}$ is the state which has not. Clearly it must also hold that $\sum_{n=1}^{\infty} \mathcal{P}_n^{Coh.} = 1 - \mathcal{P}_0^{Coh.}$. We can then rewrite the above as:

$$\begin{aligned}&\sqrt{\mathcal{P}_0^{Coh.}}\, |0\rangle_B |\Psi_0^{Coh.}\rangle_{ACD} \\ &= |0\rangle_B \frac{1}{2}\Big[|00\rangle_{AC} |\sqrt{2}|\alpha|\rangle_D + |11\rangle_{AC} |-\sqrt{2}|\alpha|\rangle_D + e^{-|\alpha|^2} |0\rangle_D (|01\rangle_{AC} + |10\rangle_{AC})\Big],\end{aligned} \tag{3.13}$$

where the factor of $\frac{1}{2}$ is the normalisation of the state prior to the vacuum projection ($|\Psi^{Coh.}\rangle_{ABCD}$, see Eq. 3.6), and so it then follows that:

$$\mathrm{Tr}_{ACD}\left[\mathcal{P}_0^{Coh.} \rho_{ACD}\right] = \mathcal{P}_0^{Coh.}, \tag{3.14}$$

by definition, if, and only if, ρ_{ACD} is normalised, where $\rho_{ACD} = |\Psi_0^{Coh.}\rangle_{ACD} \langle\Psi_0^{Coh.}|$. Note that we have dropped the $|0\rangle_B$ term in the above, for convenience of notation. If we then trace-out modes A, C and D from the density matrix ρ_{ACD} we get:

$$\begin{aligned}\mathrm{Tr}_{ACD}\left[\mathcal{P}_0^{Coh.} \rho_{ACD}\right] &= \frac{1}{4}(2 + 2e^{-2|\alpha|^2}) = \mathcal{P}_0^{Coh.} \\ \therefore \quad \mathcal{P}_0^{Coh.} &= \frac{1 + e^{-2|\alpha|^2}}{2}.\end{aligned} \tag{3.15}$$

It then follows that for $|\alpha| = 0$ the success probability is unity, and in the limit of large $|\alpha|$ the success probability of this measurement tends to $\mathcal{P}_0^{Coh.} \to \frac{1}{2}$, however

this will be more formally discussed in Chapter 6, Sec. 6.1.

3.2 Coherent ES - No Loss (continued)

The next step in this protocol is to apply a homodyne measurement projector at an angle of $\frac{\pi}{2}$ to mode D; this is only undertaken conditional on the successful vacuum projection of mode B (as discussed in the previous section). This homodyne projector is described mathematically as $\hat{\Pi}_{HD}(x_\theta) = |x_\theta\rangle \langle x_\theta|$ (derived in Chapter 2, Sec. 2.6, Eq. 2.25, where the subscript HD indicates "homodyne detection", and θ gives the phase angle in which the measurement takes place ($\theta = \frac{\pi}{2}$ for our coherent state entanglement swapping protocol). Applying this homodyne measurement to mode D in our quantum state projects Eq. 3.7 to:

$$\begin{aligned}\hat{\Pi}_{HD}(x_{\frac{\pi}{2}})\,|\Psi^{Coh.}\rangle_{ACD} =& |x_{\frac{\pi}{2}}\rangle_D \langle x_{\frac{\pi}{2}}|\Psi^{Coh.}\rangle_{ACD} \\ =& \mathcal{N}^{Coh.}\Big[\,|00\rangle_{AC}\,{}_D\langle x_{\frac{\pi}{2}}|\sqrt{2}\,|\alpha|\rangle_D + |11\rangle_{AC}\,{}_D\langle x_{\frac{\pi}{2}}|-\sqrt{2}\,|\alpha|\rangle_D \\ &+ e^{-|\alpha|^2}\,{}_D\langle x_{\frac{\pi}{2}}|0\rangle_D\Big(\,|01\rangle_{AC} + |10\rangle_{AC}\,\Big)\Big], \end{aligned} \tag{3.16}$$

where, $\mathcal{N}$ is the normalisation and we have omitted the $|0\rangle_B$ term in Eq. 3.7 for convenience. Note that $\mathcal{N}$ will be the generic symbol to denote the normalisation after a homodyne measurement (which is being made conditional on the vacuum projection being successful), with the superscript denoting the particular protocol. The outputs for this homodyne detection (as derived in Appendix B for the general case) are then calculated as:

$$|x_{\frac{\pi}{2}}\rangle_D \,\langle x_{\frac{\pi}{2}}|\pm\sqrt{2}\,|\alpha|\rangle_D = |x_{\frac{\pi}{2}}\rangle_D \,\langle x_{\frac{\pi}{2}}|0\rangle_D \exp\left[\mp 2\sqrt{2}\,\mathrm{i}|\alpha|x_{\frac{\pi}{2}}\right], \tag{3.17}$$

where ${}_D\langle x_{\frac{\pi}{2}}|0\rangle_D = \frac{1}{2^{-\frac{1}{4}}\pi^{\frac{1}{4}}} \exp\left[-(x_{\frac{\pi}{2}})^2\right]$ is part of the output of any homodyne measurement, and so we can effectively ignore this as it will be accounted for in the normalisation in any case. It then follows that our total quantum state after this homodyne measurement is:

$$\begin{aligned}&|\Psi^{Coh.}\rangle_{AC} = \\ &\mathcal{N}^{Coh.}\Big(e^{-2\sqrt{2}\,\mathrm{i}|\alpha|x_{\frac{\pi}{2}}}\,|00\rangle_{AC} + e^{2\sqrt{2}\,\mathrm{i}|\alpha|x_{\frac{\pi}{2}}}\,|11\rangle_{AC} + e^{-|\alpha|^2}\Big(\,|01\rangle_{AC} + |10\rangle_{AC}\,\Big)\Big), \end{aligned} \tag{3.18}$$

in which we have omitted the $|x_{\frac{\pi}{2}}\rangle$ term for convenience as this is dealt with when forming our final density matrix. In the limit of $|\alpha| >> 1$ our final quantum state becomes

$$|\Psi^{Coh.}\rangle_{AC} = \frac{1}{\sqrt{2}}\Big(e^{-2\sqrt{2}\,\mathrm{i}|\alpha|x_{\frac{\pi}{2}}}\,|00\rangle_{AC} + e^{2\sqrt{2}\,\mathrm{i}|\alpha|x_{\frac{\pi}{2}}}\,|11\rangle_{AC}\,\Big), \tag{3.19}$$

and for the most ideal homodyne measurement outcome of $x_{\frac{\pi}{2}} = 0$ this becomes:

$$|\Psi^{Coh.}\rangle_{AC} = \frac{1}{\sqrt{2}}\Big(|00\rangle_{AC} + |11\rangle_{AC}\Big), \tag{3.20}$$

which is the maximally entangled $|\Phi^+\rangle$ Bell state. It is important to note that the homodyne measurement outcome, denoted by $x_{\frac{\pi}{2}}$ in this case, is absolutely not a discrete variable; the homodyne outcome, if being represented realistically, should be expressed as a distribution of outcomes as it is a continuous variable. Nevertheless, for now we consider the most optimum *discrete* outcomes, and a more formal representation and analysis of homodyne detection will be covered later in this work in Chapter 5, and in Chapter 6 where we consider the success probability of this homodyne projection.

The following position and momentum phase space diagram simplistically illustrates how the *average* homodyne detection outcome for this protocol is $x_{\frac{\pi}{2}} = 0$:

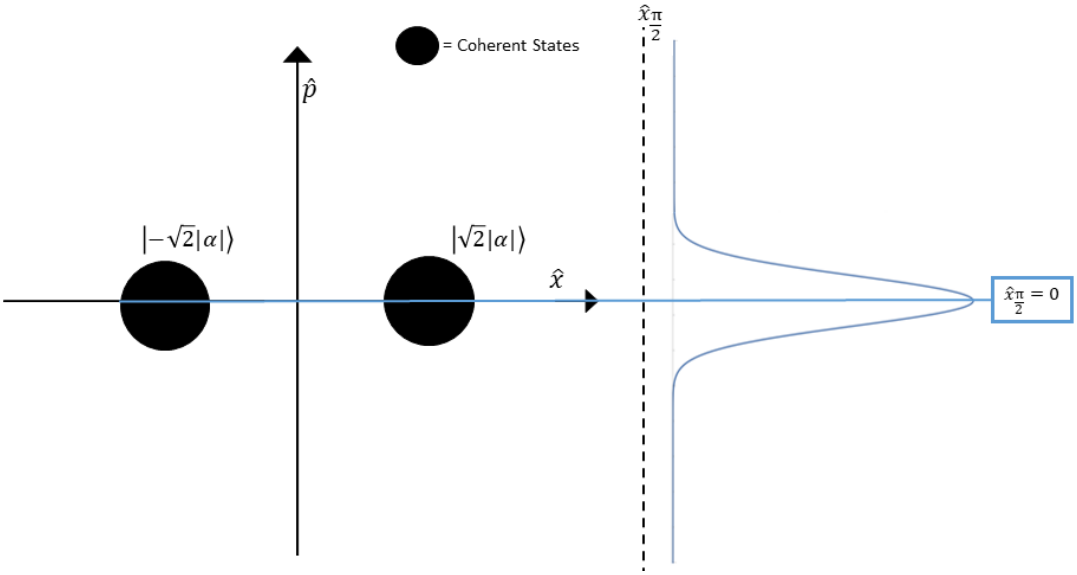

FIGURE 3.2: Diagram to represent the phase space in which the coherent states in mode D occupy, combined with a probability distribution showing the most likely homodyne measurement outcome, $x_{\frac{\pi}{2}} = 0$.

Clearly in this phase space diagram, if one performs a quadrature measurement along the $\frac{\pi}{2}$ axis then the most probable outcome is $x_{\frac{\pi}{2}} = 0$. It is important to note here that we choose to measure along the $\frac{\pi}{2}$ axis to ensure that an entangled state is resultant from this measurement; by measuring along this axis the two coherent states shown in Fig. 3.2 are indistinguishable, and as such produce an entangled state upon their measurement. Conversely, were we to choose to measure along the $\hat{x}$ axis then we would have a phase space probability distribution showing two peaks, and as such the measurement would indeed distinguish between the two states shown in Fig. 3.2, thus causing the resultant state after this measurement to not be entangled.

Intrinsically, there will be errors in the phase angle of this measurement θ, such that $\theta \neq \frac{\pi}{2}$. In this circumstance we no longer project to the ideal states (as assessed already in this section) - by increasing the error in θ this causes two peaks in the probability distribution to eventually appear, as we are no longer indistinguishably erasing the quantum information between the coherent states given in Fig. 3.2. This then means that the resultant quantum state after this measurement will no longer be entangled. This error will not be accounted for in this thesis, as we investigate alternate forms of imperfections in the homodyne measurement (see Chapter 5), however this would make interesting further work.

3.2.1 Justifying our Measurement Processes

In this section we will shortly discuss and justify our choice of measurement operations. Within our proposed entanglement swapping protocols we apply a projective vacuum measurement to mode B and a homodyne measurement to mode D, so as to achieve a highly entangled resultant state.

Firstly, let us consider the circumstance in which we theoretically measure a vacuum state in both mode B and mode D, by beginning the mathematical proof with the state immediately after the 50:50 beam-splitter operation that mixes modes B and D (prior to any measurement operations), given in Eq. 3.6. If we apply a vacuum measurement operation to modes B and D (using the outputs of this measurement given in Eq. 3.10) then the outcome state is described as:

$$|\Psi^{Coh.}\rangle_{AC} = \mathcal{N} e^{-|\alpha|^2} \Big(|00\rangle_{AC} + |01\rangle_{AC} + |10\rangle_{AC} + |11\rangle_{AC} \Big), \tag{3.21}$$

where it is evident that in this circumstance we introduce an exponential dampening exponent into each state. This exponent would be removed by the normalisation of the quantum state, however what we are then left with would be a linear combination of all possible two qubit states, which is not entangled at all and is therefore useless for further quantum communication purposes.

Now, let us instead consider the case of performing a homodyne measurement to modes B and D. Again, we begin with Eq. 3.6, but instead apply a homodyne measurement to modes B and D (using the homodyne detection outcomes detailed in Eq. 3.17), which gives:

$$\begin{aligned} |\Psi^{Coh.}\rangle_{AC} = \mathcal{N} \Big(& e^{-2\sqrt{2}\,\mathrm{i}|\alpha| x_{\frac{\pi}{2}}} |00\rangle_{AC} + e^{-2\sqrt{2}\,\mathrm{i}|\alpha| x_{\frac{\pi}{2}}} |01\rangle_{AC} \\ & + e^{2\sqrt{2}\,\mathrm{i}|\alpha| x_{\frac{\pi}{2}}} |10\rangle_{AC} + e^{2\sqrt{2}\,\mathrm{i}|\alpha| x_{\frac{\pi}{2}}} |11\rangle_{AC} \Big). \end{aligned} \tag{3.22}$$

Again, we have a similar issue as we had in the protocol of applying a vacuum measurement to modes B and D: in Eq. 3.22 we have now introduced a phase into each state via this homodyne measurement, and recalling that the ideal outcome for this homodyne measurement here is $x_{\frac{\pi}{2}} = 0$ (see Fig. 3.2), then the outcome state is also a linear combination of all possible two qubit states, and as such is not

entangled. It is therefore easy to see why our measurement choice of applying a vacuum measurement to mode B, and performing homodyne detection in mode D gives us an entangled, and therefore useful, final quantum state. It should also be noted here that the same issue arises when considering losses, and also in the cat state entanglement swapping protocol.

3.2.2 Equal Loss in Modes B and D

We have seen that the ideal zero-loss outcome for our proposed entanglement swapping protocol using coherent states is (in the limit of large coherent state amplitude and the most ideal homodyne outcome) the maximally entangled $|\Phi^+\rangle$ Bell state. We will now show that the most ideal state for this protocol when also allowing for relatively low levels of photon loss tends to the same maximally entangled Bell state.

For the *lossy* protocol (see Fig. 2.2 for a schematic), our input states are the same as for the no loss case, however this time we must also apply a beam-splitter of transmission T combined with vacuum states (see Fig. 2.2). Therefore our starting point is the following:

$$|\Psi^{Coh.}_{loss}\rangle_{AB\varepsilon_B CD\varepsilon_D} = BS^T_{B,\varepsilon_B} BS^T_{D,\varepsilon_D} |\psi^{Coh.}_{HE}\rangle_{AB} \, |0\rangle_{\varepsilon_B} \, |\psi^{Coh.}_{HE}\rangle_{CD} \, |0\rangle_{\varepsilon_D} \tag{3.23}$$

$$= BS^T_{B,\varepsilon_B} BS^T_{D,\varepsilon_D} \frac{1}{2}\Big[\Big(|0\rangle_A \, ||\alpha|\rangle_B + |1\rangle_A \, |-|\alpha|\rangle_B \Big) |0\rangle_{\varepsilon_B} \otimes \Big(|0\rangle_C \, ||\alpha|\rangle_D + |1\rangle_C \, |-|\alpha|\rangle_D \Big) |0\rangle_{\varepsilon_D} \Big], \tag{3.24}$$

where,

$$\begin{aligned} BS^T_{i,\varepsilon_i} \, ||\alpha|\rangle_i \, |0\rangle_{\varepsilon_i} &= |\sqrt{T}\,|\alpha|\rangle_i \, |\sqrt{1-T}\,|\alpha|\rangle_{\varepsilon_i} \\ BS^T_{i,\varepsilon_i} \, |-|\alpha|\rangle_i \, |0\rangle_{\varepsilon_i} &= |-\sqrt{T}\,|\alpha|\rangle_i \, |-\sqrt{1-T}\,|\alpha|\rangle_{\varepsilon_i} . \end{aligned} \tag{3.25}$$

The above beam-splitter transformations were derived in Chapter 2, Sec. 2.3, Eq. 2.14, and allow us to model modes B and D as (equally) lossy modes, giving the following lossy total quantum state:

$$|\Psi^{Coh.}_{loss}\rangle_{AB\varepsilon_B CD\varepsilon_D} = \tag{3.26}$$

$$\frac{1}{2}\Big[\Big(|0\rangle_A \, |\sqrt{T}\,|\alpha|\rangle_B \, |\sqrt{1-T}\,|\alpha|\rangle_{\varepsilon_B} + |1\rangle_A \, |-\sqrt{T}\,|\alpha|\rangle_B \, |-\sqrt{1-T}\,|\alpha|\rangle_{\varepsilon_B} \Big) \otimes \Big(|0\rangle_C \, |\sqrt{T}\,|\alpha|\rangle_D \, |\sqrt{1-T}\,|\alpha|\rangle_{\varepsilon_D} + |1\rangle_C \, |-\sqrt{T}\,|\alpha|\rangle_D \, |-\sqrt{1-T}\,|\alpha|\rangle_{\varepsilon_D} \Big)\Big] \tag{3.27}$$

$$\begin{aligned} = \frac{1}{2}\Big[&|00\rangle_{AC} \, |\sqrt{T}\,|\alpha|\rangle_B \, |\sqrt{T}\,|\alpha|\rangle_D \, |\sqrt{1-T}\,|\alpha|\rangle_{\varepsilon_B} \, |\sqrt{1-T}\,|\alpha|\rangle_{\varepsilon_D} \\ &+ |01\rangle_{AC} \, |\sqrt{T}\,|\alpha|\rangle_B \, |-\sqrt{T}\,|\alpha|\rangle_D \, |\sqrt{1-T}\,|\alpha|\rangle_{\varepsilon_B} \, |-\sqrt{1-T}\,|\alpha|\rangle_{\varepsilon_D} \\ &+ |10\rangle_{AC} \, |-\sqrt{T}\,|\alpha|\rangle_B \, |\sqrt{T}\,|\alpha|\rangle_D \, |-\sqrt{1-T}\,|\alpha|\rangle_{\varepsilon_B} \, |\sqrt{1-T}\,|\alpha|\rangle_{\varepsilon_D} \\ &+ |11\rangle_{AC} \, |-\sqrt{T}\,|\alpha|\rangle_B \, |-\sqrt{T}\,|\alpha|\rangle_D \, |-\sqrt{1-T}\,|\alpha|\rangle_{\varepsilon_B} \, |-\sqrt{1-T}\,|\alpha|\rangle_{\varepsilon_D} \Big]. \end{aligned} \tag{3.28}$$

We then apply a 50:50 beam-splitter to modes B and D as before, giving:

$$
\begin{aligned}
&BS^{1/2}_{B,D}\,|\Psi^{Coh.}_{loss}\rangle_{AB\varepsilon_B CD\varepsilon_D} = \\
&\frac{1}{2}\Big[\,|00\rangle_{AC}\,|0\rangle_B\,|\sqrt{2T}\,|\alpha|\rangle_D\,|\sqrt{1-T}\,|\alpha|\rangle_{\varepsilon_B}\,|\sqrt{1-T}\,|\alpha|\rangle_{\varepsilon_D} \\
&+|01\rangle_{AC}\,|\sqrt{2T}\,|\alpha|\rangle_B\,|0\rangle_D\,|\sqrt{1-T}\,|\alpha|\rangle_{\varepsilon_B}\,|-\sqrt{1-T}\,|\alpha|\rangle_{\varepsilon_D} \\
&+|10\rangle_{AC}\,|-\sqrt{2T}\,|\alpha|\rangle_B\,|0\rangle_D\,|-\sqrt{1-T}\,|\alpha|\rangle_{\varepsilon_B}\,|\sqrt{1-T}\,|\alpha|\rangle_{\varepsilon_D} \\
&+|11\rangle_{AC}\,|0\rangle_B\,|-\sqrt{2T}\,|\alpha|\rangle_D\,|-\sqrt{1-T}\,|\alpha|\rangle_{\varepsilon_B}\,|-\sqrt{1-T}\,|\alpha|\rangle_{\varepsilon_D}\Big] \qquad (3.29)\\
=\frac{1}{2}\Big[\,&|0\rangle_B\Big(|00\rangle_{AC}\,|\sqrt{2T}\,|\alpha|\rangle_D\,|\sqrt{1-T}\,|\alpha|\rangle_{\varepsilon_B}\,|\sqrt{1-T}\,|\alpha|\rangle_{\varepsilon_D} \\
&\quad+|11\rangle_{AC}\,|-\sqrt{2T}\,|\alpha|\rangle_D\,|-\sqrt{1-T}\,|\alpha|\rangle_{\varepsilon_B}\,|-\sqrt{1-T}\,|\alpha|\rangle_{\varepsilon_D}\Big) \\
&+|0\rangle_D\Big(|01\rangle_{AC}\,|\sqrt{2T}\,|\alpha|\rangle_B\,|\sqrt{1-T}\,|\alpha|\rangle_{\varepsilon_B}\,|-\sqrt{1-T}\,|\alpha|\rangle_{\varepsilon_D} \\
&\quad+|10\rangle_{AC}\,|-\sqrt{2T}\,|\alpha|\rangle_B\,|-\sqrt{1-T}\,|\alpha|\rangle_{\varepsilon_B}\,|\sqrt{1-T}\,|\alpha|\rangle_{\varepsilon_D}\Big)\Big]. \qquad (3.30)
\end{aligned}
$$

Measuring a vacuum in mode B, using the outcomes of ${}_B\langle 0|\pm\sqrt{2T}\,|\alpha|\rangle_B = e^{-T|\alpha|^2}$ gives us:

$$
\begin{aligned}
|\Psi^{Coh.}_{loss}\rangle_{A\varepsilon_B CD\varepsilon_D} = \sqrt{\mathcal{P}^{Coh.}_0}\Big[\,&|00\rangle_{AC}\,|\sqrt{2T}\,|\alpha|\rangle_D\,|\sqrt{1-T}\,|\alpha|\rangle_{\varepsilon_B}\,|\sqrt{1-T}\,|\alpha|\rangle_{\varepsilon_D} \\
&+|11\rangle_{AC}\,|-\sqrt{2T}\,|\alpha|\rangle_D\,|-\sqrt{1-T}\,|\alpha|\rangle_{\varepsilon_B}\,|-\sqrt{1-T}\,|\alpha|\rangle_{\varepsilon_D} \\
&+|0\rangle_D\,e^{-T|\alpha|^2}\Big(|01\rangle_{AC}\,|\sqrt{1-T}\,|\alpha|\rangle_{\varepsilon_B}\,|-\sqrt{1-T}\,|\alpha|\rangle_{\varepsilon_D} \\
&\quad+|10\rangle_{AC}\,|-\sqrt{1-T}\,|\alpha|\rangle_{\varepsilon_B}\,|\sqrt{1-T}\,|\alpha|\rangle_{\varepsilon_D}\Big)\Big], \qquad (3.31)
\end{aligned}
$$

where, $\mathcal{P}^{Coh.}_0$ is again the success probability of performing this vacuum projection - following the same method as given in the no loss case (see Subsec. 3.1.2), the success probability for the lossy case at hand is then $\mathcal{P}^{Coh.}_0 = \frac{1+e^{-2T|\alpha|^2}}{2}$ (note equivalence of the lossy vacuum success probability, with that of the no loss coherent state case, Eq. 3.15). Next, we perform homodyne detection on mode D, using:

$$
|x_{\frac{\pi}{2}}\rangle_D\,\langle x_{\frac{\pi}{2}}|\pm\sqrt{2T}\,|\alpha|\rangle_D = |x_{\frac{\pi}{2}}\rangle_D\,\langle x_{\frac{\pi}{2}}|0\rangle_D \exp\left[\mp 2\sqrt{2}\,\mathrm{i}\sqrt{T}\,|\alpha|x_{\frac{\pi}{2}}\right], \qquad (3.32)
$$

which gives us:

$$
\begin{aligned}
|\Psi^{Coh.}_{loss}\rangle_{A\varepsilon_B C\varepsilon_D} = \mathcal{N}\Big[&e^{-2\sqrt{2}\,\mathrm{i}\sqrt{T}\,|\alpha|x_{\frac{\pi}{2}}}\,|00\rangle_{AC}\,|\sqrt{1-T}\,|\alpha|\rangle_{\varepsilon_B}\,|\sqrt{1-T}\,|\alpha|\rangle_{\varepsilon_D} \\
&+e^{2\sqrt{2}\,\mathrm{i}\sqrt{T}\,|\alpha|x_{\frac{\pi}{2}}}\,|11\rangle_{AC}\,|-\sqrt{1-T}\,|\alpha|\rangle_{\varepsilon_B}\,|-\sqrt{1-T}\,|\alpha|\rangle_{\varepsilon_D} \\
&e^{-T|\alpha|^2}\Big(|01\rangle_{AC}\,|\sqrt{1-T}\,|\alpha|\rangle_{\varepsilon_B}\,|-\sqrt{1-T}\,|\alpha|\rangle_{\varepsilon_D} \\
&\quad+|10\rangle_{AC}\,|-\sqrt{1-T}\,|\alpha|\rangle_{\varepsilon_B}\,|\sqrt{1-T}\,|\alpha|\rangle_{\varepsilon_D}\Big)\Big]. \qquad (3.33)
\end{aligned}
$$

The final step in this theoretical protocol is to trace out the lossy modes ε_B and

ε_D. There are several possible ways to do this, however we will demonstrate two examples here; using the Fock (number) state to trace out the lossy modes, and using the coherent state to trace.

3.2.3 Fock State Trace Method

As previously explained in Subsec. 1.2.7 (Eq. 1.7), a coherent state $|\beta\rangle$ can be represented in the Fock basis as a summation of all possible number states, such that:

$$|\beta\rangle = e^{-\frac{|\beta|^2}{2}} \sum_{n=0}^{\infty} \frac{\beta^n}{\sqrt{n!}} |n\rangle . \tag{3.34}$$

It therefore follows that Eq. 3.33 can be re-written in the Fock basis as:

$$\begin{aligned} |\Psi_{loss}^{Coh.}\rangle_{A\varepsilon_B C\varepsilon_D} = \mathcal{N} e^{(T-1)|\alpha|^2} \sum_{n,m=0}^{\infty} \frac{(\sqrt{1-T}|\alpha|)^{n+m}}{\sqrt{n!}\sqrt{m!}} |n\rangle_{\varepsilon_B} |m\rangle_{\varepsilon_D} \\ \times \Big[e^{-2\sqrt{2}\,\mathrm{i}\sqrt{T}|\alpha| x_{\frac{\pi}{2}}} |00\rangle_{AC} + (-1)^{n+m} e^{2\sqrt{2}\,\mathrm{i}\sqrt{T}|\alpha| x_{\frac{\pi}{2}}} |11\rangle_{AC} \\ + e^{-T|\alpha|^2} \Big((-1)^m |01\rangle_{AC} + (-1)^n |10\rangle_{AC} \Big) \Big]. \end{aligned} \tag{3.35}$$

Tracing out the state in lossy modes ε_B and ε_D then gives us a mixed state in modes A and C, given by:

$$\rho_{AC}^{Coh.} = \mathrm{Tr}_{\varepsilon_B,\varepsilon_D} \Big[|\Psi_{loss}^{Coh.}\rangle_{A\varepsilon_B C\varepsilon_D} \langle \Psi_{loss}^{Coh.}| \Big]. \tag{3.36}$$

This Fock state trace method works well for very large values of n and m, however, this was found to be computationally expensive, and so a different method was used, namely using a coherent state to trace out these lossy modes. Of course this summation in Eq. 3.36 is fully satisfied (that is to say that it is not in any way approximated) for the case where n and m are summed to infinity, however, this is not possible computationally and so to pick large values for n and m (i.e. $n, m \approx 40$) would seem sufficient. However, n and m represent the average photon number of the coherent state, where the average photon number is also given by the modulus squared of the amplitude of the coherent state. In other words, for a coherent state $|\beta\rangle$, with amplitude $\beta = 10$ the Fock basis values would need to be at least $|10|^2 = 100$.

Therefore, it is easy to see that if we instead use the coherent state basis for this trace calculation, then there is no need for an unwieldy summation as described above.

3.2.4 Coherent State Trace Method

As opposed to using the above Fock state trace method we can instead use a coherent state to remove the lossy modes from our system. This method uses a Gaussian integral to trace out the loss modes. The following method is for the general case of

tracing out two arbitrary coherent states $|\alpha\rangle$ and $|\beta\rangle$:

$$I_{\alpha\beta} = \frac{1}{\pi}\int \mathrm{d}^2\beta \, \langle\beta|\alpha\rangle \, \langle\alpha|\beta\rangle \,, \tag{3.37}$$

(for further details on this relation refer to Appendix A). We again make use of the Fock basis representation of the coherent state, giving:

$$I_{\alpha\beta} = \frac{1}{\pi}\int \mathrm{d}^2\beta \left(e^{-|\alpha|^2-|\beta|^2+\beta^*\alpha+\alpha^*\beta}\right). \tag{3.38}$$

Next, we can then express the amplitudes in terms of of phase space, such that:

$$\alpha = \alpha_x + \mathrm{i}\alpha_y \quad \text{and} \quad \alpha^* = \alpha_x - \mathrm{i}\alpha_y, \tag{3.39}$$

$$\therefore \beta^*\alpha + \alpha^*\beta = 2\alpha_x\beta_x + 2\alpha_y\beta_y, \tag{3.40}$$

$$\therefore |\alpha|^2 = \alpha_x^2 + \alpha_y^2. \tag{3.41}$$

We can then rewrite Eq. 3.38 using the above expressions, separating the integral into the x and y components and expressing the integral in Cartesian coordinates:

$$\begin{aligned} I_{\alpha\beta} &= \frac{e^{-\left(\alpha_x^2+\alpha_y^2\right)}}{\pi}\int_{-\infty}^{\infty}\mathrm{d}\beta_x\int_{-\infty}^{\infty}\mathrm{d}\beta_y e^{-\left(\beta_x^2+\beta_y^2+2\alpha x\beta_x+2\alpha y\beta y\right)} \\ &= \frac{e^{-\left(\alpha_x^2+\alpha_y^2\right)}}{\pi}\int_{-\infty}^{\infty}\mathrm{d}\beta_x\int_{-\infty}^{\infty}\mathrm{d}\beta_y e^{-(\beta_x-\alpha_x)^2}e^{\alpha_x^2}e^{-(\beta_y-\alpha_y)^2}e^{\alpha_y^2} \\ &= \frac{1}{\pi}\int_{-\infty}^{\infty}\mathrm{d}\beta_x e^{-\beta_x^2}\int_{-\infty}^{\infty}\mathrm{d}\beta_y e^{-\beta_y^2}. \end{aligned} \tag{3.42}$$

Finally, we then convert the integral to cylindrical polar coordinates, as is standard in a Gaussian integration, such that:

$$\begin{aligned} I_{\alpha\beta} &= \frac{1}{\pi}\int_0^{2\pi}\mathrm{d}\theta\int_0^{\infty}\mathrm{d}r.re^{-r^2} \\ &= \frac{1}{\pi}2\pi\left[-\frac{1}{2}e^{-r^2}\right]_0^{\infty} = 1. \end{aligned} \tag{3.43}$$

The above result is the same for $\int \frac{\mathrm{d}^2\beta}{\pi} \langle\beta|-\alpha\rangle \, \langle-\alpha|\beta\rangle$. Using this method we can also determine that $\int \frac{\mathrm{d}^2\beta}{\pi} \langle\beta|-\alpha\rangle \, \langle\alpha|\beta\rangle = \int \frac{\mathrm{d}^2\beta}{\pi} \langle\beta|-\alpha\rangle \, \langle\alpha|\beta\rangle = e^{-2|\alpha|^2}$.

We then calculate the density matrix of the final state, having traced out the lossy modes using the above method (where we simply replace α with the relevant lossy mode, i.e. $\pm\sqrt{1-T}\,|\alpha|$):

$$\rho_{AC}^{Coh.} = \mathrm{Tr}_{\varepsilon_B,\varepsilon_D}\left[\,|\Psi_{loss}^{Coh.}\rangle_{A\varepsilon_B C\varepsilon_D} \, \langle\Psi_{loss}^{Coh.}|\right], \tag{3.44}$$

$$\rho_{AC}^{Coh.} = \mathcal{N}\begin{pmatrix} 1 & e^{-T|\alpha|^2}e^{-2\eta|\alpha|^2} & e^{-T|\alpha|^2}e^{-2\eta|\alpha|^2} & e^{-4\eta|\alpha|^2} \\ e^{-T|\alpha|^2}e^{-2\eta|\alpha|^2} & e^{-2T|\alpha|^2} & e^{-T|\alpha|^2}e^{-4\eta|\alpha|^2} & e^{-T|\alpha|^2}e^{-2\eta|\alpha|^2} \\ e^{-T|\alpha|^2}e^{-2\eta|\alpha|^2} & e^{-T|\alpha|^2}e^{-4\eta|\alpha|^2} & e^{-2T|\alpha|^2} & e^{-T|\alpha|^2}e^{-2\eta|\alpha|^2} \\ e^{-4\eta|\alpha|^2} & e^{-T|\alpha|^2}e^{-2\eta|\alpha|^2} & e^{-T|\alpha|^2}e^{-2\eta|\alpha|^2} & 1 \end{pmatrix}, \tag{3.45}$$

where, $\eta = 1 - T$ and $\mathcal{N}$ is the normalisation for the matrix, and is calculated simply by dividing by the trace of the matrix, therefore $\mathcal{N} = 1/(2 + 2e^{-2T|\alpha|^2})$.

3.3 Coherent State Entanglement Swapping Results

Now that we have successfully calculated the final density matrix describing the final two qubit state produced as a result of following our proposed entanglement swapping protocol, we are able to analyse this density matrix and determine the usefulness of this state for further quantum communication purposes.

Firstly, to evaluate the level of entanglement shared between Alice and Bob after performing this protocol, we apply an entanglement measure called "negativity". As explained in Sec. 2.8 we calculate entanglement negativity using the equation $\mathcal{N}(\rho) = -2\sum_i \lambda_i^-$.

We can also calculate the linear entropy of this system, using $S_L(\rho) = 1 - \mathrm{Tr}\left[\rho^2\right]$ outlined in Sec. 2.7.

Finally, we will determine the fidelity of our final state using the method given in Sec. 2.9. Calculating the closeness (fidelity) of our final density matrix $\rho_{AC}^{Coh.}$ to the $|\Phi^+\rangle$ Bell state will return a value of 1 if the matrix is pure, and therefore identical to that of this particular Bell state, and 0 if these two states are orthogonal (that is to say that they are as physically distinct as possible).

3.3.1 Entanglement Negativity

The following plot shows the entanglement negativity of our remaining two-qubit state (Eq. 3.45), as a function of the amplitude of the coherent state ($|\alpha|$), after following the coherent state ES protocol, for various levels of loss:

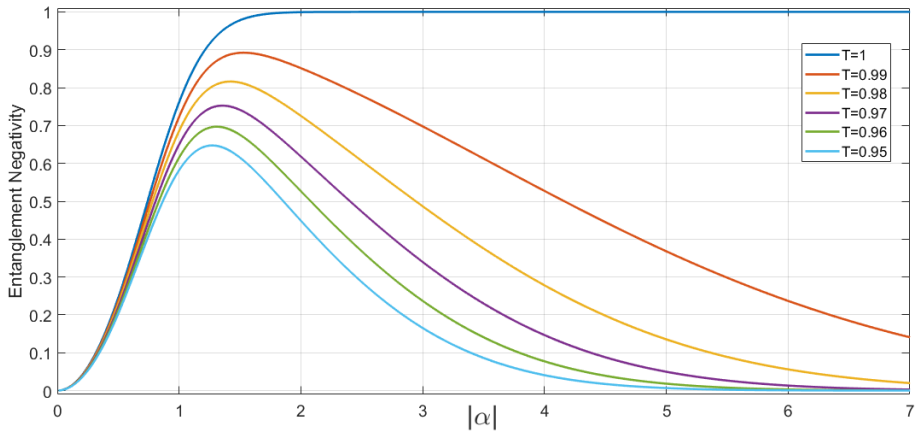

FIGURE 3.3: Entanglement negativity as a function of $|\alpha|$, for the final state generated via our coherent state entanglement swapping protocol (Eq. 3.45), for varying levels of loss.

Observing first the $T = 1$ plot we can see that as the value of $|\alpha|$ increases the entanglement value eventually reaches a limit (at $|\alpha| = 1.7$) and plateaus at unity; this is to be expected as this is the ideal case for this protocol, where we have lost no photons, and as such this protocol will produce a maximally entangled state in this case. However, this is clearly not a realistic scenario, as to achieve photonic state transmissions of any distance with no losses is still practically impossible with current technologies.

If we now consider the lossy cases (for $T < 1$) in Fig. 3.3 then there is a clear pattern that results as a function of the coherent state amplitude - a peak entanglement value is reached for a specific value of $|\alpha|$, and the maximum point of this peak shifts to lower values of $|\alpha|$ for decreasing T.

If we also consider the actual position of the peak as a function of $|\alpha|$ in Fig. 3.4 we can see that the peak (for the cases of $T \leq 0.99$) shifts as a function of $|\alpha|$ for decreasing T. We can note that this is as a result of the dampening exponent which is dependent on both T and $|\alpha|^2$, as introduced through the projective vacuum measurement on mode B. Decreasing the value of T (to consider increasing levels of photon loss) means that $|\alpha|$ must then increase to compensate for this, to allow the dampening exponent to successfully make the non-corner terms of the final density matrix (Eq. 3.45) decrease. When these non-corner terms have entirely dampened we have present a quantum state of higher fidelity against the $|\Phi^+\rangle$ Bell state.

Also interesting to analyse is a 3-dimensional plot of entanglement negativity as a function of T and $|\alpha|$:

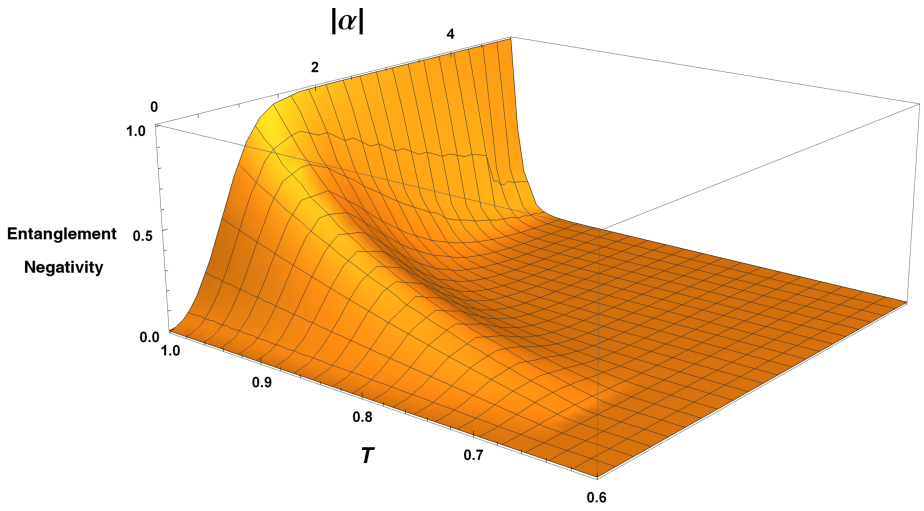

FIGURE 3.4: Entanglement negativity as a function of $|\alpha|$ and T for the final state generated via our coherent state entanglement swapping protocol (Eq. 3.45).

This 3D plot shows in more detail this peak $|\alpha|$ pattern we see emerge in Fig. 3.3, where it is clear that for $T \geq 0.80$ that this peak $|\alpha|$ value is between the range $1.2 < |\alpha| < 1.6$. This 3D plot also shows that for losses greater than 10 % yields an entanglement negativity value of less than $\mathcal{N}(\rho) = 0.50$, even in this peak $|\alpha|$ range. Finally, for $|\alpha| > 2$ and very large losses ($T \leq 0.80$) the entanglement negativity of the final two-qubit state generated from this entanglement swapping protocol is $\mathcal{N}(\rho) = 0$, and thus exhibits no entanglement.

3.3.2 Linear Entropy

Here we show linear entropy as a function of $|\alpha|$, for various T:

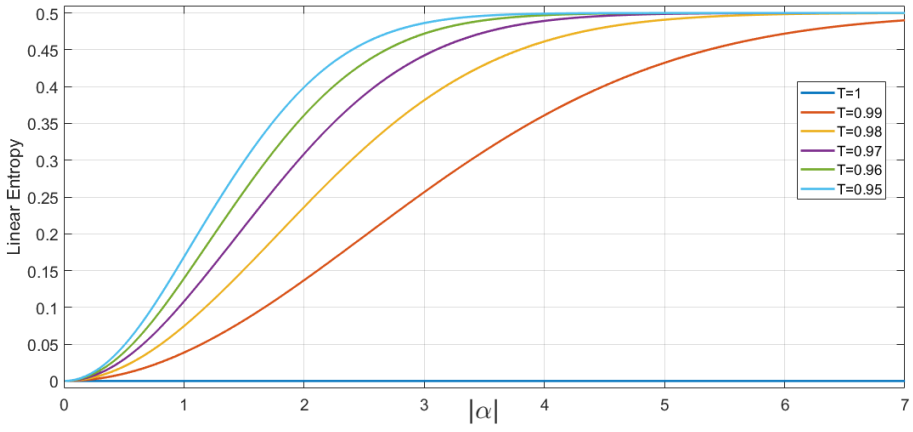

FIGURE 3.5: Linear entropy as a function of $|\alpha|$ for the final state generated via our coherent state entanglement swapping protocol (Eq. 3.45), for varying levels of loss.

As with the entanglement negativity plot (Fig. 3.3) there is a clear pattern: for no loss ($T = 1$) the plot line remains at zero for all $|\alpha|$ as a result of the state being maximally pure, however, for non-unity T the plots for linear entropy then increase as a

function of $|\alpha|$. This is perfectly complimentary to Fig. 3.3 in which the entanglement negativity value plateaus at $\mathcal{N}(\rho) = 0$ for large $|\alpha|$ and $T < 1$, thus indicating that non-zero loss and increasing coherent state amplitude cause the resultant two-qubit quantum state to become mixed.

Furthermore it should be noted that even in the largest $|\alpha|$ and most lossy limits, we are not producing a *maximally* mixed state (with the exception of $T \to 0$, in which case we would clearly have a maximally mixed state); as explained in Sec. 2.7 for a two-qubit system the maximum linear entropy value (thus indicating a maximally mixed state) is $S_L = 0.75$. In this case, to make a maximally mixed state we would have a mixture of all four of the maximally entangled Bell states, which is therefore not entangled at all, and as such is then described as maximally mixed. We can plot linear entropy as a function of both T and $|\alpha|$ to further prove this point:

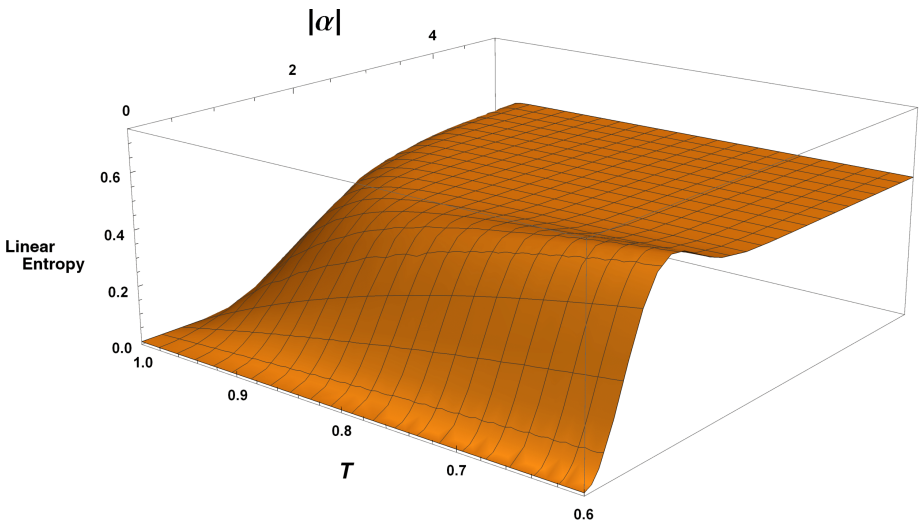

FIGURE 3.6: Linear entropy as a function of $|\alpha|$ and T for the final state generated via our coherent state entanglement swapping protocol (Eq. 3.45).

Clearly, for large $|\alpha|$ and $T < 0.90$ the linear entropy plot has flattened at an entropy value of $S_L = 0.50$. This further justifies that we are not producing a maximally mixed state. If this entropy plot is extended to cover a range of values reaching $T \approx 0$ then the entropy would reach the maximum value for a two-qubit state of $S_L = 0.75$.

It will be shown in the next section that in the limit of large $|\alpha|$ and non-unity T that we are producing a mixture of the two Bell states $|\Phi^+\rangle = \frac{1}{\sqrt{2}}(|00\rangle + |11\rangle)$ and $|\Phi^-\rangle = \frac{1}{\sqrt{2}}(|00\rangle - |11\rangle)$.

3.3.3 Fidelity

So far we have seen that in the limit of small losses and optimum $|\alpha|$ that our entanglement swapping protocol outcome is a highly entangled state. This is inherently a good result, however, practically this is somewhat useless; it is much more important to know exactly *what* entangled state we have. Therefore we calculate the fidelity of

our final quantum state, with respect to the maximally entangled Bell state that our protocol tends to (in the limit of no loss). As previously discussed, the Bell state produced from our proposed coherent state protocol is given as $|\Phi^+\rangle = \frac{1}{\sqrt{2}}(|00\rangle + |11\rangle)$, and so we first plot the fidelity of our resultant state with respect to this Bell state:

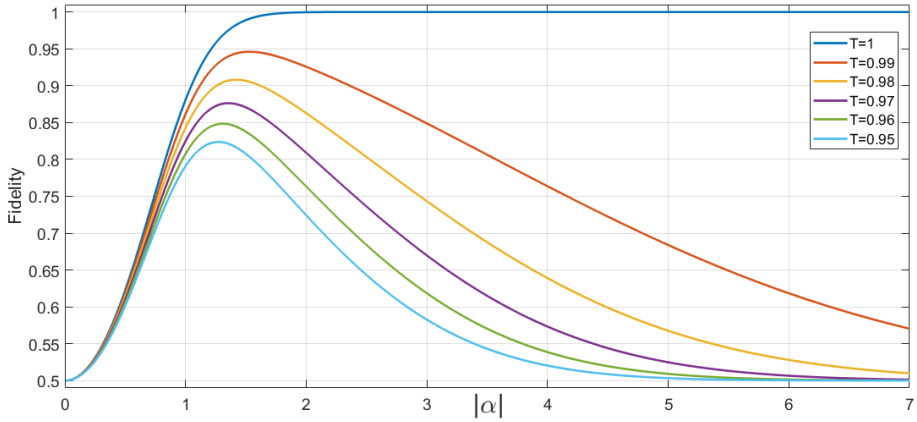

FIGURE 3.7: Fidelity against the $|\Phi^+\rangle = \frac{1}{\sqrt{2}}(|00\rangle + |11\rangle)$ Bell state as a function of $|\alpha|$ for the final state generated via our coherent state entanglement swapping protocol (Eq. 3.45), for varying levels of loss.

We can see that for the case of no photon losses ($T = 1$) the fidelity quickly increases to $F = 1$ as a function of $|\alpha|$ and plateaus here for all $|\alpha|$, as expected. Similar to the plot of entanglement negativity as a function of $|\alpha|$ (Fig. 3.3), the above plot of fidelity shows a clear peak for the cases where $T < 1$, before being exponentially dampened for higher $|\alpha|$, where the fidelity plots then plateau at $F = 0.50$. At the point where $F = 0.50$, the fidelity value tells us that we have half of the maximally entangled $|\Phi^+\rangle = \frac{1}{\sqrt{2}}(|00\rangle + |11\rangle)$ Bell state present, and so let us now plot the fidelity of our final quantum state with respect to the orthogonal Bell state, $|\Phi^-\rangle = \frac{1}{\sqrt{2}}(|00\rangle - |11\rangle)$:

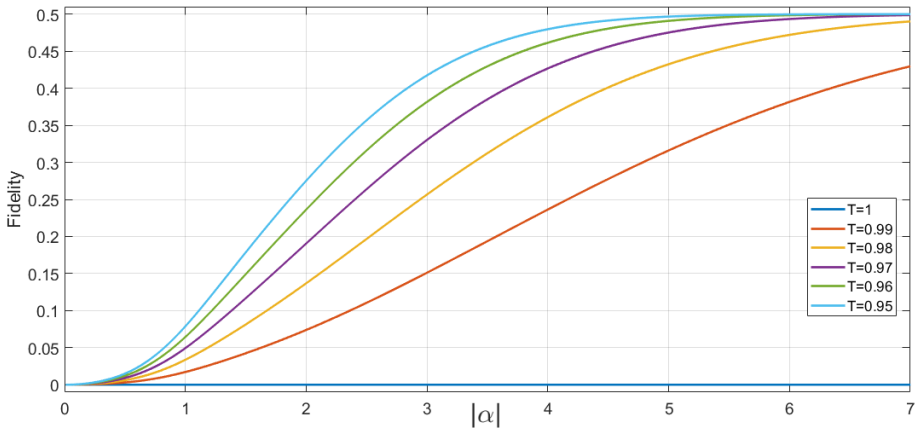

FIGURE 3.8: Fidelity against the $|\Phi^-\rangle = \frac{1}{\sqrt{2}}(|00\rangle - |11\rangle)$ Bell state as a function of $|\alpha|$ for the final state generated via our coherent state entanglement swapping protocol (Eq. 3.45), for varying levels of loss.

Let us first look at the case for $T = 1$: in the above plot the fidelity against the orthogonal Bell state does not change from $F = 0$ for all $|\alpha|$, which is as expected as we can see from Fig. 3.7 that for $|\alpha| > 1.7$ our quantum state is exactly $\frac{1}{\sqrt{2}}(|00\rangle + |11\rangle)$. If we now look at the cases for $T < 1$ in Fig, 3.8, then we can see that the fidelity against the orthogonal $|\Phi^-\rangle = \frac{1}{\sqrt{2}}(|00\rangle - |11\rangle)$ Bell state increases as a function of $|\alpha|$, which is absolutely what we would expect to see here. For clarity, we now overlay the plots of Figs. 3.7 and 3.8:

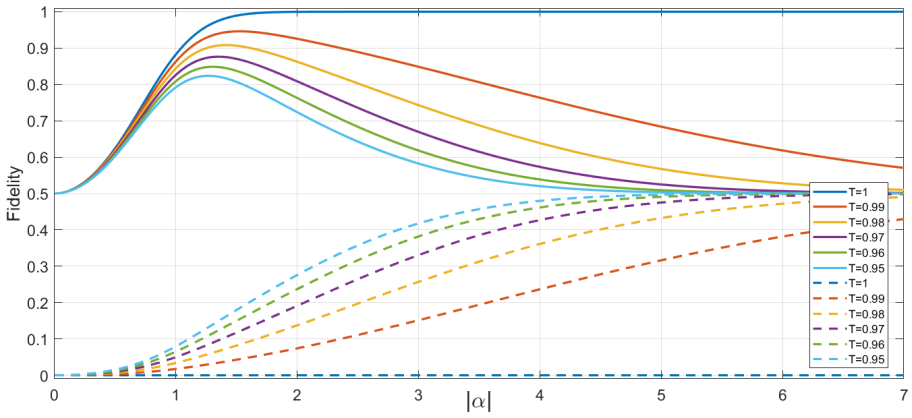

FIGURE 3.9: Fidelity against the $|\Phi^+\rangle = \frac{1}{\sqrt{2}}(|00\rangle + |11\rangle)$ Bell state (solid lines) and the $|\Phi^-\rangle = \frac{1}{\sqrt{2}}(|00\rangle - |11\rangle)$ Bell state (dashed lines), as a function of $|\alpha|$ for the final state generated via our coherent state entanglement swapping protocol (Eq. 3.45), for varying levels of loss.

The combination of the two fidelity plots actually complement our linear entropy results given in Fig. 3.5, where it was found that for $T < 1$ and large $|\alpha|$, the linear entropy tended to $S_L = 0.5$, thus indicating that our final quantum state could be a mixture of two Bell states. This result has now been confirmed by Fig. 3.9.

3.3.4 Quantum State Tomography

Finally, we can plot the quantum state tomography (QST) of our final density matrix to visualise this density matrix in terms of its exact values for a given $|\alpha|$ and T, for example:

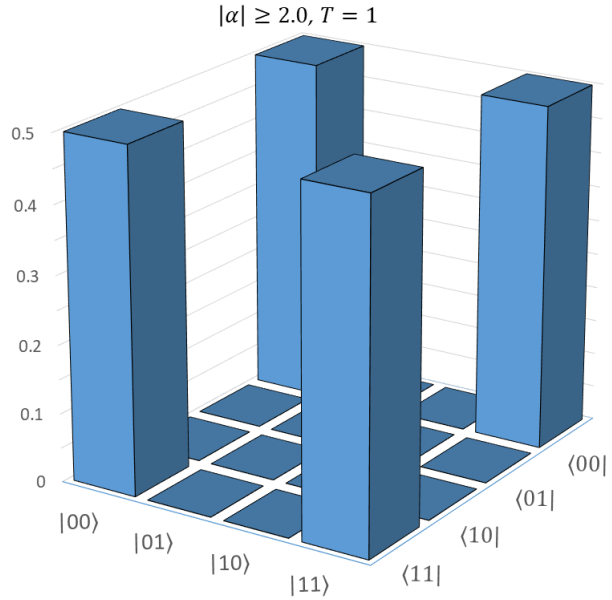

FIGURE 3.10: Quantum state tomography for the final state generated via our coherent state entanglement swapping protocol (Eq. 3.45), for $|\alpha| = 2.0$ and $T = 1$.

(Note that typically QST plots are usually separated into their real and imaginary components, however for the case at hand here our final state has no phases present, and such the final density matrix is purely real). Clearly in Fig. 3.10 it is simple to see that the density matrix here is exactly that of the $|\Phi^+\rangle = \frac{1}{\sqrt{2}}(|00\rangle + |11\rangle)$ Bell state. If we now look at the peak value for the $T = 0.99$ fidelity plot (Fig. 3.7) then the QST at this peak value of $|\alpha|$ is:

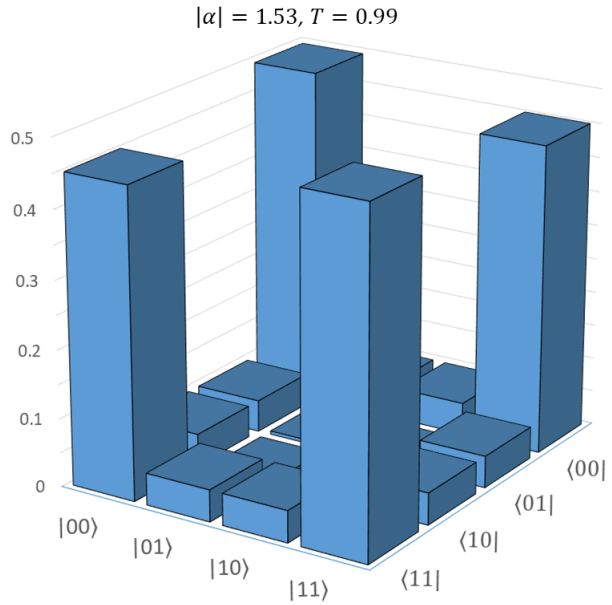

FIGURE 3.11: Quantum state tomography for the final state generated via our coherent state entanglement swapping protocol (Eq. 3.45), for $|\alpha| = 1.53$ and $T = 0.99$.

As expected, when including a small amount of loss, even at the peak $|\alpha|$ value,

which gives a fidelity of $F = 0.95$, then the QST shows that this state has become slightly mixed. This is also shown in Fig. 3.5 where we can see that the entropy is not 0 for these values of T and $|\alpha|$. Finally, let us look at the QST for the "worst case scenario" of $T = 0.95$ and the corresponding peak amplitude value, given in Fig. 3.7:

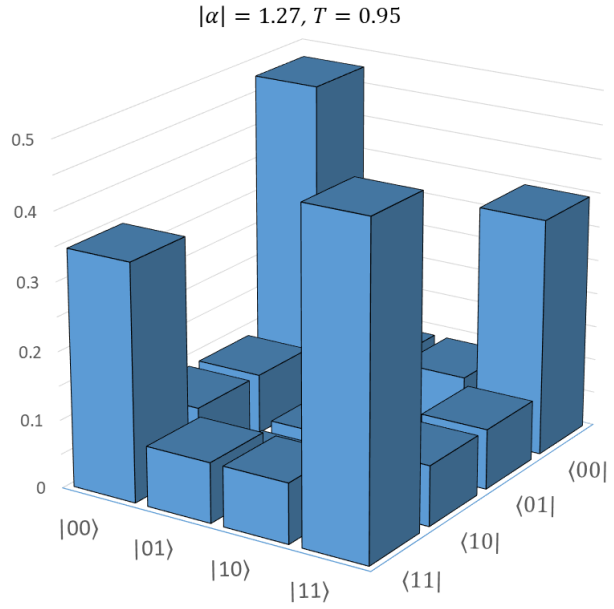

FIGURE 3.12: Quantum state tomography for the final state generated via our coherent state entanglement swapping protocol (Eq. 3.45), for $|\alpha| = 1.27$ and $T = 0.95$.

Evidently, as we have shown in the entanglement negativity, fidelity and linear entropy plots so far, we can conclude that as the loss increases, the state becomes more mixed. The QST for higher loss levels (Fig. 3.12) shows a more mixed matrix than that of lower loss levels (Fig. 3.11). Interestingly, the QST of Fig. 3.12 shows that there are weaker contributions to the density matrix of Eq. 3.45 by the four central terms in the QST, compared to the eight other non-corner terms - in fact this is a direct consequence of the lossy modes, which have been traced out and as such dampening exponents have been introduced. For the cases of the four middle terms the exponents in the final density matrix (Eq. 3.45 are not as strongly dampening as a function of loss and α, whereas the eight other non-corner terms are more strongly influenced by this exponential dampening.

Finally, we can look at the QST for the point in which the fidelity plot plateaus at $F = 0.50$, for example $T = 0.95$ and $|\alpha| \geq 6.0$:

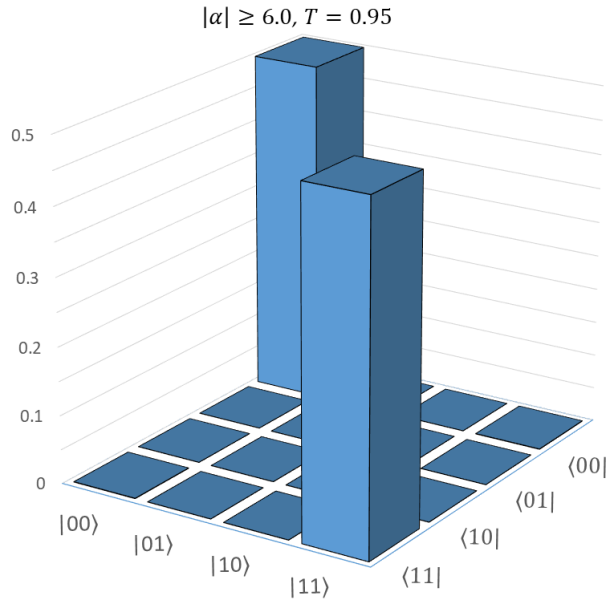

FIGURE 3.13: Quantum state tomography for the final state generated via our coherent state entanglement swapping protocol (Eq. 3.45), for $|\alpha| \geq 6.0$ and $T = 0.95$.

It is now clear why, when including losses, and for an amplitude value greater than that of the peak value, the fidelity plots (for fidelity against the $|\Phi^+\rangle$ and the orthogonal $|\Phi^-\rangle$ Bell states) both plateau at $F = 0.50$; a combination of the $|\Phi^+\rangle = \frac{1}{\sqrt{2}}(|00\rangle + |11\rangle)$ and $|\Phi^-\rangle = \frac{1}{\sqrt{2}}(|00\rangle - |11\rangle)$ Bell states in terms of their respective density matrix representations gives a mixed state:

$$\rho_{AC}^{\Phi^+} = |\Phi^+\rangle_{AC}\,\langle\Phi^+| = \frac{1}{2}\begin{pmatrix} 1 & 0 & 0 & 1 \\ 0 & 0 & 0 & 0 \\ 0 & 0 & 0 & 0 \\ 1 & 0 & 0 & 1 \end{pmatrix},$$

$$\rho_{AC}^{\Phi^-} = |\Phi^-\rangle_{AC}\,\langle\Phi^-| = \frac{1}{2}\begin{pmatrix} 1 & 0 & 0 & -1 \\ 0 & 0 & 0 & 0 \\ 0 & 0 & 0 & 0 \\ -1 & 0 & 0 & 1 \end{pmatrix},$$

$$\therefore \frac{1}{2}\left(\rho_{AC}^{\Phi^+} + \rho_{AC}^{\Phi^-}\right) = \frac{1}{2}\begin{pmatrix} 1 & 0 & 0 & 0 \\ 0 & 0 & 0 & 0 \\ 0 & 0 & 0 & 0 \\ 0 & 0 & 0 & 1 \end{pmatrix} \tag{3.46}$$

Looking at the entanglement plot (Fig. 3.3), it is easy to see that once our fidelity plots show that we have an exact 50:50 mixture of both of these Bell states, then the entanglement plots plateau at $\mathcal{N}(\rho) = 0$, indicating that our quantum state is then the mixed state (of linear entropy $S_L = 0.50$) described in Eq. 3.46.

3.4 Cat State ES

We now explore an entanglement swapping protocol that is more complex than the case where we use coherent states, as discussed in the previous section of this chapter. In the following protocol we instead use Schrödinger cat states, which are coherent state superpositions (as introduced in Subsec. 1.2.7).

3.4.1 No Loss

The initial hybrid entangled state in our proposed cat state entanglement swapping protocol, for no loss (see Fig. 3.1 for a schematic), is given by:

$$|\Psi^{Cat}\rangle_{ABCD} = BS^{1/2}_{B,D}\,|\psi^{Cat}_{HE}\rangle_{AB}\,|\psi^{Cat}_{HE}\rangle_{CD}\,. \tag{3.47}$$

Here, the hybrid entangled states are described as

$$|\psi^{Cat}_{HE}\rangle_{AB} = \frac{N^{+}_{\alpha}}{\sqrt{2}}\Big(\,|0\rangle_A\,(\,||\alpha|\rangle_B + |-|\alpha|\rangle_B) + |1\rangle_A\,(\,|\mathrm{i}|\alpha|\rangle_B + |-\mathrm{i}|\alpha|\rangle_B)\Big), \tag{3.48}$$

where $N^{\pm}_{\alpha} = 1/\sqrt{2 \pm 2e^{-2|\alpha|^2}}$ is the normalisation of a cat state, and the hybrid state as described above is the same for modes C and D. Therefore we can expand Eq. 3.47 as:

$$\begin{aligned}
|\Psi^{Cat}_{HE}\rangle_{ABCD} = \frac{(N^{+}_{\alpha})^2}{2}\Big[\,&|00\rangle_{AC}\,(\,||\alpha|\rangle_B + |-|\alpha|\rangle_B)(\,||\alpha|\rangle_D + |-|\alpha|\rangle_D)\\
&+|01\rangle_{AC}\,(\,||\alpha|\rangle_B + |-|\alpha|\rangle_B)(\,|\mathrm{i}|\alpha|\rangle_D + |-\mathrm{i}|\alpha|\rangle_D)\\
&+|10\rangle_{AC}\,(\,|\mathrm{i}|\alpha|\rangle_B + |-\mathrm{i}|\alpha|\rangle_B)(\,||\alpha|\rangle_D + |-|\alpha|\rangle_D)\\
&+|11\rangle_{AC}\,(\,|\mathrm{i}|\alpha|\rangle_B + |-\mathrm{i}|\alpha|\rangle_B)(\,|\mathrm{i}|\alpha|\rangle_D + |-\mathrm{i}|\alpha|\rangle_D)\Big].
\end{aligned} \tag{3.49}$$

For the case of no photon losses, the state immediately after application of a 50:50 beam-splitter on modes B and D is equal to:

$$\begin{aligned}
|\Psi^{Cat}\rangle_{ABCD} = \frac{(N^{+}_{\alpha})^2}{2}\Big[\,&|00\rangle_{AC}\Big(\,|0\rangle_B\,|\sqrt{2}\,|\alpha|\rangle_D + |\sqrt{2}\,|\alpha|\rangle_B\,|0\rangle_D\\
&\qquad+|-\sqrt{2}\,|\alpha|\rangle_B\,|0\rangle_D + |0\rangle_B\,|-\sqrt{2}\,|\alpha|\rangle_D\Big)\\
&+|01\rangle_{AC}\Big(\,||\alpha|e^{-\frac{\mathrm{i}\pi}{4}}\rangle_B\,||\alpha|e^{\frac{\mathrm{i}\pi}{4}}\rangle_D + ||\alpha|e^{\frac{\mathrm{i}\pi}{4}}\rangle_B\,||\alpha|e^{-\frac{\mathrm{i}\pi}{4}}\rangle_D\\
&\qquad+|-|\alpha|e^{\frac{\mathrm{i}\pi}{4}}\rangle_B\,|-|\alpha|e^{-\frac{\mathrm{i}\pi}{4}}\rangle_D + |-|\alpha|e^{-\frac{\mathrm{i}\pi}{4}}\rangle_B\,|-|\alpha|e^{\frac{\mathrm{i}\pi}{4}}\rangle_D\Big)\\
&+|10\rangle_{AC}\Big(\,|-|\alpha|e^{-\frac{\mathrm{i}\pi}{4}}\rangle_B\,||\alpha|e^{\frac{\mathrm{i}\pi}{4}}\rangle_D + ||\alpha|e^{\frac{\mathrm{i}\pi}{4}}\rangle_B\,|-|\alpha|e^{-\frac{\mathrm{i}\pi}{4}}\rangle_D\\
&\qquad+|-|\alpha|e^{\frac{\mathrm{i}\pi}{4}}\rangle_B\,||\alpha|e^{-\frac{\mathrm{i}\pi}{4}}\rangle_D + ||\alpha|e^{-\frac{\mathrm{i}\pi}{4}}\rangle_B\,|-|\alpha|e^{\frac{\mathrm{i}\pi}{4}}\rangle_D\Big)\\
&+|11\rangle_{AC}\Big(\,|0\rangle_B\,|\sqrt{2}\,\mathrm{i}|\alpha|\rangle_D + |\sqrt{2}\,\mathrm{i}|\alpha|\rangle_B\,|0\rangle_D\\
&\qquad+|-\sqrt{2}\,\mathrm{i}|\alpha|\rangle_B\,|0\rangle_D + |0\rangle_B\,|-\sqrt{2}\,\mathrm{i}|\alpha|\rangle_D\Big)\Big],
\end{aligned} \tag{3.50}$$

where we have used the beam-splitter transformation results as per Eq. 2.18. The successful measurement of a vacuum state in mode B (using the vacuum measurement projector given in Eq. 2.19), where $\langle 0|\pm|\alpha|e^{\pm\frac{\mathrm{i}\pi}{4}}\rangle = e^{-\frac{|\alpha|^2}{2}}$, then gives us:

$$
\begin{aligned}
|\Psi^{Cat}\rangle_{ACD} = \sqrt{\mathcal{P}_0^{Cat}}& \\
&\times |0\rangle_B \Big[|00\rangle_{AC} \Big(|\sqrt{2}\,|\alpha|\rangle_D + 2e^{-|\alpha|^2}|0\rangle_D + |-\sqrt{2}\,|\alpha|\rangle_D \Big) \\
&+e^{-\frac{|\alpha|^2}{2}} |01\rangle_{AC} \Big(||\alpha|e^{\frac{\mathrm{i}\pi}{4}}\rangle_D + ||\alpha|e^{-\frac{\mathrm{i}\pi}{4}}\rangle_D + |-|\alpha|e^{-\frac{\mathrm{i}\pi}{4}}\rangle_D + |-|\alpha|e^{\frac{\mathrm{i}\pi}{4}}\rangle_D \Big) \\
&+e^{-\frac{|\alpha|^2}{2}} |10\rangle_{AC} \Big(||\alpha|e^{\frac{\mathrm{i}\pi}{4}}\rangle_D + |-|\alpha|e^{-\frac{\mathrm{i}\pi}{4}}\rangle_D + ||\alpha|e^{-\frac{\mathrm{i}\pi}{4}}\rangle_D + |-|\alpha|e^{\frac{\mathrm{i}\pi}{4}}\rangle_D \Big) \\
&\quad + |11\rangle_{AC} \Big(|\sqrt{2}\,\mathrm{i}|\alpha|\rangle_D + 2e^{-|\alpha|^2}|0\rangle_D + |-\sqrt{2}\,\mathrm{i}|\alpha|\rangle_D \Big) \Big],
\end{aligned}
\tag{3.51}
$$

where, as per the coherent state protocol, $\mathcal{P}_0^{Cat}$ is the success probability of this vacuum projection: following the same method as outlined in 3.1.2 the success probability for the no loss cat state protocol is calculated as:

$$
\mathcal{P}_0^{Cat} = \left(\frac{(N_\alpha^+)^2}{2\mathcal{N}'} \right)^2 \tag{3.52}
$$

where,

$$
\mathcal{N}' = 1/\sqrt{4 + 8e^{-|\alpha|^2} + 24e^{-2|\alpha|^2} + 8e^{-3|\alpha|^2} + 4e^{-4|\alpha|^2} + 8e^{-(2+\mathrm{i})|\alpha|^2} + 8e^{-(2-\mathrm{i})|\alpha|^2}}. \tag{3.53}
$$

It follows that $\mathcal{P}_0^{Cat} = 1$ for $|\alpha| \to 0$ and $\mathcal{P}_0^{Cat} = 0.25$ for $|\alpha| \to \infty$, however, as before, this will be more formally discussed in Chapter 6, Sec. 6.1.

Now we perform homodyne detection in mode D (using the homodyne measurement projector given in Eq. 2.25). For the cat state protocol we wish to perform a quadrature measurement along the $\frac{\pi}{4}$ axis, so as to give a resultant entangled state (see Fig. 3.14); as with the coherent state homodyne measurement, we choose this specific angle of measurement such that we *quantum erase* information between certain peaks. This yields our final state for the entanglement swapping protocol using cat states for no loss:

$$
\begin{aligned}
|\Psi^{Cat}\rangle_{AC} = \mathcal{N}\Big[|00\rangle_{AC} \Big(&\exp\Big[(1-\mathrm{i})2|\alpha|x_{\frac{\pi}{4}} + (\mathrm{i}-1)|\alpha|^2\Big] \\
&+ \exp\Big[-(1-\mathrm{i})2|\alpha|x_{\frac{\pi}{4}} + (\mathrm{i}-1)|\alpha|^2\Big] + 2e^{-|\alpha|^2}\Big) \\
+e^{-\frac{|\alpha|^2}{2}}(\,|01\rangle_{AC} + |10\rangle_{AC}) \Big(&\exp\Big[2|\alpha|x_{\frac{\pi}{4}} - |\alpha|^2\Big] + \exp\Big[2\mathrm{i}|\alpha|x_{\frac{\pi}{4}}\Big] \\
&+ \exp\Big[-2\mathrm{i}|\alpha|x_{\frac{\pi}{4}}\Big] + \exp\Big[-2|\alpha|x_{\frac{\pi}{4}} - |\alpha|^2\Big]\Big) \\
&+ |11\rangle_{AC} \Big(\exp\Big[(1+\mathrm{i})2|\alpha|x_{\frac{\pi}{4}} - (1+\mathrm{i})|\alpha|^2\Big] \\
&+ \exp\Big[-(1+\mathrm{i})2|\alpha|x_{\frac{\pi}{4}} - (1+\mathrm{i})|\alpha|^2\Big] + 2e^{-|\alpha|^2}\Big)\Big].
\end{aligned}
\tag{3.54}
$$

The ideal homodyne outcomes for this protocol are $x_{\frac{\pi}{4}} = \pm|\alpha|$, and can be shown diagrammatically as:

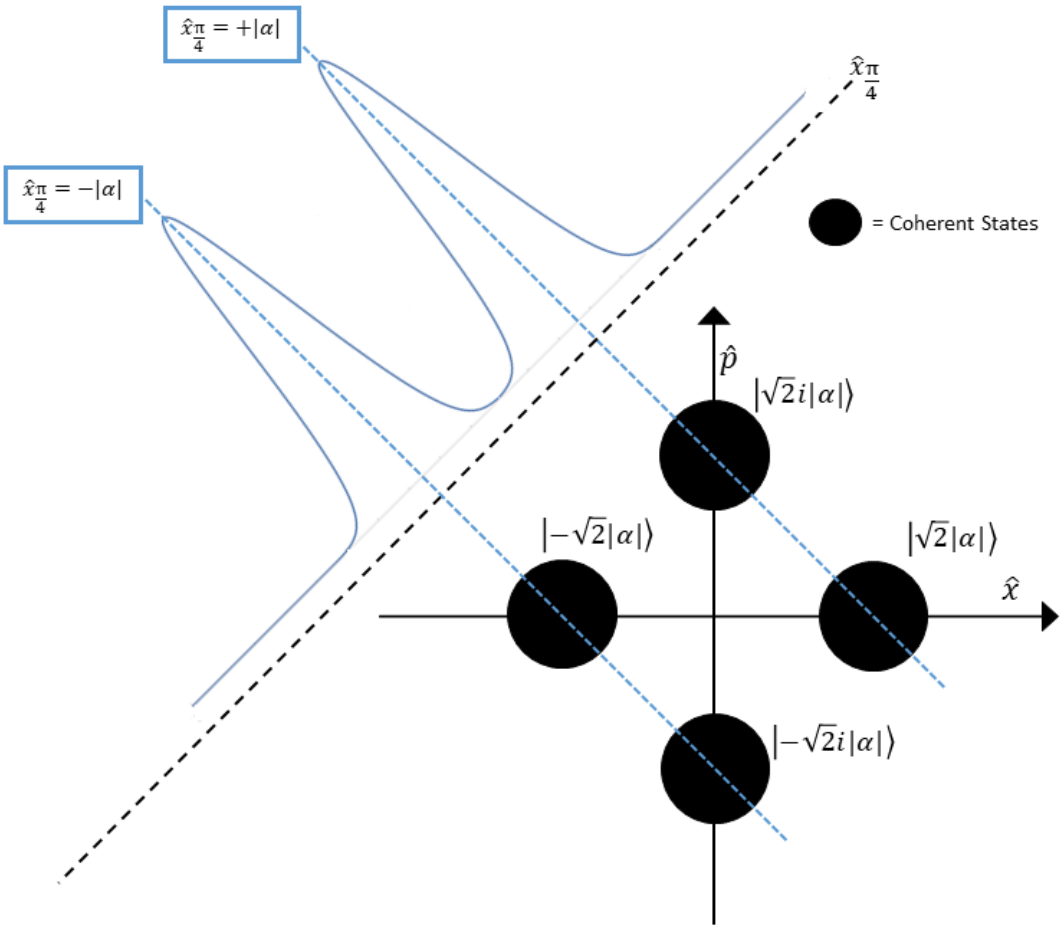

FIGURE 3.14: Diagram to represent the phase space in which the cat states in mode D occupy, combined with a probability distribution showing the two possible homodyne measurement outcomes, $x_{\frac{\pi}{4}} = \pm|\alpha|$.

(note that in the Fig. 3.14 the coherent states that are part of the $|01\rangle_{AC}$ and $|10\rangle_{AC}$ terms are exponentially dampened by $e^{-\frac{|\alpha|^2}{2}}$ (see Eq. 3.54), and so they are omitted for ease of simplification). By completing the square in Eq. 3.54 we know that the ideal homodyne outcomes must be $x_{\frac{\pi}{4}} = \pm|\alpha|$: for a detailed mathematical derivation of this result, see Appendix C.

Therefore, replacing $x_{\frac{\pi}{4}} = +|\alpha|$ in Eq. 3.54 gives:

$$
\begin{aligned}
|\Psi^{Cat}\rangle_{AC} = \mathcal{N}\Big[\,|00\rangle_{AC}\Big(&\exp\big[(1-\mathrm{i})2|\alpha|^2 + (\mathrm{i}-1)|\alpha|^2\big] \\
&+ \exp\big[-(1-\mathrm{i})2|\alpha|^2 + (\mathrm{i}-1)|\alpha|^2\big] + 2e^{-|\alpha|^2}\Big) \\
+e^{-\frac{|\alpha|^2}{2}}(\,|01\rangle_{AC} + |10\rangle_{AC})\Big(&\exp\big[|\alpha|^2\big] + \exp\big[2\mathrm{i}|\alpha|^2\big] + \exp\big[-2\mathrm{i}|\alpha|^2\big] + \exp\big[-3|\alpha|^2\big]\Big) \\
+\,|11\rangle_{AC}\Big(&\exp\big[(1+\mathrm{i})2|\alpha|^2 - (1+\mathrm{i})|\alpha|^2\big] \\
&+ \exp\big[-(1+\mathrm{i})2|\alpha|^2 - (1+\mathrm{i})|\alpha|^2\big] + 2e^{-|\alpha|^2}\Big)\Big]
\end{aligned}
\tag{3.55}
$$

$$= \mathcal{N}\Big[|00\rangle_{AC} \Big(\exp\big[|\alpha|^2 - \mathrm{i}|\alpha|^2\big] + \exp\big[-3|\alpha|^2 + 3\mathrm{i}|\alpha|^2\big] + 2e^{-|\alpha|^2} \Big)$$
$$+ e^{-\frac{|\alpha|^2}{2}} (|01\rangle_{AC} + |10\rangle_{AC}) \Big(\exp\big[|\alpha|^2\big] + \exp\big[2\mathrm{i}|\alpha|^2\big] + \exp\big[-2\mathrm{i}|\alpha|^2\big] + \exp\big[-3|\alpha|^2\big] \Big)$$
$$+ |11\rangle_{AC} \Big(\exp\big[|\alpha|^2 + \mathrm{i}|\alpha|^2\big] + \exp\big[-3|\alpha|^2 - 3\mathrm{i}|\alpha|^2\big] + 2e^{-|\alpha|^2} \Big) \Big]. \tag{3.56}$$

(Note that the quantum state produced from a homodyne measurement outcome of $x_{\frac{\pi}{4}} = +|\alpha|$ in Eq. 3.56 is the same for the outcome $x_{\frac{\pi}{4}} = -|\alpha|$). If we then take the large $|\alpha|$ limit then the $|01\rangle_{AC}$ and $|10\rangle_{AC}$ terms are exponentially dampened, and so our final quantum state for this protocol is:

$$|\Psi^{Cat}\rangle_{AC} = \frac{1}{\sqrt{2}} \Big(e^{-\mathrm{i}|\alpha|^2} |00\rangle_{AC} + e^{\mathrm{i}|\alpha|^2} |11\rangle_{AC} \Big). \tag{3.57}$$

Therefore, for no losses, and ideal homodyne measurement outcomes of $x_{\frac{\pi}{4}} = \pm|\alpha|$, the final state to our proposed entanglement swapping protocol when using cat states is a "phase-rotated" maximally entangled Bell state. This phase could be corrected for via a suitable phase-space rotation, such that the outcome state would be the maximally entangled $|\Phi^+\rangle = \frac{1}{\sqrt{2}}(|00\rangle + |11\rangle)$ Bell state. However, in the circumstance that this protocol would be used to create highly entangled states for a customer to use in further quantum communication protocols, then provided that the customer knows exactly the phases present in the state this should not matter. Again, we should note that, as with the coherent state entanglement swapping protocol, we have made the assumption that the homodyne measurement outcome is a discrete value - however an averaged distribution of homodyne outcome values will be accounted for later in this report in Chapter 5.

3.4.2 Equal Loss

Similarly to the *lossy* coherent state entanglement swapping protocol outlined in Section 3.2.2, we now demonstrate that the lossy cat state entanglement swapping protocol, when considering low levels of photon loss, still produces the phase-rotated Bell state $|\Phi^+(\alpha)\rangle = \frac{1}{\sqrt{2}}(e^{-\mathrm{i}|\alpha|^2} |00\rangle_{AC} + e^{\mathrm{i}|\alpha|^2} |11\rangle_{AC})$.

Our initial quantum state for the lossy cat state protocol is the same as in Eq. 3.47, however, we apply a lossy beam-splitter along with vacuum states in modes ε_B and ε_D (see Fig. 2.2 for a schematic) such that our new initial equation is described as:

$$|\Psi^{Cat}_{loss}\rangle_{AB\varepsilon_B CD\varepsilon_D} = BS^T_{B,\varepsilon_B} BS^T_{D,\varepsilon_D} |\psi^{Cat}_{HE}\rangle_{AB} |0\rangle_{\varepsilon_B} |\psi^{Cat}_{HE}\rangle_{CD} |0\rangle_{\varepsilon_D}, \tag{3.58}$$

where, $|\psi^{Cat}_{HE}\rangle_{ij}$ is equivalent to Eq. 3.48. Applying the lossy beam-splitter operators, as per Eq. 2.14, our lossy quantum state becomes:

$|\Psi^{Cat}_{loss}\rangle_{AB\varepsilon_B CD\varepsilon_D} =$

$$\frac{(N_\alpha^+)^2}{2}\Big[(\,|0\rangle_A\,(\,|\sqrt{T}\,|\alpha|\rangle_B\,|\gamma|\alpha|\rangle_{\varepsilon_B}+\,|-\sqrt{T}\,|\alpha|\rangle_B\,|-\gamma|\alpha|\rangle_{\varepsilon_B})+ \\ |1\rangle_A\,(\,|\sqrt{T}\,\mathbf{i}|\alpha|\rangle_B\,|\gamma\mathbf{i}|\alpha|\rangle_{\varepsilon_B}+\,|-\sqrt{T}\,\mathbf{i}|\alpha|\rangle_B\,|-\gamma\mathbf{i}|\alpha|\rangle_{\varepsilon_B}))\Big] \\ \otimes\Big[(\,|0\rangle_C\,(\,|\sqrt{T}\,|\alpha|\rangle_D\,|\gamma|\alpha|\rangle_{\varepsilon_D}+\,|-\sqrt{T}\,|\alpha|\rangle_D\,|-\gamma|\alpha|\rangle_{\varepsilon_D})+ \\ |1\rangle_C\,(\,|\sqrt{T}\,\mathbf{i}|\alpha|\rangle_D\,|\gamma\mathbf{i}|\alpha|\rangle_{\varepsilon_D}+\,|-\sqrt{T}\,\mathbf{i}|\alpha|\rangle_D\,|-\gamma\mathbf{i}|\alpha|\rangle_{\varepsilon_D}))\Big] \tag{3.59}$$

$$=\frac{(N_\alpha^+)^2}{2}\Big[\,|00\rangle_{AC}\Big(\,|\sqrt{T}\,|\alpha|\rangle_B\,|\sqrt{T}\,|\alpha|\rangle_D\,|\gamma|\alpha|\rangle_{\varepsilon_B}\,|\gamma|\alpha|\rangle_{\varepsilon_D} \\ +|\sqrt{T}\,|\alpha|\rangle_B\,|-\sqrt{T}\,|\alpha|\rangle_D\,|\gamma|\alpha|\rangle_{\varepsilon_B}\,|-\gamma|\alpha|\rangle_{\varepsilon_D} \\ +|-\sqrt{T}\,|\alpha|\rangle_B\,|\sqrt{T}\,|\alpha|\rangle_D\,|-\gamma|\alpha|\rangle_{\varepsilon_B}\,|\gamma|\alpha|\rangle_{\varepsilon_D} \\ +|-\sqrt{T}\,|\alpha|\rangle_B\,|-\sqrt{T}\,|\alpha|\rangle_D\,|-\gamma|\alpha|\rangle_{\varepsilon_B}\,|-\gamma|\alpha|\rangle_{\varepsilon_D}\Big) \\ +|01\rangle_{AC}\Big(\,|\sqrt{T}\,|\alpha|\rangle_B\,|\sqrt{T}\,\mathbf{i}|\alpha|\rangle_D\,|\gamma|\alpha|\rangle_{\varepsilon_B}\,|\gamma\mathbf{i}|\alpha|\rangle_{\varepsilon_D} \\ +|\sqrt{T}\,|\alpha|\rangle_B\,|-\sqrt{T}\,\mathbf{i}|\alpha|\rangle_D\,|\gamma|\alpha|\rangle_{\varepsilon_B}\,|-\gamma\mathbf{i}|\alpha|\rangle_{\varepsilon_D} \\ +|-\sqrt{T}\,|\alpha|\rangle_B\,|\sqrt{T}\,\mathbf{i}|\alpha|\rangle_D\,|-\gamma|\alpha|\rangle_{\varepsilon_B}\,|\gamma\mathbf{i}|\alpha|\rangle_{\varepsilon_D} \\ +|-\sqrt{T}\,|\alpha|\rangle_B\,|-\sqrt{T}\,\mathbf{i}|\alpha|\rangle_D\,|-\gamma|\alpha|\rangle_{\varepsilon_B}\,|-\gamma\mathbf{i}|\alpha|\rangle_{\varepsilon_D}\Big) \\ +|10\rangle_{AC}\Big(\,|\sqrt{T}\,\mathbf{i}|\alpha|\rangle_B\,|\sqrt{T}\,|\alpha|\rangle_D\,|\gamma\mathbf{i}|\alpha|\rangle_{\varepsilon_B}\,|\gamma|\alpha|\rangle_{\varepsilon_D} \\ +|\sqrt{T}\,\mathbf{i}|\alpha|\rangle_B\,|-\sqrt{T}\,|\alpha|\rangle_D\,|\gamma\mathbf{i}|\alpha|\rangle_{\varepsilon_B}\,|-\gamma|\alpha|\rangle_{\varepsilon_D} \\ +|-\sqrt{T}\,\mathbf{i}|\alpha|\rangle_B\,|\sqrt{T}\,|\alpha|\rangle_D\,|-\gamma\mathbf{i}|\alpha|\rangle_{\varepsilon_B}\,|\gamma|\alpha|\rangle_{\varepsilon_D} \\ +|-\sqrt{T}\,\mathbf{i}|\alpha|\rangle_B\,|-\sqrt{T}\,|\alpha|\rangle_D\,|-\gamma\mathbf{i}|\alpha|\rangle_{\varepsilon_B}\,|-\gamma|\alpha|\rangle_{\varepsilon_D}\Big) \\ +|11\rangle_{AC}\Big(\,|\sqrt{T}\,\mathbf{i}|\alpha|\rangle_B\,|\sqrt{T}\,\mathbf{i}|\alpha|\rangle_D\,|\gamma\mathbf{i}|\alpha|\rangle_{\varepsilon_B}\,|\gamma\mathbf{i}|\alpha|\rangle_{\varepsilon_D} \\ +|\sqrt{T}\,\mathbf{i}|\alpha|\rangle_B\,|-\sqrt{T}\,\mathbf{i}|\alpha|\rangle_D\,|\gamma\mathbf{i}|\alpha|\rangle_{\varepsilon_B}\,|-\gamma\mathbf{i}|\alpha|\rangle_{\varepsilon_D}+ \\ |-\sqrt{T}\,\mathbf{i}|\alpha|\rangle_B\,|\sqrt{T}\,\mathbf{i}|\alpha|\rangle_D\,|-\gamma\mathbf{i}|\alpha|\rangle_{\varepsilon_B}\,|\gamma\mathbf{i}|\alpha|\rangle_{\varepsilon_D} \\ +|-\sqrt{T}\,\mathbf{i}|\alpha|\rangle_B\,|-\sqrt{T}\,\mathbf{i}|\alpha|\rangle_D\,|-\gamma\mathbf{i}|\alpha|\rangle_{\varepsilon_B}\,|-\gamma\mathbf{i}|\alpha|\rangle_{\varepsilon_D}\Big)\Big]. \tag{3.60}$$

where, $\gamma=\sqrt{1-T}$.

Next, we apply a 50:50 beam-splitter to mix modes B and D, using the generalised transformation outlined in Eq. 2.18, which gives:

$$
\begin{aligned}
&|\Psi^{Cat}_{loss}\rangle_{AB\varepsilon_B CD\varepsilon_D} = \frac{(N^+_\alpha)^2}{2} \\
&\times\Big[|00\rangle_{AC} \\
&\quad\Big[|0\rangle_B \Big(|\sqrt{2T}\,|\alpha|\rangle_D \, |\gamma|\alpha|\rangle_{\varepsilon_B} \, |\gamma|\alpha|\rangle_{\varepsilon_D} + |-\sqrt{2T}\,|\alpha|\rangle_D \, |-\gamma|\alpha|\rangle_{\varepsilon_B} \, |-\gamma|\alpha|\rangle_{\varepsilon_D} \Big) \\
&\quad + |0\rangle_D \Big(|\sqrt{2T}\,|\alpha|\rangle_B \, |\gamma|\alpha|\rangle_{\varepsilon_B} \, |-\gamma|\alpha|\rangle_{\varepsilon_D} + |-\sqrt{2T}\,|\alpha|\rangle_B \, |-\gamma|\alpha|\rangle_{\varepsilon_B} \, |\gamma|\alpha|\rangle_{\varepsilon_D} \Big) \Big] \\
&\quad + |01\rangle_{AC} \Big[|\sqrt{T}\,|\alpha|e^{\frac{-\mathrm{i}\pi}{4}}\rangle_B \, |\sqrt{T}\,|\alpha|e^{\frac{\mathrm{i}\pi}{4}}\rangle_D \, |\gamma|\alpha|\rangle_{\varepsilon_B} \, |\gamma\mathrm{i}|\alpha|\rangle_{\varepsilon_D} \\
&\quad + |\sqrt{T}\,|\alpha|e^{\frac{\mathrm{i}\pi}{4}}\rangle_B \, |\sqrt{T}\,|\alpha|e^{\frac{-\mathrm{i}\pi}{4}}\rangle_D \, |\gamma|\alpha|\rangle_{\varepsilon_B} \, |-\gamma\mathrm{i}|\alpha|\rangle_{\varepsilon_D} \\
&\quad + |-\sqrt{T}\,|\alpha|e^{\frac{\mathrm{i}\pi}{4}}\rangle_B \, |-\sqrt{T}\,|\alpha|e^{\frac{-\mathrm{i}\pi}{4}}\rangle_D \, |-\gamma|\alpha|\rangle_{\varepsilon_B} \, |\gamma\mathrm{i}|\alpha|\rangle_{\varepsilon_D} \\
&\quad + |-\sqrt{T}\,|\alpha|e^{\frac{-\mathrm{i}\pi}{4}}\rangle_B \, |-\sqrt{T}\,|\alpha|e^{\frac{\mathrm{i}\pi}{4}}\rangle_D \, |-\gamma|\alpha|\rangle_{\varepsilon_B} \, |-\gamma\mathrm{i}|\alpha|\rangle_{\varepsilon_D} \Big] \\
&\quad + |10\rangle_{AC} \Big[|-\sqrt{T}\,|\alpha|e^{\frac{-\mathrm{i}\pi}{4}}\rangle_B \, |\sqrt{T}\,|\alpha|e^{\frac{\mathrm{i}\pi}{4}}\rangle_D \, |\gamma\mathrm{i}|\alpha|\rangle_{\varepsilon_B} \, |\gamma|\alpha|\rangle_{\varepsilon_D} \\
&\quad + |\sqrt{T}\,|\alpha|e^{\frac{\mathrm{i}\pi}{4}}\rangle_B \, |-\sqrt{T}\,|\alpha|e^{\frac{-\mathrm{i}\pi}{4}}\rangle_D \, |\gamma\mathrm{i}|\alpha|\rangle_{\varepsilon_B} \, |-\gamma|\alpha|\rangle_{\varepsilon_D} \\
&\quad + |-\sqrt{T}\,|\alpha|e^{\frac{\mathrm{i}\pi}{4}}\rangle_B \, |\sqrt{T}\,|\alpha|e^{\frac{-\mathrm{i}\pi}{4}}\rangle_D \, |-\gamma\mathrm{i}|\alpha|\rangle_{\varepsilon_B} \, |\gamma|\alpha|\rangle_{\varepsilon_D} \\
&\quad + |\sqrt{T}\,|\alpha|e^{\frac{-\mathrm{i}\pi}{4}}\rangle_B \, |-\sqrt{T}\,|\alpha|e^{\frac{\mathrm{i}\pi}{4}}\rangle_D \, |-\gamma\mathrm{i}|\alpha|\rangle_{\varepsilon_B} \, |-\gamma|\alpha|\rangle_{\varepsilon_D} \Big] \\
&\quad + |11\rangle_{AC} \\
&\quad\Big[|0\rangle_B \Big(|\sqrt{2T}\,\mathrm{i}|\alpha|\rangle_D \, |\gamma\mathrm{i}|\alpha|\rangle_{\varepsilon_B} \, |\gamma\mathrm{i}|\alpha|\rangle_{\varepsilon_D} + |-\sqrt{2T}\,\mathrm{i}|\alpha|\rangle_D \, |-\gamma\mathrm{i}|\alpha|\rangle_{\varepsilon_B} \, |-\gamma\mathrm{i}|\alpha|\rangle_{\varepsilon_D} \Big) \\
&\quad + |0\rangle_D \Big(|\sqrt{2T}\,\mathrm{i}|\alpha|\rangle_B \, |\gamma\mathrm{i}|\alpha|\rangle_{\varepsilon_B} \, |-\gamma\mathrm{i}|\alpha|\rangle_{\varepsilon_D} + |-\sqrt{2T}\,\mathrm{i}|\alpha|\rangle_B \, |-\gamma\mathrm{i}|\alpha|\rangle_{\varepsilon_B} \, |\gamma\mathrm{i}|\alpha|\rangle_{\varepsilon_D} \Big) \Big] \Big],
\end{aligned}
\tag{3.61}
$$

Measuring a vacuum state in mode B via use of the vacuum projector defined in Eq. 2.19 yields:

$$
\begin{aligned}
\langle 0|\sqrt{T}\,|\alpha|e^{\frac{\pm\mathrm{i}\pi}{4}}\rangle &= e^{\frac{-T|\alpha|^2}{2}}, \\
\langle 0|\sqrt{2T}\,|\alpha|\rangle &= e^{-T|\alpha|^2}
\end{aligned}
\tag{3.62}
$$

$$
\begin{aligned}
&|\Psi^{Cat}_{loss}\rangle_{A\varepsilon_B CD\varepsilon_D} = \sqrt{\mathcal{P}_0^{Cat}}\,|0\rangle_B \\
&\times\Big[\,|00\rangle_{AC} \\
&\quad\Big[\,|\sqrt{2T}\,|\alpha|\rangle_D\,|\gamma|\alpha|\rangle_{\varepsilon_B}\,|\gamma|\alpha|\rangle_{\varepsilon_D} + |-\sqrt{2T}\,|\alpha|\rangle_D\,|-\gamma|\alpha|\rangle_{\varepsilon_B}\,|-\gamma|\alpha|\rangle_{\varepsilon_D} \\
&\quad + e^{-T|\alpha|^2}\,|0\rangle_D\Big(\,|\gamma|\alpha|\rangle_{\varepsilon_B}\,|-\gamma|\alpha|\rangle_{\varepsilon_D} + |-\gamma|\alpha|\rangle_{\varepsilon_B}\,|\gamma|\alpha|\rangle_{\varepsilon_D}\Big)\Big] \\
&\quad + e^{\frac{-T|\alpha|^2}{2}}\,|01\rangle_{AC} \\
&\quad\Big[\,|\sqrt{T}\,|\alpha|e^{\frac{\mathrm{i}\pi}{4}}\rangle_D\,|\gamma|\alpha|\rangle_{\varepsilon_B}\,|\gamma\mathbf{i}|\alpha|\rangle_{\varepsilon_D} + |\sqrt{T}\,|\alpha|e^{\frac{-\mathrm{i}\pi}{4}}\rangle_D\,|\gamma|\alpha|\rangle_{\varepsilon_B}\,|-\gamma\mathbf{i}|\alpha|\rangle_{\varepsilon_D} \\
&\quad + |-\sqrt{T}\,|\alpha|e^{\frac{-\mathrm{i}\pi}{4}}\rangle_D\,|-\gamma|\alpha|\rangle_{\varepsilon_B}\,|\gamma\mathbf{i}|\alpha|\rangle_{\varepsilon_D} + |-\sqrt{T}\,|\alpha|e^{\frac{\mathrm{i}\pi}{4}}\rangle_D\,|-\gamma|\alpha|\rangle_{\varepsilon_B}\,|-\gamma\mathbf{i}|\alpha|\rangle_{\varepsilon_D}\Big] \\
&\quad + e^{\frac{-T|\alpha|^2}{2}}\,|10\rangle_{AC} \\
&\quad\Big[\,|\sqrt{T}\,|\alpha|e^{\frac{\mathrm{i}\pi}{4}}\rangle_D\,|\gamma\mathbf{i}|\alpha|\rangle_{\varepsilon_B}\,|\gamma|\alpha|\rangle_{\varepsilon_D} + |-\sqrt{T}\,|\alpha|e^{\frac{-\mathrm{i}\pi}{4}}\rangle_D\,|\gamma\mathbf{i}|\alpha|\rangle_{\varepsilon_B}\,|-\gamma|\alpha|\rangle_{\varepsilon_D} \\
&\quad + |\sqrt{T}\,|\alpha|e^{\frac{-\mathrm{i}\pi}{4}}\rangle_D\,|-\gamma\mathbf{i}|\alpha|\rangle_{\varepsilon_B}\,|\gamma|\alpha|\rangle_{\varepsilon_D} + |-\sqrt{T}\,|\alpha|e^{\frac{\mathrm{i}\pi}{4}}\rangle_D\,|-\gamma\mathbf{i}|\alpha|\rangle_{\varepsilon_B}\,|-\gamma|\alpha|\rangle_{\varepsilon_D}\Big] \\
&\quad + |11\rangle_{AC} \\
&Big[\,|\sqrt{2T}\,\mathbf{i}|\alpha|\rangle_D\,|\gamma\mathbf{i}|\alpha|\rangle_{\varepsilon_B}\,|\gamma\mathbf{i}|\alpha|\rangle_{\varepsilon_D} + |-\sqrt{2T}\,\mathbf{i}|\alpha|\rangle_D\,|-\gamma\mathbf{i}|\alpha|\rangle_{\varepsilon_B}\,|-\gamma\mathbf{i}|\alpha|\rangle_{\varepsilon_D} \\
&\quad + e^{-T|\alpha|^2}\,|0\rangle_D\Big(\,|\gamma\mathbf{i}|\alpha|\rangle_{\varepsilon_B}\,|-\gamma\mathbf{i}|\alpha|\rangle_{\varepsilon_D} + |-\gamma\mathbf{i}|\alpha|\rangle_{\varepsilon_B}\,|\gamma\mathbf{i}|\alpha|\rangle_{\varepsilon_D}\Big)\Big]\Big], \qquad (3.63)
\end{aligned}
$$

where $\mathcal{P}_0^{Cat}$ is once again the success probability of the vacuum measurement, and is given as:

$$
\mathcal{P}_0^{Cat} = \left(\frac{(N_\alpha^+)^2}{2\mathcal{N}'}\right)^2 \qquad (3.64)
$$

where,

$$
\mathcal{N}' = 1/\sqrt{4 + 8e^{-T|\alpha|^2} + 24e^{-2T|\alpha|^2} + 8e^{-3T|\alpha|^2} + 4e^{-4T|\alpha|^2} + 8e^{-(2+\mathrm{i})T|\alpha|^2} + 8e^{-(2-\mathrm{i})T|\alpha|^2}}, \qquad (3.65)
$$

(note equivalence of the lossy vacuum success probability, with that of the no loss cat state case, Eq. 3.52).

A homodyne measurement in mode D using the projector given in Eq. 2.25 then gives:

$$
\begin{aligned}
|\Psi_{loss}^{Cat}\rangle_{A\varepsilon_B C\varepsilon_D} = \mathcal{N} \\
&\times \Big[|00\rangle_{AC} \Big(\exp\Big[(1-\mathrm{i})2\sqrt{T}\,|\alpha| x_{\frac{\pi}{4}} + (\mathrm{i}-1)T|\alpha|^2\Big] |\gamma|\alpha|\rangle_{\varepsilon_B}\ |\gamma|\alpha|\rangle_{\varepsilon_D} \\
&\qquad + \exp\Big[-(1-\mathrm{i})2\sqrt{T}\,|\alpha| x_{\frac{\pi}{4}} + (\mathrm{i}-1)T|\alpha|^2\Big] |-\gamma|\alpha|\rangle_{\varepsilon_B}\ |-\gamma|\alpha|\rangle_{\varepsilon_D} \\
&\qquad + e^{-T|\alpha|^2}\Big(|\gamma|\alpha|\rangle_{\varepsilon_B}\ |-\gamma|\alpha|\rangle_{\varepsilon_D} + |-\gamma|\alpha|\rangle_{\varepsilon_B}\ |\gamma|\alpha|\rangle_{\varepsilon_D} \Big)\Big) \\
&+ e^{\frac{-T|\alpha|^2}{2}} |01\rangle_{AC} \Big(\exp\Big[2\sqrt{T}\,|\alpha| x_{\frac{\pi}{4}} - T|\alpha|^2\Big] |\gamma|\alpha|\rangle_{\varepsilon_B}\ |\gamma\mathrm{i}|\alpha|\rangle_{\varepsilon_D} \\
&\qquad + \exp\Big[-2\sqrt{T}\,\mathrm{i}|\alpha| x_{\frac{\pi}{4}}\Big] |\gamma|\alpha|\rangle_{\varepsilon_B}\ |-\gamma\mathrm{i}|\alpha|\rangle_{\varepsilon_D} \\
&\qquad + \exp\Big[2\sqrt{T}\,\mathrm{i}|\alpha| x_{\frac{\pi}{4}}\Big] |-\gamma|\alpha|\rangle_{\varepsilon_B}\ |\gamma\mathrm{i}|\alpha|\rangle_{\varepsilon_D} \\
&\qquad + \exp\Big[-2\sqrt{T}\,|\alpha| x_{\frac{\pi}{4}} - T|\alpha|^2\Big] |-\gamma|\alpha|\rangle_{\varepsilon_B}\ |-\gamma\mathrm{i}|\alpha|\rangle_{\varepsilon_D} \Big) \\
&+ e^{\frac{-T|\alpha|^2}{2}} |10\rangle_{AC} \Big(\exp\Big[2\sqrt{T}\,|\alpha| x_{\frac{\pi}{4}} - T|\alpha|^2\Big] |\gamma\mathrm{i}|\alpha|\rangle_{\varepsilon_B}\ |\gamma|\alpha|\rangle_{\varepsilon_D} \\
&\qquad + \exp\Big[2\sqrt{T}\,\mathrm{i}|\alpha| x_{\frac{\pi}{4}}\Big] |\gamma\mathrm{i}|\alpha|\rangle_{\varepsilon_B}\ |-\gamma|\alpha|\rangle_{\varepsilon_D} \\
&\qquad + \exp\Big[-2\sqrt{T}\,\mathrm{i}|\alpha| x_{\frac{\pi}{4}}\Big] |-\gamma\mathrm{i}|\alpha|\rangle_{\varepsilon_B}\ |\gamma|\alpha|\rangle_{\varepsilon_D} \\
&\qquad + \exp\Big[-2\sqrt{T}\,|\alpha| x_{\frac{\pi}{4}} - T|\alpha|^2\Big] |-\gamma\mathrm{i}|\alpha|\rangle_{\varepsilon_B}\ |-\gamma|\alpha|\rangle_{\varepsilon_D} \Big) \\
&+ |11\rangle_{AC} \Big(\exp\Big[(\mathrm{i}+1)2\sqrt{T}\,|\alpha| x_{\frac{\pi}{4}} - (\mathrm{i}+1)T|\alpha|^2\Big] |\gamma\mathrm{i}|\alpha|\rangle_{\varepsilon_B}\ |\gamma\mathrm{i}|\alpha|\rangle_{\varepsilon_D} \\
&\qquad + \exp\Big[-(1+\mathrm{i})2\sqrt{T}\,|\alpha| x_{\frac{\pi}{4}} - (\mathrm{i}+1)T|\alpha|^2\Big] |-\gamma\mathrm{i}|\alpha|\rangle_{\varepsilon_B}\ |-\gamma\mathrm{i}|\alpha|\rangle_{\varepsilon_D} \\
&\qquad + e^{-T|\alpha|^2}\Big(|\gamma\mathrm{i}|\alpha|\rangle_{\varepsilon_B}\ |-\gamma\mathrm{i}|\alpha|\rangle_{\varepsilon_D} + |-\gamma\mathrm{i}|\alpha|\rangle_{\varepsilon_B}\ |\gamma\mathrm{i}|\alpha|\rangle_{\varepsilon_D} \Big)\Big)\Big].
\end{aligned}
\tag{3.66}
$$

We then take the homodyne measurement outcome to be $x_{\frac{\pi}{4}} = \pm\sqrt{T}\,|\alpha|$ (see Appendix C), thus our final state (prior to tracing out the lossy modes) is:

$$
\begin{aligned}
&|\Psi^{Cat}_{loss}\rangle_{A\varepsilon_B C\varepsilon_D} = \mathcal{N} \\
&\times\Big[\,|00\rangle_{AC} \\
&\Big(\exp\Big[(1-i)T|\alpha|^2\Big]\,|\gamma|\alpha|\rangle_{\varepsilon_B}\,|\gamma|\alpha|\rangle_{\varepsilon_D} + \exp\Big[-(3-3\mathrm{i})T|\alpha|^2\Big]\,|-\gamma|\alpha|\rangle_{\varepsilon_B}\,|-\gamma|\alpha|\rangle_{\varepsilon_D} \\
&+e^{-T|\alpha|^2}\Big(\,|\gamma|\alpha|\rangle_{\varepsilon_B}\,|-\gamma|\alpha|\rangle_{\varepsilon_D} + \,|-\gamma|\alpha|\rangle_{\varepsilon_B}\,|\gamma|\alpha|\rangle_{\varepsilon_D}\Big)\Big) \\
&+e^{\frac{-T|\alpha|^2}{2}}\,|01\rangle_{AC} \\
&\Big(\exp\Big[T|\alpha|^2\Big]\,|\gamma|\alpha|\rangle_{\varepsilon_B}\,|\gamma\mathrm{i}|\alpha|\rangle_{\varepsilon_D} + \exp\Big[-2T\mathrm{i}|\alpha|^2\Big]\,|\gamma|\alpha|\rangle_{\varepsilon_B}\,|-\gamma\mathrm{i}|\alpha|\rangle_{\varepsilon_D} \\
&+\exp\Big[2T\mathrm{i}|\alpha|^2\Big]\,|-\gamma|\alpha|\rangle_{\varepsilon_B}\,|\gamma\mathrm{i}|\alpha|\rangle_{\varepsilon_D}\Big) + \exp\Big[-3T|\alpha|^2\Big]\,|-\gamma|\alpha|\rangle_{\varepsilon_B}\,|-\gamma\mathrm{i}|\alpha|\rangle_{\varepsilon_D} \\
&+e^{\frac{-T|\alpha|^2}{2}}\,|10\rangle_{AC} \\
&\Big(\exp\Big[T|\alpha|^2\Big]\,|\gamma\mathrm{i}|\alpha|\rangle_{\varepsilon_B}\,|\gamma|\alpha|\rangle_{\varepsilon_D} + \exp\Big[2T\mathrm{i}|\alpha|^2\Big]\,|\gamma\mathrm{i}|\alpha|\rangle_{\varepsilon_B}\,|-\gamma|\alpha|\rangle_{\varepsilon_D} \\
&+\exp\Big[-2T\mathrm{i}|\alpha|^2\Big]\,|-\gamma\mathrm{i}|\alpha|\rangle_{\varepsilon_B}\,|\gamma|\alpha|\rangle_{\varepsilon_D}\Big) + \exp\Big[-3T|\alpha|^2\Big]\,|-\gamma\mathrm{i}|\alpha|\rangle_{\varepsilon_B}\,|-\gamma|\alpha|\rangle_{\varepsilon_D} \\
&+\,|11\rangle_{AC} \\
&\Big(\exp\Big[(\mathrm{i}+1)T|\alpha|^2\Big]\,|\gamma\mathrm{i}|\alpha|\rangle_{\varepsilon_B}\,|\gamma\mathrm{i}|\alpha|\rangle_{\varepsilon_D} + \exp\Big[-(3+3\mathrm{i})T|\alpha|^2\Big]\,|-\gamma\mathrm{i}|\alpha|\rangle_{\varepsilon_B}\,|-\gamma\mathrm{i}|\alpha|\rangle_{\varepsilon_D} \\
&+e^{-T|\alpha|^2}\Big(\,|\gamma\mathrm{i}|\alpha|\rangle_{\varepsilon_B}\,|-\gamma\mathrm{i}|\alpha|\rangle_{\varepsilon_D} + \,|-\gamma\mathrm{i}|\alpha|\rangle_{\varepsilon_B}\,|\gamma\mathrm{i}|\alpha|\rangle_{\varepsilon_D}\Big)\Big)\Big],
\end{aligned}
\tag{3.67}
$$

(note that the above equation is for $x_{\frac{\pi}{4}} = +\sqrt{T}\,|\alpha|$, however the same result is achieved for $x_{\frac{\pi}{4}} = -\sqrt{T}\,|\alpha|$). Finally, we then trace out the lossy modes using the coherent state to trace, as shown in Subsec. 3.2.4, therefore giving our final state for the cat state entanglement swapping protocol as:

$$
\rho^{Cat}_{AC} = \mathrm{Tr}_{\varepsilon_B,\varepsilon_D}\Big[\,|\Psi^{Cat}_{loss}\rangle_{A\varepsilon_B C\varepsilon_D}\,\langle\Psi^{Cat}_{loss}|\Big]\,. \tag{3.68}
$$

3.5 Cat State Entanglement Swapping Results

In this section we present our results for the entanglement swapping protocol using cat states, including losses. As before, we calculate entanglement negativity, linear entropy and fidelity to evaluate and establish how much loss this protocol can tolerate, whilst still producing a high-quality Bell state.

3.5.1 Entanglement Negativity

Let us first present the plot of entanglement negativity as a function of the cat state amplitude $|\alpha|$:

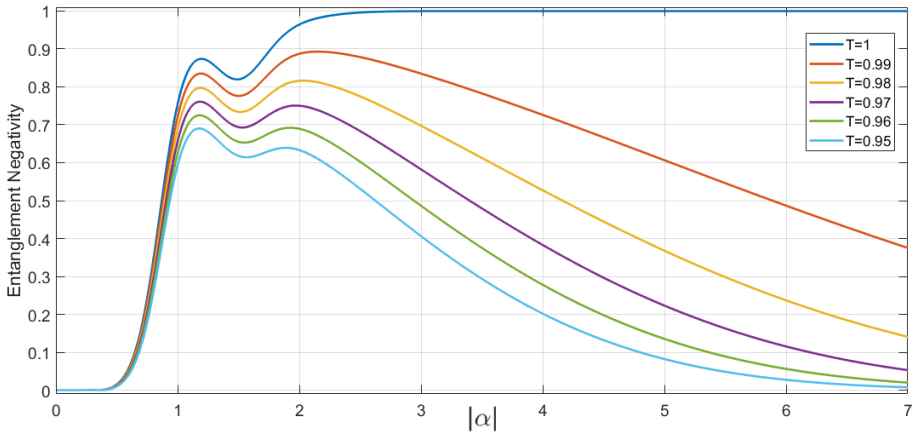

FIGURE 3.15: Entanglement negativity as a function of $|\alpha|$ for the final state generated via our cat state entanglement swapping protocol (Eq. 3.68), for varying levels of loss.

For the case of $T = 1$ the plot plateaus at unity for large $|\alpha|$, as we saw in the coherent state results (see Fig. 3.3). However, what is more interesting here is that we appear to see a small dip in the entanglement plots at around $|\alpha| = 1.5$, and this is evident in the cases where we also consider small photon losses too. Mathematically, this is a direct consequence from the numerous exponential terms that are present in our final equation describing the resultant two qubit state (see Eq. 3.56). These exponential terms can be seen as somewhat *competing* with each other, and so instead of seeing a simple peak followed by a decay (due to exponential dampening) as we saw in the coherent state entanglement negativity results (Fig. 3.3), in this case the cat state protocol introduces more exponential terms which causes this dip due to exponential interferences.

If we also consider the position of the peaks as a function of $|\alpha|$ in Fig. 3.16 we can note that the first peak is always at the same value of $|\alpha|$, for all T, whereas the second peak (for the cases of $T \leq 0.99$) shifts as a function of $|\alpha|$ for decreasing T. We in fact saw this in the coherent state regime (see Fig. 3.3), and concluded that this is as a result of the dampening exponent which is dependent on both T and $|\alpha|^2$, and was introduced through the projective vacuum measurement on mode B. As was discussed, if we decrease the value of T (to consider increasing levels of photon loss) then $|\alpha|$ must then increase to compensate for this, to cause the dampening exponent to successfully make the non-corner terms of the final density matrix decrease. When these non-corner terms have entirely dampened we have present a quantum state of higher fidelity against the $|\Phi^+(\alpha)\rangle$ Bell state. Finally, if we consider the first peak present in Fig. 3.16 then we can conclude that this is peak is caused by other exponential terms present in the final density matrix.

If we now consider the cases for loss, we can see that this dip is still present, and is the cause of a second peak we see in these plots (this second peak becomes less pronounced for increasing levels of loss). For $0.97 < T \leq 1$ this second peak corresponds to a higher entanglement negativity value than the first peak present, and vice versa for $T \leq 0.97$. Experimentally this is not a problem, due to the fact

that one is likely to already know the level of loss that the propagating cat states will undergo, and thus one would be able to engineer the amplitude of the initial cat states to match this, so as to achieve the highest level of resultant entanglement.

Again, we can plot the entanglement negativity as a function of both $|\alpha|$ and T to give:

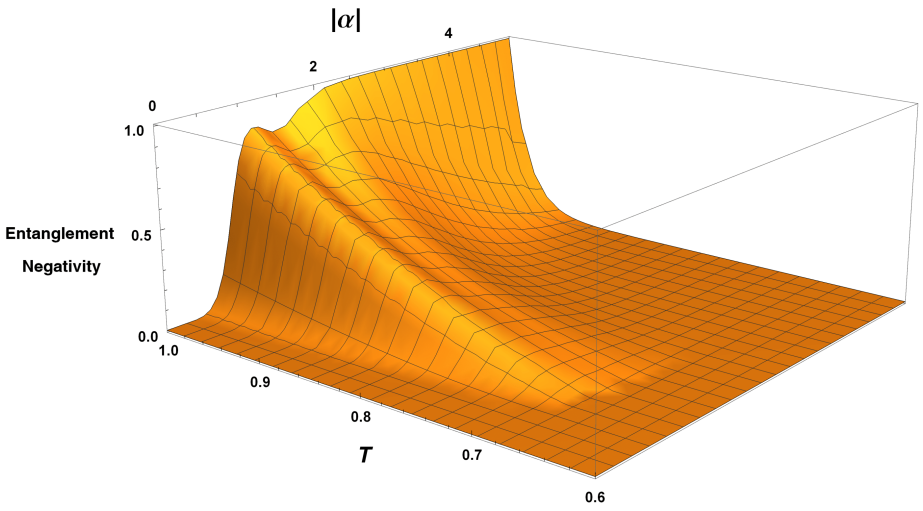

FIGURE 3.16: Entanglement negativity as a function of $|\alpha|$ and T for the final state generated via our cat state entanglement swapping protocol (Eq. 3.68).

where we can see that, as with the coherent state entanglement swapping results (Fig. 3.4), at large $|\alpha|$ and high losses ($T \leq 0.80$), the entanglement negativity plots plateau at $\mathcal{N}(\rho) = 0$, as expected.

3.5.2 Linear Entropy

Let us now investigate the linear entropy of the final quantum state produced via this cat state entanglement swapping protocol:

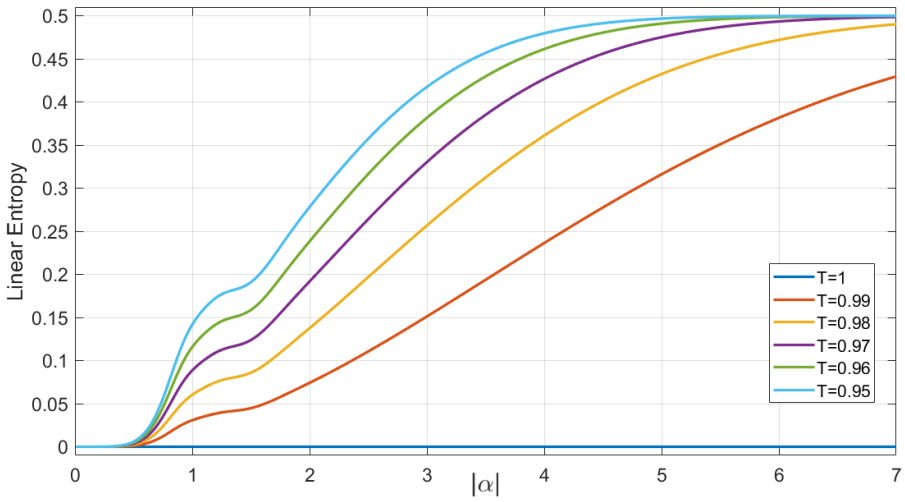

FIGURE 3.17: Linear entropy as a function of $|\alpha|$ for the final state generated via our cat state entanglement swapping protocol (Eq. 3.68), for varying levels of loss.

Evidently, for no loss the linear entropy is zero for all $|\alpha|$, as expected, and in accordance with the coherent state protocol results for linear entropy (see Fig. 3.5). If we now observe the linear entropy plots that include losses we can see that all of these plots are tending to plateau at an entropy value of $S_L = 0.50$, for large $|\alpha|$. This again is identical to the coherent state results, where we can therefore start to conclude that we must be producing not a maximally mixed state, but a highly mixed state nonetheless. Plotting the linear entropy of our final density matrix as a function of $|\alpha|$ and T further reinforces this:

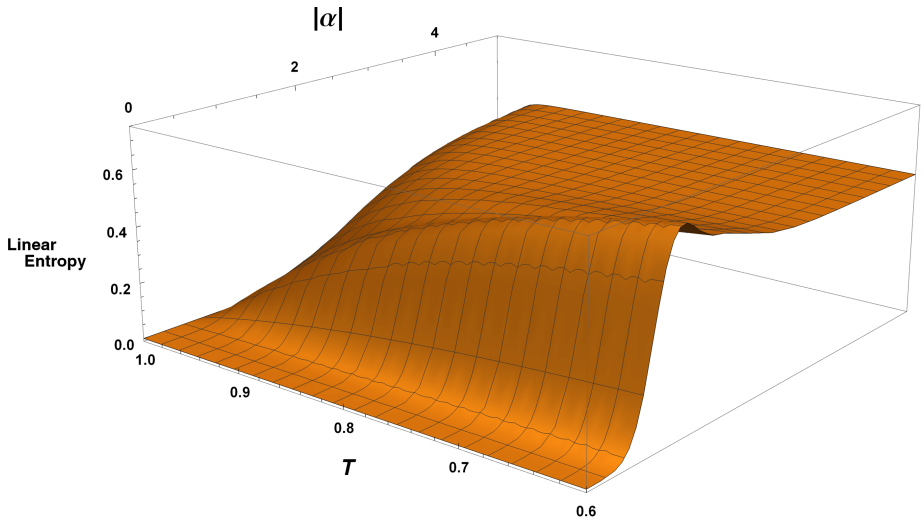

FIGURE 3.18: Linear entropy as a function of $|\alpha|$ and T for the final state generated via our cat state entanglement swapping protocol (Eq. 3.68).

Interestingly, we can also see that where the entanglement plot shows a dip (Fig. 3.15), the value of $|\alpha|$ for which this dip reaches its minimum is the same value of $|\alpha|$ where the linear entropy plots show a slight dip too. This will be further explained in the next section, where we discuss fidelity and also represent quantum state tomography describing the final density matrix.

3.5.3 Fidelity

As previously discussed, in the cat state ES protocol, for the ideal case (large $|\alpha|$ limit and $T = 1$) the state we are producing is a phase-rotated Bell state, shown in Eq. 3.57. So far we have seen from Figs. 3.15 and 3.17 that for large $|\alpha|$ and non-unity T we are producing a mixed state; it is now, as with the coherent state results, much more useful to look at the fidelity of our final quantum state, with the Bell state we *expect* to have made and also with respect to the state orthogonal to this Bell state.

Firstly, we show the plot for fidelity against the phase-rotated Bell state $|\Phi^+(\alpha)\rangle = \frac{1}{\sqrt{2}}(\,|00\rangle\, e^{-\mathrm{i}|\alpha|^2} + |11\rangle\, e^{+\mathrm{i}|\alpha|^2})$ as a function of $|\alpha|$:

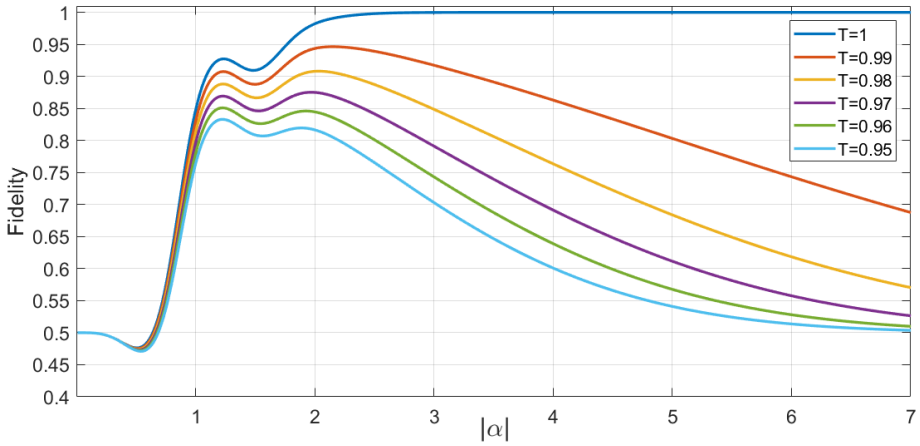

FIGURE 3.19: Fidelity against the $|\Phi^+(\alpha)\rangle = \frac{1}{\sqrt{2}}(|00\rangle e^{-i|\alpha|^2} + |11\rangle e^{+i|\alpha|^2})$ Bell state as a function of $|\alpha|$ for the final state generated via our cat state entanglement swapping protocol (Eq. 3.68), for varying levels of loss.

As with the coherent state entanglement swapping results, the fidelity plot against our ideal Bell state outcome has a similar shape to that of the entanglement plot (see Fig. 3.15), with the no loss plot plateauing at unity, indicating that in our ideal case we have the maximally entangled phase-rotated $|\Phi^+(\alpha)\rangle$ Bell state present. As we would expect, when including losses and looking at larger values of amplitude then the fidelity plot against this Bell state drops and plateaus at $F = 0.50$. It is again useful to investigate the fidelity with the state orthogonal to our ideal Bell state, $|\Phi^-(\alpha)\rangle = \frac{1}{\sqrt{2}}(|00\rangle e^{-i|\alpha|^2} - |11\rangle e^{+i|\alpha|^2})$:

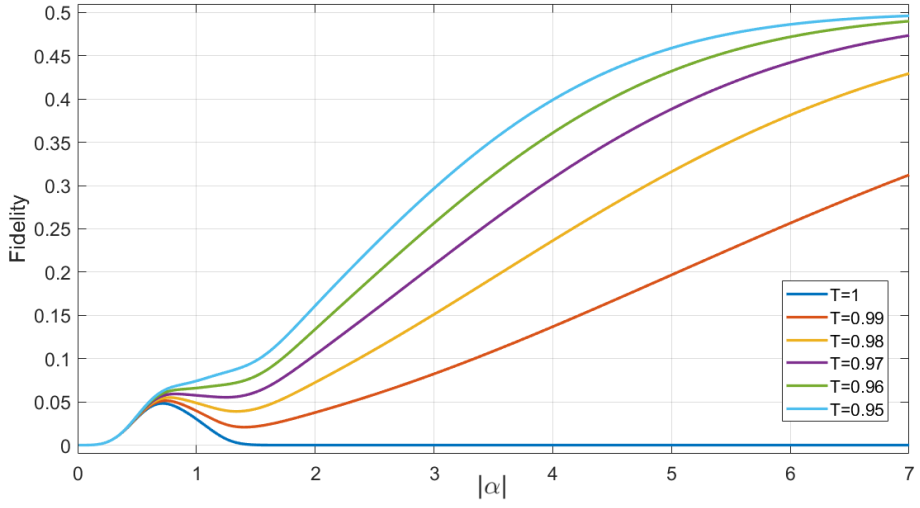

FIGURE 3.20: Fidelity against the $|\Phi^-(\alpha)\rangle = \frac{1}{\sqrt{2}}(|00\rangle e^{-i|\alpha|^2} - |11\rangle e^{+i|\alpha|^2})$ Bell state as a function of $|\alpha|$ for the final state generated via our cat state entanglement swapping protocol (Eq. 3.68), for varying levels of loss.

Again, the patterns are similar to our more simplistic coherent state entanglement swapping regime, for no losses the fidelity against this orthogonal phase-rotated Bell state exhibits a very small peak (at $|\alpha| = 0.70$) before rapidly dipping again to $F = 0$. This of course is entirely expected as we can see from Fig. 3.19 that

for larger $|\alpha|$ values our final density matrix is purely the $|\Phi^+(\alpha)\rangle$ Bell state. Once again, this small bump we see in Fig. 3.20 is due to competing exponential terms.

We now overlay Figs. 3.19 and 3.20, for clarity:

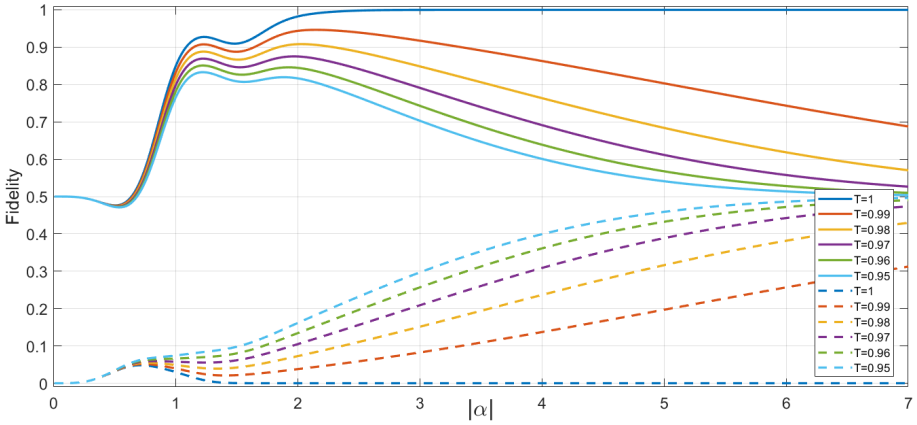

FIGURE 3.21: Fidelity against the $|\Phi^+(\alpha)\rangle = \frac{1}{\sqrt{2}}(\,|00\rangle\, e^{-i|\alpha|^2} + |11\rangle\, e^{+i|\alpha|^2})$ Bell state (solid lines) and the $|\Phi^-(\alpha)\rangle = \frac{1}{\sqrt{2}}(\,|00\rangle\, e^{-i|\alpha|^2} - |11\rangle\, e^{+i|\alpha|^2})$ Bell state (dashed lines), as a function of $|\alpha|$ for the final state generated via our cat state entanglement swapping protocol (Eq. 3.68), for varying levels of loss.

Observing Fig. 3.21, we can see that for non-unity T and very large $|\alpha|$ the plots for the fidelity against the orthogonal Bell state tend to $F = 0.50$, indicating that at these limits we have a 50:50 mixture of the $|\Phi^+(\alpha)\rangle$ state and the orthogonal $|\Phi^-(\alpha)\rangle$ state. If we now refer back to the linear entropy plot of Fig. 3.17 we already know this to be the case; as the linear entropy at the limit of very large $|\alpha|$ and $T < 1$ tends to $S_L = 0.50$, we can already conclude that we likely have a mixture of two Bell states (recall that we reached a similar conclusion regarding the coherent state protocol). This will be covered in further detail in the next section where we plot the QST of our final density matrix.

Finally, it is useful to look at the fidelity (against the ideal $|\Phi^+(\alpha)\rangle$ Bell state) as a function of both T and $|\alpha|$:

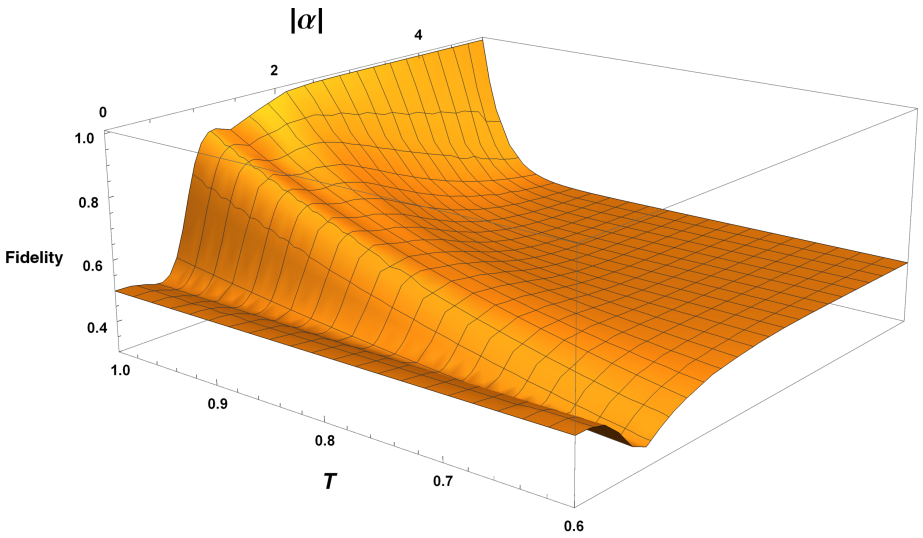

FIGURE 3.22: Fidelity against the $|\Phi^+(\alpha)\rangle = \frac{1}{\sqrt{2}}(\,|00\rangle\, e^{-\mathrm{i}|\alpha|^2} + |11\rangle\, e^{+\mathrm{i}|\alpha|^2})$ Bell state as a function of $|\alpha|$ and T for the final state generated via our cat state entanglement swapping protocol (Eq. 3.68).

As we found before, in the limits of very large losses $T \leq 0.80$ there are no values of $|\alpha|$ which yield a useful level of fidelity. This of course corresponds well with the 3D plot for entanglement in Fig. 3.16, where at these same limits the entanglement plot plateaus at $\mathcal{N}(\rho) = 0$.

3.5.4 Quantum State Tomography

As a final verification as to which quantum state our final density matrix is describing, we can once more consider the quantum state tomography (QST) of this quantum state as a visual aid.

The QSTs for the coherent state entanglement swapping protocol (Figs. 3.10, 3.11, 3.12 and 3.13) were simplistic, as we considered only the most idealistic homodyne measurement outcome ($x_{\frac{\pi}{2}} = 0$) which removed any phases from our final quantum state, and so the QSTs for this case represented the real values only. However, as should be apparent by now, our proposed cat state protocol is more complicated, and as such we have many more phases present (most of which are not removed by our most ideal homodyne measurement outcomes), and as such, as is typically shown in QST diagrams, we will now need to plot the separate real and imaginary components of our final density matrix (denoted as $\mathrm{Re}(\rho)$ and $\mathrm{Im}(\rho)$ respectively).

It is useful to investigate the QST for the peaks in our ideal outcome fidelity plots, so that we can ascertain exactly what quantum state we have at these points. Firstly, let us look at the QST describing the maximum point of the first peak (at $|\alpha| = 1.24$) in the fidelity plot of Fig. 3.19 for the no loss ($T = 1$) circumstance:

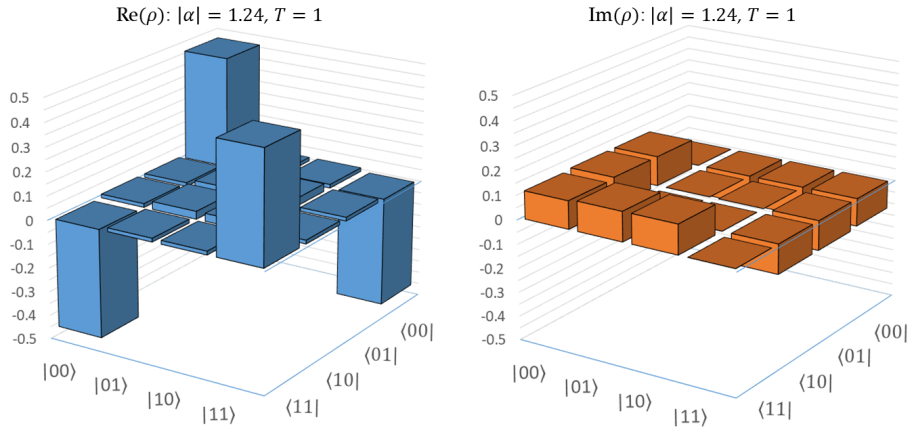

FIGURE 3.23: Quantum state tomography for the final state generated via our cat state entanglement swapping protocol (Eq. 3.68), for $|\alpha| = 1.24$ (maximum point of the first peak in fidelity plot) and $T = 1$.

The above QST diagram shows that, for the value of $|\alpha|$ at the first peak for $T = 1$, we do not yet have a state that is identical to the $|\Phi^+(\alpha)\rangle$ Bell state; this is easy to see when looking at the imaginary component of Fig. 3.23, where the imaginary component values are fairly small, and as such we clearly do not yet have a state with a phase similar to that present in the $|\Phi^+(\alpha)\rangle$ Bell state. If we now look at the QST describing the minimum point at the dip in the fidelity plot (at $|\alpha| = 1.48$) then we will see that the QST shows slightly more *mixing*:

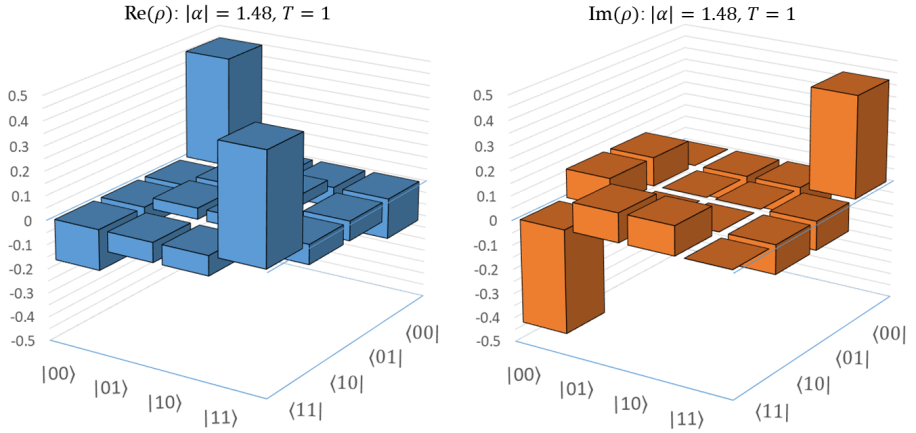

FIGURE 3.24: Quantum state tomography for the final state generated via our cat state entanglement swapping protocol (Eq. 3.68), for $|\alpha| = 1.48$ (minimum point of the dip in fidelity plot) and $T = 1$.

This mixing is present due to the "non-corner terms" (i.e. the terms that are not $|00\rangle\langle 00|$, $|00\rangle\langle 11|$, $|11\rangle\langle 00|$ or $|11\rangle\langle 11|$) having slightly higher values (in both the real and imaginary components) compared to Fig. 3.23. Of course, we would expect this as the fidelity plot in Fig. 3.19 shows that the fidelity against our ideal Bell state is lower for $|\alpha| = 1.48$ than it is for $|\alpha| = 1.24$. Interestingly, in the imaginary part of Fig. 3.24 we can observe that the $|00\rangle\langle 11|$ and $|11\rangle\langle 00|$ terms are increasing in

value, which is what we need for our final density matrix to have a high fidelity against the $|\Phi^+(\alpha)\rangle$ Bell state.

Next, we show the QST at the point in which the fidelity plot for $T = 1$ plateuas at $F = 1$ (at $|\alpha| = 2.30$):

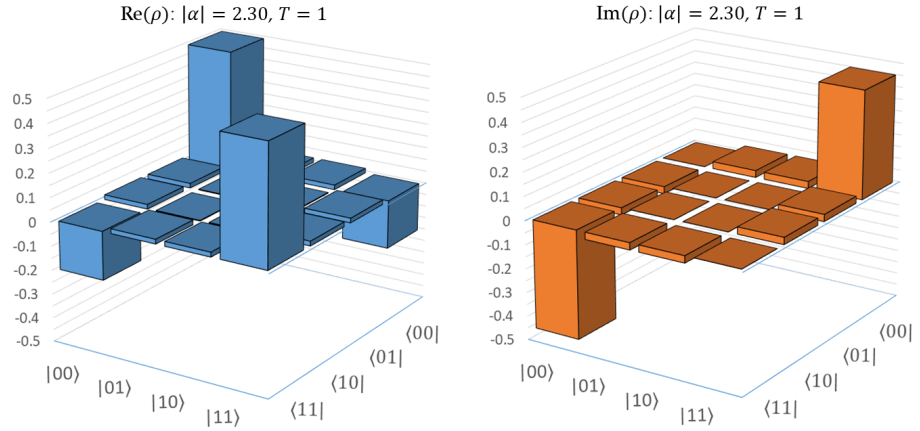

FIGURE 3.25: Quantum state tomography for the final state generated via our cat state entanglement swapping protocol (Eq. 3.68), for $|\alpha| \geq 2.30$ (point at which fidelity plot plateaus) and $T = 1$.

Here, the imaginary component QST exhibits almost no mixing (all off-diagonal terms, with the exception of $|00\rangle\langle 11|$ and $|11\rangle\langle 00|$, are close to zero). The problem in analysing these QST diagrams when we consider phases is that, if we consider the $|\Phi^+(\alpha)\rangle$ Bell state, then the phases present are dependent on $|\alpha|^2$, and as such oscillate rapidly as a function of $|\alpha|$. Thus, as a comparison, it is useful to also look at the QST for the $|\Phi^+(\alpha)\rangle$ Bell state at precisely $|\alpha| = 2.30$:

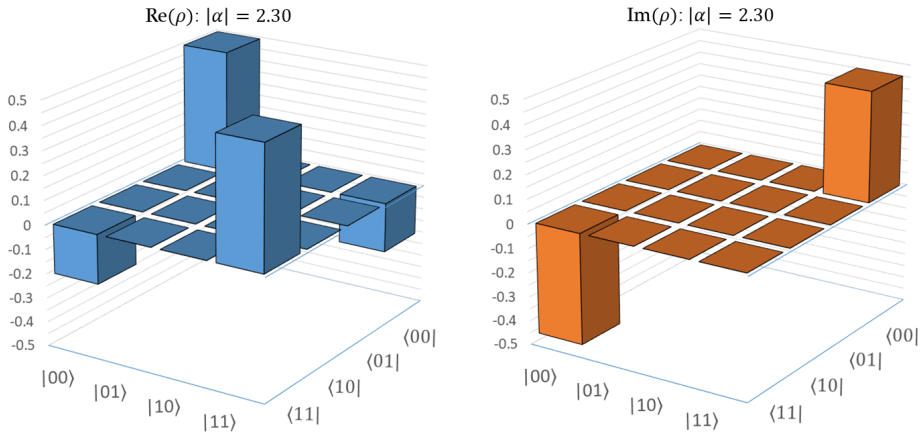

FIGURE 3.26: Quantum state tomography for the $|\Phi^+(\alpha)\rangle = \frac{1}{\sqrt{2}}(|00\rangle e^{-i|\alpha|^2} + |11\rangle e^{+i|\alpha|^2})$ phase-rotated Bell state, for $|\alpha| = 2.30$ (point at which fidelity plot against this Bell state plateaus for $T = 1$).

Inherently, the QST diagram for the phase-rotated Bell state must show that all off-diagonal terms, with the exception of $|00\rangle\langle 11|$ and $|11\rangle\langle 00|$, are equal to zero, thus indicating that the quantum state here is entirely pure. It therefore follows that if we compare this QST plot with the equivalent QST for our final density matrix

at $|\alpha| = 2.30$ (Fig. 3.25) then it is evident that these two QST plots are effectively identical. We can therefore, again, conclude that in the limit of of $|\alpha| \geq 2.30$ and $T = 1$ that for the cat state protocol (for ideal homodyne measurement outcomes of $x_{\frac{\pi}{4}} = \pm\sqrt{T}\,|\alpha|$) we create precisely the $|\Phi^+(\alpha)\rangle$ Bell state, and hence the fidelity plot of Fig. 3.19 reaches unity at these limits.

Let us now consider the lossy case, for $T = 0.95$. To begin with, we show the QST plot for the amplitude value corresponding to the maximum point of the first peak in the fidelity plot for $T = 0.95$, which is $|\alpha| = 1.23$:

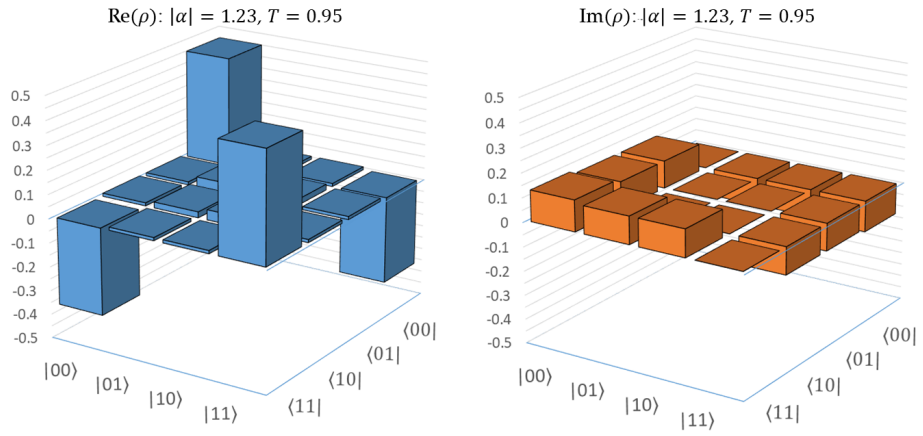

FIGURE 3.27: Quantum state tomography for the final state generated via our cat state entanglement swapping protocol (Eq. 3.68), for $|\alpha| = 1.23$ (maximum point of the first peak in fidelity plot) and $T = 0.95$.

Directly comparing the above QST with the QST for the first peak in the $T = 1$ limit (Fig. 3.23) it is cler why the fidelity is worse in this case; observing the off-diagonal corner terms ($|00\rangle\langle 11|$ and $|11\rangle\langle 00|$) for the $T = 0.95$ real component QST plot shows that these terms are slightly dampened (and are therefore less than 0.50). and are in fact more dampened than the same terms for the $T = 1$ QST plot. This therefore means that for $T = 0.95$ the quantum state we have, for the $|\alpha|$ value corresponding to the maximum point of the first peak in the fidelity plot, is more mixed (and hence has a lower fidelity value with respect to the $|\Phi^+(\alpha)\rangle$ Bell state compared to the $T = 1$ case). As before, looking at the fidelity plot of Fig. 3.19 for $T = 0.95$, it is clear that we have a dip in the plot at slightly larger $|\alpha|$ than the first peak, so it is useful to observe this as a QST:

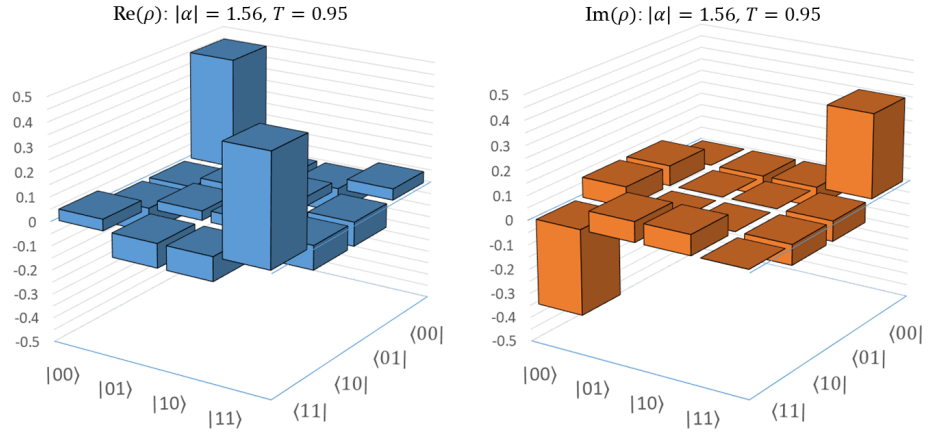

FIGURE 3.28: Quantum state tomography for the final state generated via our cat state entanglement swapping protocol (Eq. 3.68), for $|\alpha| = 1.56$ (minimum point of the dip in fidelity plot) and $T = 0.95$.

The above QST shows a more mixed state than that shown in Fig. 3.27, due to the off-diagonal terms being non-zero, and therefore contributing to the mixing of the density matrix - of course, this is entirely unsurprising as we know that the fidelity drops here, and therefore so must the level of purity of this quantum state.

Lastly, we show the QST for the $|\alpha|$ value at the maximum of the second peak in the fidelity plot for $T = 0.95$, as well as the $|\Phi^+(\alpha)\rangle$ Bell state QST plot for a comparative:

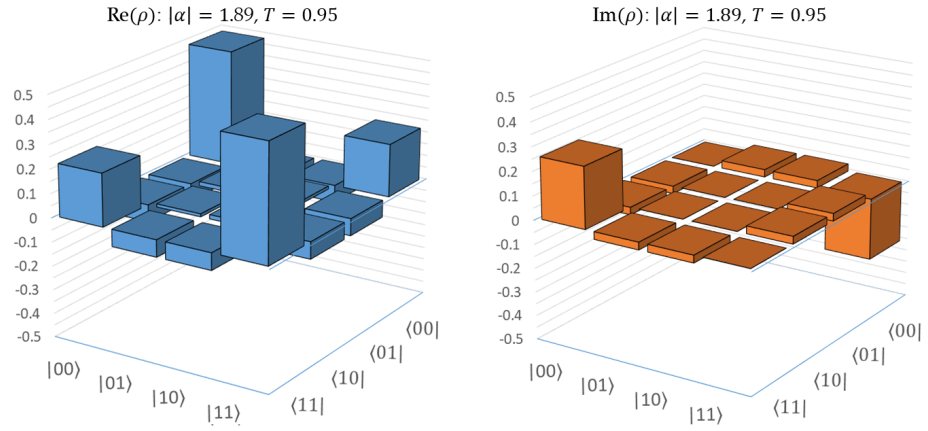

FIGURE 3.29: Quantum state tomography for the final state generated via our cat state entanglement swapping protocol (Eq. 3.68), for $|\alpha| = 1.89$ (maximum point of the second peak in fidelity plot) and $T = 0.95$.

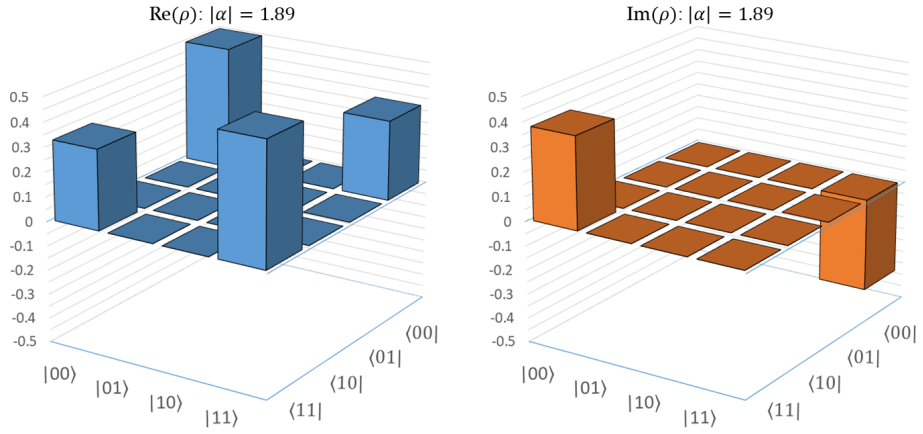

FIGURE 3.30: Quantum state tomography for the $|\Phi^+(\alpha)\rangle = \frac{1}{\sqrt{2}}(|00\rangle e^{-i|\alpha|^2} + |11\rangle e^{+i|\alpha|^2})$ phase-rotated Bell state, for $|\alpha| = 1.89$ (point at which fidelity plot reaches the maximum of its second peak against this Bell state for $T = 0.95$).

As can be seen from looking at the above QST diagrams, they show a similar overall shape, however when looking at the actual values it is clear that for $T = 0.95$ the level of loss present causes the state to become more mixed (due to the dampening exponent dependent on T and $|\alpha|^2$ being present in the $|00\rangle\langle 11|$ and $|11\rangle\langle 00|$ terms); this is evident in the QST (Fig. 3.29), where if we compare this to the ideal case for the same $|\alpha|$ value (Fig. 3.30) it becomes apparent why the fidelity for $T = 0.95$ against this phase-rotated Bell state is not near unity.

Importantly, we come to the same conclusion here as we can in the coherent state regime - introducing photonic losses into our protocol causes dampening exponents to be present on the $|00\rangle\langle 11|$ and $|11\rangle\langle 00|$ terms in the final density matrices, and as such as we increase the levels of loss present these terms are dampened more strongly. By doing so, this causes the fidelity against the ideal Bell state to decrease, as we saw in the QST plots in this section.

3.6 Summary

In this chapter we have applied our theoretical entanglement swapping protocol (described by Fig. 2.2) to two different initial CV-DV hybrid entangled quantum states. In the first instance, the CV half of this hybrid entangled state was the coherent state, and in the second half of this chapter we considered coherent state superpositions (so-called cat states) as the CV half. Through successful (no loss) entanglement swapping we are able to generate a final state in both protocols, of the form of the $|\Phi^+\rangle = \frac{1}{\sqrt{2}}(|00\rangle + |11\rangle)$ Bell state in the coherent state case, and the $|\Phi^+(\alpha)\rangle = \frac{1}{\sqrt{2}}(|00\rangle e^{-i|\alpha|^2} + |11\rangle e^{+i|\alpha|^2})$ phase-rotated Bell state in the cat state case.

Through assessing entanglement negativity, as a function of the amplitude $|\alpha|$, of these final states we show that in both circumstances there is a sharp peak $|\alpha|$ value in which the entanglement negativity reaches an optimum when considering small

levels of photon loss. When considering losses, the entanglement negativity rapidly exponentially decays as a function of $|\alpha|$.

We also plotted linear entropy to compliment the entanglement negativity plots, and showed that as we increase the levels of loss then the entropy, again in both protocol circumstances, also increases as a function of $|\alpha|$. Thus showing that as the entanglement negativity rapidly decays to $\mathcal{N}(\rho) = 0$, the linear entropy plateaus at $S_L = 1/2$. This then identifies that we have a highly mixed state present, therefore suggesting that we no longer have a Bell state.

Hence, we then moved on to discuss fidelity, which is arguably the most useful calculation we perform in our analysis of our final state produced through the entanglement swapping protocol. For the coherent state protocol, we plotted fidelity with respect to the maximally entangled $|\Phi^+\rangle = \frac{1}{\sqrt{2}}(|00\rangle + |11\rangle)$ Bell state, and showed that there is once again a region of $|\alpha|$ in which the fidelity plots reach a maximum, when allowing for small photon losses. This peak $|\alpha|$ value matches that of the entanglement negativity plots, and the same is true for the cat state protocol.

The fidelity values at the maximum of these peak $|\alpha|$ regions have been tabulated in Appendix D (Tab. D.1 and Tab. D.2), where the green cells correspond to high-fidelity values ($F \geq 0.90$) and the amber cells signify slightly lower level fidelities ($F \geq 0.80$), which may be increased via a suitable entanglement purification protocol. Entanglement purification will be addressed in Chapter 6, in which we discuss optimisation of our proposed entanglement swapping protocol.

Finally, we then plotted quantum state tomography of the density matrices describing our final state at these peak $|\alpha|$ values, and compared this with the relevant Bell states for each protocol. All of these calculations determine exactly what final state our protocols have produced, when allowing for relatively low levels of photon losses, with the practical viewpoint to be able to distribute these entangled pairs of qubits to a potential customer (or indeed customers), for further uses in quantum communications or even computation.

Conclusively, we have found that introducing photonic losses into our entanglement swapping protocol causes our final two-qubit state to become less entangled, and as exhibits lower fidelities when compared with the ideal-case Bell states. However, importantly, we must note that introducing low levels of photon losses ($T \geq 0.95$) does not mean that the fidelity fall unacceptably low, and so this protocol *is* resilient to this level of loss, and could therefore be used to distribute entanglement over short distances (to avoid unacceptable levels of photon losses).

In the next chapter we further our notion of photon losses, and evaluate the potential impact to our final state if we consider unequal photon losses in the propagating continuous variable modes B and D.

Chapter 4

Unequal Optical Fibre Losses Investigation

Part of the work detailed in this section was published in [1]: R. C. Parker, J. Joo, M. Razavi and T. P. Spiller, *J. Opt*, **19**, 10 (2017).

4.1 Unequal Beam-Splitters

In reality, the first two beam-splitters in our proposed entanglement swapping protocols ($BS^{T_B}_{B,\varepsilon_B}$ and $BS^{T_D}_{D,\varepsilon_D}$) will not have equal transmission coefficients; this could be down to something as simple as an engineer not being physically able to "fit" the optical fibres evenly into the respective beam-splitters. As a result of this, we must determine whether allowing for a small difference (which we shall denote as υ) in these transmission coefficients has an impact on the overall final entanglement shared by modes A and C, as well as fidelity and success probability. We demonstrate here that the entanglement shared between Alice and Bob is not significantly damaged if we consider unequal optical fibre losses.

4.1.1 Parametrising υ

Firstly we must parametrise this "unequal loss" υ value. Of course, we need to avoid an unphysical regime of T exceeding unity, and as such we parametrise the loss mismatch in a manner which ensures that this unphysical circumstance does not arise.

Therefore we parametrise the uneven beam-splitters ($BS^{T_B}_{B,\varepsilon_B}$ and $BS^{T_D}_{D,\varepsilon_D}$) by incorporating this υ value into just one of the lossy modes. Hence we set the loss in mode B equal to $1-T$ and the loss in mode D equal to $1-T+\upsilon$, where $0 \leq \upsilon \leq T$, thus giving:

$$\begin{aligned} \sqrt{T_B} &= \sqrt{T} \\ \sqrt{T_D} &= \sqrt{T-\upsilon}\,. \end{aligned} \tag{4.1}$$

In using this parametrisation method we shall avoid exceeding unity for the transmission values. We should specify here that although υ can indeed physically take

any value between 0 and T, we of course will not consider the cases in which υ tends to T. This is simply due to the fact that in a realistic, experimental scenario there would likely never be a circumstance in which the loss mismatch would be that large (and if it was then the experiment would inherently need to be made far more accurate such that υ is closer to 0 than T).

The two terms of Eq. 4.1 can now be applied to the analytical solutions of the density matrices for, both, the coherent state and cat state protocols. In doing so, we will obtain new density matrices describing modes A and C which will contain this υ value (we shall denote the new density matrices as $\rho_{AC}^{(\upsilon)}$).

4.1.2 Case for Coherent State ES with Unequal Losses

The coherent state entanglement swapping protocol will first be investigated. Following on from Eq. 3.24, we then set the lossy beam-splitters to act such that:

$$\begin{aligned} BS^{T}_{B,\varepsilon_B} \left|\left|\alpha\right|\right\rangle_B \left|0\right\rangle_{\varepsilon_B} &= \left|\sqrt{T_B}\left|\alpha\right|\right\rangle_B \left|\sqrt{1-T_B}\left|\alpha\right|\right\rangle_{\varepsilon_B} \\ &= \left|\sqrt{T}\left|\alpha\right|\right\rangle_B \left|\sqrt{1-T}\left|\alpha\right|\right\rangle_{\varepsilon_B} \\ BS^{T}_{D,\varepsilon_D} \left|\left|\alpha\right|\right\rangle_D \left|0\right\rangle_{\varepsilon_D} &= \left|\sqrt{T_D}\left|\alpha\right|\right\rangle_D \left|\sqrt{1-T_D}\left|\alpha\right|\right\rangle_{\varepsilon_D} \\ &= \left|\sqrt{T-\upsilon}\left|\alpha\right|\right\rangle_D \left|\sqrt{1-T+\upsilon}\left|\alpha\right|\right\rangle_{\varepsilon_D}, \end{aligned} \tag{4.2}$$

where we have used the parametrisation detailed in Eq. 4.1. This then gives an "unequal loss" representation of Eq. 3.28 such that:

$$\left|\Psi_{\upsilon}^{Coh.}\right\rangle_{AB\varepsilon_B CD\varepsilon_D} = \tag{4.3}$$

$$\begin{aligned} &\frac{1}{2}\Big[\Big(\left|0\right\rangle_A \left|\sqrt{T}\left|\alpha\right|\right\rangle_B \left|\sqrt{1-T}\left|\alpha\right|\right\rangle_{\varepsilon_B} + \left|1\right\rangle_A \left|-\sqrt{T}\left|\alpha\right|\right\rangle_B \left|-\sqrt{1-T}\left|\alpha\right|\right\rangle_{\varepsilon_B}\Big) \\ &\qquad \otimes\Big(\left|0\right\rangle_C \left|\sqrt{T-\upsilon}\left|\alpha\right|\right\rangle_D \left|\sqrt{1-T+\upsilon}\left|\alpha\right|\right\rangle_{\varepsilon_D} \\ &\qquad\qquad + \left|1\right\rangle_C \left|-\sqrt{T-\upsilon}\left|\alpha\right|\right\rangle_D \left|-\sqrt{1-T+\upsilon}\left|\alpha\right|\right\rangle_{\varepsilon_D}\Big)\Big], \end{aligned} \tag{4.4}$$

$$\begin{aligned} = \frac{1}{2}\Big[&\left|00\right\rangle_{AC} \left|\sqrt{T}\left|\alpha\right|\right\rangle_B \left|\sqrt{T-\upsilon}\left|\alpha\right|\right\rangle_D \left|\sqrt{1-T}\left|\alpha\right|\right\rangle_{\varepsilon_B} \left|\sqrt{1-T+\upsilon}\left|\alpha\right|\right\rangle_{\varepsilon_D} \\ &+ \left|01\right\rangle_{AC} \left|\sqrt{T}\left|\alpha\right|\right\rangle_B \left|-\sqrt{T-\upsilon}\left|\alpha\right|\right\rangle_D \left|\sqrt{1-T}\left|\alpha\right|\right\rangle_{\varepsilon_B} \left|-\sqrt{1-T+\upsilon}\left|\alpha\right|\right\rangle_{\varepsilon_D} \\ &+ \left|10\right\rangle_{AC} \left|-\sqrt{T}\left|\alpha\right|\right\rangle_B \left|\sqrt{T-\upsilon}\left|\alpha\right|\right\rangle_D \left|-\sqrt{1-T}\left|\alpha\right|\right\rangle_{\varepsilon_B} \left|\sqrt{1-T+\upsilon}\left|\alpha\right|\right\rangle_{\varepsilon_D} \\ &+ \left|11\right\rangle_{AC} \left|-\sqrt{T}\left|\alpha\right|\right\rangle_B \left|-\sqrt{T-\upsilon}\left|\alpha\right|\right\rangle_D \left|-\sqrt{1-T}\left|\alpha\right|\right\rangle_{\varepsilon_B} \left|-\sqrt{1-T+\upsilon}\left|\alpha\right|\right\rangle_{\varepsilon_D}\Big], \end{aligned} \tag{4.5}$$

where the subscript υ on the state $\left|\Psi_{\upsilon}^{Coh.}\right\rangle_{AB\varepsilon_B CD\varepsilon_D}$ denotes that this state is now evaluated for unequal losses. Next, as before, we then apply a 50:50 beam-splitter as

per Eq. 2.18, which yields:

$$
\begin{aligned}
&|\Psi_{\upsilon}^{Coh.}\rangle_{AB\varepsilon_B CD\varepsilon_D} = \\
&\frac{1}{2}\Bigg[|00\rangle_{AC} \left|\frac{\mathcal{T}^{-}|\alpha|}{\sqrt{2}}\right\rangle_B \left|\frac{\mathcal{T}^{+}|\alpha|}{\sqrt{2}}\right\rangle_D |\sqrt{1-T}\,|\alpha|\rangle_{\varepsilon_B} |\sqrt{1-T+\upsilon}\,|\alpha|\rangle_{\varepsilon_D} \\
&+ |01\rangle_{AC} \left|\frac{\mathcal{T}^{+}|\alpha|}{\sqrt{2}}\right\rangle_B \left|\frac{\mathcal{T}^{-}|\alpha|}{\sqrt{2}}\right\rangle_D |\sqrt{1-T}\,|\alpha|\rangle_{\varepsilon_B} |-\sqrt{1-T+\upsilon}\,|\alpha|\rangle_{\varepsilon_D} \\
&+ |10\rangle_{AC} \left|\frac{-\mathcal{T}^{+}|\alpha|}{\sqrt{2}}\right\rangle_B \left|\frac{-\mathcal{T}^{-}|\alpha|}{\sqrt{2}}\right\rangle_D |-\sqrt{1-T}\,|\alpha|\rangle_{\varepsilon_B} |\sqrt{1-T+\upsilon}\,|\alpha|\rangle_{\varepsilon_D} \\
&+ |11\rangle_{AC} \left|\frac{-\mathcal{T}^{-}|\alpha|}{\sqrt{2}}\right\rangle_B \left|\frac{-\mathcal{T}^{+}|\alpha|}{\sqrt{2}}\right\rangle_D |-\sqrt{1-T}\,|\alpha|\rangle_{\varepsilon_B} |-\sqrt{1-T+\upsilon}\,|\alpha|\rangle_{\varepsilon_D} \Bigg], \qquad (4.6)
\end{aligned}
$$

where we have used the substitutions $\sqrt{T} \pm \sqrt{T-\upsilon} = \mathcal{T}^{\pm}$ for simplification. Next, we measure a vacuum in mode B, using the operator $\hat{P}_B^0$ detailed in Eq. 2.19, such that:

$$
\hat{P}_B^0 \left|\frac{\mathcal{T}^{\pm}|\alpha|}{\sqrt{2}}\right\rangle_B = e^{\frac{-|\mathcal{T}^{\pm}\alpha|^2}{4}} |0\rangle_B . \qquad (4.7)
$$

We note here that, as we saw in the equal loss case (Chapter 3, Subsec. 3.1.2), there is an intrinsic success probability associated with the vacuum measurement. For the case of the success probability for this measurement in the unequal loss protocol at hand, we discuss this in more detail in Chapter 6, Sec. 6.1.

Next, via homodyne detection we measure mode D using the method detailed in 2.6 such that:

$$
{}_D\left\langle x_{\frac{\pi}{2}}\right| \frac{\mathcal{T}^{\pm}|\alpha|}{\sqrt{2}}\Big\rangle_D = {}_D\langle x_{\frac{\pi}{2}}|0\rangle_D \, e^{-\sqrt{2}\mathcal{T}^{\pm}\mathrm{i}|\alpha|x_{\frac{\pi}{2}}} . \qquad (4.8)
$$

We then apply the expressions given in Eq. 4.7 and Eq. 4.8, to give a final quantum state (prior to tracing out the lossy modes) described as:

$$
\begin{aligned}
&|\Psi_{\upsilon}^{Coh.}\rangle_{AC\varepsilon_B\varepsilon_D} = \\
&\mathcal{N}\Big[e^{\frac{-|\mathcal{T}^{-}\alpha|^2}{4}} e^{-\sqrt{2}\mathcal{T}^{+}\mathrm{i}|\alpha|x_{\frac{\pi}{2}}} |00\rangle_{AC} |\sqrt{1-T}\,|\alpha|\rangle_{\varepsilon_B} |\sqrt{1-T+\upsilon}\,|\alpha|\rangle_{\varepsilon_D} \\
&+ e^{\frac{-|\mathcal{T}^{+}\alpha|^2}{4}} e^{-\sqrt{2}\mathcal{T}^{-}\mathrm{i}|\alpha|x_{\frac{\pi}{2}}} |01\rangle_{AC} |\sqrt{1-T}\,|\alpha|\rangle_{\varepsilon_B} |-\sqrt{1-T+\upsilon}\,|\alpha|\rangle_{\varepsilon_D} \\
&+ e^{\frac{-|\mathcal{T}^{+}\alpha|^2}{4}} e^{\sqrt{2}\mathcal{T}^{-}\mathrm{i}|\alpha|x_{\frac{\pi}{2}}} |10\rangle_{AC} |-\sqrt{1-T}\,|\alpha|\rangle_{\varepsilon_B} |\sqrt{1-T+\upsilon}\,|\alpha|\rangle_{\varepsilon_D} \\
&+ e^{\frac{-|\mathcal{T}^{-}\alpha|^2}{4}} e^{\sqrt{2}\mathcal{T}^{+}\mathrm{i}|\alpha|x_{\frac{\pi}{2}}} |11\rangle_{AC} |-\sqrt{1-T}\,|\alpha|\rangle_{\varepsilon_B} |-\sqrt{1-T+\upsilon}\,|\alpha|\rangle_{\varepsilon_D} \Big], \qquad (4.9)
\end{aligned}
$$

where, $\mathcal{N}$ is the normalisation, and, as we assumed in the equal loss circumstance, the homodyne measurement outcomes will be taken to be discrete, hence we set $x_{\frac{\pi}{2}} = 0$ (as previously mentioned, an investigation into homodyne measurement imperfections and non-idealities, will be covered in Chapter 5). Finally, the last step is to mathematically trace out the lossy modes, which will give us a final density

matrix that can assess unequal photon losses between our lossy modes, given by $\rho_{AC}^{Coh.}(\upsilon)$. Following the method outlined in Subsec. 3.2.4, our final density matrix is calculated as:

$$\rho_{AC}^{Coh.}(\upsilon) = \mathrm{Tr}_{\varepsilon_B,\varepsilon_D}\left[\,|\Psi_{\upsilon}^{Coh.}\rangle_{A\varepsilon_B C\varepsilon_D}\,\langle\Psi_{\upsilon}^{Coh.}|\right]. \tag{4.10}$$

(This density matrix is large, containing many terms, and so will not be written explicitly here).

4.1.3 Case for Cat State ES with Unequal Losses

Following the same parametrisation for evaluating unequal optical fibre losses as above, we may apply this to the cat state entanglement swapping protocol. As a result of the complicated nature of the cat state ES protocol we propose, we do not show the analytical method of our protocol here as it is very lengthy - for the derivation of this analytical calculation please refer to Appendix F. Nevertheless, the principle of the calculation is exactly as per the coherent state case, detailed in Subsec. 4.1.2.

Our final density matrix for the unequal loss cat state scenario is calculated as:

$$\rho_{AC}^{Cat}(\upsilon) = \mathrm{Tr}_{\varepsilon_B,\varepsilon_D}\left[\,|\Psi_{\upsilon}^{Cat}\rangle_{A\varepsilon_B C\varepsilon_D}\,\langle\Psi_{\upsilon}^{Cat.}|\right], \tag{4.11}$$

in which the state $|\Psi_{\upsilon}^{Cat}\rangle_{A\varepsilon_B C\varepsilon_D}$ is determined using the same method as outlined in Chapter 3, Sec. 3.4.2, but for unequal losses in modes B and D. Also note that in the cat state protocol the ideal homodyne measurement outcome differs between the equal loss and unequal loss cases; for the equal loss case the ideal homodyne outcome is given as $x_{\frac{\pi}{4}} = \pm\sqrt{T}\,|\alpha|$ (where both results give the same overall final state), however for the case in which we have unequal losses the ideal homodyne outcome is $x_{\frac{\pi}{4}} = \pm\frac{(\sqrt{T}+\sqrt{T-\upsilon})|\alpha|}{2}$ (where, again, both results give the same outcome state). We should also note here that the ideal homodyne outcome for the coherent state state cases, for both equal and unequal losses, is identical and is still $x_{\frac{\pi}{2}} = 0$. In the next chapter we will move on to the circumstances in which we do not assume that the homodyne measurement outcomes are "perfect" and "ideal".

4.2 Averaging over υ

Experimentally, different lengths of optical fibres correspond to different levels of loss - shorter fibres would result in lower photon losses. In fact, optical fibres of equal length may even exhibit varying levels of photon losses. As previously stated, there are also potential errors in coupling optical fibre to components, such as the beam-splitters used to model loss, hence even if the lengths of fibre are identical, slightly different optical coupling in the two modes (B and D) could give a small mismatch in losses.

Moreover, there is a potential *thermal drift* (temperature changes in the optical fibre) effect which can happen over time, in which this "drift" could potentially cause a difference between the properties of different fibres; one property that may be impacted by thermal drift is the propagation time of photons through optical fibres, such that the photon loss level can vary between the fibres - there are, however, efforts in research to resolve this issue [176].

Rather than taking a specific value of mismatch υ, as it may not be known exactly (for the reasons stated above), it is logical to explore an average over υ according to a distribution. We can therefore instead look at our unequal loss variable υ as a Gaussian function, and as such, we are then able to integrate over this function (via standard Gaussian integration) to determine an "averaged" parametrisation of unequal loss, which we shall label Υ, to form our averaged density matrix $\bar{\rho}_{AC}(\Upsilon)$.

The reason one may wish to do this is because so far we have considered the case where a system is set up for matched loss $(1-T)$, but there is a small, unknown mismatch. As such, by integrating over υ we obtain an average over a distribution of υ, where the width (standard deviation) of this distribution we denote Υ. Taking an average over the level of unequal loss is a rational step; if we consider this average as an *ensemble average*, then it follows that an experimentalist performing our proposed entanglement swapping protocol could have in mind a threshold of Υ of which they would know to not allow the mismatch in the loss to fall below.

Investigation of this loss mismatch is beneficial, so as to check and ensure that there are no unexpected results or trends that appear when allowing for an unknown (averaged) loss mismatch.

4.2.1 Deriving the Averaged Unequal Loss Function

$$\begin{aligned}
\text{Let, } \; I &= \int_{-\infty}^{\infty} e^{-\frac{x^2}{2\Upsilon^2}} \mathrm{d}x, \\
\text{Then, } \; I^2 &= \int_{-\infty}^{\infty} e^{-\frac{x^2+y^2}{2\Upsilon^2}} \mathrm{d}x\mathrm{d}y, \\
&= \int_0^{\infty} \int_0^{2\pi} r e^{-\frac{r^2}{2\Upsilon^2}} \mathrm{d}r\mathrm{d}\phi \\
&= 2\pi \left[-\Upsilon^2 e^{-\frac{r^2}{2\Upsilon^2}} \right]_0^{\infty} = 2\pi\Upsilon^2,
\end{aligned} \tag{4.12}$$

hence, $f(\upsilon,\Upsilon) = \frac{1}{\sqrt{2\pi}\Upsilon} e^{-\frac{\upsilon^2}{2\Upsilon^2}}$ is normalised for $\int_{-\infty}^{\infty} f(\upsilon,\Upsilon)\mathrm{d}\upsilon = 1$, however, we want to consider only positive values of υ, and so we instead consider the integral as one-sided. Therefore, the function $f(\upsilon,\Upsilon) = \sqrt{\frac{2}{\pi\Upsilon^2}}\, e^{-\frac{\upsilon^2}{2\Upsilon^2}}$ is normalised for $\int_0^{\infty} f(\upsilon,\Upsilon)\mathrm{d}\upsilon = 1$. For clarification, we remind readers that υ is limited from 0 to T, and so technically what is given in the above derivation is only an approximation, which is accurate and valid provided that the width of the Gaussian distribution is much less than T. However, as previously stated, this will always be the case within

this work as it represents the realistic experimental scenario in which one would perform this protocol.

As an example, the following is a plot of this Gaussian distribution $f(\upsilon, \Upsilon)$ as a function of υ for width $\Upsilon = 0.10$:

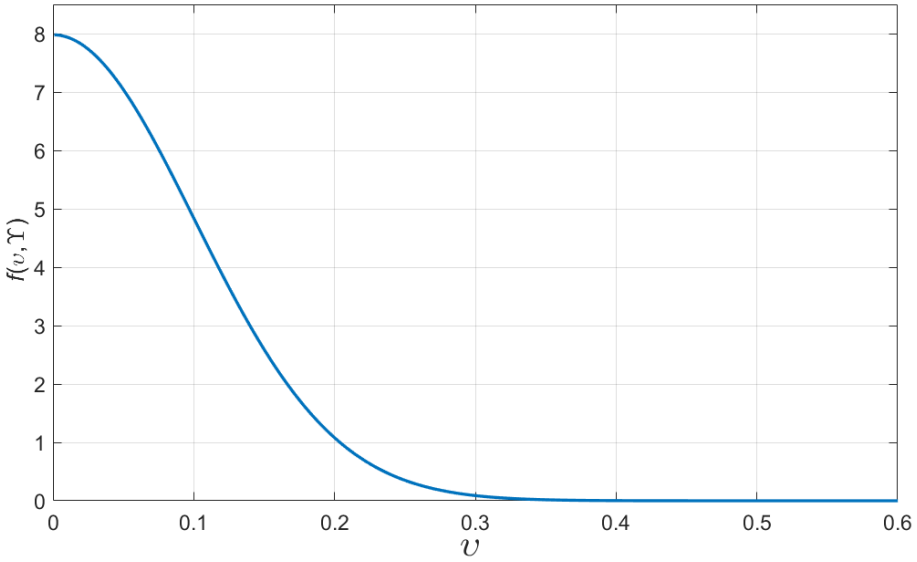

FIGURE 4.1: The Gaussian distribution for the unequal loss function $f(\upsilon, \Upsilon)$, as a function of υ for width (standard deviation) $\Upsilon = 0.10$.

To find the averaged density matrix for some width in the distribution of the loss mismatch υ, which we label as Υ, we must integrate the *non-averaged* density matrix $\rho_{AC}(\upsilon)$ over all positive values of υ. The distribution of the loss mismatch is a one-sided (positive) Gaussian curve (see above Fig. 4.1), and so the integral is of the form:

$$\bar{\rho}_{AC}(\Upsilon) \equiv \int_0^\infty f(\upsilon, \Upsilon)\rho_{AC}(\upsilon)\mathrm{d}\upsilon, \tag{4.13}$$

where, $f(\upsilon, \Upsilon) = \sqrt{\frac{2}{\pi\Upsilon^2}}\, e^{\frac{-\upsilon^2}{2\Upsilon^2}}$ and $\sqrt{\frac{2}{\pi\Upsilon^2}}$ is the normalisation coefficient of the function. Of course, in the limit of $\lim_{\Upsilon\to 0} f(\upsilon) = \upsilon(0)$, thus as we make $\Upsilon \to 0$ we should approach the equal loss results given in Sec. 3.2.2 and Sec. 3.4.2.

After following the general entanglement swapping protocol outlined in Chapter 3, for both the coherent state and cat state cases, and allowing for unequal losses, which we average over using Eq. 4.13, the final states for both protocols are then given as:

$$\bar{\rho}_{AC}^{Coh.}(\Upsilon) = \int_0^\infty f(\upsilon, \Upsilon)\rho_{AC}^{Coh.}(\upsilon)\mathrm{d}\upsilon, \tag{4.14}$$

$$\bar{\rho}_{AC}^{Cat.}(\Upsilon) = \int_0^\infty f(\upsilon, \Upsilon)\rho_{AC}^{Cat}(\upsilon)\mathrm{d}\upsilon, \tag{4.15}$$

where, $\rho_{AC}^{Coh.}(\upsilon)$ and $\rho_{AC}^{Cat}(\upsilon)$ correspond to Eqs. 4.10 and 4.11 respectively.

4.3 Results for Coherent State ES with Averaged Unequal Losses

First we will present and discuss the results for the coherent state unequal loss circumstance. To avoid too much duplication of results (as the unequal loss results differ little, in terms of trends, from the equal loss case), we show the extremal (largest mismatch in loss) results for entanglement negativity and entropy.

The following are plots of entanglement negativity (Fig. 4.2) and linear entropy (Fig. 4.3) as a function of both the coherent state amplitude $|\alpha|$ and the width of the unequal loss distribution Υ, for $T = 1$ (so as to show the extremal case in which we have no loss in mode B and losses in mode D):

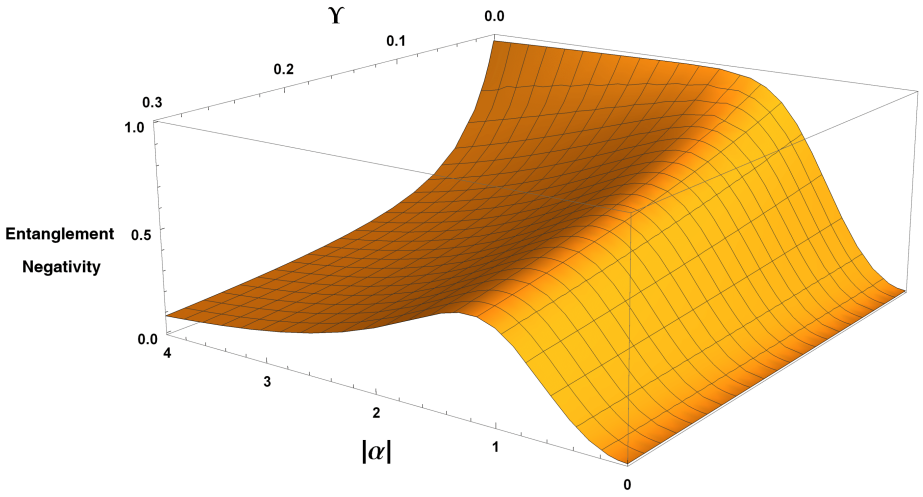

FIGURE 4.2: Entanglement negativity as a function of $|\alpha|$ and Υ for the final state generated via our coherent state entanglement swapping protocol for unequal losses in modes B and D (Eq. 4.14), for $T = 1$.

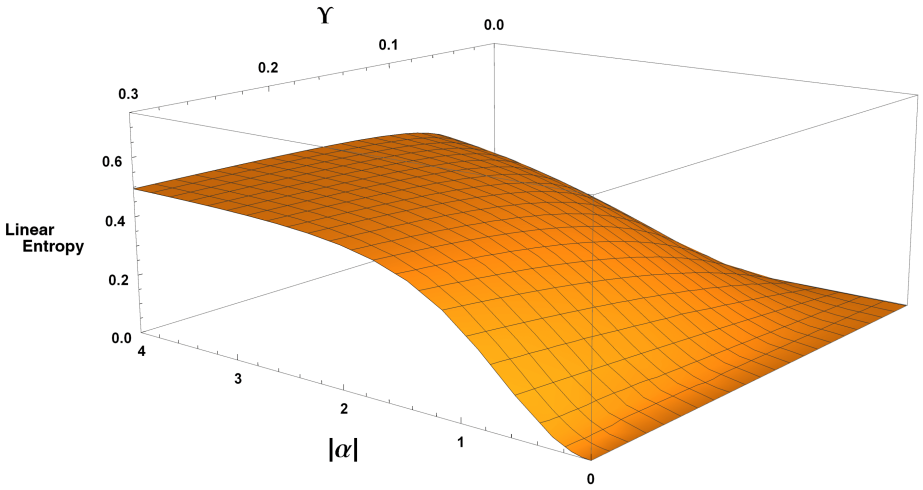

FIGURE 4.3: Linear entropy as a function of $|\alpha|$ and Υ for the final state generated via our coherent state entanglement swapping protocol for unequal losses in modes B and D (Eq. 4.14), for $T = 1$.

As we saw in the coherent state ES equal loss 3D plots for entanglement negativity and linear entropy (Figs. 3.4 and 3.6 respectively), the plots above complement each other perfectly; as the entanglement negativity plot approaches $\mathcal{N}(\rho) = 0$ at large $|\alpha|$ and large Υ, the linear entropy plot approaches $S_L = 0.50$. Recall here that the maximum value for linear entropy, corresponding to a maximally mixed quantum state, is $S_L = 0.75$ for a two qubit state: in this protocol, in the limit of large $|\alpha|$ and high loss ($T << 1$) we are creating a mixture of two Bell states (as discussed at the end of Chapter 3, Subsec. 3.3.4), and so the maximum linear entropy value we expect, in these limits, is $S_L = 0.50$.

The entanglement negativity plot of Fig. 4.2 does not quite reach unity, even at the peak $|\alpha|$ value, it reaches $\mathcal{N}(\rho) \approx 0.99$. The reason for this is that the calculation cannot be evaluated for Υ very close to 0, as the Gaussian function then becomes a delta function (i.e. no longer a continuous spectrum as per Fig. 4.1, but instead is zero everywhere except for $\upsilon = 0$). Intrinsically, we expect that in the limit of $\Upsilon = 0$ we return to the results shown in the equal loss scenario, and so we would indeed then expect the plot of Fig. 4.2 to reach, and plateau at, unity.

We now move onto the plots for fidelity. As previously stated, fidelity is arguably one of the most useful calculations we perform to analyse our final density matrices; the entanglement negativity and linear entropy plots of Figs. 4.2 and 4.3 inform us that, when allowing for small levels of unequal losses between modes B and D (for $\Upsilon \leq 0.10$), we indeed still have an entangled state, however it is necessary for practical purposes to know which entangled state we actually have created.

We first plot fidelity as a function of $|\alpha|$, for no loss ($T = 1$) and larger losses in both modes ($T = 0.95$), and also explore a range of Υ values, to see if we still produce the $|\Phi^+\rangle = \frac{1}{\sqrt{2}}(|00\rangle + |11\rangle)$ Bell state with an acceptable fidelity when allowing for unequal losses in modes B and D:

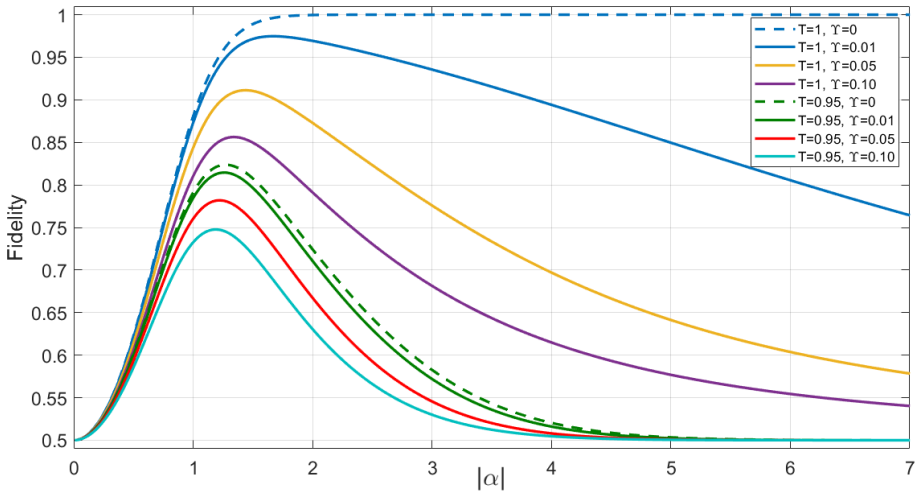

FIGURE 4.4: Fidelity against the $|\Phi^+\rangle = \frac{1}{\sqrt{2}}(|00\rangle + |11\rangle)$ Bell state as a function of $|\alpha|$ for the final state generated via our coherent state entanglement swapping protocol (Eq. 4.14), for varying levels of equal loss, and averaged unequal loss (Υ).

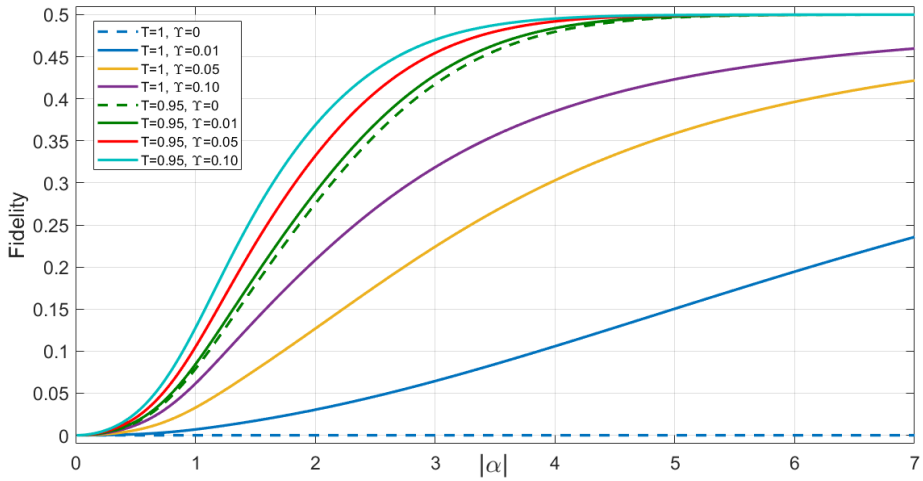

FIGURE 4.5: Fidelity against the $|\Phi^-\rangle = \frac{1}{\sqrt{2}}(|00\rangle - |11\rangle)$ Bell state as a function of $|\alpha|$ for the final state generated via our coherent state entanglement swapping protocol (Eq. 4.14), for varying levels of equal loss, and averaged unequal loss (Υ).

Let us first discuss the plots for $T = 1$. In both fidelity graphs we plot the cases for equal loss as a comparison, and so we can directly see the impact that allowing loss in only one mode (mode D) has on our protocol outcome. Once again these above fidelity plots are very similar to those of the equal loss case, and so it is evident that the loss mismatch variable Υ scales in the same manner as the equal loss value $(1 - T)$. Moreover, introducing unequal loss into our coherent state protocol does not change the actual Bell state we are producing - even in the limit of high loss mismatch ($\Upsilon = 0.10$ and $T = 1$, see Fig. 4.4) there is still a peak $|\alpha|$ value for which we are producing the $|\Phi^+\rangle = \frac{1}{\sqrt{2}}(|00\rangle + |11\rangle)$ Bell state, with a relatively high fidelity of $F = 0.86$.

To further explore fidelity of our final density matrix in this protocol we now plot fidelity against the $|\Phi^+\rangle$ Bell state as a function of $|\alpha|$ and the ensemble averaged unequal loss value Υ, for $T = 1$ (so as to once again explore the extremal case in which we have no loss in mode B and some loss in mode D):

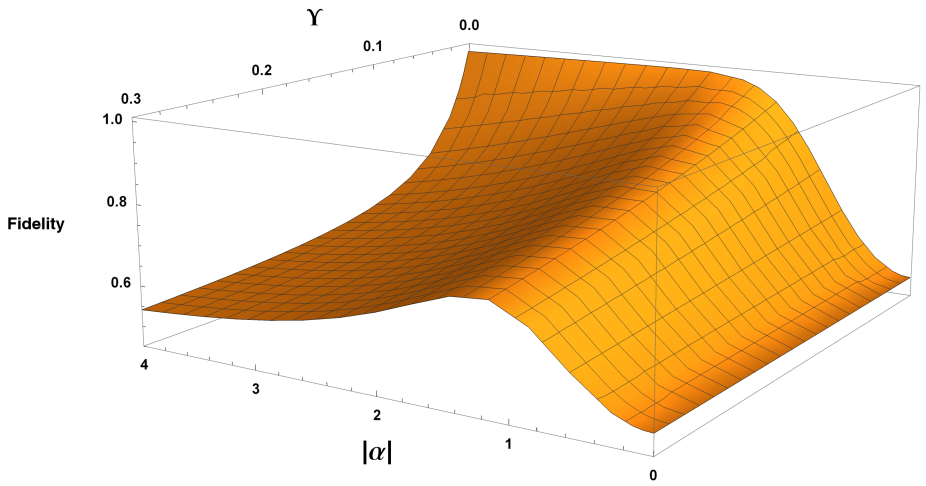

FIGURE 4.6: Fidelity against the $|\Phi^+\rangle = \frac{1}{\sqrt{2}}(|00\rangle + |11\rangle)$ Bell state as a function of $|\alpha|$ and Υ for the final state generated via our coherent state entanglement swapping protocol (Eq. 4.14) for averaged unequal loss value $T = 1$

As we discerned from the 3D plots of entanglement and fidelity for the equal loss coherent state protocol (Figs. 3.4 and 3.7 respectively), the actual shape of the above fidelity plot (Fig. 4.6) is very similar to that of the unequal loss 3D entanglement plot (Fig. 4.2). Of course, the exception is that the plots plateau at different values, but this is absolutely expected, and the unequal loss fidelity plot above tends to $F = 0.50$ at high $|\alpha|$ and $\Upsilon \geq 0.10$. It should be clear by now that we would not desire a loss mismatch value of greater than $\Upsilon = 0.10$, as, for all $|\alpha|$, this level of loss mismatch gives an undesirably low fidelity (see Appendix D, Tab. D.3); indeed the 3D entanglement and entropy plots for the coherent state unequal loss protocol (Figs. 4.2 and 4.3 respectively) agree with this notion.

4.4 Results for Cat State ES with Averaged Unequal Losses

We now present and discuss the results for the cat state unequal loss regime, where, again, to avoid too much duplication of results we show only the extremal (largest mismatch in loss) results for entanglement negativity and entropy.

The following are plots of entanglement negativity (Fig. 4.7) and linear entropy (Fig. 4.8) as a function of both the cat state amplitude $|\alpha|$ and the width of the unequal loss distribution Υ, for $T = 1$ (so as to show the extremal case in which we have no loss in mode B and losses in mode D):

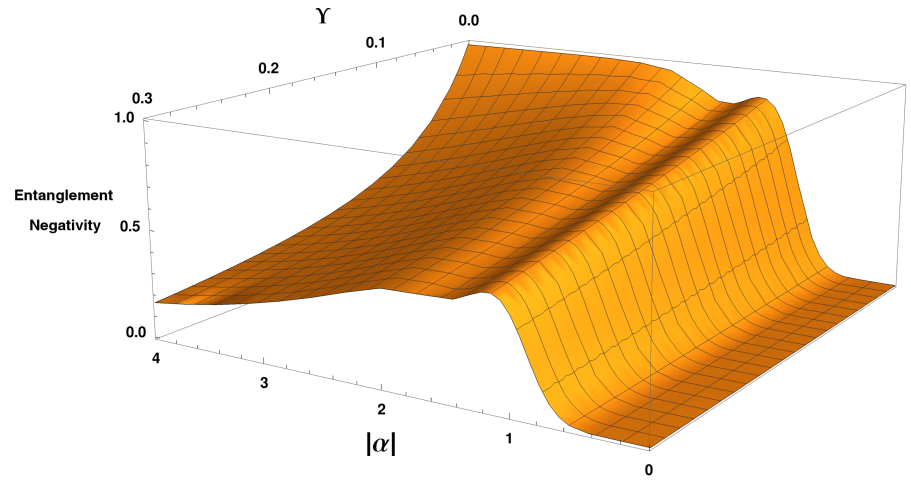

FIGURE 4.7: Entanglement negativity as a function of $|\alpha|$ and Υ for the final state generated via our cat state entanglement swapping protocol for unequal losses in modes B and D (Eq. 4.15), for $T = 1$.

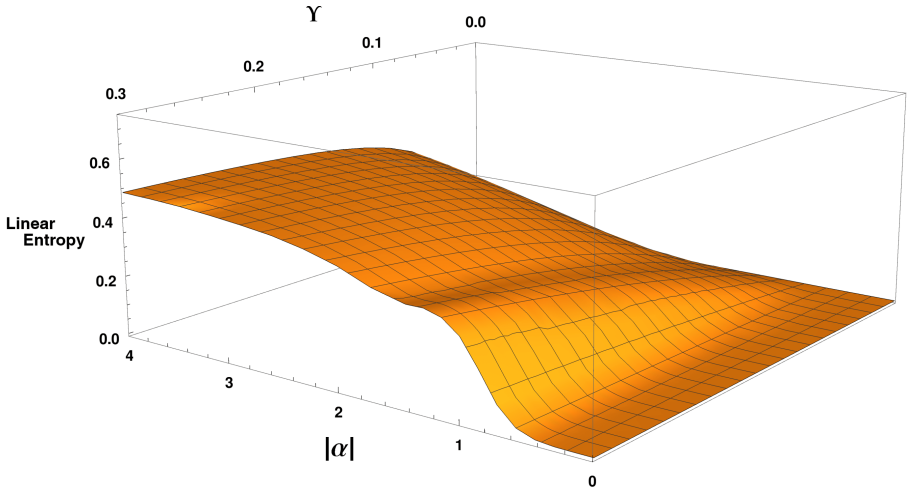

FIGURE 4.8: Linear entropy as a function of $|\alpha|$ and Υ for the final state generated via our cat state entanglement swapping protocol for unequal losses in modes B and D (Eq. 4.15), for $T = 1$.

We can once again directly compare the trends seen in the above entanglement negativity and linear entropy 3D plots, with those of the equal loss case (Figs. 3.16 and 3.18 respectively): there is still the characteristic "double-peak" present in the entanglement negativity plot (Fig. 4.7), and as we saw in the equal loss circumstance, the entanglement negativity drops rapidly as the level of loss increases (parametrised by an increase in Υ for the unequal loss protocol), and as such the linear entropy increases as the level of loss does too. Again, we should note that the linear entropy does not increase to above $S_L = 0.50$ for the levels of loss mismatch we are concerned with, and so we can still discern that we are creating a mixture of two Bell states in the high loss and large $|\alpha|$ limit (see previous discussion of this in Eq. 3.46 and surrounding text).

Let us now move on to fidelity, as a function of the cat state amplitude $|\alpha|$. We first plot fidelity against the $|\Phi^+(\alpha)\rangle = \frac{1}{\sqrt{2}}(|00\rangle\, e^{-\mathrm{i}|\alpha|^2} + |11\rangle\, e^{+\mathrm{i}|\alpha|^2})$ Bell state and

then against the $|\Phi^-(\alpha)\rangle = \frac{1}{\sqrt{2}}(|00\rangle\, e^{-i|\alpha|^2} - |11\rangle\, e^{+i|\alpha|^2})$ Bell state, for $T = 1$ and $T = 0.95$, for various ensemble averaged loss mismatch Υ:

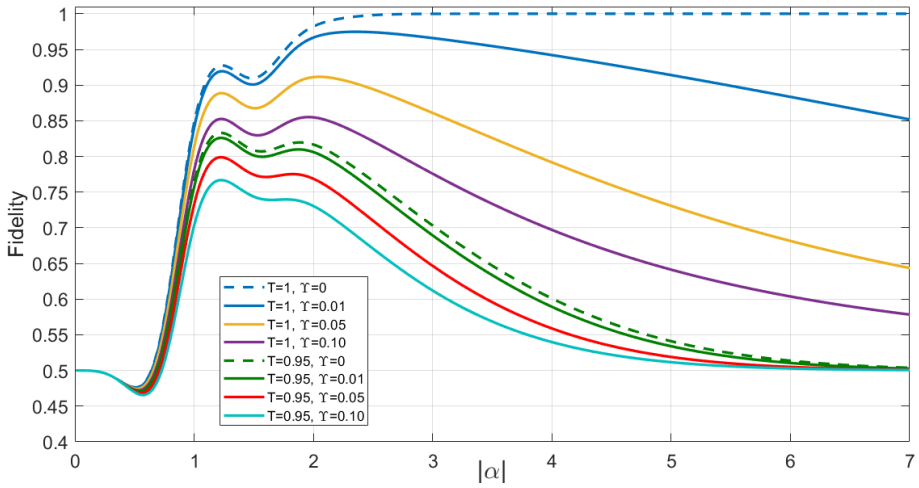

FIGURE 4.9: Fidelity against the $|\Phi^+(\alpha)\rangle = \frac{1}{\sqrt{2}}(|00\rangle\, e^{-i|\alpha|^2} + |11\rangle\, e^{+i|\alpha|^2})$ Bell state as a function of $|\alpha|$ for the final state generated via our coherent state entanglement swapping protocol (Eq. 4.15), for varying levels of equal loss, and averaged unequal loss (Υ).

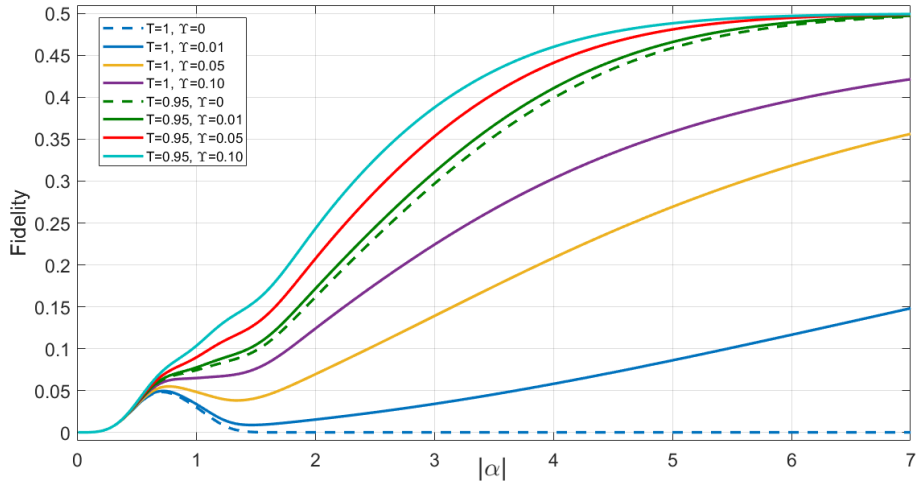

FIGURE 4.10: Fidelity against the $|\Phi^-(\alpha)\rangle = \frac{1}{\sqrt{2}}(|00\rangle\, e^{-i|\alpha|^2} - |11\rangle\, e^{+i|\alpha|^2})$ Bell state as a function of $|\alpha|$ for the final state generated via our coherent state entanglement swapping protocol (Eq. 4.15), for varying levels of equal loss, and averaged unequal loss (Υ).

We can again see the distinctive double-peak present in the cat state fidelity plots (see Fig. 3.7 for the equal loss equivalent), which becomes less pronounced as the overall level of loss increases. As we concluded from the coherent state unequal loss fidelity results (Figs. 4.4 and 4.5), the actual *target* Bell state we are producing is not changed by introducing some level of loss mismatch - however, of course, as Υ increases the fidelity against the $|\Phi^+(\alpha)\rangle$ Bell state decreases (and subsequently the fidelity against the $|\Phi^-(\alpha)\rangle$ Bell state then increases).

To further investigate the fidelity for the unequal loss case, we once again plot fidelity against the $|\Phi^+(\alpha)\rangle$ Bell state in Fig. 4.11, as a function of $|\alpha|$ and Υ, for $T = 1$:

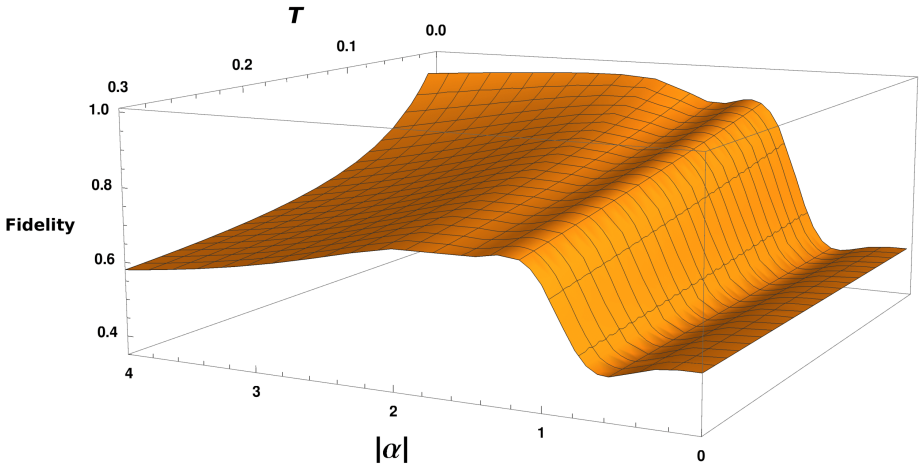

FIGURE 4.11: Fidelity against the $|\Phi^+(\alpha)\rangle = \frac{1}{\sqrt{2}}(|00\rangle\, e^{-i|\alpha|^2} + |11\rangle\, e^{+i|\alpha|^2})$ Bell state as a function of $|\alpha|$ and Υ for the final state generated via our cat state entanglement swapping protocol for unequal losses in modes B and D (Eq. 4.15), for $T = 1$.

As was seen in the coherent state unequal loss 3D fidelity plot (Fig. 4.6), the above cat state unequal loss fidelity plot differs little from the equal loss circumstance of Fig. 3.22. As before we absolutely expect this to be the case, as we have already shown when comparing the entanglement negativity and linear entropy cat state unequal loss plots of Figs. 4.7 and 4.8 with the equal loss equivalents of Figs. 3.16 and 3.18 respectively, increasing Υ impacts the outcome state of our proposed entanglement swapping protocol similarly to simply increasing the overall level of loss (by decreasing T). This exact trend was seen when comparing the coherent state unequal loss and equal loss results, as discussed in the previous section. Once more, we can easily conclude, looking at the above plot, that we do not desire an ensemble averaged loss mismatch value of $\Upsilon > 0.10$, as this gives an unacceptably low fidelity ($F \leq 0.80$) for all $|\alpha|$.

It should be acknowledged here that this limit we have for unequal losses ($\Upsilon \leq 0.10$) to give an acceptable protocol output is a positive result: as previously stated, we refer to Υ as an *ensemble average* for unequal losses, as this variable is intended to reflect the practical perspective of running this protocol as an experiment, in which one would perhaps have a range of optical fibres, each of differing length, for example. Recall here that the length of an optical fibre is directly linked to the photon losses exhibited when using the fibre - longer fibre lengths intrinsically correspond to greater levels of loss. It then follows that an ensemble averaged loss mismatch value of $\Upsilon = 0.10$ represents quite a large range of optical fibre lengths, and so it would be unlikely for an experimentalist to evaluate unequal losses greater than this limit proposed in any case.

4.5 Summary

In this chapter we have introduced and parametrised a variable that allows us to investigate the effect that allowing for a small level of "loss mismatch" between modes B and D has on our protocol outcome, for both the coherent state and cat state ES protocols.

We have then investigated the entanglement negativity, linear entropy and fidelity of the final density matrices (evaluated for unequal losses) and shown that increasing the level of averaged loss mismatch Υ scales similarly to merely increasing the overall loss. Although we must be careful to not assume that these two parameters scale *exactly* the same, as Υ is an averaged value and T is not, however we mean to conclude that introducing this loss mismatch variable Υ does not change any of the patterns and trends already witnessed in the equal loss coherent state ES and cat state ES results. We note that we still witness the peak $|\alpha|$ value in all fidelity plots for the coherent state regime, and two peaks for the cat state case (these results are tabulated in Appendix D, Table D.3 and Appendix D, Table D.4 for the coherent state and cat state results respectively).

Moreover, in this chapter we have shown that even when evaluating relatively large loss mismatches (i.e. $T = 1$ and $\Upsilon = 0.1$) we are still tending to produce the $|\Phi^+\rangle = \frac{1}{\sqrt{2}}(|00\rangle + |11\rangle)$ and $|\Phi^+(\alpha)\rangle = \frac{1}{\sqrt{2}}(|00\rangle\, e^{-\mathrm{i}|\alpha|^2} + |11\rangle\, e^{+\mathrm{i}|\alpha|^2})$ Bell states for the coherent state and cat state protocols respectively. In fact, when allowing for high levels of loss mismatch we are still producing these Bell states with acceptable fidelity. If we now refer to the unequal loss coherent state tabulated fidelity data of Appendix D, Table D.3, we can see that, to produce the $|\Phi^+\rangle = \frac{1}{\sqrt{2}}(|00\rangle + |11\rangle)$ Bell state with high fidelity of $F \geq 0.90$, we can tolerate a fairly high loss mismatch of $\Upsilon \leq 0.05$ for no loss in mode B (i.e. $T = 1$). However, when allowing for any level of loss in mode B (i.e. $T < 1$) we can then only accept an ensemble averaged loss mismatch of $\Upsilon = 0.01$ for $T \geq 0.98$. If we instead aim for a slightly lower, but still modest, fidelity of $F = 0.80$ we can see from this table that we can accept a much broader range of Υ and T values.

Let us now look to the tabulated unequal loss fidelity data for the cat state protocol, of Appendix D, Table D.4. We can again conclude, from looking at the fidelity values at the two peak $|\alpha|$ regions, that to produce the $|\Phi^+(\alpha)\rangle = \frac{1}{\sqrt{2}}(|00\rangle\, e^{-\mathrm{i}|\alpha|^2} + |11\rangle\, e^{+\mathrm{i}|\alpha|^2})$ Bell state with high fidelity of $F \geq 0.90$, we can only accept Υ values of $\Upsilon \leq 0.05$ and $T = 1$, or $\Upsilon \leq 0.01$ and $T \geq 0.98$. However, if we instead aim for $F \geq 0.80$, then we can instead accept almost all combinations of T and Υ, in the regions of $T \geq 0.95$ and $\Upsilon \leq 0.10$ (with a few exceptions). This, in fact, is the same result we can conclude from the coherent state tabulated data of Appendix D, Table D.3, and so we can summarise that both protocols are relatively resilient to unequal photon losses in the propagating modes B and D.

We should note here that we have not plotted any quantum state tomography (QST) plots for the final density matrices in this chapter, as we did in the equal loss

results. This is due to the fact that, as concluded throughout all results presented in this chapter, introducing this level of loss mismatch does not change our results in any particularly *interesting* way, and so the QST plots will be very similar to the equal loss cases. We return to plotting QSTs in the next chapter, in which we investigate non-ideal and imperfect homodyne detection, as the QSTs are dramatically changed in these circumstances.

Finally, it is worth once more highlighting the importance of the results presented in this chapter. As previously discussed, introducing a loss mismatch between the lossy modes B and D does not drastically impact our output entangled states any more than simply increasing the overall loss. Although this is not especially intriguing, it is nonetheless just as important, as we are able to conclude that if one were to experimentally perform our proposed protocols then one could allow for a respectable level of "unknown" loss mismatch, as parametrised by Υ, by referring to our tabulated data, as discussed above. This means that one would not have to be overly cautious when selecting lengths of optical fibres, for example, when constructing this experiment, as the fibres would not have to exhibit exactly identical photon loss levels.

In the next chapter we investigate more thoroughly the homodyne detection we theoretically perform on mode D of our protocol, by considering *non-ideal* homodyne outcomes, and *imperfect* homodyne measurements, and evaluate entanglement negativity, linear entropy and fidelity for the resultant density matrices of the coherent state and cat state entanglement swapping protocols.

Chapter 5

Imperfect and Non-Ideal Homodyne Measurements

Throughout this thesis so far, we have analysed homodyne detection of mode D as being *perfect*; that is to say that we assume that the homodyne measurement outcome x_θ is the most ideal case, and that we know it with absolute certainty.

In reality, homodyne detection is a measurement of the continuous quadrature variable (which we denote as x_θ), specified by the phase angle θ. Hence, there is no way of guaranteeing a particular quadrature outcome for a *perfect-case* homodyne measurement. It therefore follows that to establish homodyne *imperfections* we need to model the more realistic circumstance in which the quadrature measurement outcome is instead a resolution bandwidth (which we label Δx) around the expected measurement outcome. As such, consider this as accounting for a given amount of uncertainty within the detection outcome.

Furthermore, to investigate what we denote as *non-ideal* homodyne measurement outcomes, we will assume that our outcome is no longer exactly where it is expected, and is instead shifted along the relevant quadrature by a given value (which we denote as ϵ).

In this chapter, we will first explore non-ideal homodyne measurements, for the equal loss (in modes B and D) coherent state and cat state protocols, to establish a limit on how far we can tolerate the homodyne measurement outcome to be shifted away from the ideal outcome. We will then move on to discuss homodyne imperfections as a bandwidth about the most ideal outcome for both protocols, before combining non-ideal and imperfect homodyne detection to investigate a bandwidth about a non-ideal measurement outcome.

5.1 Non-Ideal Homodyne Detection

Thus far, when looking into our entanglement swapping protocol, we have assumed that we have the most ideal homodyne measurement outcome, which is the maximum point of the peaks of the probability distributions (see Figs. 5.1 and 5.2). Hence, we fixed $x_{\frac{\pi}{2}} = 0$ for coherent state entanglement swapping, and $x_{\frac{\pi}{4}} = \pm\sqrt{T}|\alpha|$ for the cat state protocol, when including equal losses in modes B and D.

Therefore, to account for non-ideal homodyne measurement outcomes we parametrise this with ϵ as follows:

$$\begin{aligned} &\text{For the coherent state protocol: } x_{\frac{\pi}{2}} = 0 \pm \epsilon = \pm\epsilon \\ &\text{For the cat state protocol: } x_{\frac{\pi}{4}} = \pm\sqrt{T}\,|\alpha| \pm \epsilon \quad \text{or} \quad x_{\frac{\pi}{4}} = \pm\sqrt{T}\,|\alpha| \mp \epsilon \end{aligned} \tag{5.1}$$

Note that we do not include phases in the parametrisation of ϵ (i.e. for the coherent state case we only want to use $x_{\frac{\pi}{2}} = \pm\epsilon$ as opposed to $x_{\frac{\pi}{2}} = \pm i\epsilon$) as the phases have been accounted for in the homodyne projection, hence x_θ is purely a real number.

These non-idealities can be shown diagrammatically in terms of position ($\hat{x}$) and momentum ($\hat{p}$) phase space, as follows:

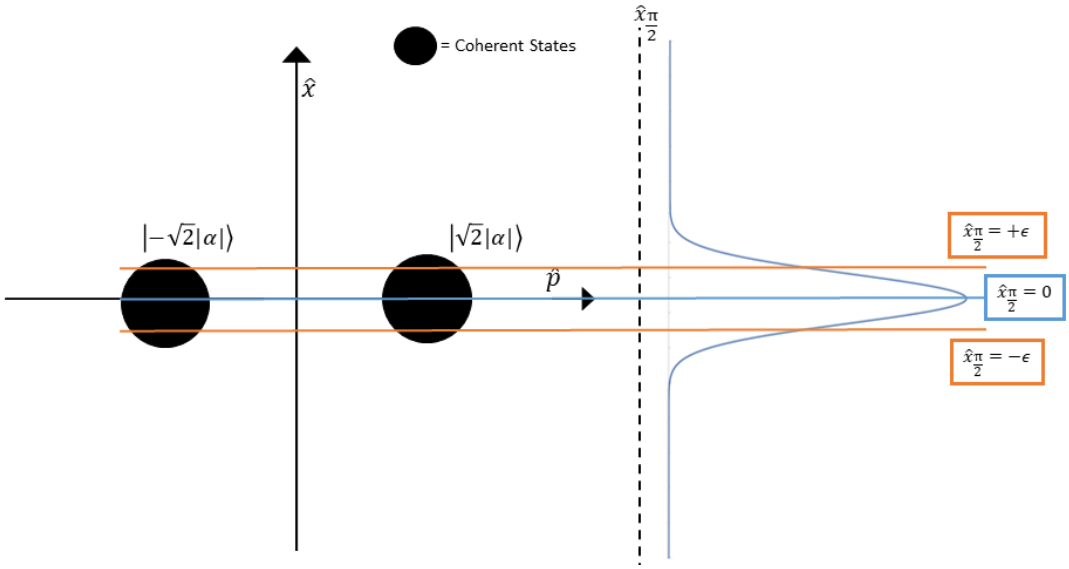

FIGURE 5.1: Diagram to present the phase space in which the non-ideal homodyne measurement outcomes are assessed as, for the coherent state entanglement swapping protocol.

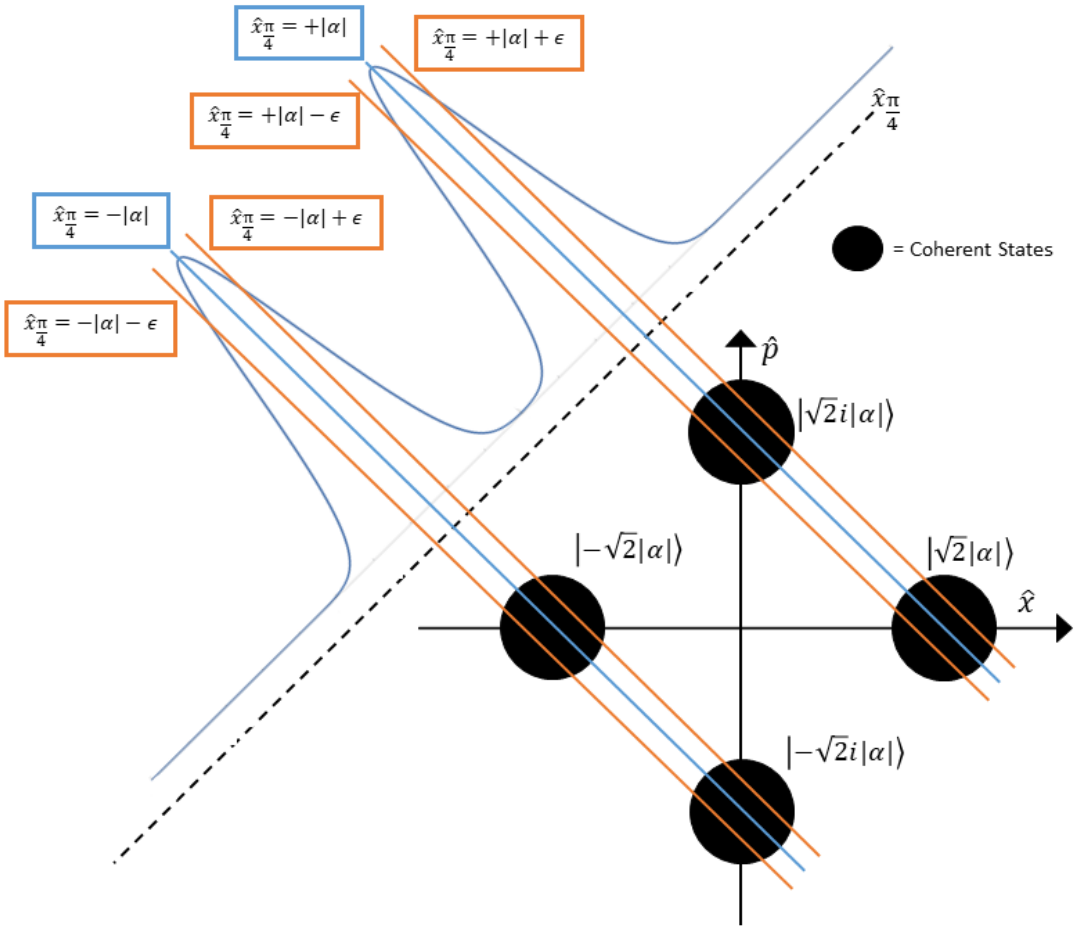

FIGURE 5.2: Diagram to present the phase space in which the non-ideal homodyne measurement outcomes are assessed as, for the cat state entanglement swapping protocol.

In Figs. 5.1 and 5.2 it is evident that a shift in the expected homodyne outcome is easily parametrised by ϵ. Here, we consider ϵ to be a positive (real) number, where $\epsilon = 0$ should inherently return us to our ideal homodyne outcome case once again.

5.2 Non-Ideal Homodyne for Coherent State ES

To form our final density matrix, describing the outcome of the coherent state ES protocol, when allowing for equal losses in modes B and D, and for non-ideal homodyne outcomes $x_{\frac{\pi}{2}} = 0 \pm \epsilon$, we follow the same method outlined in Chapter 3, Sec. 3.2.2. Therefore, if we then set the homodyne measurement outcome to contain non-idealities, we replace $x_{\frac{\pi}{2}}$ in Eq. 3.33 (the state immediately after performing the

homodyne measurement) with the non-ideal outcome, thus giving:

$$\begin{aligned}|\Psi_{\epsilon}^{Coh.}\rangle_{A\varepsilon_B C\varepsilon_D} = \mathcal{N}\Big[& e^{\pm 2\sqrt{2}\,\mathrm{i}\sqrt{T}\,|\alpha|\epsilon}\,|00\rangle_{AC}\;|\sqrt{1-T}\,|\alpha|\rangle_{\varepsilon_B}\;|\sqrt{1-T}\,|\alpha|\rangle_{\varepsilon_D} \\ & + e^{\pm 2\sqrt{2}\,\mathrm{i}\sqrt{T}\,|\alpha|\epsilon}\,|11\rangle_{AC}\;|-\sqrt{1-T}\,|\alpha|\rangle_{\varepsilon_B}\;|-\sqrt{1-T}\,|\alpha|\rangle_{\varepsilon_D} \\ & e^{-T|\alpha|^2}\Big(\,|01\rangle_{AC}\;|\sqrt{1-T}\,|\alpha|\rangle_{\varepsilon_B}\;|-\sqrt{1-T}\,|\alpha|\rangle_{\varepsilon_D} \\ & + |10\rangle_{AC}\;|-\sqrt{1-T}\,|\alpha|\rangle_{\varepsilon_B}\;|\sqrt{1-T}\,|\alpha|\rangle_{\varepsilon_D}\,\Big)\Big], \end{aligned} \tag{5.2}$$

in which the subscript ϵ in the quantum state $|\Psi_{\epsilon}^{Coh.}\rangle_{A\varepsilon_B C\varepsilon_D}$ denotes that this state is evaluated for homodyne non-idealities. We then trace out the lossy modes ε_B and ε_D using the coherent state to trace (as per Subsec. 3.2.4), which gives us our final two qubit density matrix of:

$$\rho_{AC}^{Coh.}(\epsilon) = \mathrm{Tr}_{\varepsilon_B,\varepsilon_D}\left[\,|\Psi_{\epsilon}^{Coh.}\rangle_{A\varepsilon_B C\varepsilon_D}\;\langle\Psi_{\epsilon}^{Coh.}|\right]. \tag{5.3}$$

Using this density matrix we may now investigate entanglement negativity, linear entropy and fidelity of the final state produced through the coherent state protocol, when allowing for non-ideal homodyne measurement outcomes.

5.2.1 Entanglement Negativity and Linear Entropy

Before discussing the fidelity results for this density matrix, we should first briefly discuss entanglement negativity and linear entropy. In fact, increasing ϵ has absolutely no impact on entanglement negativity and linear entropy, for all α and T. This may seem surprising at first, however, if we look at Eq. 5.2 and set $T = 1$ (for simplicity) then the resultant quantum state is:

$$\begin{aligned}&|\Psi_{\epsilon}^{Coh.}\rangle_{A\varepsilon_B C\varepsilon_D} = \\ &\mathcal{N}\Big[e^{\pm 2\sqrt{2}\,\mathrm{i}|\alpha|\epsilon}\,|00\rangle_{AC} + e^{\pm 2\sqrt{2}\,\mathrm{i}|\alpha|\epsilon}\,|11\rangle_{AC} + e^{-|\alpha|^2}\Big(\,|01\rangle_{AC} + |10\rangle_{AC}\,\Big)\Big].\end{aligned} \tag{5.4}$$

Hence, increasing the value of ϵ does nothing more than simply changing the value of the phase of the $|00\rangle_{AC}$ and $|11\rangle_{AC}$ terms, and as such does not change the amplitudes of the off-diagonal $|00\rangle_{AC}\langle 11|$ and $|11\rangle_{AC}\langle 00|$ terms. It then follows that if the amplitudes of these off-diagonal terms remain unaffected, then the resultant quantum state will still be maximally entangled for all ϵ, and so the linear entropy will be zero for all ϵ in the no loss regime. However, as we have stated, increasing the value of ϵ does affect the phases of these off-diagonal terms, and so we must critically investigate the fidelity against the $|\Phi^+\rangle = \frac{1}{\sqrt{2}}(|00\rangle + |11\rangle)$ Bell state, to ensure that the phases present in our final density matrix do not impact the fidelity to intolerable levels.

5.2.2 Fidelity

To begin with, we here show fidelity of the above density matrix (Eq. 5.3), against the $|\Phi^+\rangle$ Bell state, but only show fidelity values for $F \geq 0.80$, so as to establish a window of accepted values for ϵ, in which we can guarantee to produce a Bell state of acceptable fidelity. We plot fidelity as a function of $|\alpha|$ and non-ideal homodyne outcome ϵ, for $T = 1$, $T = 0.99$ and $T = 0.95$ (Figs. 5.3, 5.4 and 5.5 respectively):

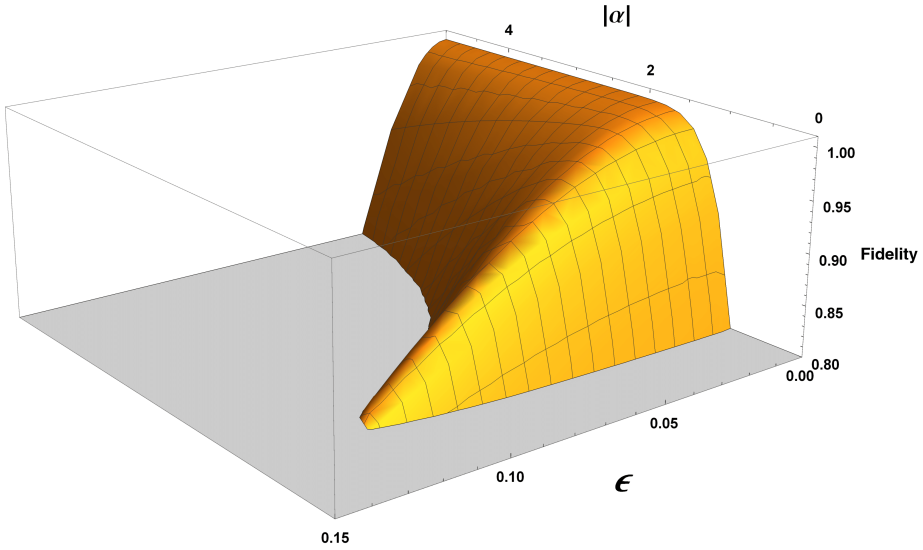

FIGURE 5.3: Fidelity against the $|\Phi^+\rangle = \frac{1}{\sqrt{2}}(|00\rangle + |11\rangle)$ Bell state as a function of $|\alpha|$ for the final state generated via our coherent state entanglement swapping protocol (Eq. 5.3), for no loss ($T = 1$), and varying non-ideal homodyne measurement outcome $x_{\frac{\pi}{2}} = \pm\epsilon$.

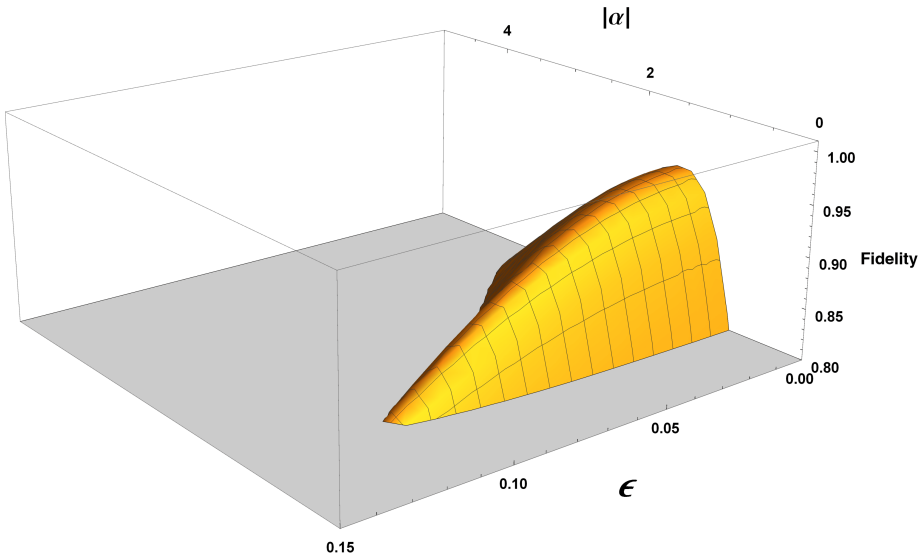

FIGURE 5.4: Fidelity against the $|\Phi^+\rangle = \frac{1}{\sqrt{2}}(|00\rangle + |11\rangle)$ Bell state as a function of $|\alpha|$ for the final state generated via our coherent state entanglement swapping protocol (Eq. 5.3), for equal losses of $T = 0.99$, and varying non-ideal homodyne measurement outcome $x_{\frac{\pi}{2}} = \pm\epsilon$.

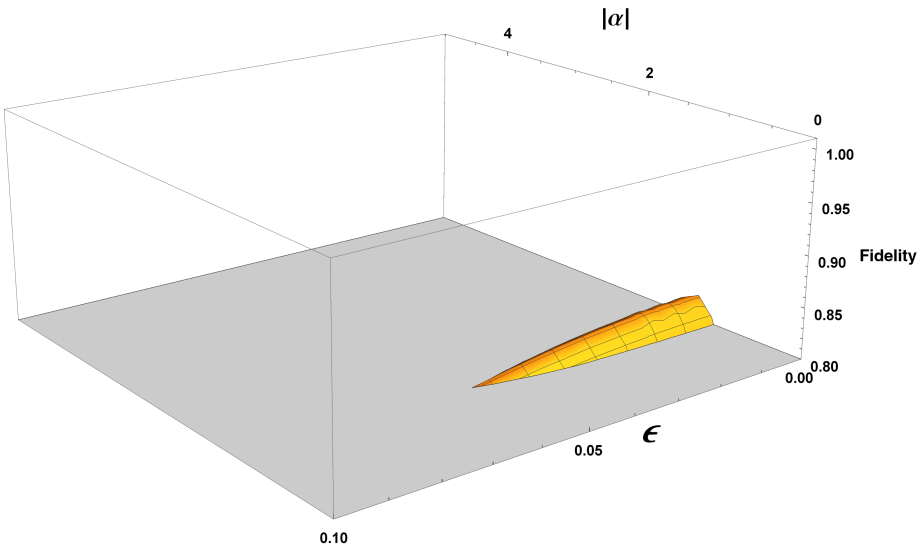

FIGURE 5.5: Fidelity against the $|\Phi^+\rangle = \frac{1}{\sqrt{2}}(|00\rangle + |11\rangle)$ Bell state as a function of $|\alpha|$ for the final state generated via our coherent state entanglement swapping protocol (Eq. 5.3), for equal losses of $T = 0.95$, and varying non-ideal homodyne measurement outcome $x_{\frac{\pi}{2}} = \pm\epsilon$.

Regarding these 3D fidelity plots, if we wish to produce the $|\Phi^+\rangle$ Bell state with a fidelity of $F \geq 0.80$, it is evident that for $T \geq 0.95$ we can only tolerate a modest non-ideal homodyne outcome shift of $\pm\epsilon \leq 0.05$, however, if we allow smaller levels of loss such that $T \geq 0.99$, then we can allow $\pm\epsilon \leq 0.12$. We can see in the lossy plots of Figs. 5.4 and 5.5 that there is still an optimum $|\alpha|$ value in which the fidelity reaches a maximum, as we saw in the equal loss and unequal loss results in the previous chapters.

To further investigate how allowing for non-ideal homodyne outcomes affects the final state produced by the coherent state protocol, we plot the fidelity against both the $|\Phi^+\rangle$ and the orthogonal $|\Phi^-\rangle$ Bell states, as a function of $|\alpha|$, for no loss and with varying ϵ:

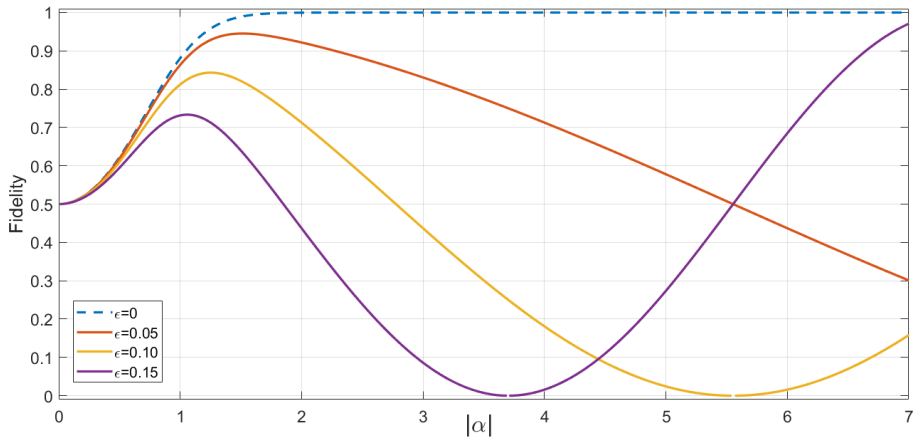

FIGURE 5.6: Fidelity against the $|\Phi^+\rangle = \frac{1}{\sqrt{2}}(|00\rangle + |11\rangle)$ Bell state as a function of $|\alpha|$ for the final state generated via our coherent state entanglement swapping protocol (Eq. 5.3), for no loss ($T = 1$), and varying non-ideal homodyne measurement outcome $x_{\frac{\pi}{2}} = \pm\epsilon$.

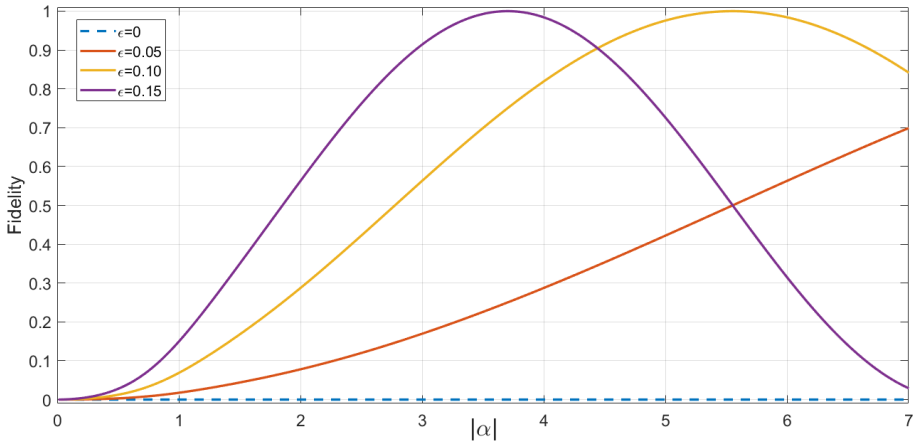

FIGURE 5.7: Fidelity against the $|\Phi^-\rangle = \frac{1}{\sqrt{2}}(|00\rangle - |11\rangle)$ Bell state as a function of $|\alpha|$ for the final state generated via our coherent state entanglement swapping protocol (Eq. 5.3), for no loss ($T = 1$), and varying non-ideal homodyne measurement outcome $x_{\frac{\pi}{2}} = \pm\epsilon$.

Evidently, as ϵ increases the above plots becomes more oscillatory: if we look at the no loss state, given by Eq. 5.4, it is clear that for non-zero ϵ we are introducing a phase into the $|00\rangle_{AC}$ and $|11\rangle_{AC}$ terms, hence plotting the fidelity of this state against a Bell state that does *not* contain a phase (such as the $|\Phi^+\rangle$ Bell state) would result in an oscillatory graph, as we indeed see in Figs. 5.6 and 5.7. However, we remind the reader here that the purpose of this investigation is to establish how non-ideal the homodyne measurement outcome can be, whilst still giving us the Bell state we produce in the ideal regime, and so even though we are now producing a Bell state that contains a phase, we nonetheless should still compare the fidelity with respect to the $|\Phi^+\rangle = \frac{1}{\sqrt{2}}(|00\rangle + |11\rangle)$ Bell state.

We now consider the circumstance in which we have higher levels of loss, for $T = 0.95$ with homodyne non-idealities, and plot fidelity against the $|\Phi^+\rangle$ Bell state (Fig. 5.8) and the orthogonal $|\Phi^-\rangle$ Bell state (Fig. 5.9), as a function of the coherent state amplitude $|\alpha|$:

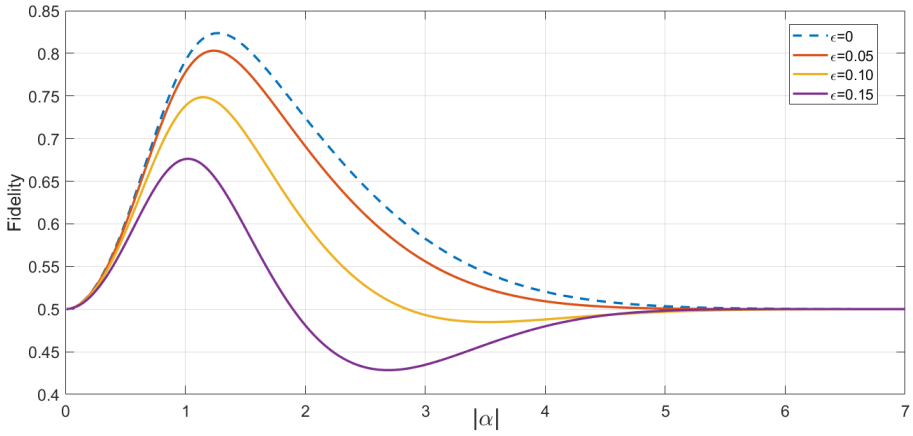

FIGURE 5.8: Fidelity against the $|\Phi^+\rangle = \frac{1}{\sqrt{2}}(|00\rangle + |11\rangle)$ Bell state as a function of $|\alpha|$ for the final state generated via our coherent state entanglement swapping protocol (Eq. 5.3), for equal losses of $T = 0.95$, and varying non-ideal homodyne measurement outcome $x_{\frac{\pi}{2}} = \pm\epsilon$.

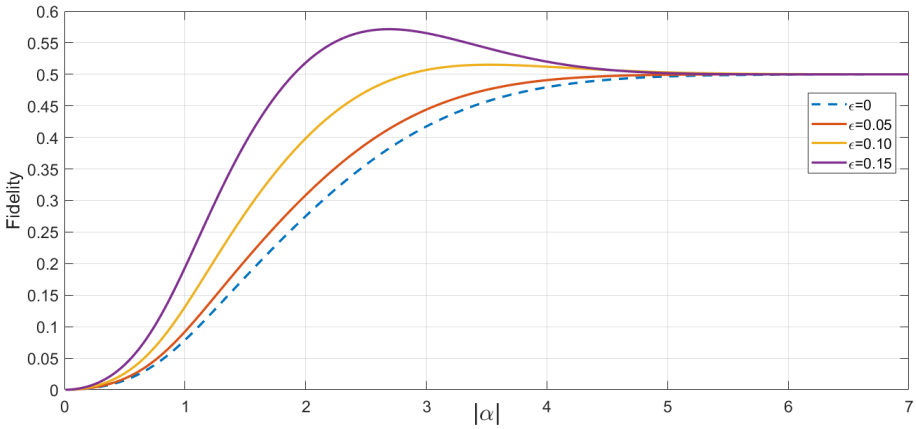

FIGURE 5.9: Fidelity against the $|\Phi^-\rangle = \frac{1}{\sqrt{2}}(|00\rangle - |11\rangle)$ Bell state as a function of $|\alpha|$ for the final state generated via our coherent state entanglement swapping protocol (Eq. 5.3), for equal losses of $T = 0.95$, and varying non-ideal homodyne measurement outcome $x_{\frac{\pi}{2}} = \pm\epsilon$.

Clearly, we no longer see the oscillatory behaviour in the above plots, as we did in the no loss ones (Figs. 5.6 and 5.7). Analytically, this is clear if we consider the final state that is being investigated, Eq. 5.2: once the lossy modes ε_B and ε_D have been numerically traced out, we introduce dampening exponents of $\exp\left[-4(1-T)|\alpha|^2\right]$ into the off-diagonal $|00\rangle_{AC}\langle 11|$ and $|11\rangle_{AC}\langle 00|$ terms (see Eq. 3.45), and so for non-unity T these dampening exponents will cause the amplitudes of these off-diagonal terms to decrease as a function of $|\alpha|$. This dampening exponent affects the final quantum state more strongly than the oscillatory phase term, which contains ϵ, and so this explains why we no longer witness this oscillatory behaviour in the above plots, for $T = 0.95$, and instead we now see a sharp peak in Fig. 5.6. Although we see this sharp peak here, we should stipulate that at this level of loss we evidently cannot tolerate a big shift in the homodyne measurement outcome, as the fidelity drops below $F = 0.80$ for $T = 0.95$ and $\epsilon \geq 0.05$.

5.3 Non-Ideal Homodyne for Cat State ES

We now move on the cat state protocol, and show in this section that we still tend to the $|\Phi^+(\alpha)\rangle = \frac{1}{\sqrt{2}}(\,|00\rangle\, e^{-\mathrm{i}|\alpha|^2} + |11\rangle\, e^{+\mathrm{i}|\alpha|^2})$ Bell state, even when allowing for small levels of loss and homodyne non-idealities.

To form our final density matrix for the cat state protocol, when allowing for equal losses in modes B and D, and for non-ideal homodyne outcomes $x_{\frac{\pi}{4}} = \pm\sqrt{T}\,|\alpha| \pm \epsilon$, we follow the same method outlined in Chapter 3, Sec. 3.4.2. Therefore, if we then set the homodyne measurement outcome to contain non-idealities, we replace $x_{\frac{\pi}{4}}$ in Eq. 3.66 (the state immediately after performing the homodyne measurement) with the non-ideal outcome, giving:

$$
\begin{aligned}
|\Psi^{Cat}_{\pm\epsilon}\rangle_{AC} &= \mathcal{N} \\
&\times\Big[\,|00\rangle_{AC}\Big(\exp\Big[(1-\mathrm{i})T|\alpha|^2 + (1-\mathrm{i})2\sqrt{T}\,|\alpha|\epsilon\Big]\,|\gamma|\alpha|\rangle_{\varepsilon_B}\,|\gamma|\alpha|\rangle_{\varepsilon_D} \\
&\quad + \exp\Big[-(3-3\mathrm{i})T|\alpha|^2 - (1-\mathrm{i})2\sqrt{T}\,|\alpha|\epsilon\Big]\,|-\gamma|\alpha|\rangle_{\varepsilon_B}\,|-\gamma|\alpha|\rangle_{\varepsilon_D} \\
&\quad + e^{-T|\alpha|^2}\Big(\,|\gamma|\alpha|\rangle_{\varepsilon_B}\,|-\gamma|\alpha|\rangle_{\varepsilon_D} + \,|-\gamma|\alpha|\rangle_{\varepsilon_B}\,|\gamma|\alpha|\rangle_{\varepsilon_D}\Big)\Big) \\
&+ e^{\frac{-T|\alpha|^2}{2}}\,|01\rangle_{AC}\Big(\exp\Big[2\sqrt{T}\,|\alpha|\epsilon + T|\alpha|^2\Big]\,|\gamma|\alpha|\rangle_{\varepsilon_B}\,|\gamma\mathrm{i}|\alpha|\rangle_{\varepsilon_D} \\
&\quad + \exp\Big[-2T\mathrm{i}|\alpha|^2 - 2\sqrt{T}\,\mathrm{i}|\alpha|\epsilon\Big]\,|\gamma|\alpha|\rangle_{\varepsilon_B}\,|-\gamma\mathrm{i}|\alpha|\rangle_{\varepsilon_D} \\
&\quad + \exp\Big[2\sqrt{T}\,\mathrm{i}|\alpha|\epsilon + 2T\mathrm{i}|\alpha|^2\Big]\,|-\gamma|\alpha|\rangle_{\varepsilon_B}\,|\gamma\mathrm{i}|\alpha|\rangle_{\varepsilon_D} \\
&\quad + \exp\Big[-2\sqrt{T}\,|\alpha|\epsilon - 3T|\alpha|^2\Big]\,|-\gamma|\alpha|\rangle_{\varepsilon_B}\,|-\gamma\mathrm{i}|\alpha|\rangle_{\varepsilon_D}\Big) \\
&+ e^{\frac{-T|\alpha|^2}{2}}\,|10\rangle_{AC}\Big(\exp\Big[2\sqrt{T}\,|\alpha|\epsilon + T|\alpha|^2\Big]\,|\gamma\mathrm{i}|\alpha|\rangle_{\varepsilon_B}\,|\gamma|\alpha|\rangle_{\varepsilon_D} \\
&\quad + \exp\Big[2\sqrt{T}\,\mathrm{i}|\alpha|\epsilon + 2T\mathrm{i}|\alpha|^2\Big]\,|\gamma\mathrm{i}|\alpha|\rangle_{\varepsilon_B}\,|-\gamma|\alpha|\rangle_{\varepsilon_D} \\
&\quad + \exp\Big[-2T\mathrm{i}|\alpha|^2 - 2\sqrt{T}\,\mathrm{i}|\alpha|\epsilon\Big]\,|-\gamma\mathrm{i}|\alpha|\rangle_{\varepsilon_B}\,|\gamma|\alpha|\rangle_{\varepsilon_D} \\
&\quad + \exp\Big[-2\sqrt{T}\,|\alpha|\epsilon - 3T|\alpha|^2\Big]\,|-\gamma\mathrm{i}|\alpha|\rangle_{\varepsilon_B}\,|-\gamma|\alpha|\rangle_{\varepsilon_D}\Big) \\
&+ |11\rangle_{AC}\Big(\exp\Big[(\mathrm{i}+1)T|\alpha|^2 + (\mathrm{i}+1)2\sqrt{T}\,|\alpha|\epsilon\Big]\,|\gamma\mathrm{i}|\alpha|\rangle_{\varepsilon_B}\,|\gamma\mathrm{i}|\alpha|\rangle_{\varepsilon_D} \\
&\quad + \exp\Big[-(3+3\mathrm{i})T|\alpha|^2 - (1+\mathrm{i})2\sqrt{T}\,|\alpha|\epsilon\Big]\,|-\gamma\mathrm{i}|\alpha|\rangle_{\varepsilon_B}\,|-\gamma\mathrm{i}|\alpha|\rangle_{\varepsilon_D} \\
&\quad + e^{-T|\alpha|^2}\Big(\,|\gamma\mathrm{i}|\alpha|\rangle_{\varepsilon_B}\,|-\gamma\mathrm{i}|\alpha|\rangle_{\varepsilon_D} + \,|-\gamma\mathrm{i}|\alpha|\rangle_{\varepsilon_B}\,|\gamma\mathrm{i}|\alpha|\rangle_{\varepsilon_D}\Big)\Big)\Big], \qquad (5.5)
\end{aligned}
$$

in which the above quantum state is for the homodyne non-ideal outcome $x_{\frac{\pi}{4}} = +\sqrt{T}\,|\alpha| + \epsilon$, however identical results for entanglement negativity, linear entropy and fidelity are achieved when setting the outcome to $x_{\frac{\pi}{4}} = -\sqrt{T}\,|\alpha| - \epsilon$, as we saw in the ideal homodyne equal loss case in Eq. 3.67. Note that we use the notation of a subscript $\pm\epsilon$ in the quantum state $|\Psi^{Cat}_{\pm\epsilon}\rangle_{AC}$ to indicate that this state is evaluated for the non-ideal homodyne outcome of $x_{\frac{\pi}{4}} = \pm\sqrt{T}\,|\alpha| \pm \epsilon$.

Recall that, when considering homodyne measurement non-idealities, there are now four possible outcomes for the cat state lossy protocol (see Fig. 5.2):

$x_{\frac{\pi}{4}} = \pm\sqrt{T}\,|\alpha| \pm \epsilon$ and $x_{\frac{\pi}{4}} = \pm\sqrt{T}\,|\alpha| \mp \epsilon$, in which the outcomes $x_{\frac{\pi}{4}} = +\sqrt{T}\,|\alpha| + \epsilon$ and $x_{\frac{\pi}{4}} = -\sqrt{T}\,|\alpha| - \epsilon$ give the same resultant final state, as do the $x_{\frac{\pi}{4}} = +\sqrt{T}\,|\alpha| - \epsilon$ and $x_{\frac{\pi}{4}} = -\sqrt{T}\,|\alpha| + \epsilon$ outcomes.

Looking at the phase space diagram of Fig. 5.2 it is evident why this is the case; this phase space diagram is symmetric about the $x_{\frac{3\pi}{4}}$ axis, and so the two "outermost" shifted outcomes, $x_{\frac{\pi}{4}} = +\sqrt{T}\,|\alpha| + \epsilon$ and $x_{\frac{\pi}{4}} = -\sqrt{T}\,|\alpha| - \epsilon$, will give the same entangled output, as will the two "innermost" outcomes, $x_{\frac{\pi}{4}} = +\sqrt{T}\,|\alpha| - \epsilon$ and $x_{\frac{\pi}{4}} = -\sqrt{T}\,|\alpha| + \epsilon$. It will be shown in this section that we in fact desire the outcome to be $x_{\frac{\pi}{4}} = \pm\sqrt{T}\,|\alpha| \pm \epsilon$ as opposed to $x_{\frac{\pi}{4}} = \pm\sqrt{T}\,|\alpha| \mp \epsilon$, however this will be elucidated analytically (Subsec. 5.3.3) once the results have been presented.

The above state (Eq. 5.5) was evaluated for homodyne outcomes $x_{\frac{\pi}{4}} = \pm\sqrt{T}\,|\alpha| \pm \epsilon$, and so, using the same method to derive Eq. 5.5, we can evaluate this instead for the $x_{\frac{\pi}{4}} = \pm\sqrt{T}\,|\alpha| \mp \epsilon$ outcome, which gives:

$$
\begin{aligned}
|\Psi^{Cat}_{\mp\epsilon}\rangle_{AC} &= \mathcal{N} \\
&\times\Big[\,|00\rangle_{AC}\Big(\exp\Big[(1-\mathrm{i})T|\alpha|^2-(1-\mathrm{i})2\sqrt{T}\,|\alpha|\epsilon\Big]\,|\gamma|\alpha|\rangle_{\varepsilon_B}\,|\gamma|\alpha|\rangle_{\varepsilon_D} \\
&\quad+\exp\Big[-(3-3\mathrm{i})T|\alpha|^2+(1-\mathrm{i})2\sqrt{T}\,|\alpha|\epsilon\Big]\,|-\gamma|\alpha|\rangle_{\varepsilon_B}\,|-\gamma|\alpha|\rangle_{\varepsilon_D} \\
&\quad+e^{-T|\alpha|^2}\Big(\,|\gamma|\alpha|\rangle_{\varepsilon_B}\,|-\gamma|\alpha|\rangle_{\varepsilon_D}+\,|-\gamma|\alpha|\rangle_{\varepsilon_B}\,|\gamma|\alpha|\rangle_{\varepsilon_D}\Big)\Big) \\
&+e^{\frac{-T|\alpha|^2}{2}}\,|01\rangle_{AC}\Big(\exp\Big[-2\sqrt{T}\,|\alpha|\epsilon+T|\alpha|^2\Big]\,|\gamma|\alpha|\rangle_{\varepsilon_B}\,|\gamma\mathrm{i}|\alpha|\rangle_{\varepsilon_D} \\
&\quad+\exp\Big[-2T\mathrm{i}|\alpha|^2+2\sqrt{T}\,\mathrm{i}|\alpha|\epsilon\Big]\,|\gamma|\alpha|\rangle_{\varepsilon_B}\,|-\gamma\mathrm{i}|\alpha|\rangle_{\varepsilon_D} \\
&\quad+\exp\Big[-2\sqrt{T}\,\mathrm{i}|\alpha|\epsilon+2T\mathrm{i}|\alpha|^2\Big]\,|-\gamma|\alpha|\rangle_{\varepsilon_B}\,|\gamma\mathrm{i}|\alpha|\rangle_{\varepsilon_D} \\
&\quad+\exp\Big[+2\sqrt{T}\,|\alpha|\epsilon-3T|\alpha|^2\Big]\,|-\gamma|\alpha|\rangle_{\varepsilon_B}\,|-\gamma\mathrm{i}|\alpha|\rangle_{\varepsilon_D}\Big) \\
&+e^{\frac{-T|\alpha|^2}{2}}\,|10\rangle_{AC}\Big(\exp\Big[-2\sqrt{T}\,|\alpha|\epsilon+T|\alpha|^2\Big]\,|\gamma\mathrm{i}|\alpha|\rangle_{\varepsilon_B}\,|\gamma|\alpha|\rangle_{\varepsilon_D} \\
&\quad+\exp\Big[-2\sqrt{T}\,\mathrm{i}|\alpha|\epsilon+2T\mathrm{i}|\alpha|^2\Big]\,|\gamma\mathrm{i}|\alpha|\rangle_{\varepsilon_B}\,|-\gamma|\alpha|\rangle_{\varepsilon_D} \\
&\quad+\exp\Big[-2T\mathrm{i}|\alpha|^2+2\sqrt{T}\,\mathrm{i}|\alpha|\epsilon\Big]\,|-\gamma\mathrm{i}|\alpha|\rangle_{\varepsilon_B}\,|\gamma|\alpha|\rangle_{\varepsilon_D} \\
&\quad+\exp\Big[+2\sqrt{T}\,|\alpha|\epsilon-3T|\alpha|^2\Big]\,|-\gamma\mathrm{i}|\alpha|\rangle_{\varepsilon_B}\,|-\gamma|\alpha|\rangle_{\varepsilon_D}\Big) \\
&\quad+|11\rangle_{AC}\Big(\exp\Big[(\mathrm{i}+1)T|\alpha|^2-(\mathrm{i}+1)2\sqrt{T}\,|\alpha|\epsilon\Big]\,|\gamma\mathrm{i}|\alpha|\rangle_{\varepsilon_B}\,|\gamma\mathrm{i}|\alpha|\rangle_{\varepsilon_D} \\
&\quad+\exp\Big[-(3+3\mathrm{i})T|\alpha|^2+(1+\mathrm{i})2\sqrt{T}\,|\alpha|\epsilon\Big]\,|-\gamma\mathrm{i}|\alpha|\rangle_{\varepsilon_B}\,|-\gamma\mathrm{i}|\alpha|\rangle_{\varepsilon_D} \\
&\quad+e^{-T|\alpha|^2}\Big(\,|\gamma\mathrm{i}|\alpha|\rangle_{\varepsilon_B}\,|-\gamma\mathrm{i}|\alpha|\rangle_{\varepsilon_D}+\,|-\gamma\mathrm{i}|\alpha|\rangle_{\varepsilon_B}\,|\gamma\mathrm{i}|\alpha|\rangle_{\varepsilon_D}\Big)\Big)\Big], \qquad (5.6)
\end{aligned}
$$

in which the above quantum state is for the homodyne non-ideal outcome $x_{\frac{\pi}{4}} = +\sqrt{T}\,|\alpha| - \epsilon$, however the same result is achieved when setting the outcome to $x_{\frac{\pi}{4}} = -\sqrt{T}\,|\alpha| + \epsilon$. Note that we denote this quantum state as $|\Psi^{Cat}_{\mp\epsilon}\rangle_{AC}$, in which the subscript $\mp\epsilon$ is indicative of the $x_{\frac{\pi}{4}} = \pm\sqrt{T}\,|\alpha| \mp \epsilon$ non-ideal homodyne outcome.

We note here that in the limits of no loss ($T = 1$), $\epsilon = 0$ and large $|\alpha|$ we return to the $|\Phi^+(\alpha)\rangle = \frac{1}{\sqrt{2}}(|00\rangle\, e^{-\mathrm{i}|\alpha|^2} + |11\rangle\, e^{+\mathrm{i}|\alpha|^2})$ Bell state for both homodyne outcome

states given in Eqs. 5.5 and 5.6, as expected.

Following on from Eqs. 5.5 and 5.6, we then trace out the lossy modes ε_B and ε_D using the coherent state to trace (as per Subsec. 3.2.4), which gives us our final two qubit density matrices of:

$$\rho_{AC}^{Cat}(\pm\epsilon) = \mathrm{Tr}_{\varepsilon_B,\varepsilon_D}\left[\,|\Psi_{\pm\epsilon}^{Cat}\rangle_{A\varepsilon_B C\varepsilon_D}\,\langle\Psi_{\pm\epsilon}^{Cat}|\right], \tag{5.7}$$

$$\rho_{AC}^{Cat}(\mp\epsilon) = \mathrm{Tr}_{\varepsilon_B,\varepsilon_D}\left[\,|\Psi_{\mp\epsilon}^{Cat}\rangle_{A\varepsilon_B C\varepsilon_D}\,\langle\Psi_{\mp\epsilon}^{Cat}|\right]. \tag{5.8}$$

Using these density matrices we may now investigate entanglement negativity, linear entropy and fidelity of the final state produced through the cat state protocol, when allowing for non-ideal homodyne measurement outcomes.

5.3.1 Entanglement Negativity and Linear Entropy

As was the case with the coherent state protocol evaluated for non-ideal homodyne outcomes in the previous section, we focus primarily on fidelity in the discussion of results for the cat state circumstance. We saw that in the coherent state protocol, increasing the value of ϵ does not affect entanglement negativity and linear entropy at all, for all $|\alpha|$ and T, however the more complicated cat state regime is not as straightforward. In this case, the entanglement negativity plots *are* affected by ϵ for either non-ideal outcomes $x_{\frac{\pi}{4}} = \pm\sqrt{T}\,|\alpha| \pm \epsilon$ and $x_{\frac{\pi}{4}} = \pm\sqrt{T}\,|\alpha| \mp \epsilon$. We show entanglement negativity as a function of $|\alpha|$, for no loss (Fig. 5.10) and for $T = 0.95$ (Fig. 5.11), for both non-ideal homodyne measurement outcomes with varying ϵ:

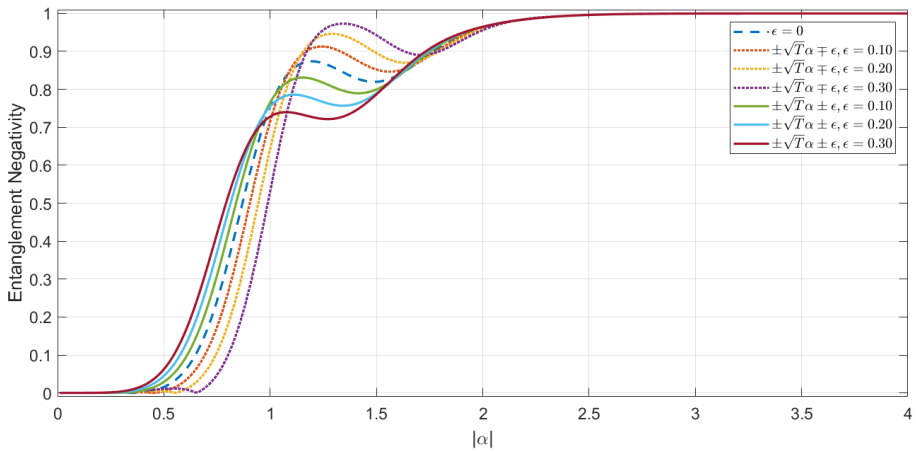

FIGURE 5.10: Entanglement negativity as a function of $|\alpha|$ for the final states generated via our cat state entanglement swapping protocol (Eqs. 5.7 and 5.8), for $T = 1$, with non-ideal homodyne measurement outcomes of $x_{\frac{\pi}{4}} = \pm\sqrt{T}\,|\alpha| \pm \epsilon$ (solid lines in plot) and $x_{\frac{\pi}{4}} = \pm\sqrt{T}\,|\alpha| \mp \epsilon$ (dotted lines in plot).

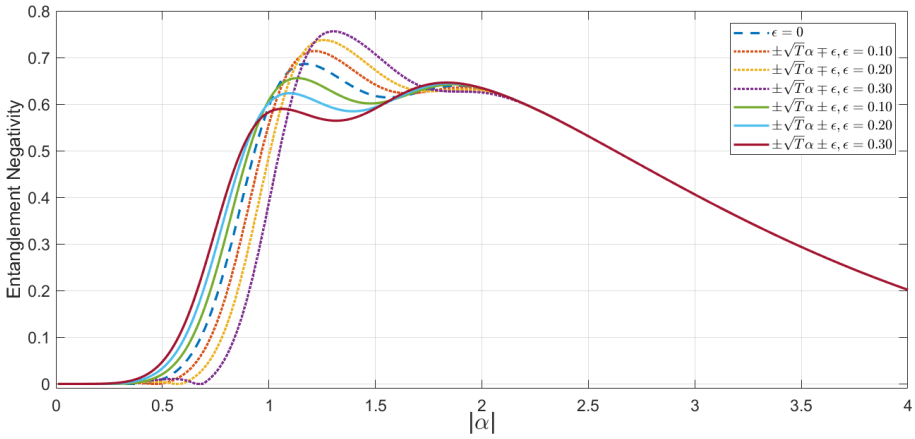

FIGURE 5.11: Entanglement negativity as a function of $|\alpha|$ for the final states generated via our cat state entanglement swapping protocol (Eqs. 5.7 and 5.8), for $T = 0.95$, with non-ideal homodyne measurement outcomes of $x_{\frac{\pi}{4}} = \pm\sqrt{T}\,|\alpha| \pm \epsilon$ (solid lines in plot) and $x_{\frac{\pi}{4}} = \pm\sqrt{T}\,|\alpha| \mp \epsilon$ (dotted lines in plot).

Interestingly, these plots exhibit a somewhat peculiar feature: for either of the above figures we can see that ϵ has an impact on the entanglement negativity value only up to $|\alpha| \approx 2.0$, and beyond this $|\alpha|$ value all plots, regardless of the value of ϵ, overlap one another and tend to the same value (unity for $T = 1$ in Fig. 5.10, and zero for $T = 0.95$ in Fig. 5.11). Analytically, this is relatively simple to justify: consider the quantum state for the $x_{\frac{\pi}{4}} = \pm\sqrt{T}\,|\alpha| \pm \epsilon$ outcome, given in Eq. 5.5, in which clearly ϵ is no longer contained only within an exponential phase, as we saw in the coherent state case (Eq. 5.2). Hence, for the cat state case, ϵ will indeed impact the amplitudes of the terms in the final density matrix, and not just impact the phases. It is for this reason that we see changes in the entanglement negativity plots displayed above. This trend will be explained further in Subsec. 5.3.3, once we have discussed the plots for fidelity.

Moreover, the reason both plots, Figs. 5.10 and 5.11, converge toward the same value of entanglement negativity (although note that they converge to *different* values, for $T = 1$ and $T = 0.95$), regardless of the value of ϵ, is as a result of the dampening exponents $e^{-|\alpha|^2}$ present in most terms in Eqs. 5.5 and 5.6 which have a stronger effect on the final density matrix. These dampening exponents will cause the impact of ϵ to be lessened the larger $|\alpha|$ becomes, as we indeed see in Figs. 5.10 and 5.11.

Lastly, we note here that the linear entropy for the no loss case does not change with respect to ϵ. This again seems peculiar at first, however we must recall that linear entropy is monotonic as a function of any variables which cause the level of mixture in our system to increase, such as photon losses (as discussed in Chapter 2, Sec. 2.7), or the exponential dampening term dependent on α in the off-diagonal terms in our final density matrix. Therefore, linear entropy will not reflect the slight change in the entanglement negativity we see in Fig. 5.10 because, as already discussed, each plot tends to the same entanglement negativity value regardless of ϵ for

large $|\alpha|$. Contrastingly, for the case where we consider loss, for $T = 0.95$, the linear entropy plot *does* change with respect to ϵ, as we show now:

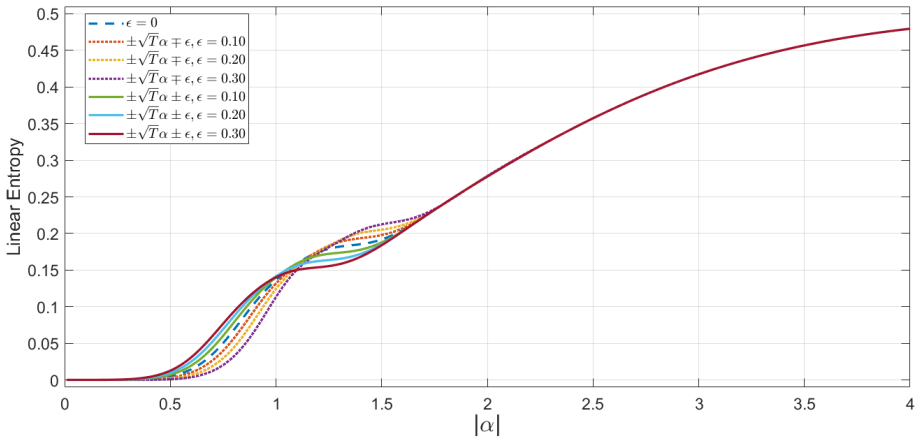

FIGURE 5.12: Linear entropy as a function of $|\alpha|$ for the final states generated via our cat state entanglement swapping protocol (Eqs. 5.7 and 5.8), for $T = 0.95$, with non-ideal homodyne measurement outcomes of $x_{\frac{\pi}{4}} = \pm\sqrt{T}\,|\alpha| \pm \epsilon$ (solid lines in plot) and $x_{\frac{\pi}{4}} = \pm\sqrt{T}\,|\alpha| \mp \epsilon$ (dotted lines in plot).

Evidently, we see a small variation in the linear entropy plot in the region of $|\alpha| < 2.0$, as we saw in the $T = 0.95$ entanglement negativity plot of Fig. 5.11. As we have just mentioned, linear entropy is monotonic as a function of α, as a result of exponential dampening in the off-diagonal density matrix terms, and as such does not reflect small changes of ϵ when we have $T = 1$. This is due to the fact that, for no loss, entanglement negativity still tends to unity for large $|\alpha|$, for all ϵ, and as such linear entropy will always remain at $S_L = 0$.

Contrastingly, when we consider losses, as per Fig. 5.12, because the quantum state is becoming more mixed (due to introducing losses) the entropy will reflect this change, and as such the linear entropy plot here plateaus at $S_L = 0.50$ for large $|\alpha|$, for all ϵ. Hence, as the linear entropy plot for $T = 0.95$ does not remain at 0 for all $|\alpha|$, we see small changes in the entropy value as we increase ϵ, corresponding to the same changes in entanglement negativity we see in Fig.5.11.

5.3.2 Fidelity

Once again, we emphasise that the fidelity plots are more useful for investigating and analysing the impact that homodyne non-idealities have on our final density matrix. Additionally, and even more importantly, fidelity gives one an insight into the state which we are actually producing, which is arguably far more useful in terms of quantifying the usefulness of this protocol in generating specific entangled states to then provide to a potential customer, or indeed customers.

We therefore move on to plot the fidelity against the $|\Phi^+(\alpha)\rangle = \frac{1}{\sqrt{2}}(|00\rangle\, e^{-\mathrm{i}|\alpha|^2} + |11\rangle\, e^{+\mathrm{i}|\alpha|^2})$ Bell state as a function of $|\alpha|$ and ϵ, but only show fidelity values for $F \geq 0.80$, so as to establish a window of accepted values for ϵ, in which we can guarantee to produce a Bell state of acceptable fidelity.

The following three plots (Figs. 5.13, 5.14 and 5.15) are for the homodyne measurement outcome of $x_{\frac{\pi}{4}} = \pm\sqrt{T}\,|\alpha| \pm \epsilon$:

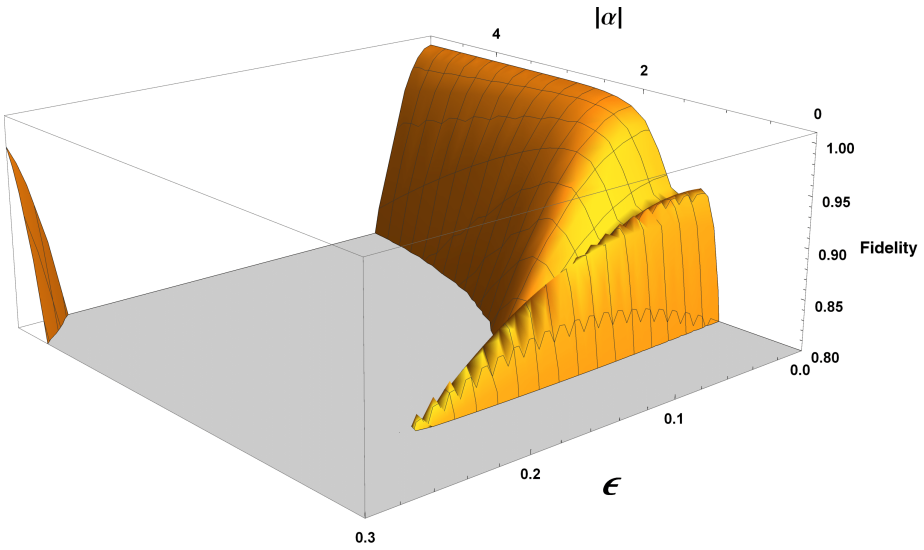

FIGURE 5.13: Fidelity against the $|\Phi^+(\alpha)\rangle = \frac{1}{\sqrt{2}}(|00\rangle\, e^{-i|\alpha|^2} + |11\rangle\, e^{+i|\alpha|^2})$ Bell state as a function of $|\alpha|$ and ϵ for the final state generated via our cat state entanglement swapping protocol (Eq. 5.7), for $T = 1$, with non-ideal homodyne measurement outcome of $x_{\frac{\pi}{4}} = \pm\sqrt{T}\,|\alpha| \pm \epsilon$.

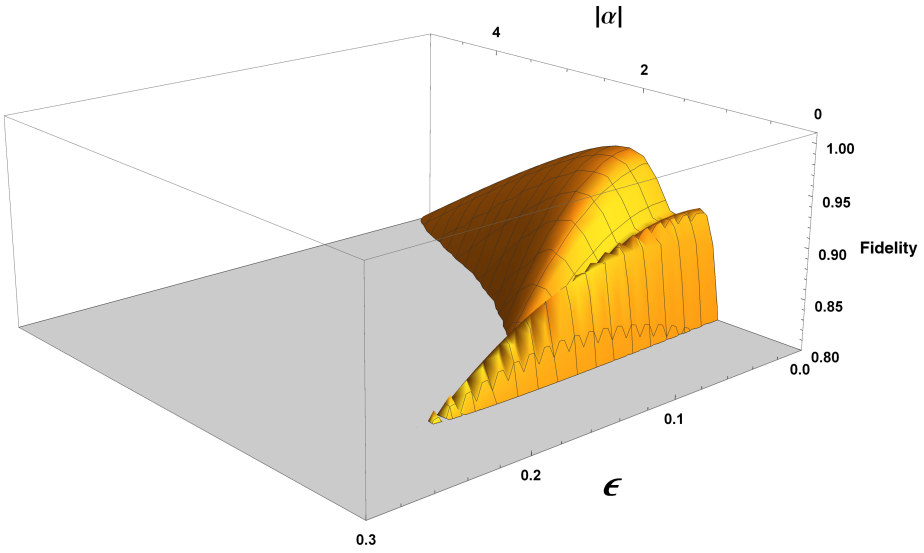

FIGURE 5.14: Fidelity against the $|\Phi^+(\alpha)\rangle = \frac{1}{\sqrt{2}}(|00\rangle\, e^{-i|\alpha|^2} + |11\rangle\, e^{+i|\alpha|^2})$ Bell state as a function of $|\alpha|$ and ϵ for the final state generated via our cat state entanglement swapping protocol (Eq. 5.7), for $T = 0.99$, with non-ideal homodyne measurement outcome of $x_{\frac{\pi}{4}} = \pm\sqrt{T}\,|\alpha| \pm \epsilon$.

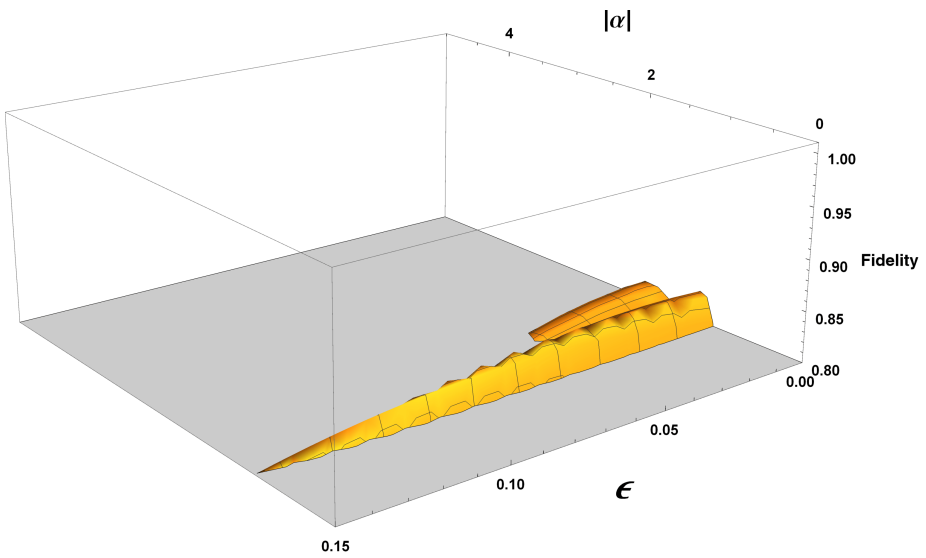

FIGURE 5.15: Fidelity against the $|\Phi^+(\alpha)\rangle = \frac{1}{\sqrt{2}}(|00\rangle\, e^{-i|\alpha|^2} + |11\rangle\, e^{+i|\alpha|^2})$ Bell state as a function of $|\alpha|$ and ϵ for the final state generated via our cat state entanglement swapping protocol (Eq. 5.7), for $T = 0.95$, with non-ideal homodyne measurement outcome of $x_{\frac{\pi}{4}} = \pm\sqrt{T}\,|\alpha| \pm \epsilon$.

From looking at the above 3D fidelity plots we can easily confirm that, for $T \geq 0.95$, we can tolerate a non-ideal homodyne measurement shift of $\epsilon \leq 0.15$ for homodyne outcome $x_{\frac{\pi}{4}} = \pm\sqrt{T}\,|\alpha| \pm \epsilon$, if we wish to produce the $|\Phi^+(\alpha)\rangle$ Bell state with a respectable fidelity of $F \geq 0.80$. Furthermore, if we accept lower levels of loss, such that $T \geq 0.99$ then we can tolerate even greater ϵ values of $\epsilon \geq 0.20$.

For comparison, the following three plots (Figs. 5.16, 5.17 and 5.18) are for the homodyne measurement outcome of $x_{\frac{\pi}{4}} = \pm\sqrt{T}\,|\alpha| \mp \epsilon$, for $T = 1$, $T = 0.99$ and $T = 0.95$, respectively:

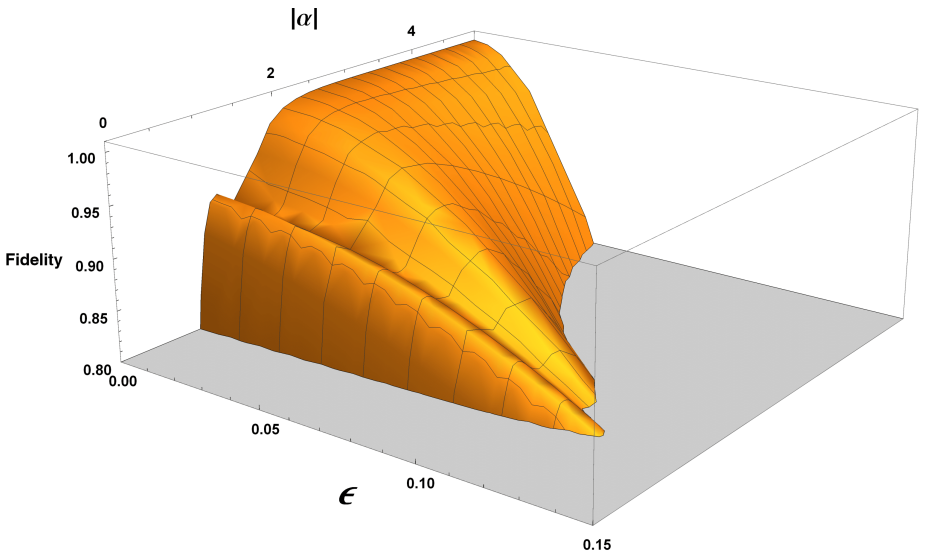

FIGURE 5.16: Fidelity against the $|\Phi^+(\alpha)\rangle = \frac{1}{\sqrt{2}}(|00\rangle\, e^{-i|\alpha|^2} + |11\rangle\, e^{+i|\alpha|^2})$ Bell state as a function of $|\alpha|$ and ϵ for the final state generated via our cat state entanglement swapping protocol (Eq. 5.8), for $T = 1$, with non-ideal homodyne measurement outcome of $x_{\frac{\pi}{4}} = \pm\sqrt{T}\,|\alpha| \mp \epsilon$.

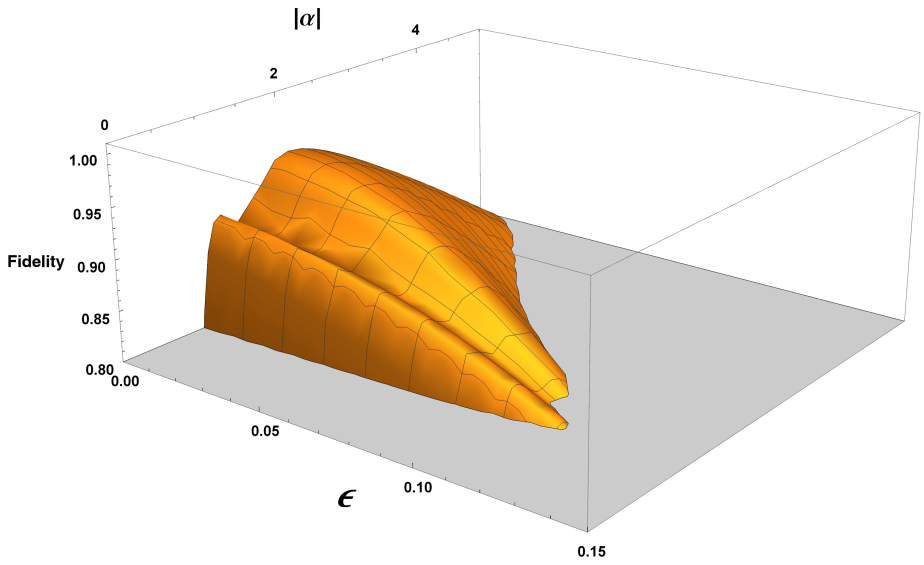

FIGURE 5.17: Fidelity against the $|\Phi^+(\alpha)\rangle = \frac{1}{\sqrt{2}}(|00\rangle\, e^{-\mathrm{i}|\alpha|^2} + |11\rangle\, e^{+\mathrm{i}|\alpha|^2})$ Bell state as a function of $|\alpha|$ and ϵ for the final state generated via our cat state entanglement swapping protocol (Eq. 5.8), for $T = 0.99$, with non-ideal homodyne measurement outcome of $x_{\frac{\pi}{4}} = \pm\sqrt{T}\,|\alpha| \mp \epsilon$.

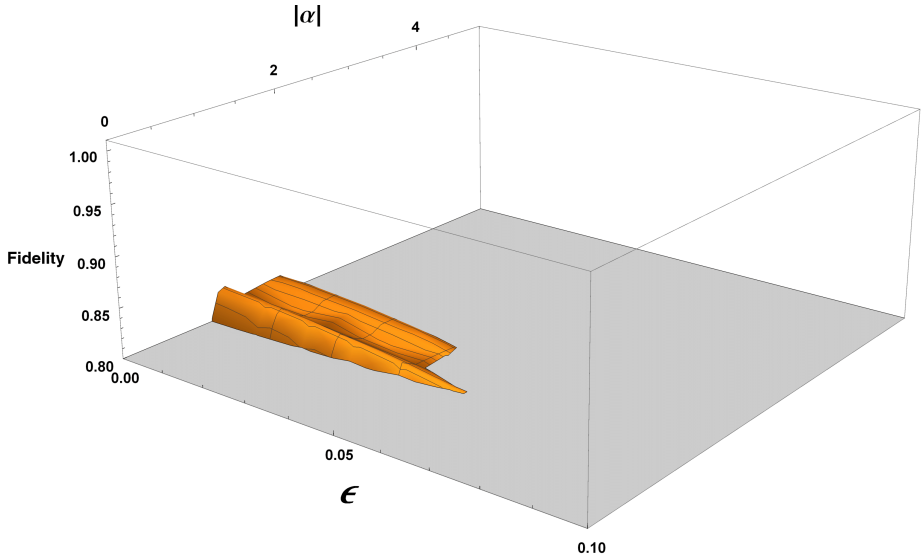

FIGURE 5.18: Fidelity against the $|\Phi^+(\alpha)\rangle = \frac{1}{\sqrt{2}}(|00\rangle\, e^{-\mathrm{i}|\alpha|^2} + |11\rangle\, e^{+\mathrm{i}|\alpha|^2})$ Bell state as a function of $|\alpha|$ and ϵ for the final state generated via our cat state entanglement swapping protocol (Eq. 5.8), for $T = 0.95$, with non-ideal homodyne measurement outcome of $x_{\frac{\pi}{4}} = \pm\sqrt{T}\,|\alpha| \mp \epsilon$.

What is instantly clear from these plots is that if the non-ideal homodyne measurement outcome is $x_{\frac{\pi}{4}} = \pm\sqrt{T}\,|\alpha| \mp \epsilon$ then we cannot tolerate as high values of ϵ as we can for the $x_{\frac{\pi}{4}} = \pm\sqrt{T}\,|\alpha| \pm \epsilon$ case (Figs. 5.13, 5.14 and 5.15). Interestingly, this seems somewhat counter-intuitive to the entanglement negativity results given in Figs. 5.10 and 5.11, in which we saw that the entanglement negativity value was higher for non-zero ϵ for the $x_{\frac{\pi}{4}} = \pm\sqrt{T}\,|\alpha| \mp \epsilon$ non-ideal homodyne outcome, as opposed to the $x_{\frac{\pi}{4}} = \pm\sqrt{T}\,|\alpha| \pm \epsilon$ outcome.

The straightforward answer to this is simply that the entanglement negativity of a quantum state is not affected by changes in only the phase; refer to the coherent state non-ideal homodyne measurement results, Subsec. 5.2.1 in which the entanglement negativity and linear entropy plots remained completely unchanged by introducing non-zero ϵ, yet the fidelity plots were affected. However, as already discussed, in the cat state protocol our final state has terms dependent on ϵ that are not just contained in phases, and as such we would indeed expect entanglement negativity, and also linear entropy, to be somewhat affected by non-zero ϵ. This trend will be discussed in more detail in Subsec. 5.3.3.

For now, let us consider fidelity against the $|\Phi^+(\alpha)\rangle$ and the orthogonal $|\Phi^-(\alpha)\rangle$ Bell states as a function of $|\alpha|$, for no loss ($T = 1$) and for non-ideal homodyne measurement outcome $x_{\frac{\pi}{4}} = \pm\sqrt{T}\,|\alpha| \pm \epsilon$:

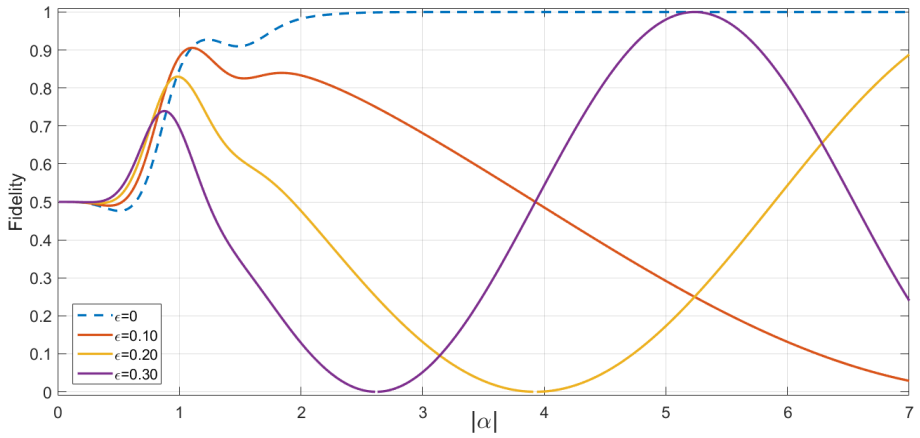

FIGURE 5.19: Fidelity against the $|\Phi^+(\alpha)\rangle = \frac{1}{\sqrt{2}}(\,|00\rangle\, e^{-\mathrm{i}|\alpha|^2} + |11\rangle\, e^{+\mathrm{i}|\alpha|^2})$ Bell state as a function of $|\alpha|$ for the final state generated via our cat state entanglement swapping protocol (Eq. 5.7), for no loss ($T = 1$), and varying non-ideal homodyne measurement outcome $x_{\frac{\pi}{4}} = \pm\sqrt{T}\,|\alpha| \pm \epsilon$.

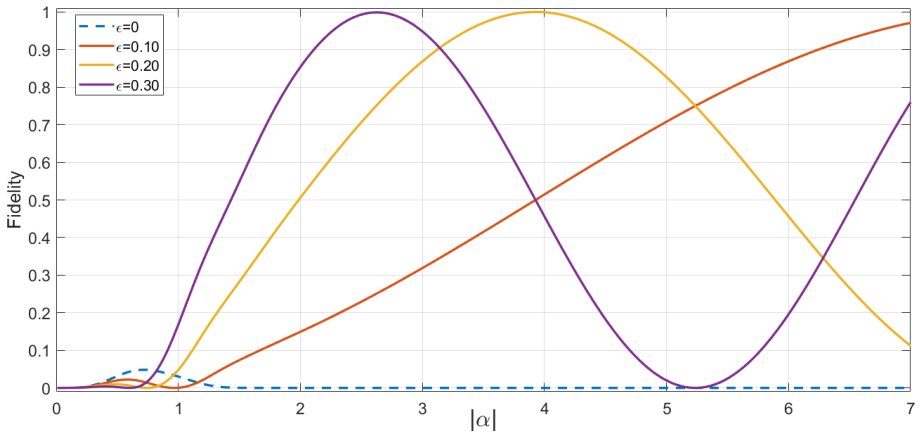

FIGURE 5.20: Fidelity against the $|\Phi^-(\alpha)\rangle = \frac{1}{\sqrt{2}}(\,|00\rangle\, e^{-\mathrm{i}|\alpha|^2} - |11\rangle\, e^{+\mathrm{i}|\alpha|^2})$ Bell state as a function of $|\alpha|$ for the final state generated via our cat state entanglement swapping protocol (Eq. 5.7), for no loss ($T = 1$), and varying non-ideal homodyne measurement outcome $x_{\frac{\pi}{4}} = \pm\sqrt{T}\,|\alpha| \pm \epsilon$.

We can see from the above graphs that plotting fidelity against either of the Bell states, $|\Phi^+(\alpha)\rangle$ and $|\Phi^-(\alpha)\rangle$, results in an oscillatory plot as a function of $|\alpha|$, which becomes more oscillatory the higher ϵ is. Comparably, we witnessed this behaviour in the coherent state plots of Figs. 5.6 and 5.7, in which the final density matrix (Eq. 5.3) contained phases in the off-diagonal $|00\rangle_{AC}\langle 11|$ and $|11\rangle_{AC}\langle 00|$ terms, and so when calculating fidelity against a Bell state which did *not* contain phases (the $|\Phi^+\rangle$ Bell state) we of course see oscillations in the plot.

Conversely, in the cat state case for the non-ideal homodyne measurement outcome $x_{\frac{\pi}{4}} = \pm\sqrt{T}\,|\alpha| \pm \epsilon$, we can see from the final state (Eqs. 5.5) that there are indeed phases present that are dependent on ϵ. It therefore follows that, for no loss, calculating fidelity of this state against either of the $|\Phi^+(\alpha)\rangle$ and $|\Phi^-(\alpha)\rangle$ Bell states will still give a plot exhibiting oscillatory behaviour; the phases in the final density matrix change more rapidly as they are dependent on ϵ, as well as $|\alpha|^2$. This also justifies why the plots for $\epsilon = 0.10$ and $\epsilon = 0.20$ in Figs. 5.19 and 5.20 are less oscillatory than that of $\epsilon = 0.30$.

We now plot fidelity of the final density matrix, for non-ideal homodyne outcome $x_{\frac{\pi}{4}} = \pm\sqrt{T}\,|\alpha| \pm \epsilon$, against the $|\Phi^+(\alpha)\rangle$ and $|\Phi^-(\alpha)\rangle$ Bell states (Figs. 5.21 and 5.22 respectively), but for $T = 0.95$:

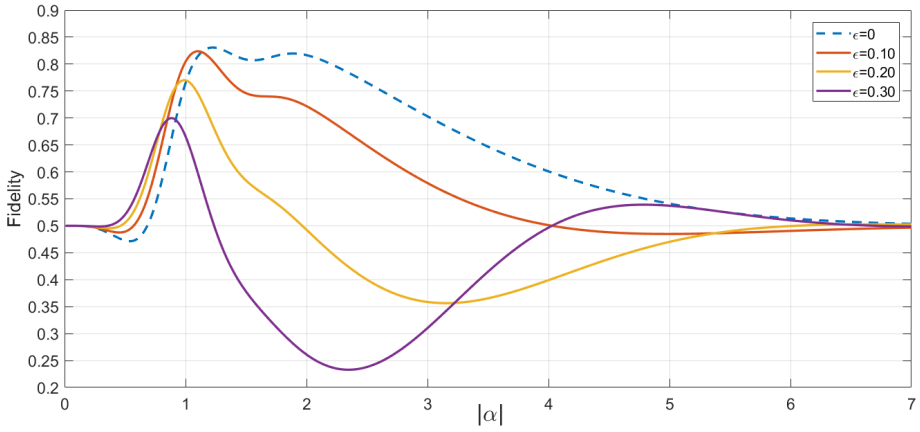

FIGURE 5.21: Fidelity against the $|\Phi^+(\alpha)\rangle = \frac{1}{\sqrt{2}}(\,|00\rangle\, e^{-i|\alpha|^2} + |11\rangle\, e^{+i|\alpha|^2})$ Bell state as a function of $|\alpha|$ for the final state generated via our cat state entanglement swapping protocol (Eq. 5.7), for equal losses of $T = 0.95$, and varying non-ideal homodyne measurement outcome $x_{\frac{\pi}{4}} = \pm\sqrt{T}\,|\alpha| \pm \epsilon$.

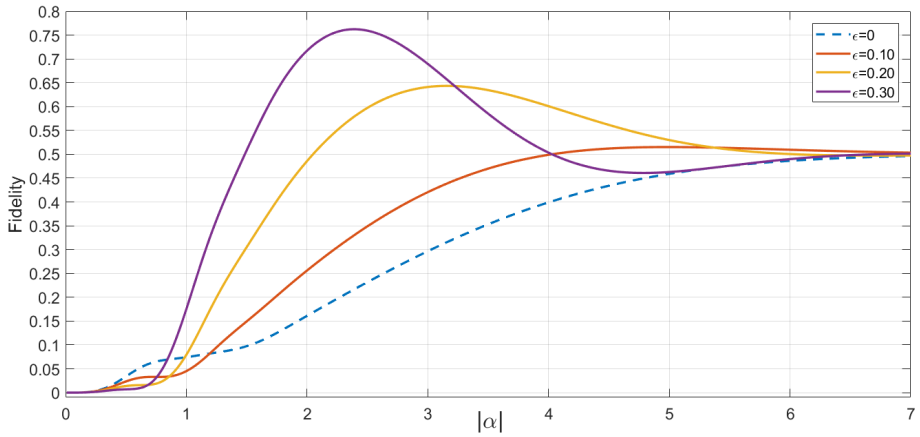

FIGURE 5.22: Fidelity against the $|\Phi^-(\alpha)\rangle = \frac{1}{\sqrt{2}}(|00\rangle\, e^{-i|\alpha|^2} - |11\rangle\, e^{+i|\alpha|^2})$ Bell state as a function of $|\alpha|$ for the final state generated via our cat state entanglement swapping protocol (Eq. 5.7), for equal losses of $T = 0.95$, and varying non-ideal homodyne measurement outcome $x_{\frac{\pi}{4}} = \pm\sqrt{T}|\alpha| \pm \epsilon$.

Here we can see that, when allowing for loss, the oscillatory behaviour displayed in the no loss fidelity plots (Figs. 5.19 and 5.20) is no longer present in the graphs above. In fact, we witnessed this pattern in the coherent state plots (compare the no loss plots of Figs. 5.6 and 5.7 with the lossy plots of Figs. 5.8 and 5.9), and the reason for this pattern is the same in the cat state circumstance at hand: the dampening exponents present in all terms (due to tracing out the lossy modes) affects the final density matrix more than the exponents containing phases dependent on $|\alpha|$ and ϵ. It therefore follows that, for non-unity T, as $|\alpha|$ increases the plots plateau and do not exhibit oscillations.

Let us now move on to the cat state protocol for the non-ideal homodyne measurement outcome $x_{\frac{\pi}{4}} = \pm\sqrt{T}|\alpha| \mp \epsilon$, in which we first plot fidelity against the $|\Phi^+(\alpha)\rangle$ and $|\Phi^-(\alpha)\rangle$ Bell states (Figs. 5.23 and 5.24 respectively), for no loss:

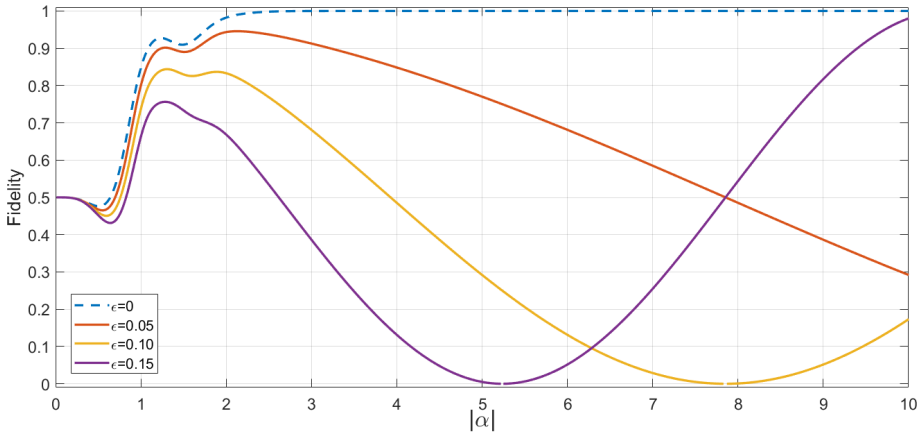

FIGURE 5.23: Fidelity against the $|\Phi^+(\alpha)\rangle = \frac{1}{\sqrt{2}}(|00\rangle\, e^{-i|\alpha|^2} + |11\rangle\, e^{+i|\alpha|^2})$ Bell state as a function of $|\alpha|$ for the final state generated via our cat state entanglement swapping protocol (Eq. 5.8), for no loss ($T = 1$), and varying non-ideal homodyne measurement outcome $x_{\frac{\pi}{4}} = \pm\sqrt{T}|\alpha| \mp \epsilon$.

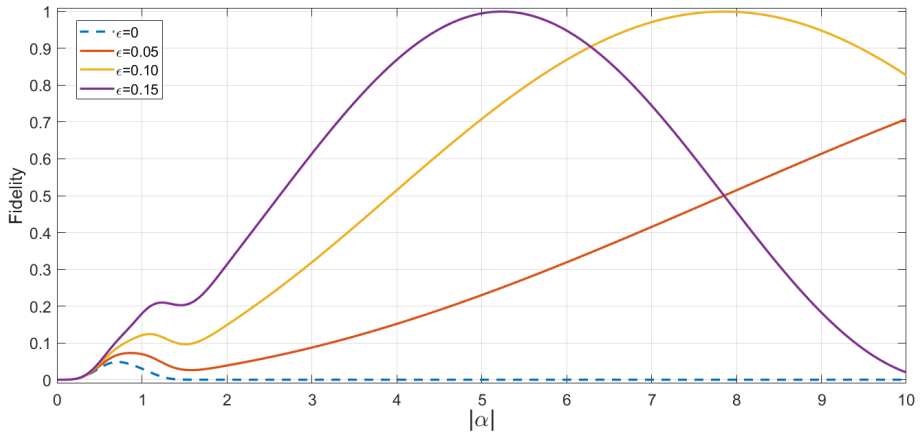

FIGURE 5.24: Fidelity against the $|\Phi^{-}(\alpha)\rangle = \frac{1}{\sqrt{2}}(|00\rangle\, e^{-\mathrm{i}|\alpha|^2} - |11\rangle\, e^{+\mathrm{i}|\alpha|^2})$ Bell state as a function of $|\alpha|$ for the final state generated via our cat state entanglement swapping protocol (Eq. 5.8), for no loss ($T = 1$), and varying non-ideal homodyne measurement outcome $x_{\frac{\pi}{4}} = \pm\sqrt{T}\,|\alpha| \mp \epsilon$.

Note that we have plotted the above up to higher values of $|\alpha|$ than typical so far, to demonstrate that there is oscillatory behaviour. However, these oscillations are not as rapid as the case for the non-ideal homodyne measurement outcome $x_{\frac{\pi}{4}} = \pm\sqrt{T}\,|\alpha| \pm \epsilon$, as seen in Figs. 5.19 and 5.20. The reason for this is simply that we are calculating fidelity for lower values of ϵ in the cases where the outcome is $x_{\frac{\pi}{4}} = \pm\sqrt{T}\,|\alpha| \mp \epsilon$, as opposed to $x_{\frac{\pi}{4}} = \pm\sqrt{T}\,|\alpha| \pm \epsilon$, as we ideally are only concerned with values of ϵ which still result in a fidelity of $F \geq 0.80$. For clarity, we now overlay fidelity plots for $\epsilon = 0.30$ with both homodyne outcomes $x_{\frac{\pi}{4}} = \pm\sqrt{T}\,|\alpha| \pm \epsilon$ and $x_{\frac{\pi}{4}} = \pm\sqrt{T}\,|\alpha| \mp \epsilon$, against the $|\Phi^{+}(\alpha)\rangle$ Bell state, to demonstrate the difference:

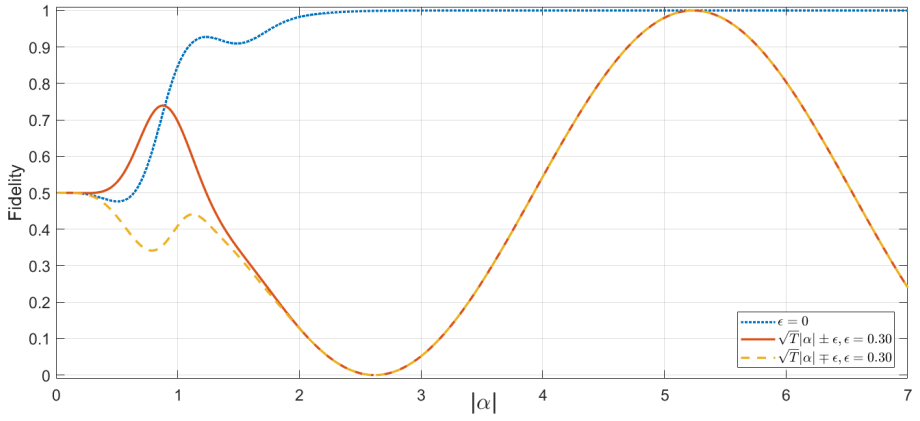

FIGURE 5.25: Fidelity against the $|\Phi^{+}(\alpha)\rangle = \frac{1}{\sqrt{2}}(|00\rangle\, e^{-\mathrm{i}|\alpha|^2} + |11\rangle\, e^{+\mathrm{i}|\alpha|^2})$ Bell state as a function of $|\alpha|$ for the final states generated via our cat state entanglement swapping protocol (Eqs. 5.7 and 5.8), for no loss ($T = 1$), and varying non-ideal homodyne measurement outcomes $x_{\frac{\pi}{4}} = \pm\sqrt{T}\,|\alpha| \pm \epsilon$ (solid line) and $x_{\frac{\pi}{4}} = \pm\sqrt{T}\,|\alpha| \mp \epsilon$ (dashed line).

Evidently, when ϵ is identical in value in both non-ideal outcomes $x_{\frac{\pi}{4}} = \pm\sqrt{T}\,|\alpha| \pm \epsilon$ and $x_{\frac{\pi}{4}} = \pm\sqrt{T}\,|\alpha| \mp \epsilon$, then at large values of $|\alpha|$ ($|\alpha| \geq 1.50$) the

plots overlap - we note here that the same effect occurs for all values of T. Contrastingly, at lower values of $|\alpha|$, namely the region in which we are mostly concerned with in this work ($1.0 \leq |\alpha| \leq 1.50$), realistically and experimentally, the plots do indeed differ. In fact, Fig. 5.25 starkly demonstrates that the most desirable non-ideal homodyne measurement outcome is $x_{\frac{\pi}{4}} = \pm\sqrt{T}\,|\alpha| \pm \epsilon$ as opposed to $x_{\frac{\pi}{4}} = \pm\sqrt{T}\,|\alpha| \mp \epsilon$. We will discuss the reasons for this in the next subsection (Subsec. 5.3.3), once we have discussed the $T = 0.95$ fidelity plots, as follows.

We now plot fidelity against the $|\Phi^+(\alpha)\rangle$ and $|\Phi^-(\alpha)\rangle$ Bell states (Figs. 5.26 and 5.27 respectively), for the extremal loss case of $T = 0.95$, for non-ideal homodyne outcome $x_{\frac{\pi}{4}} = \pm\sqrt{T}\,|\alpha| \mp \epsilon$:

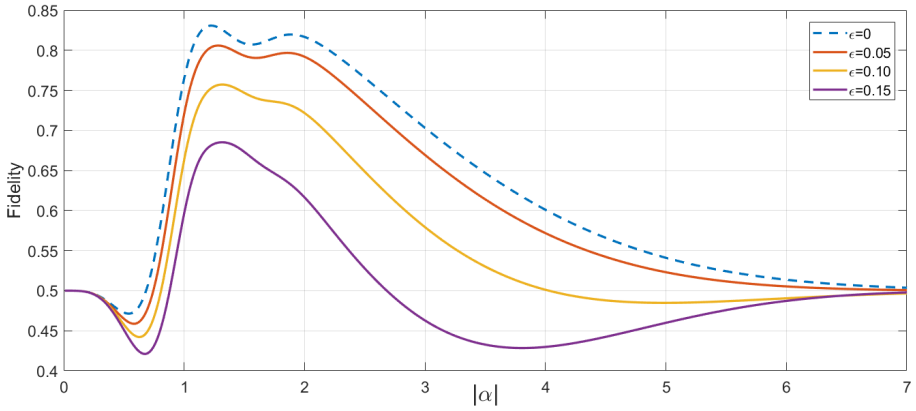

FIGURE 5.26: Fidelity against the $|\Phi^+(\alpha)\rangle = \frac{1}{\sqrt{2}}(\,|00\rangle\, e^{-i|\alpha|^2} + |11\rangle\, e^{+i|\alpha|^2})$ Bell state as a function of $|\alpha|$ for the final state generated via our cat state entanglement swapping protocol (Eq. 5.8), for equal losses of $T = 0.95$, and varying non-ideal homodyne measurement outcome $x_{\frac{\pi}{4}} = \pm\sqrt{T}\,|\alpha| \mp \epsilon$.

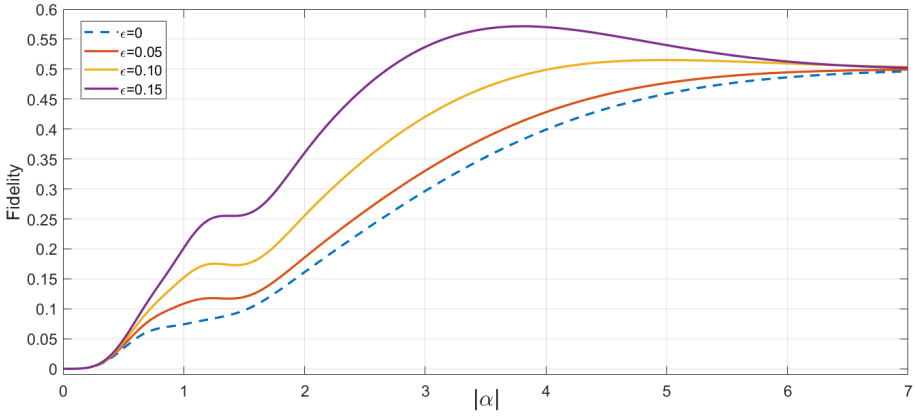

FIGURE 5.27: Fidelity against the $|\Phi^-(\alpha)\rangle = \frac{1}{\sqrt{2}}(\,|00\rangle\, e^{-i|\alpha|^2} - |11\rangle\, e^{+i|\alpha|^2})$ Bell state as a function of $|\alpha|$ for the final state generated via our cat state entanglement swapping protocol (Eq. 5.8), for equal losses of $T = 0.95$, and varying non-ideal homodyne measurement outcome $x_{\frac{\pi}{4}} = \pm\sqrt{T}\,|\alpha| \mp \epsilon$.

Once more, as we saw for the non-ideal homodyne outcome $x_{\frac{\pi}{4}} = \pm\sqrt{T}\,|\alpha| \pm \epsilon$ fidelity results for $T = 0.95$ (Figs. 5.21 and 5.22) we no longer witness any oscillatory behaviour in the above plots - this, as before, is due to the fact that we now have

exponential dampening that is dependent on the level of loss being evaluated for, which has a greater effect on the final density matrix being analysed compared to the phase oscillations dependent on ϵ. Nonetheless, we still see the characteristic "double peak" in Fig. 5.26 as we do in all cat state fidelity plots.

5.3.3 Comparison of Cat State Non-Ideal Homodyne Outcomes

Thus far, we have seen in our investigation for non-ideal homodyne measurement outcomes, in the cat state regime, that we have a preferable non-ideal outcome; the no loss fidelity plot of Fig. 5.25 demonstrates this trend perfectly, and we can see, for low $|\alpha|$ (i.e. $|\alpha| < 1.5$), that the best non-ideal outcome is for $x_{\frac{\pi}{4}} = \pm\sqrt{T}\,|\alpha| \pm \epsilon$, whereas the $x_{\frac{\pi}{4}} = \pm\sqrt{T}\,|\alpha| \mp \epsilon$ outcome gives us lower fidelity results.

On the other hand, we have also seen that plotting entanglement negativity shows higher values (in the peak $|\alpha|$ region) for the $x_{\frac{\pi}{4}} = \pm\sqrt{T}\,|\alpha| \mp \epsilon$ non-ideal homodyne measurement outcome (see Figs. 5.10 and 5.11). At first this seems counter-intuitive, yet this trend can be explained quite simply: we see that the preferable non-ideal outcome of $x_{\frac{\pi}{4}} = \pm\sqrt{T}\,|\alpha| \pm \epsilon$ gives better results for fidelity against the $|\Phi^{+}(\alpha)\rangle$ Bell state (see Fig. 5.25), and this is justified by the fact that off-diagonal $|00\rangle\langle 11|$ and $|11\rangle\langle 00|$ terms, containing phases dependent on both ϵ and $|\alpha|$, for no loss, oscillate.

Although these plots do indeed differ in the peak $|\alpha|$ region we focus on as an area of interest (namely $1.0 \leq |\alpha| \leq 2.50$), all entanglement negativity plots, regardless of which non-ideal outcome we have, tend to the same value, as shown in Figs. 5.10 and 5.11. This was discussed previously, but we remind the reader here that this is as a result of the exponential dampening terms, dependent on $|\alpha|^2$, having a far stronger influence on the density matrix coefficients at higher values of $|\alpha|$, than ϵ has on the phase of the coefficients.

To explain these trends described above in the entanglement negativity and fidelity plots, we now plot fidelity of our final density matrices (Eqs. 5.7 and 5.8), against a Bell state that contains an arbitrary phase. We denote this Bell state as $|\Phi_{\theta}^{+}\rangle = \frac{1}{\sqrt{2}}(\,|00\rangle\, e^{-\mathrm{i}\theta} + |11\rangle\, e^{+\mathrm{i}\theta})$, and so by plotting fidelity against this Bell state, as a function of θ, we should expect that the patterns we see in the entanglement negativity plot of Fig. 5.10 are also shown here.

Firstly, we show fidelity against the arbitrary phase Bell state, as a function of θ, for no loss and $|\alpha| = 1.25$:

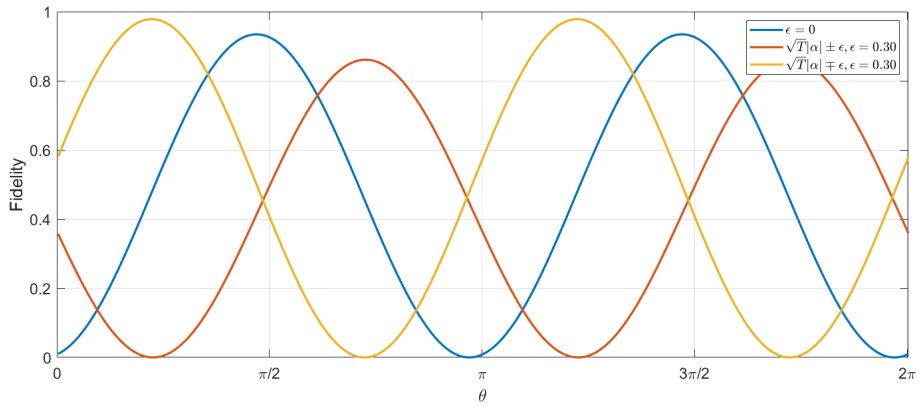

FIGURE 5.28: Fidelity against the $|\Phi_\theta^+\rangle = \frac{1}{\sqrt{2}}(\,|00\rangle\, e^{-i\theta} + |11\rangle\, e^{+i\theta})$ Bell state, as a function of θ, for the final states generated via our cat state entanglement swapping protocol (Eqs. 5.7 and 5.8), for no loss ($T = 1$), and $|\alpha| = 1.25$.

Note that the value of $|\alpha| = 1.25$ was selected as this amplitude value shows clear differences in the entanglement negativity plot of Fig. 5.10 for the non-ideal homodyne outcomes, for non-zero ϵ. Evidently, observing Fig. 5.28, we can see that the plot which gives the highest fidelity values is for the $x_{\frac{\pi}{4}} = \pm\sqrt{T}\,|\alpha| \mp \epsilon$ non-ideal homodyne outcome. Contrastingly, the plot which shows the lowest peak fidelity value is for the $x_{\frac{\pi}{4}} = \pm\sqrt{T}\,|\alpha| \pm \epsilon$ outcome. Both of these statements agree entirely with what we witness in the entanglement negativity plot of Fig. 5.10.

To confirm what we have just stated, we now show fidelity against the arbitrary phase Bell state, as a function of θ, for no loss and $|\alpha| = 3.0$:

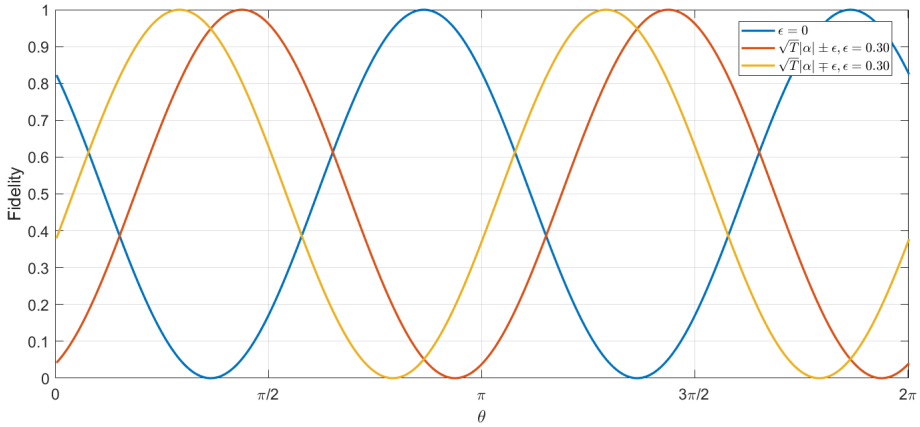

FIGURE 5.29: Fidelity against the $|\Phi_\theta^+\rangle = \frac{1}{\sqrt{2}}(\,|00\rangle\, e^{-i\theta} + |11\rangle\, e^{+i\theta})$ Bell state, as a function of θ, for the final states generated via our cat state entanglement swapping protocol (Eqs. 5.7 and 5.8), for no loss ($T = 1$), and $|\alpha| = 3.0$.

Note that the value of $|\alpha| = 3.0$ was selected as this amplitude value shows no differences in the entanglement negativity plot of Fig. 5.10. Clearly, observing Fig. 5.29, we now see that all plots, irrespective of which non-ideal outcome we have, all reach unity at some point. It should now be clear why this is: we know, for no loss, that all plots, regardless of which non-ideal homodyne outcome we have, will tend to unity at large values of $|\alpha|$, due to the fact that the dampening exponents

dependent on $|\alpha|$ have a far stronger impact on the density matrix amplitudes, and so effectively cancel out the impact of any phases present, which are dependent on ϵ.

We remind the reader here that of course one could theoretically determine precisely which Bell state we are producing for the $x_{\frac{\pi}{4}} = \pm\sqrt{T}\,|\alpha| \mp \epsilon$ non-ideal homodyne outcome, for non-zero ϵ. However, the point of this thesis is to produce a Bell state which could be supplied to a customer (or customers) for further communication/computational purposes. Indeed, were we to determine the exact phase needed to produce this Bell state of higher entanglement (shown in the entanglement negativity plot of Fig. 5.10) we could, in theory, supply said customer with a more entangled pair of qubits. Unfortunately, this in turn causes the protocol's implementation to become far more tedious, as we would then need to notify the customer precisely which phase the Bell state we are giving them has, which would be dependent on the non-ideal outcome that has occurred, as well as $|\alpha|$ and T.

Not only this, but for commercial purposes a customer would most likely prefer to know exactly what state they will receive at any time, and so for implementing our protocol we would merely need to say: "you are receiving the $|\Phi^{+}(\alpha)\rangle = \frac{1}{\sqrt{2}}(\,|00\rangle\, e^{-\mathrm{i}|\alpha|^2} + |11\rangle\, e^{+\mathrm{i}|\alpha|^2})$ Bell state, for a given $|\alpha|$ value (determined at the beginning of the experiment), with a given *minimum* fidelity".

5.4 Imperfect Homodyne Detection

We now want to assess how tolerant our protocol is when considering "imperfect" homodyne measurements (as opposed to *perfect* non-ideal homodyne outcomes, as already discussed in this chapter) to investigate the uncertainty, in terms of a resolution bandwidth, of the homodyne measurement. For this, we apply the analytical method derived by A. Laghaout *et al.* in [177].

The reason we want to evaluate imperfections in the homodyne measurement is because so far we have assumed that we know *precisely* the outcome (i.e. for coherent states we assume the homodyne outcome is $x_{\frac{\pi}{2}} = 0$) - this, however, is unrealistic because no practical homodyne detection device has high enough resolution to project to a *precise* quadrature ($|x_\theta\rangle\langle x_\theta|$). Furthermore, even if we could measure a quadrature exactly we would not necessarily want to as this would lower the success probability of the protocol as the experiment would have to run many times to achieve this exact result, as will be discussed in Chapter 6, Subsec. 6.1.2.

We therefore instead use our new imperfect homodyne operator given as:

$$\hat{\Pi}_{HD}(x_0, \Delta x) = \int_{x_0 - \frac{\Delta x}{2}}^{x_0 + \frac{\Delta x}{2}} |x_\theta\rangle\langle x_\theta|\,\mathrm{d}x_\theta, \tag{5.9}$$

where, x_0 is the expected measured value and Δx is the resolution bandwidth around this measured value (for the "perfect" homodyne projector equivalent to Eq. 5.9 see

Eq. 2.25). Intuitively, in the limit of $\Delta x \to 0$ we should approach the perfect homodyne measurement scenario as before. By increasing this value of Δx we are now able to assess how large we can allow this resolution bandwidth to be without damaging the protocol outcome fidelity and entanglement to an unacceptable limit.

As an example of this, consider the probability distribution of a single coherent state of amplitude $|\alpha| = 0$ (the vacuum state) as a function of position in phase space. This is given mathematically (using Eq. 2.24) as:

$$\begin{aligned} \langle x||\alpha|\rangle &= \frac{1}{2^{-\frac{1}{4}}\pi^{\frac{1}{4}}} \exp\left[-x^2 + 2|\alpha|x - |\alpha|^2\right] \\ \langle x||\alpha|\rangle &\xrightarrow{|\alpha|\to 0} \langle x|0\rangle = \frac{1}{2^{-\frac{1}{4}}\pi^{\frac{1}{4}}} \exp\left[-x^2\right], \end{aligned} \tag{5.10}$$

We may square this probability amplitude to give us a probability distribution:

$$|\langle x|0\rangle|^2 = \frac{\sqrt{2}}{\sqrt{\pi}} \exp\left[-2x^2\right]. \tag{5.11}$$

Plotting the above probability distribution as a function of position x gives us:

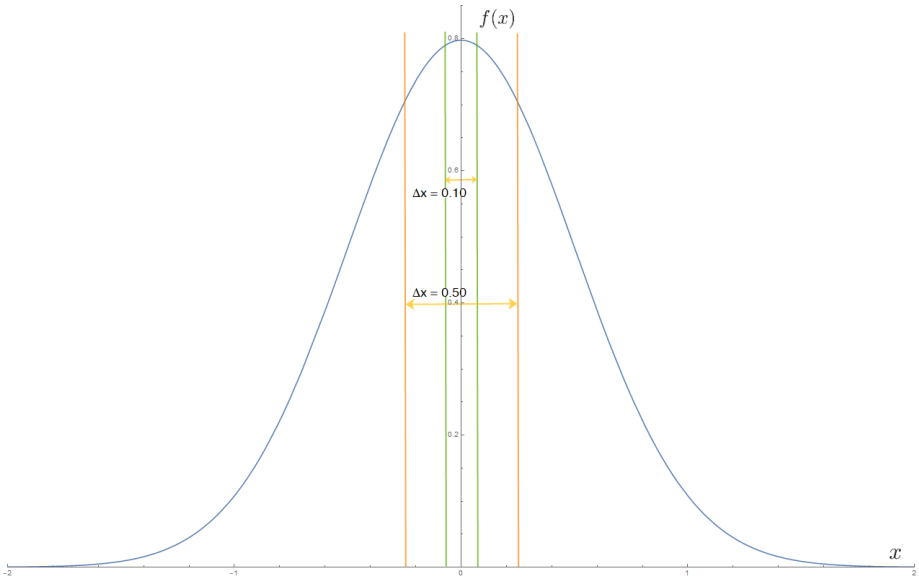

FIGURE 5.30: Probability distribution of a coherent state of amplitude $|\alpha| = 0$ (the vacuum state) as a function of position x including the homodyne measurement bandwidth Δx, where $\Delta x = 0.1$ and $\Delta x = 0.5$.

in which we have also given two different homodyne resolution bandwidths of $\Delta x = 0.1$ and $\Delta x = 0.5$ to show the extremal cases. Note that if we apply the imperfect homodyne projector of Eq. 5.9 to the probability distribution given in Eq. 5.11 then we would only see a distribution between the limits of whatever we set Δx to.

Clearly as we reduce this bandwidth we are then *allowing* for fewer homodyne measurement outcomes. This, in fact, is how we determine success probability for

the homodyne measurement (which we denote as $\mathcal{P}_{HD}$) - if we consider the "success" of performing a homodyne measurement as the fraction of *accepted* outcomes, then determining success probability for this measurement is done by simply calculating the ratio of how much of the probability distribution we allow for (given by the bandwidth Δx) by the whole probability distribution (i.e. every possible measurement outcome). This will be covered in detail for specific values of the coherent state amplitude $|\alpha|$ in Chapter 6, Subsec. 6.1.2.

5.5 Imperfect Homodyne for Coherent State ES

To build our final density matrix, containing a resolution bandwidth Δx, to assess homodyne measurement imperfections in the coherent state equal loss protocol we begin with Eq. 3.31 (the state immediately after the vacuum projection, and before the homodyne measurement). We then apply the imperfect homodyne operator as per Eq. 5.9, for measurement angle $\theta = \frac{\pi}{2}$, such that:

$$
\begin{aligned}
|\Psi^{Coh.}_{loss}\rangle_{A\varepsilon_B CD\varepsilon_D} = \mathcal{N}\Big[& |00\rangle_{AC}\, |\sqrt{2T}\,|\alpha|\rangle_D\, |\sqrt{1-T}\,|\alpha|\rangle_{\varepsilon_B}\, |\sqrt{1-T}\,|\alpha|\rangle_{\varepsilon_D} \\
& + |11\rangle_{AC}\, |-\sqrt{2T}\,|\alpha|\rangle_D\, |-\sqrt{1-T}\,|\alpha|\rangle_{\varepsilon_B}\, |-\sqrt{1-T}\,|\alpha|\rangle_{\varepsilon_D} \\
& + |0\rangle_D\, e^{-T|\alpha|^2}\Big(|01\rangle_{AC}\, |\sqrt{1-T}\,|\alpha|\rangle_{\varepsilon_B}\, |-\sqrt{1-T}\,|\alpha|\rangle_{\varepsilon_D} \\
& + |10\rangle_{AC}\, |-\sqrt{1-T}\,|\alpha|\rangle_{\varepsilon_B}\, |\sqrt{1-T}\,|\alpha|\rangle_{\varepsilon_D} \Big)\Big],
\end{aligned}
\tag{5.12}
$$

$$
\begin{aligned}
\int_{x_0-\frac{\Delta x}{2}}^{x_0+\frac{\Delta x}{2}} & |x_{\frac{\pi}{2}}\rangle_D\, \langle x_{\frac{\pi}{2}}|\Psi^{Coh.}_{loss}\rangle_{A\varepsilon_B CD\varepsilon_D}\, \mathrm{d}x_{\frac{\pi}{2}} = \int_{-\frac{\Delta x}{2}}^{+\frac{\Delta x}{2}} |\Psi^{Coh.}_{loss}\rangle_{A\varepsilon_B C\varepsilon_D}\, \mathrm{d}x_{\frac{\pi}{2}} \\
= & \ |\Psi^{Coh.}_{\Delta x}\rangle_{A\varepsilon_B C\varepsilon_D} \\
= & \int_{-\frac{\Delta x}{2}}^{+\frac{\Delta x}{2}} \mathcal{N}\frac{\exp\left[-(x_{\frac{\pi}{2}})^2\right]}{2^{-\frac{1}{4}}\pi^{\frac{1}{4}}} \\
& \Big[e^{-2\sqrt{2}\, i\sqrt{T}\,|\alpha| x_{\frac{\pi}{2}}}\, |00\rangle_{AC}\, |\sqrt{1-T}\,|\alpha|\rangle_{\varepsilon_B}\, |\sqrt{1-T}\,|\alpha|\rangle_{\varepsilon_D} \\
& + e^{2\sqrt{2}\, i\sqrt{T}\,|\alpha| x_{\frac{\pi}{2}}}\, |11\rangle_{AC}\, |-\sqrt{1-T}\,|\alpha|\rangle_{\varepsilon_B}\, |-\sqrt{1-T}\,|\alpha|\rangle_{\varepsilon_D} \\
& e^{-T|\alpha|^2}\Big(|01\rangle_{AC}\, |\sqrt{1-T}\,|\alpha|\rangle_{\varepsilon_B}\, |-\sqrt{1-T}\,|\alpha|\rangle_{\varepsilon_D} \\
& + |10\rangle_{AC}\, |-\sqrt{1-T}\,|\alpha|\rangle_{\varepsilon_B}\, |\sqrt{1-T}\,|\alpha|\rangle_{\varepsilon_D} \Big)\Big] \mathrm{d}x_{\frac{\pi}{2}},
\end{aligned}
\tag{5.13}
$$

in which we have set $x_0 = 0$ in the final step (as this is the ideal homodyne outcome), and the subscript Δx on the total quantum state $|\Psi^{Coh.}_{\Delta x}\rangle_{A\varepsilon_B CD\varepsilon_D}$ denotes that this is being evaluated for homodyne imperfections.

Note that thus far in this work we have omitted the $\frac{\exp\left[-(x_{\frac{\pi}{2}})^2\right]}{2^{-\frac{1}{4}}\pi^{\frac{1}{4}}}$ term following all homodyne measurements (as done so in the analytical derivation of our final density matrices in Chapters 3 and 4); this term describes the probability amplitude

at the vacuum - i.e. $\langle x_\theta|0\rangle = \frac{\exp\left[-(x_\theta)^2\right]}{2^{-\frac{1}{4}}\pi^{\frac{1}{4}}}$ - and so this is present in all homodyne outcomes (all other terms are merely a shift of this probability amplitude in the position/momentum phase space), and hence is removed by the normalisation. The reason we do *not* wish to omit this term in this case is that it is inherently vital for the subsequent integration calculation.

Lastly, to build our final density matrix from the above quantum state (Eq. 5.13) we then trace out the lossy modes ε_B and ε_D as per the method outlined in Chapter 3, Subsec. 3.2.4, to then give us:

$$\rho_{AC}^{Coh.}(\Delta x) = \mathrm{Tr}_{\varepsilon_B,\varepsilon_D}\left[\int_{-\frac{\Delta x}{2}}^{+\frac{\Delta x}{2}} |\Psi^{Coh.}\rangle_{A\varepsilon_B C\varepsilon_D}\, \mathrm{d}x_{\frac{\pi}{2}} \int_{-\frac{\Delta x}{2}}^{+\frac{\Delta x}{2}} {}_{A\varepsilon_B C\varepsilon_D}\langle\Psi^{Coh.}|\, \mathrm{d}x_{\frac{\pi}{2}}\right]. \tag{5.14}$$

We can now determine entanglement negativity, linear entropy and fidelity (against the $|\Phi^+\rangle = \frac{1}{\sqrt{2}}(|00\rangle + |11\rangle)$ Bell state) of the above density matrix, to investigate the impact in which allowing for a resolution bandwidth Δx of the homodyne measurement may have on our entanglement swapping protocol outcome.

5.5.1 Entanglement Negativity and Linear Entropy

Firstly, we present plots for entanglement negativity and linear entropy as a function of the coherent state amplitude $|\alpha|$, with varying Δx, before moving on to discuss fidelity.

The following plots are entanglement negativity for $T = 1$ and $T = 0.95$ (Figs. 5.31 and 5.32 respectively):

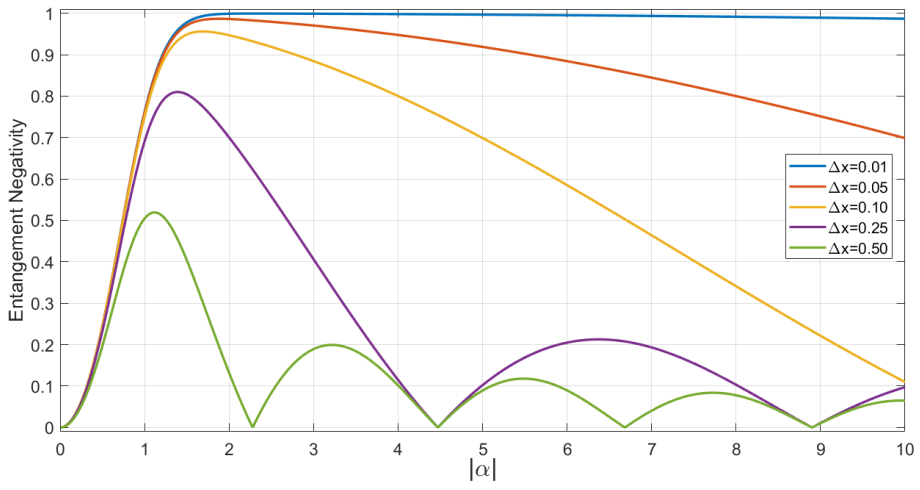

FIGURE 5.31: Entanglement negativity as a function of $|\alpha|$ for the final state generated via our coherent state entanglement swapping protocol (Eq. 5.14), for $T = 1$ and varying homodyne measurement bandwidth Δx.

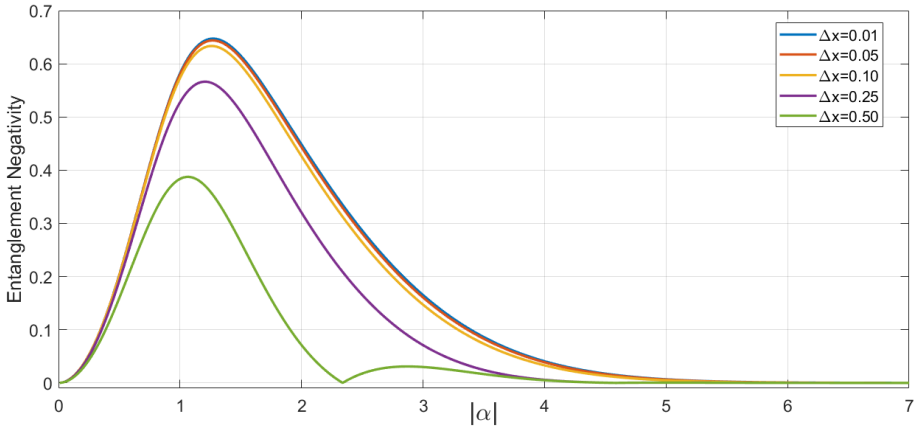

FIGURE 5.32: Entanglement negativity as a function of $|\alpha|$ for the final state generated via our coherent state entanglement swapping protocol (Eq. 5.14), for $T = 0.95$ and varying homodyne measurement bandwidth Δx.

We can immediately notice from the above plots that introducing a homodyne resolution bandwidth Δx causes oscillations to appear - this oscillatory behaviour becomes less pronounced when allowing for loss, as per Fig. 5.32, and this trend has been noticed when introducing non-ideal homodyne measurement outcomes (compare the fidelity plots of Figs. 5.6 and 5.8). This is, again, because the exponential dampening terms, which are dependent on both T and $|\alpha|$, that are introduced when tracing out the lossy modes have a stronger influence on the amplitudes of each term in the final density matrix (Eq. 5.14) than the phases do. This oscillatory behaviour will be justified in the following subsection in terms of fidelity.

What is also noticeable in Figs. 5.31 and 5.32 is that there is only a very small difference between the peak entanglement negativity values when increasing the resolution bandwidth from $\Delta x = 0.01$ to $\Delta x = 0.10$, and in fact the difference between the peak values is lessened even more in the $T = 0.95$ plot. This is a positive result, as the purpose of this investigation into homodyne measurement imperfections is that we wish to assume that a homodyne detector has a relatively high resolution bandwidth (i.e. $0.10 \leq \Delta x \leq 0.25$). We will see in the next section whether, more importantly, the fidelity results follow this pattern that the value at the peak $|\alpha|$ region does not vary a lot for $0 \leq \Delta x \leq 0.10$.

Let us now compare the entanglement negativity plots of Figs. 5.31 and 5.32 with plots for linear entropy (Figs. 5.33 and 5.34):

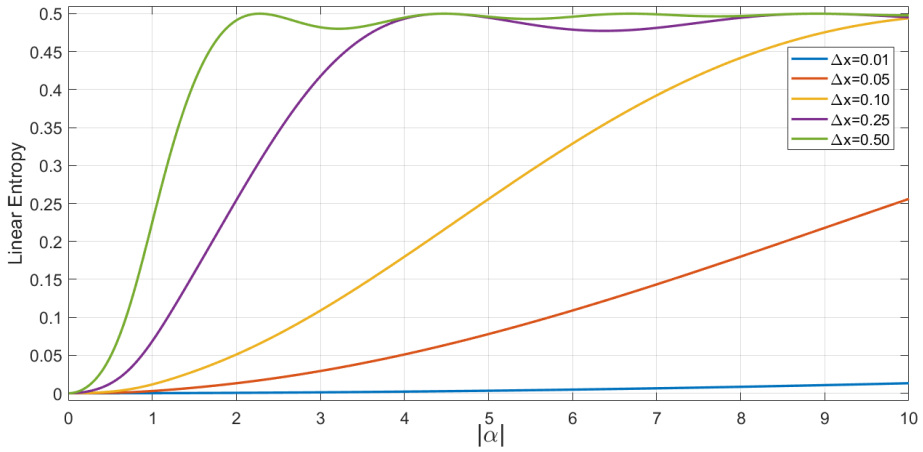

FIGURE 5.33: Linear entropy as a function of $|\alpha|$ for the final state generated via our coherent state entanglement swapping protocol (Eq. 5.14), for $T = 1$ and varying homodyne measurement bandwidth Δx.

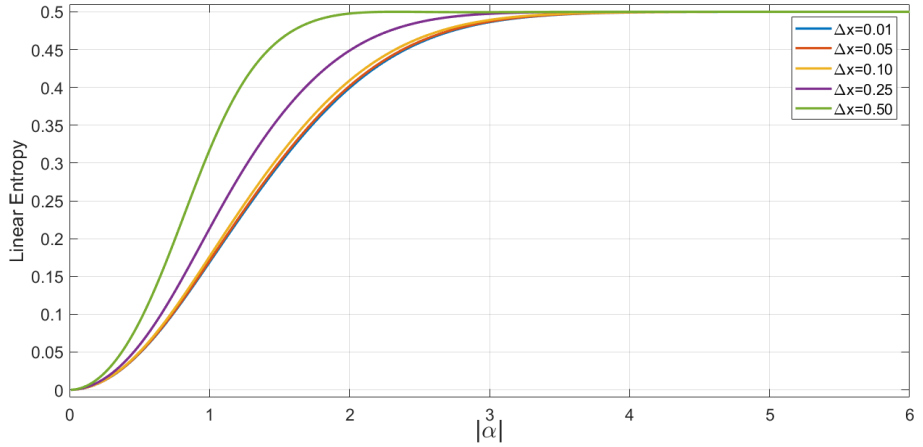

FIGURE 5.34: Linear entropy as a function of $|\alpha|$ for the final state generated via our coherent state entanglement swapping protocol (Eq. 5.14), for $T = 0.95$ and varying homodyne measurement bandwidth Δx.

Patently, it is immediately clear when observing the above linear entropy plots, particularly in the no loss regime, that the regions in which the entanglement negativity plots reach $\mathcal{N}(\rho) = 0$ (see Figs. 5.31 and 5.32) correspond perfectly with the points in which the above linear entropy plots reach their maximum of $S_L = 0.50$. As always, we absolutely expect linear entropy to compliment, and somewhat mirror, the effects we see in the equivalent entanglement negativity plots, and so the above linear entropy plots of Figs. 5.33 and 5.34 indeed follow this pattern well.

5.5.2 Fidelity

We now discuss fidelity against the $|\Phi^+\rangle = \frac{1}{\sqrt{2}}(|00\rangle + |11\rangle)$ Bell state and the orthogonal $|\Phi^-\rangle = \frac{1}{\sqrt{2}}(|00\rangle - |11\rangle)$ Bell state as a function of the coherent state amplitude $|\alpha|$, to investigate how high we can allow our homodyne measurement resolution bandwidth Δx to be whilst still giving an acceptable resultant fidelity.

Firstly, in Fig. 5.35 we plot the case for no loss ($T = 1$):

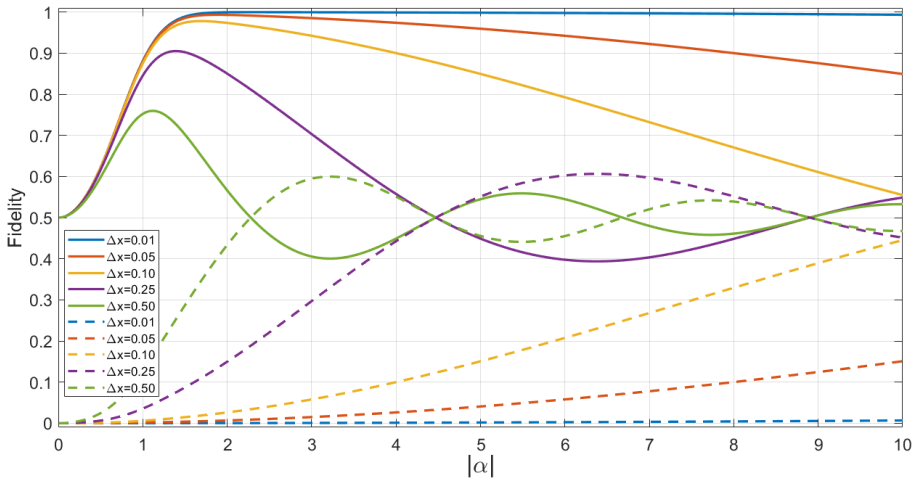

FIGURE 5.35: Fidelity against the $|\Phi^+\rangle = \frac{1}{\sqrt{2}}(|00\rangle + |11\rangle)$ Bell state (solid lines in plot) and the orthogonal $|\Phi^-\rangle = \frac{1}{\sqrt{2}}(|00\rangle - |11\rangle)$ Bell state (dotted lines in plot) as a function of $|\alpha|$ for the final state generated via our coherent state entanglement swapping protocol (Eq. 5.14), for $T = 1$ and varying homodyne measurement bandwidth Δx.

Once more, we can see that there are oscillations present in this plot (Fig. 5.35), which again we can conclude is due to the phases present in the final density matrix Eq. 5.14. In fact, we can easily see that when the fidelity against the $|\Phi^+\rangle$ Bell state drops to $F = 0.50$, the fidelity against the orthogonal $|\Phi^-\rangle$ Bell state increases to $F = 0.50$ - furthermore, the exact $|\alpha|$ value in which this effect occurs at matches the $|\alpha|$ value in which the entanglement negativity plot (Fig. 5.31) drops to $\mathcal{N}(\rho) = 0$. Of course, we intrinsically expect this to be the case, since a 50:50 mixture of two orthogonal Bell states must also exhibit no entanglement. This is also confirmed by the linear entropy plot of Fig. 5.33, in which the entropy reaches the plot maximum of $S_L = 0.50$ at these corresponding $|\alpha|$ values, also demonstrating oscillatory behaviour, as already discussed.

Encouragingly, Fig. 5.35 indicates that, as demonstrated in the entanglement negativity plot of Fig. 5.31, there is only a very slight difference between the fidelity results at the peak $|\alpha|$ value for $0 \leq \Delta x \leq 0.10$. As already stated, this is a positive result as it means that we can tolerate a small resolution bandwidth of the homodyne measurement, and even were we to allow the bandwidth to increase even higher to $\Delta x = 0.25$ then the fidelity, for the no loss regime, is still $F = 0.90$.

We now investigate the circumstance in which we have high levels of loss ($T = 0.95$) in Figs. 5.36 and 5.37, to see whether we can tolerate this level of homodyne imperfections, whilst still giving a decent resultant fidelity:

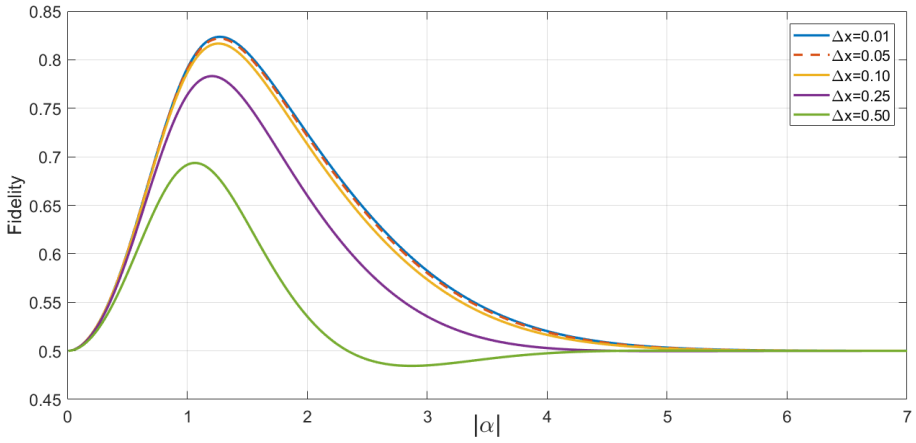

FIGURE 5.36: Fidelity against the $|\Phi^+\rangle = \frac{1}{\sqrt{2}}(|00\rangle + |11\rangle)$ Bell state as a function of $|\alpha|$ for the final state generated via our coherent state entanglement swapping protocol (Eq. 5.14), for $T = 0.95$ and varying homodyne measurement bandwidth Δx.

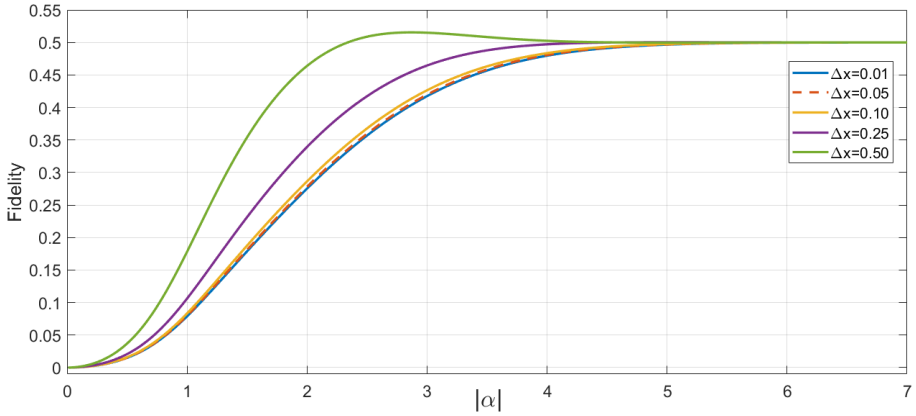

FIGURE 5.37: Fidelity against the $|\Phi^-\rangle = \frac{1}{\sqrt{2}}(|00\rangle - |11\rangle)$ Bell state as a function of $|\alpha|$ for the final state generated via our coherent state entanglement swapping protocol (Eq. 5.14), for $T = 0.95$ and varying homodyne measurement bandwidth Δx.

Comparing the above plots (Figs. 5.36 and 5.37), we see that we no longer have oscillations present, and this is again due to introducing a dampening exponent via tracing out the lossy modes ε_B and ε_D, which has a stronger influence on the final density matrix than the oscillatory behaviour dependent on Δx does. Moreover, as expected, we can see that when the fidelity against the $|\Phi^+\rangle$ Bell state decreases and plateaus at $F = 0.50$ in Fig. 5.36, the fidelity against the $|\Phi^-\rangle$ Bell state increases and plateaus at $F = 0.50$ in Fig. 5.37, as seen in the no loss plot of Fig. 5.35.

Finally, we can conclude that there is effectively no difference in the resultant fidelity values, in the peak $|\alpha|$ regions, for $0 \leq \Delta x \leq 0.10$, as was seen in the no loss plot. In fact, even when allowing for relatively high photon losses of $T = 0.95$, we can still tolerate a resolution bandwidth of $\Delta x = 0.25$ and still produce an entangled pair of photons, via our coherent state entanglement swapping protocol, although the fidelity in this case is slightly below our target of $F = 0.80$ against the $|\Phi^+\rangle$ Bell state.

5.6 Imperfect Homodyne for Cat State ES

We now move on to discuss imperfect homodyne detection for our proposed cat state entanglement swapping protocol, to determine if we can tolerate a relatively small resolution bandwidth Δx, whilst still giving acceptable fidelity results against the $|\Phi^+(\alpha)\rangle = \frac{1}{\sqrt{2}}(|00\rangle\, e^{-i|\alpha|^2} + |11\rangle\, e^{+i|\alpha|^2})$ Bell state.

To build the density matrix containing the homodyne bandwidth variable Δx for the cat state lossy protocol, we begin with the equal loss state, immediately after the vacuum measurement and before the homodyne measurement, given by Eq. 3.63. We then apply the imperfect homodyne operator as per Eq. 5.9, for measurement angle $\theta = \frac{\pi}{4}$, such that:

$$
\begin{aligned}
&|\Psi^{Cat}_{loss}\rangle_{A\varepsilon_B CD\varepsilon_D} = \mathcal{N} \\
&\times\Big[\, |00\rangle_{AC}\Big[\, |\sqrt{2T}\,|\alpha|\rangle_D\, |\gamma|\alpha|\rangle_{\varepsilon_B}\, |\gamma|\alpha|\rangle_{\varepsilon_D} + |-\sqrt{2T}\,|\alpha|\rangle_D\, |-\gamma|\alpha|\rangle_{\varepsilon_B}\, |-\gamma|\alpha|\rangle_{\varepsilon_D} \\
&+e^{-T|\alpha|^2}\,|0\rangle_D\Big(\, |\gamma|\alpha|\rangle_{\varepsilon_B}\, |-\gamma|\alpha|\rangle_{\varepsilon_D} + |-\gamma|\alpha|\rangle_{\varepsilon_B}\, |\gamma|\alpha|\rangle_{\varepsilon_D}\Big)\Big] \\
&+e^{\frac{-T|\alpha|^2}{2}}\,|01\rangle_{AC} \\
&\quad\Big[\, |\sqrt{T}\,|\alpha|e^{\frac{i\pi}{4}}\rangle_D\, |\gamma|\alpha|\rangle_{\varepsilon_B}\, |\gamma\mathbf{i}|\alpha|\rangle_{\varepsilon_D} + |\sqrt{T}\,|\alpha|e^{\frac{-i\pi}{4}}\rangle_D\, |\gamma|\alpha|\rangle_{\varepsilon_B}\, |-\gamma\mathbf{i}|\alpha|\rangle_{\varepsilon_D} \\
&+|-\sqrt{T}\,|\alpha|e^{\frac{-i\pi}{4}}\rangle_D\, |-\gamma|\alpha|\rangle_{\varepsilon_B}\, |\gamma\mathbf{i}|\alpha|\rangle_{\varepsilon_D} + |-\sqrt{T}\,|\alpha|e^{\frac{i\pi}{4}}\rangle_D\, |-\gamma|\alpha|\rangle_{\varepsilon_B}\, |-\gamma\mathbf{i}|\alpha|\rangle_{\varepsilon_D}\Big] \\
&+e^{\frac{-T|\alpha|^2}{2}}\,|10\rangle_{AC} \\
&\quad\Big[\, |\sqrt{T}\,|\alpha|e^{\frac{i\pi}{4}}\rangle_D\, |\gamma\mathbf{i}|\alpha|\rangle_{\varepsilon_B}\, |\gamma|\alpha|\rangle_{\varepsilon_D} + |-\sqrt{T}\,|\alpha|e^{\frac{-i\pi}{4}}\rangle_D\, |\gamma\mathbf{i}|\alpha|\rangle_{\varepsilon_B}\, |-\gamma|\alpha|\rangle_{\varepsilon_D} \\
&+|\sqrt{T}\,|\alpha|e^{\frac{-i\pi}{4}}\rangle_D\, |-\gamma\mathbf{i}|\alpha|\rangle_{\varepsilon_B}\, |\gamma|\alpha|\rangle_{\varepsilon_D} + |-\sqrt{T}\,|\alpha|e^{\frac{i\pi}{4}}\rangle_D\, |-\gamma\mathbf{i}|\alpha|\rangle_{\varepsilon_B}\, |-\gamma|\alpha|\rangle_{\varepsilon_D}\Big] \\
&+|11\rangle_{AC}\Big[\, |\sqrt{2T}\,\mathbf{i}|\alpha|\rangle_D\, |\gamma\mathbf{i}|\alpha|\rangle_{\varepsilon_B}\, |\gamma\mathbf{i}|\alpha|\rangle_{\varepsilon_D} + |-\sqrt{2T}\,\mathbf{i}|\alpha|\rangle_D\, |-\gamma\mathbf{i}|\alpha|\rangle_{\varepsilon_B}\, |-\gamma\mathbf{i}|\alpha|\rangle_{\varepsilon_D} \\
&+e^{-T|\alpha|^2}\,|0\rangle_D\Big(\, |\gamma\mathbf{i}|\alpha|\rangle_{\varepsilon_B}\, |-\gamma\mathbf{i}|\alpha|\rangle_{\varepsilon_D} + |-\gamma\mathbf{i}|\alpha|\rangle_{\varepsilon_B}\, |\gamma\mathbf{i}|\alpha|\rangle_{\varepsilon_D}\Big)\Big]\Big], \qquad (5.15)
\end{aligned}
$$

$$
\begin{aligned}
&\int_{x_0-\frac{\Delta x}{2}}^{x_0+\frac{\Delta x}{2}} |x_{\frac{\pi}{4}}\rangle_D\, \langle x_{\frac{\pi}{4}}|\Psi^{Cat}_{loss}\rangle_{A\varepsilon_B CD\varepsilon_D}\, \mathrm{d}x_{\frac{\pi}{4}} = \int_{\pm\sqrt{T}|\alpha|-\frac{\Delta x}{2}}^{\pm\sqrt{T}|\alpha|+\frac{\Delta x}{2}} |\Psi^{Cat}_{loss}\rangle_{A\varepsilon_B C\varepsilon_D}\, \mathrm{d}x_{\frac{\pi}{4}} \\
&= |\Psi^{Cat}_{\Delta x}\rangle_{A\varepsilon_B C\varepsilon_D} \qquad (5.16)
\end{aligned}
$$

$$
\begin{aligned}
&= \int_{\pm\sqrt{T}\,|\alpha|-\frac{\Delta x}{2}}^{\pm\sqrt{T}\,|\alpha|+\frac{\Delta x}{2}} \mathcal{N}\frac{\exp\left[-(x_{\frac{\pi}{4}})^2\right]}{2^{-\frac{1}{4}}\pi^{\frac{1}{4}}} \\
&\quad\times\Big[\,|00\rangle_{AC}\Big(\exp\Big[(1-\mathrm{i})2\sqrt{T}\,|\alpha|x_{\frac{\pi}{4}}+(\mathrm{i}-1)T|\alpha|^2\Big]\,|\gamma|\alpha|\rangle_{\varepsilon_B}\,|\gamma|\alpha|\rangle_{\varepsilon_D} \\
&\qquad+\exp\Big[-(1-\mathrm{i})2\sqrt{T}\,|\alpha|x_{\frac{\pi}{4}}+(\mathrm{i}-1)T|\alpha|^2\Big]\,|-\gamma|\alpha|\rangle_{\varepsilon_B}\,|-\gamma|\alpha|\rangle_{\varepsilon_D} \\
&\qquad+e^{-T|\alpha|^2}\Big(\,|\gamma|\alpha|\rangle_{\varepsilon_B}\,|-\gamma|\alpha|\rangle_{\varepsilon_D}+\,|-\gamma|\alpha|\rangle_{\varepsilon_B}\,|\gamma|\alpha|\rangle_{\varepsilon_D}\Big)\Big) \\
&+e^{\frac{-T|\alpha|^2}{2}}\,|01\rangle_{AC}\Big(\exp\Big[2\sqrt{T}\,|\alpha|x_{\frac{\pi}{4}}-T|\alpha|^2\Big]\,|\gamma|\alpha|\rangle_{\varepsilon_B}\,|\gamma\mathrm{i}|\alpha|\rangle_{\varepsilon_D} \\
&\qquad+\exp\Big[-2\sqrt{T}\,\mathrm{i}|\alpha|x_{\frac{\pi}{4}}\Big]\,|\gamma|\alpha|\rangle_{\varepsilon_B}\,|-\gamma\mathrm{i}|\alpha|\rangle_{\varepsilon_D} \\
&\qquad+\exp\Big[2\sqrt{T}\,\mathrm{i}|\alpha|x_{\frac{\pi}{4}}\Big]\,|-\gamma|\alpha|\rangle_{\varepsilon_B}\,|\gamma\mathrm{i}|\alpha|\rangle_{\varepsilon_D} \\
&\qquad+\exp\Big[-2\sqrt{T}\,|\alpha|x_{\frac{\pi}{4}}-T|\alpha|^2\Big]\,|-\gamma|\alpha|\rangle_{\varepsilon_B}\,|-\gamma\mathrm{i}|\alpha|\rangle_{\varepsilon_D}\Big) \\
&+e^{\frac{-T|\alpha|^2}{2}}\,|10\rangle_{AC}\Big(\exp\Big[2\sqrt{T}\,|\alpha|x_{\frac{\pi}{4}}-T|\alpha|^2\Big]\,|\gamma\mathrm{i}|\alpha|\rangle_{\varepsilon_B}\,|\gamma|\alpha|\rangle_{\varepsilon_D} \\
&\qquad+\exp\Big[2\sqrt{T}\,\mathrm{i}|\alpha|x_{\frac{\pi}{4}}\Big]\,|\gamma\mathrm{i}|\alpha|\rangle_{\varepsilon_B}\,|-\gamma|\alpha|\rangle_{\varepsilon_D} \\
&\qquad+\exp\Big[-2\sqrt{T}\,\mathrm{i}|\alpha|x_{\frac{\pi}{4}}\Big]\,|-\gamma\mathrm{i}|\alpha|\rangle_{\varepsilon_B}\,|\gamma|\alpha|\rangle_{\varepsilon_D} \\
&\qquad+\exp\Big[-2\sqrt{T}\,|\alpha|x_{\frac{\pi}{4}}-T|\alpha|^2\Big]\,|-\gamma\mathrm{i}|\alpha|\rangle_{\varepsilon_B}\,|-\gamma|\alpha|\rangle_{\varepsilon_D}\Big) \\
&\quad+|11\rangle_{AC}\Big(\exp\Big[(\mathrm{i}+1)2\sqrt{T}\,|\alpha|x_{\frac{\pi}{4}}-(\mathrm{i}+1)T|\alpha|^2\Big]\,|\gamma\mathrm{i}|\alpha|\rangle_{\varepsilon_B}\,|\gamma\mathrm{i}|\alpha|\rangle_{\varepsilon_D} \\
&\qquad+\exp\Big[-(1+\mathrm{i})2\sqrt{T}\,|\alpha|x_{\frac{\pi}{4}}-(\mathrm{i}+1)T|\alpha|^2\Big]\,|-\gamma\mathrm{i}|\alpha|\rangle_{\varepsilon_B}\,|-\gamma\mathrm{i}|\alpha|\rangle_{\varepsilon_D} \\
&\qquad+e^{-T|\alpha|^2}\Big(\,|\gamma\mathrm{i}|\alpha|\rangle_{\varepsilon_B}\,|-\gamma\mathrm{i}|\alpha|\rangle_{\varepsilon_D}+\,|-\gamma\mathrm{i}|\alpha|\rangle_{\varepsilon_B}\,|\gamma\mathrm{i}|\alpha|\rangle_{\varepsilon_D}\Big)\Big)\Big]\,\mathrm{d}x_{\frac{\pi}{4}},
\end{aligned}
\tag{5.17}
$$

in which we have set $x_0 = \pm\sqrt{T}\,|\alpha|$ in the final step (as these are the ideal homodyne outcomes). Note that, as we saw in the equal loss *perfect* homodyne case (Chapter 3, Sec 3.4.2), either ideal homodyne measurement outcome, $x_0 = +\sqrt{T}\,|\alpha|$ or $x_0 = -\sqrt{T}\,|\alpha|$, gives the same protocol outcome.

Lastly, to build our final density matrix from the above quantum state (Eq. 5.17) we then trace out the lossy modes ε_B and ε_D as per the method outlined in Chapter 3, Subsec. 3.2.4, to then give us:

$$
\begin{aligned}
&\rho_{AC}^{Cat}(\Delta x) = \\
&\mathrm{Tr}_{\varepsilon_B,\varepsilon_D}\left[\int_{\pm\sqrt{T}\,|\alpha|-\frac{\Delta x}{2}}^{\pm\sqrt{T}\,|\alpha|+\frac{\Delta x}{2}} |\Psi_{loss}^{Cat}\rangle_{A\varepsilon_B C\varepsilon_D}\,\mathrm{d}x_{\frac{\pi}{4}}\int_{\pm\sqrt{T}\,|\alpha|-\frac{\Delta x}{2}}^{\pm\sqrt{T}\,|\alpha|+\frac{\Delta x}{2}} {}_{A\varepsilon_B C\varepsilon_D}\langle\Psi_{loss}^{Cat}|\,\mathrm{d}x_{\frac{\pi}{4}}\right].
\end{aligned}
\tag{5.18}
$$

We can now determine entanglement negativity, linear entropy and fidelity (against the $|\Phi^+(\alpha)\rangle = \frac{1}{\sqrt{2}}(|00\rangle\, e^{-\mathrm{i}|\alpha|^2} + |11\rangle\, e^{+\mathrm{i}|\alpha|^2})$ Bell state) of the above density matrix, to investigate the impact in which allowing for a resolution bandwidth Δx of the homodyne measurement may have on our entanglement swapping protocol outcome.

5.6.1 Entanglement Negativity and Linear Entropy

Firstly, we present plots for entanglement negativity and linear entropy as a function of the coherent state amplitude $|\alpha|$, with varying Δx, before moving on to discuss fidelity.

The following plots are entanglement negativity for $T = 1$ and $T = 0.95$ (Figs. 5.38 and 5.39 respectively):

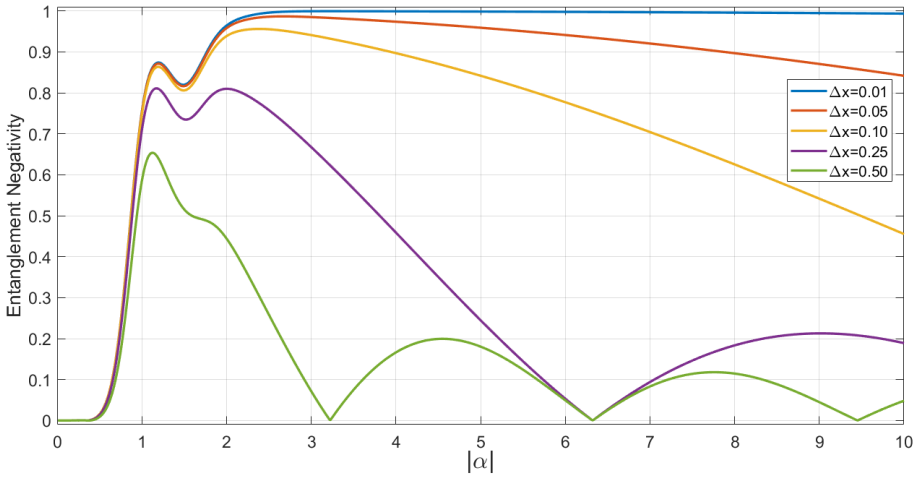

FIGURE 5.38: Entanglement negativity as a function of $|\alpha|$ for the final state generated via our cat state entanglement swapping protocol (Eq. 5.18), for $T = 1$ and varying homodyne measurement bandwidth Δx.

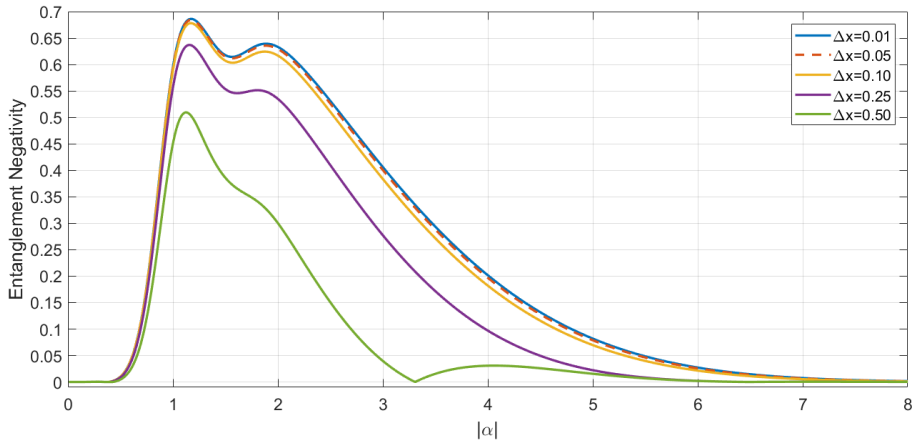

FIGURE 5.39: Entanglement negativity as a function of $|\alpha|$ for the final state generated via our cat state entanglement swapping protocol (Eq. 5.18), for $T = 0.95$ and varying homodyne measurement bandwidth Δx.

Unsurprisingly, the no loss entanglement negativity plot of Fig. 5.38 shown above also demonstrates the oscillatory behaviour we saw in the no loss coherent state imperfect homodyne plot (Figs 5.31). We would absolutely expect to see oscillations as a function of Δx and $|\alpha|$, because we can see in Eq. 5.17 that there are homodyne measurement outcome variables, $x_{\frac{\pi}{4}}$, included in many phase terms - once we integrate between the limits of $\int_{\pm\sqrt{T}|\alpha|-\frac{\Delta x}{2}}^{\pm\sqrt{T}|\alpha|+\frac{\Delta x}{2}}$, then clearly we have phase

terms that are dependent on Δx. The same is true for the coherent state protocol results of Figs. 5.31 and 5.32.

Furthermore, for $T = 0.95$, we see the typical feature, noticed throughout this work, that the oscillatory behaviour is reduced as a result of exponential dampening dependent on T and $|\alpha|$ (see equivalent coherent state result of Fig. 5.32). We also see, in both the no loss and $T = 0.95$ plots (Figs. 5.38 and 5.39 respectively) the distinctive, characteristic double-peak feature we saw in most cat state entanglement negativity plots, which is due to competing exponential terms, as already discussed in this work. Promisingly, in these plots we can also note that for $0 \leq \Delta x \leq 0.10$ there is only a negligible difference between the resultant entanglement negativity values in the peak $|\alpha|$ regions, as was witnessed in the coherent state regime.

We now compare these entanglement negativity plots with the equivalent linear entropy plots, for no loss (Fig. 5.40) and $T = 0.95$ (Fig. 5.41):

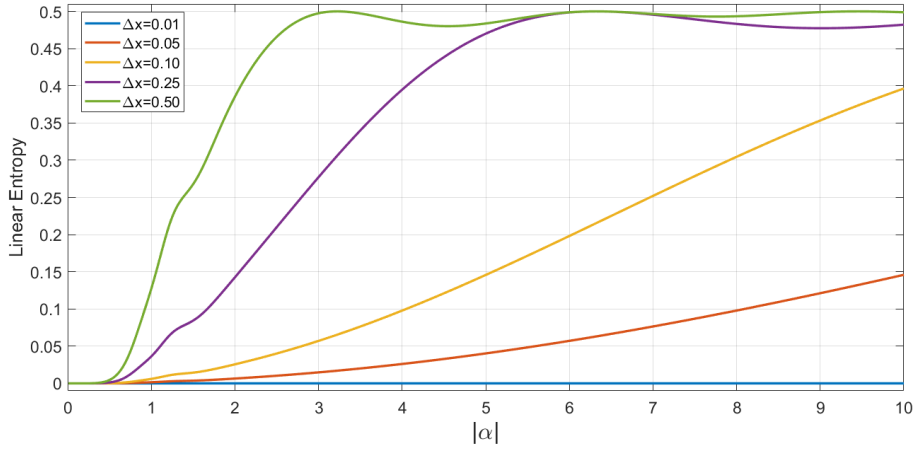

FIGURE 5.40: Linear entropy as a function of $|\alpha|$ for the final state generated via our cat state entanglement swapping protocol (Eq. 5.18), for $T = 1$ and varying homodyne measurement bandwidth Δx.

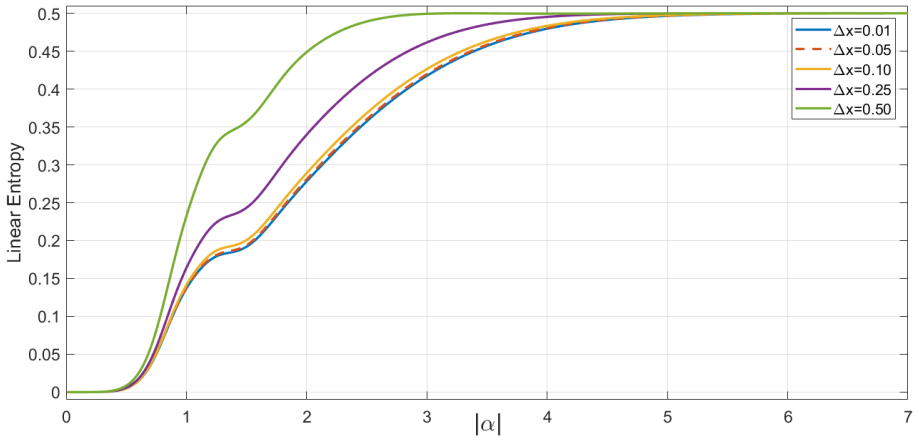

FIGURE 5.41: Linear entropy as a function of $|\alpha|$ for the final state generated via our cat state entanglement swapping protocol (Eq. 5.18), for $T = 0.95$ and varying homodyne measurement bandwidth Δx.

Once more, as we saw in the coherent state linear entropy plots (Figs. 5.33 and 5.34, for no loss and $T = 0.95$ respectively), there is oscillatory behaviour present in the no loss plots for very large Δx, and these oscillations are dampened in the case for $T = 0.95$. As before, the above linear entropy plots compliment the equivalent entanglement negativity plots of Figs. 5.38 and 5.39 perfectly - as the entanglement negativity drops to $\mathcal{N}(\rho) = 0$, then the linear entropy plots reach their maximum of $S_L = 0.50$ at the same value of $|\alpha|$. Evidently, increasing the resolution bandwidth Δx, increases the mixedness of our final density matrix.

5.6.2 Fidelity

We now discuss fidelity against the $|\Phi^+(\alpha)\rangle = \frac{1}{\sqrt{2}}(|00\rangle\, e^{-\mathrm{i}|\alpha|^2} + |11\rangle\, e^{+\mathrm{i}|\alpha|^2})$ Bell state and the orthogonal $|\Phi^-(\alpha)\rangle = \frac{1}{\sqrt{2}}(|00\rangle\, e^{-\mathrm{i}|\alpha|^2} - |11\rangle\, e^{+\mathrm{i}|\alpha|^2})$ Bell state as a function of the coherent state amplitude $|\alpha|$, to investigate how high we can allow our homodyne measurement resolution bandwidth Δx to be whilst still giving an acceptable resultant fidelity.

Firstly, in Fig. 5.42 we plot the case for no loss ($T = 1$):

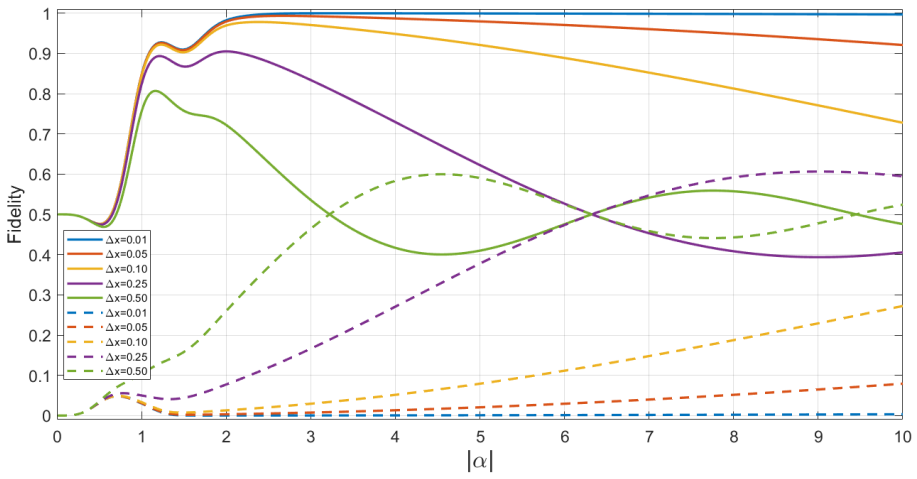

FIGURE 5.42: Fidelity against the $|\Phi^+(\alpha)\rangle = \frac{1}{\sqrt{2}}(|00\rangle\, e^{-\mathrm{i}|\alpha|^2} + |11\rangle\, e^{+\mathrm{i}|\alpha|^2})$ Bell state (solid lines in plot) and the orthogonal $|\Phi^-(\alpha)\rangle = \frac{1}{\sqrt{2}}(|00\rangle\, e^{-\mathrm{i}|\alpha|^2} - |11\rangle\, e^{+\mathrm{i}|\alpha|^2})$ Bell state (dotted lines in plot) as a function of $|\alpha|$ for the final state generated via our cat state entanglement swapping protocol (Eq. 5.18), for $T = 1$ and varying homodyne measurement bandwidth Δx.

Owing to the phases present in the final density matrix of Eq. 5.18, we again witness oscillatory behaviour in the above fidelity plot. In fact, as we saw in the equivalent coherent state circumstance, when the fidelity against the $|\Phi^+(\alpha)\rangle$ Bell state drops to $F = 0.50$, the fidelity against the orthogonal $|\Phi^-(\alpha)\rangle$ Bell state increases to $F = 0.50$, and as such the $|\alpha|$ values in which this occurs at in Fig. 5.42 correspond to the same values of $|\alpha|$ in which the entanglement negativity drops to 0 (see Fig. 5.38) and also the points in which the linear entropy reaches the plot maximum of $S_L = 0.50$ (see Fig. 5.40). As before we absolutely expect this pattern

to occur, because if one has a perfect 50:50 mixture of two orthogonal Bell states then the entanglement negativity must also be $\mathcal{N}(\rho) = 0$.

Moreover, what is favourable here is that there is a negligible difference between the fidelity values at the peak $|\alpha|$ values in Fig. 5.42, when increasing the homodyne measurement bandwidth from $\Delta x = 0$ to $\Delta x = 0.10$. In fact, even when increasing the measurement bandwidth window to $\Delta x = 0.25$ (which is likely to be the maximum, most extremal case we realistically consider), there is still only a very small difference in the peak fidelity values. Recall that we also saw this trend in the coherent state regime.

We now look to the higher loss case (Figs. 5.43 and 5.44 for fidelity against the $|\Phi^+(\alpha)\rangle$ and $|\Phi^-(\alpha)\rangle$ Bell states respectively), for $T = 0.95$

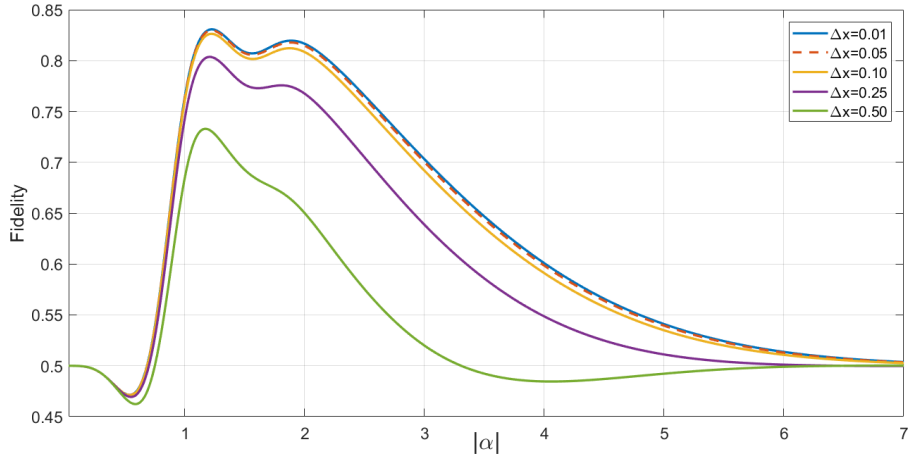

FIGURE 5.43: Fidelity against the $|\Phi^+(\alpha)\rangle = \frac{1}{\sqrt{2}}(|00\rangle\, e^{-i|\alpha|^2} + |11\rangle\, e^{+i|\alpha|^2})$ Bell state as a function of $|\alpha|$ for the final state generated via our cat state entanglement swapping protocol (Eq. 5.18), for $T = 0.95$ and varying homodyne measurement bandwidth Δx.

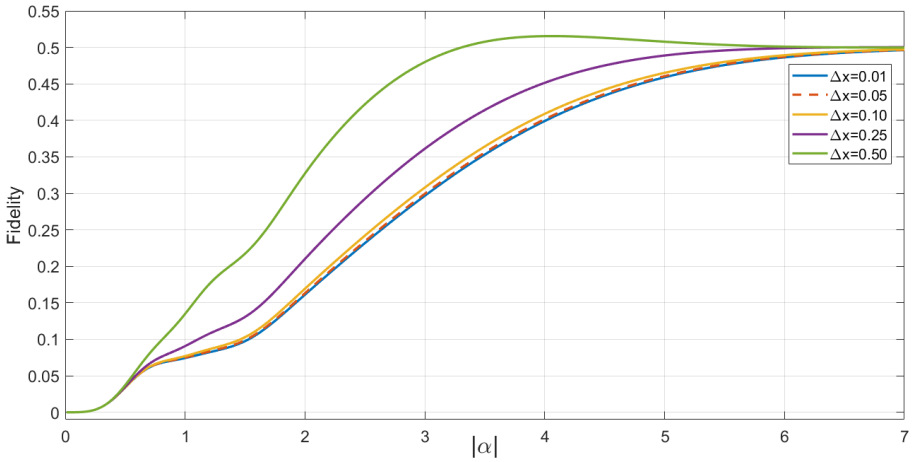

FIGURE 5.44: Fidelity against the $|\Phi^-(\alpha)\rangle = \frac{1}{\sqrt{2}}(|00\rangle\, e^{-i|\alpha|^2} - |11\rangle\, e^{+i|\alpha|^2})$ Bell state as a function of $|\alpha|$ for the final state generated via our cat state entanglement swapping protocol (Eq. 5.18), for $T = 0.95$ and varying homodyne measurement bandwidth Δx.

Evidently, we see the expected lack of oscillatory behaviour as a function of $|\alpha|$ - once more, this is entirely anticipated as we know there will be exponential dampening as a function of the level of loss exhibited in our system. Furthermore, we can conclude here that there is, again, only a very small difference when increasing the homodyne measurement bandwidth between the bounds of $0 \leq \Delta x \leq 0.10$.

Lastly, we note that the fact that the more complicated cat state entanglement swapping protocol exhibits similar oscillatory effects in the fidelity, entanglement negativity and linear entropy plots (for no loss), as we witness in the equivalent coherent state plots, is promising as it means that, despite the protocol being far more complex to calculate mathematically, one is not introducing any bizarre, undesirable effects into the protocol outcome. Indeed, one would expect the introduction of a homodyne measurement bandwidth, given as Δx, to effect the protocol outcome in a similar way regardless if the input quantum state is a hybrid entangled coherent state or a cat state.

What is also promising is that despite the cat state protocol perhaps being more complicated to implement, both theoretically and experimentally, we do see an improvement in the fidelity results for low levels of loss; this improvement is not in fact a better result in terms of the fidelity values obtained at the peak $|\alpha|$ point in the plots, but actually with respect to the fact that, because we witness a characteristic double-peak in the cat state plots, there is often a broader range of $|\alpha|$ values which give an acceptable fidelity, compared to the single sharp peak we see in the coherent state plots. This result is evident in most of the cat state results we present in this work, and is particularly noticeable in the no loss or lower loss regimes.

5.7 Combining Non-Ideal and Imperfect Homodyne Detection

In this section, we look to combine non-ideal homodyne detection (parametrised by ϵ), with imperfect homodyne detection given by the homodyne resolution bandwidth Δx. We will investigate the extremal cases, in which we push the non-ideal outcome ϵ as high as we can whilst allowing for a relatively small homodyne bandwidth of $\Delta x = 0.25$. Realistically, this is likely to be the case, as the resolution of a homodyne detector will be (and indeed should be) good enough such that Δx is relatively small.

Importantly, we must note here that despite perhaps allowing for a relatively sharp resolution bandwidth of $\Delta x \approx 0.25$ we must bear in mind that this comes at the cost of drastically lowering the success probability of this homodyne measurement. We return to an in-depth discussion of this in the following chapter (see Chapter 6, Subsec. 6.1.2).

To investigate both non-ideal and imperfect homodyne detection, we simply replace the integral limits in Eqs. 5.14 and 5.18 (for the coherent state and cat state

protocols respectively) with limits that also include ϵ, to allow for a shift in the ideal homodyne measurement outcome.

5.7.1 Coherent State ES for Non-Ideal and Imperfect Homodyne Detection

Firstly, we will investigate the more simple coherent state protocol. We therefore take the density matrix equation, evaluated for imperfect homodyne detection, of Eq. 5.14, but replace the integral limits to include ϵ, such that:

$$\begin{aligned}\rho_{AC}^{Coh.}(\Delta x,\epsilon) &= \mathrm{Tr}_{\varepsilon_B,\varepsilon_D}\left[\int_{\epsilon-\frac{\Delta x}{2}}^{\epsilon+\frac{\Delta x}{2}} |\Psi_{loss}^{Coh.}\rangle_{A\varepsilon_B C\varepsilon_D}\,\mathrm{d}x_{\frac{\pi}{2}} \int_{\epsilon-\frac{\Delta x}{2}}^{\epsilon+\frac{\Delta x}{2}} {}_{A\varepsilon_B C\varepsilon_D}\langle\Psi_{loss}^{Coh.}|\,\mathrm{d}x_{\frac{\pi}{2}}\right] \\ &= \mathrm{Tr}_{\varepsilon_B,\varepsilon_D}\left[|\Psi_{\Delta x}^{Coh.}\rangle_{A\varepsilon_B C\varepsilon_D}\,\langle\Psi_{\Delta x}^{Coh.}|\right], \end{aligned} \tag{5.19}$$

in which the quantum state $|\Psi_{\Delta x}^{Coh.}\rangle_{A\varepsilon_B C\varepsilon_D}$ is given by Eq. 5.13. This state, as before, is then computationally integrated numerically such that subsequent calculations can be carried out.

We now plot fidelity, as a function of $|\alpha|$ and ϵ, for fixed Δx. As stated previously, we wish to investigate the extremal circumstance in which the non-ideal homodyne measurement is pushed as far as can be tolerated, whilst allowing for a small homodyne resolution bandwidth. If we remind ourselves of the fidelity results given in Subsec. 5.2.2, we can see that, if we wish to produce an entangled pair of photons via our coherent state ES protocol with a fidelity of $F \geq 0.80$ against the $|\Phi^+\rangle$ Bell state, we can only tolerate a non-ideal homodyne outcome of $\epsilon \leq 0.12$ for $T \geq 0.99$, or $\epsilon \leq 0.05$ for $T = 0.95$. Therefore, we take this into consideration when plotting fidelity to involve both non-ideal and imperfect homodyne measurements, and as such the following plots are of fidelity against the $|\Phi^+\rangle$ Bell state, as a function of $|\alpha|$ and ϵ, for $T = 1$, $T = 0.99$ and $T = 0.97$ (Figs. 5.45, 5.46 and 5.47 respectively), and for $\Delta x = 0.25$:

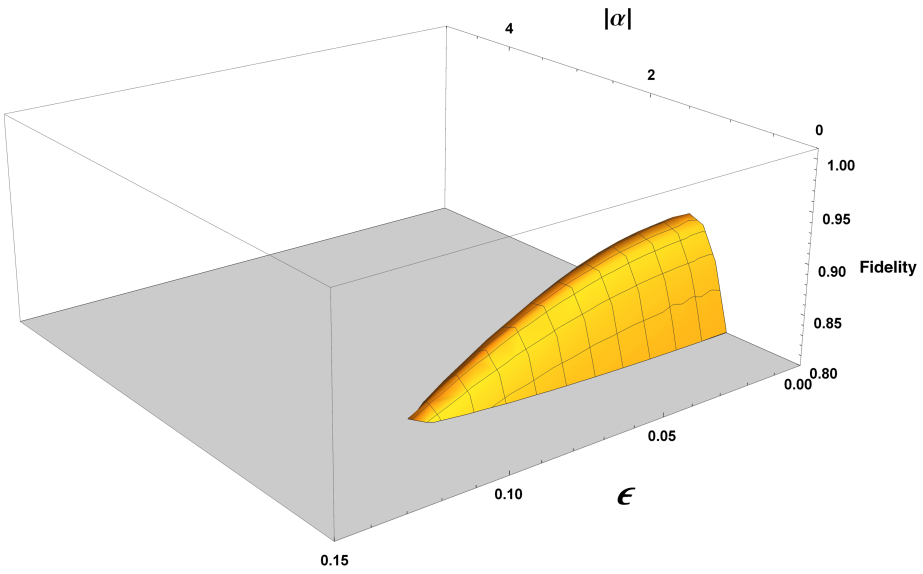

FIGURE 5.45: Fidelity against the $|\Phi^+\rangle = \frac{1}{\sqrt{2}}(|00\rangle + |11\rangle)$ Bell state as a function of $|\alpha|$ and ϵ for the final state generated via our coherent state entanglement swapping protocol (Eq. 5.19), for no loss ($T = 1$) and $\Delta x = 0.25$.

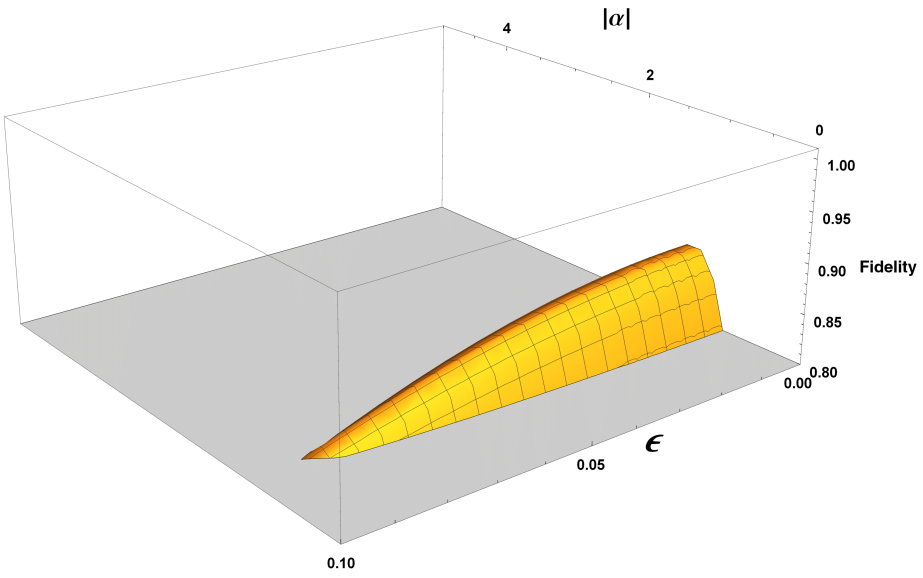

FIGURE 5.46: Fidelity against the $|\Phi^+\rangle = \frac{1}{\sqrt{2}}(|00\rangle + |11\rangle)$ Bell state as a function of $|\alpha|$ and ϵ for the final state generated via our coherent state entanglement swapping protocol (Eq. 5.19), for $T = 0.99$ and $\Delta x = 0.25$.

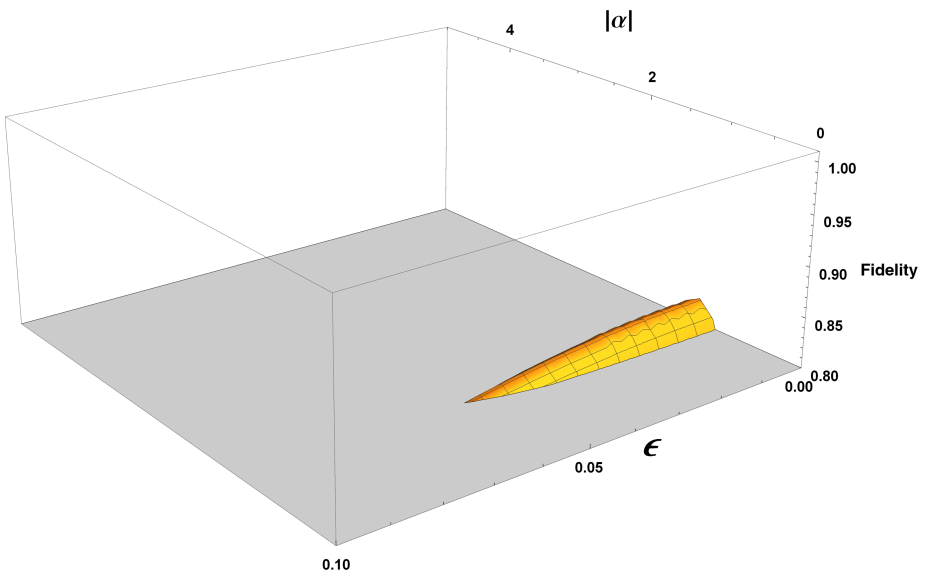

FIGURE 5.47: Fidelity against the $|\Phi^+\rangle = \frac{1}{\sqrt{2}}(|00\rangle + |11\rangle)$ Bell state as a function of $|\alpha|$ and ϵ for the final state generated via our coherent state entanglement swapping protocol (Eq. 5.19), for $T = 0.97$ and $\Delta x = 0.25$.

Firstly, we point out that we only investigate levels of photon loss up to $T = 0.97$ (Fig. 5.47) - any results for fidelity beyond this level of loss result in $F < 0.80$, for $\epsilon > 0.05$ and $\Delta x = 0.25$. Clearly, any values of non-ideal homodyne measurement outcome below $\epsilon = 0.10$ are hardly worth considering. Hence, we may easily conclude that if we allow a homodyne resolution bandwidth of $\Delta x = 0.25$, then, for our proposed coherent state ES protocol, we cannot tolerate levels of loss beyond $T = 0.99$ if we wish to allow for a fair level of non-ideal homodyne outcome, namely $\epsilon \approx 0.10$.

In truth, even when allowing for losses of $T = 0.97$, there is only a very small region in which we see a peak $|\alpha|$ value for $\epsilon = 0.05$ to give a fidelity of $F = 0.80$ - inherently, once we begin to also combine non-ideal and imperfect homodyning with unequal losses in modes B and D (see the following chapter, Chapter 6, Sec. 6.3) this region will no longer exist once we allow for any level of unequal loss for $T = 0.97$.

For now, however, we may discuss the no loss, and small loss ($T = 0.99$) plots of Figs. 5.45 and 5.46 respectively. In the no loss case it is easy to see that there is a wide range of $|\alpha|$ values that produce a high-fidelity ($F > 0.90$) $|\Phi^+\rangle$ Bell state, and if we wish to produce this Bell state with fidelity of $F \geq 0.80$, we can tolerate non-ideal outcomes of $\epsilon \leq 0.10$. Of course, assuming zero photon loss is physically unrealistic, and would never be the case in a real-life implementation of this protocol. Hence, if we now observe the $T = 0.99$ loss circumstance, of Fig. 5.46, we see that the results are slightly less tolerant with respect to ϵ: to produce the $|\Phi^+\rangle$ Bell state with fidelity of $F \geq 0.80$, we can only tolerate a non-ideal outcome of $\epsilon \leq 0.09$, and in fact there are no regions for $|\alpha|$ in which we produce this Bell state a fidelity of $F \geq 0.90$.

5.7.2 Cat State ES for Non-Ideal and Imperfect Homodyne Detection

We now move on to discuss the circumstance of non-ideal and imperfect homodyne measurements in our proposed cat state ES protocol. We again start with the density matrix equation, evaluated for imperfect homodyne detection, of Eq. 5.18, but replace the integral limits to include ϵ, such that:

$$\rho_{AC}^{Cat}(\Delta x, \pm\epsilon) = \mathrm{Tr}_{\varepsilon_B,\varepsilon_D}\left[\int_{\pm\sqrt{T}|\alpha|\pm\epsilon-\frac{\Delta x}{2}}^{\pm\sqrt{T}|\alpha|\pm\epsilon+\frac{\Delta x}{2}} |\Psi_{loss}^{Cat}\rangle_{A\varepsilon_B C\varepsilon_D}\,\mathrm{d}x_{\frac{\pi}{4}} \int_{\pm\sqrt{T}|\alpha|\pm\epsilon-\frac{\Delta x}{2}}^{\pm\sqrt{T}|\alpha|\pm\epsilon+\frac{\Delta x}{2}} {}_{A\varepsilon_B C\varepsilon_D}\langle\Psi_{loss}^{Cat}|\,\mathrm{d}x_{\frac{\pi}{4}}\right], \tag{5.20}$$

$$\rho_{AC}^{Cat}(\Delta x, \mp\epsilon) = \mathrm{Tr}_{\varepsilon_B,\varepsilon_D}\left[\int_{\pm\sqrt{T}|\alpha|\mp\epsilon-\frac{\Delta x}{2}}^{\pm\sqrt{T}|\alpha|\mp\epsilon+\frac{\Delta x}{2}} |\Psi_{loss}^{Cat}\rangle_{A\varepsilon_B C\varepsilon_D}\,\mathrm{d}x_{\frac{\pi}{4}} \int_{\pm\sqrt{T}|\alpha|\mp\epsilon-\frac{\Delta x}{2}}^{\pm\sqrt{T}|\alpha|\mp\epsilon+\frac{\Delta x}{2}} {}_{A\varepsilon_B C\varepsilon_D}\langle\Psi_{loss}^{Cat}|\,\mathrm{d}x_{\frac{\pi}{4}}\right], \tag{5.21}$$

in which we once again have two final density matrices describing the two possible outcomes for our protocol - recall that, as discussed in Sec. 5.3, there are multiple potential non-ideal homodyne measurement outcomes, given as $x_{\frac{\pi}{4}} = \pm\sqrt{T}|\alpha| \pm \epsilon$ and $x_{\frac{\pi}{4}} = \pm\sqrt{T}|\alpha| \mp \epsilon$, in which we found that the $x_{\frac{\pi}{4}} = \pm\sqrt{T}|\alpha| \pm \epsilon$ outcomes give better results for entanglement negativity and fidelity. Hence, we denote the above density matrices, given in Eqs. 5.20 and 5.21, as $\rho_{AC}^{Cat}(\Delta x, \pm\epsilon)$ and $\rho_{AC}^{Cat}(\Delta x, \mp\epsilon)$ respectively, to indicate the non-ideal homodyne measurement outcome.

Firstly, we will investigate fidelity against the $|\Phi^+(\alpha)\rangle$ Bell state as a function of $|\alpha|$ and ϵ for no loss, $T = 0.99$ and the extremal case of $T = 0.96$ (Figs. 5.48, 5.49 and 5.50 respectively), allowing for a homodyne measurement bandwidth of $\Delta x = 0.25$, for non-ideal homodyne measurement outcome $x_{\frac{\pi}{4}} = \pm\sqrt{T}|\alpha| \pm \epsilon$:

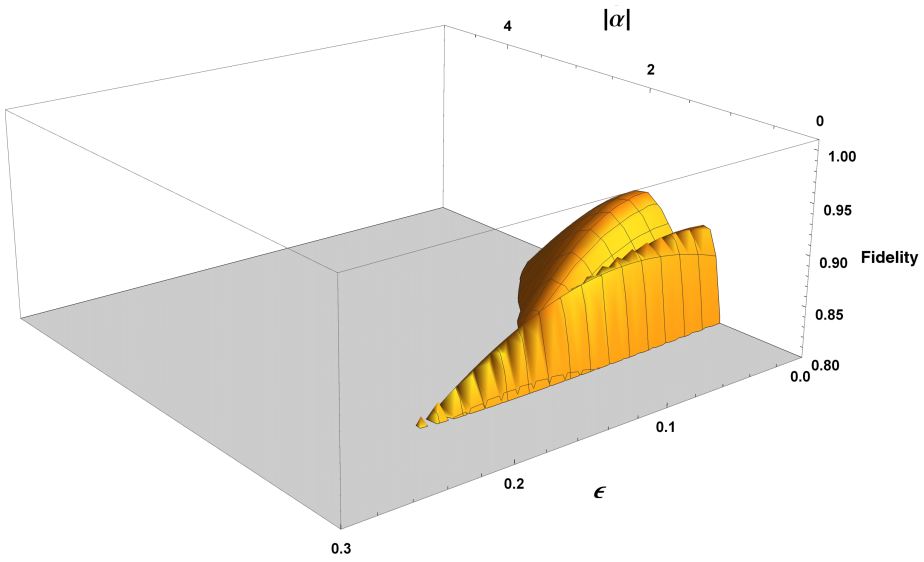

FIGURE 5.48: Fidelity against the $|\Phi^+(\alpha)\rangle = \frac{1}{\sqrt{2}}(|00\rangle\, e^{-i|\alpha|^2} + |11\rangle\, e^{+i|\alpha|^2})$ Bell state as a function of $|\alpha|$ and ϵ for the final state generated via our coherent state entanglement swapping protocol (Eq. 5.20), for no loss ($T = 1$) and $\Delta x = 0.25$, for non-ideal homodyne measurement outcome $x_{\frac{\pi}{4}} = \pm\sqrt{T}\,|\alpha| \pm \epsilon$.

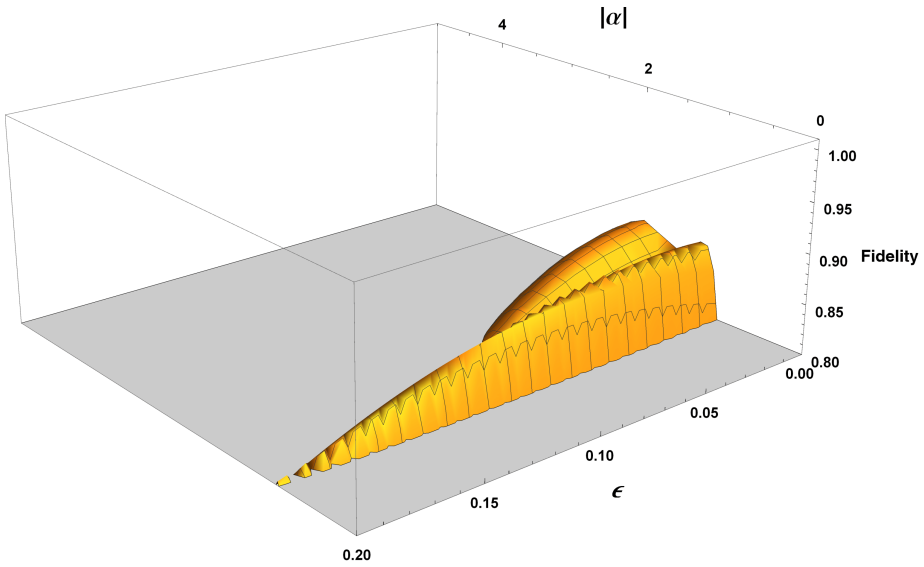

FIGURE 5.49: Fidelity against the $|\Phi^+(\alpha)\rangle = \frac{1}{\sqrt{2}}(|00\rangle\, e^{-i|\alpha|^2} + |11\rangle\, e^{+i|\alpha|^2})$ Bell state as a function of $|\alpha|$ and ϵ for the final state generated via our coherent state entanglement swapping protocol (Eq. 5.20), for $T = 0.99$ and $\Delta x = 0.25$, for non-ideal homodyne measurement outcome $x_{\frac{\pi}{4}} = \pm\sqrt{T}\,|\alpha| \pm \epsilon$.

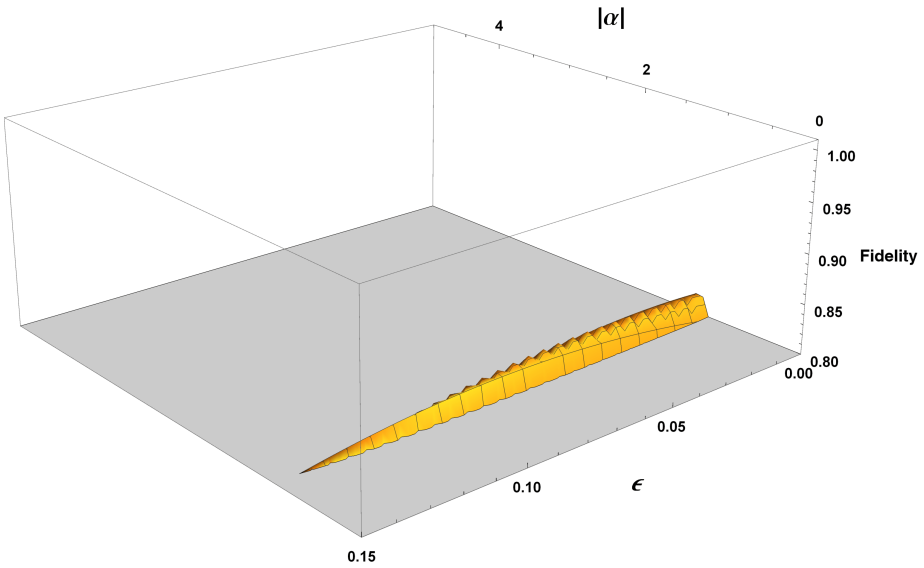

FIGURE 5.50: Fidelity against the $|\Phi^+(\alpha)\rangle = \frac{1}{\sqrt{2}}(|00\rangle\, e^{-\mathrm{i}|\alpha|^2} + |11\rangle\, e^{+\mathrm{i}|\alpha|^2})$ Bell state as a function of $|\alpha|$ and ϵ for the final state generated via our coherent state entanglement swapping protocol (Eq. 5.20), for $T = 0.96$ and $\Delta x = 0.25$, for non-ideal homodyne measurement outcome $x_{\frac{\pi}{4}} = \pm\sqrt{T}\,|\alpha| \pm \epsilon$.

Firstly, we note that the results in the extremal limit of higher losses ($T = 0.96$, as per Fig. 5.50) are more promising than those of the coherent state case - in fact, the most extremal loss case we can tolerate for the non-ideal and imperfect homodyne scenario in the coherent state regime is losses up to $T = 0.97$ and even then we can only allow a non-ideal outcome of $\epsilon \leq 0.05$ to give an acceptable fidelity of $F \geq 0.80$ against the $|\Phi^+\rangle$ Bell state (see Fig. 5.47). For the cat state regime, in the limit of $T = 0.96$ we are actually able to push the non-ideal homodyne outcome to $\epsilon \approx 0.15$ (for $x_{\frac{\pi}{4}} = \pm\sqrt{T}\,|\alpha| \pm \epsilon$) whilst still producing the $|\Phi^+(\alpha)\rangle$ Bell state with acceptable fidelity of $F = 0.80$, when allowing for a wide homodyning resolution window of $\Delta x = 0.25$.

Moreover, for lower levels of photon loss, namely $T = 0.99$ (see Fig. 5.49), we are able to accept non-ideal measurement values of $\epsilon \leq 0.20$ whilst still producing the $|\Phi^+(\alpha)\rangle$ Bell state with fidelity of $F \geq 0.80$. In addition to this, if we consider lower non-ideal measurement values of $\epsilon \leq 0.10$ then we produce this Bell state with a fidelity that almost reaches $F = 0.90$. We note that we do not quite approach fidelity greater than this, however, in the next chapter we discuss potential entanglement purification methods to increase this level of fidelity (see Chapter 6, Sec. 6.2).

All of this is very promising, as it means that the cat state protocol is more resilient to non-idealities and imperfections in the homodyne measurement, however, we must recall that there are multiple potential non-ideal homodyne outcomes for this protocol ($x_{\frac{\pi}{4}} = \pm\sqrt{T}\,|\alpha| \pm \epsilon$ and $x_{\frac{\pi}{4}} = \pm\sqrt{T}\,|\alpha| \mp \epsilon$). Thus far, in Figs. 5.48, 5.49 and 5.50, we have seen that the protocol outcomes of $x_{\frac{\pi}{4}} = \pm\sqrt{T}\,|\alpha| \pm \epsilon$ give encouraging results, in that we are able to tolerate relatively high levels of homodyne non-ideality, whilst assuming a homodyne imperfection window of $\Delta x = 0.25$.

We therefore now investigate the circumstance in which we have the non-ideal outcome of $x_{\frac{\pi}{4}} = \pm\sqrt{T}\,|\alpha| \mp \epsilon$, for no loss, $T = 0.99$, and the most extremal loss case we can tolerate in this circumstance of $T = 0.97$ (corresponding to Figs. 5.51, 5.52 and 5.53 respectively), for imperfect homodyne resolution bandwidth of $\Delta x = 0.25$:

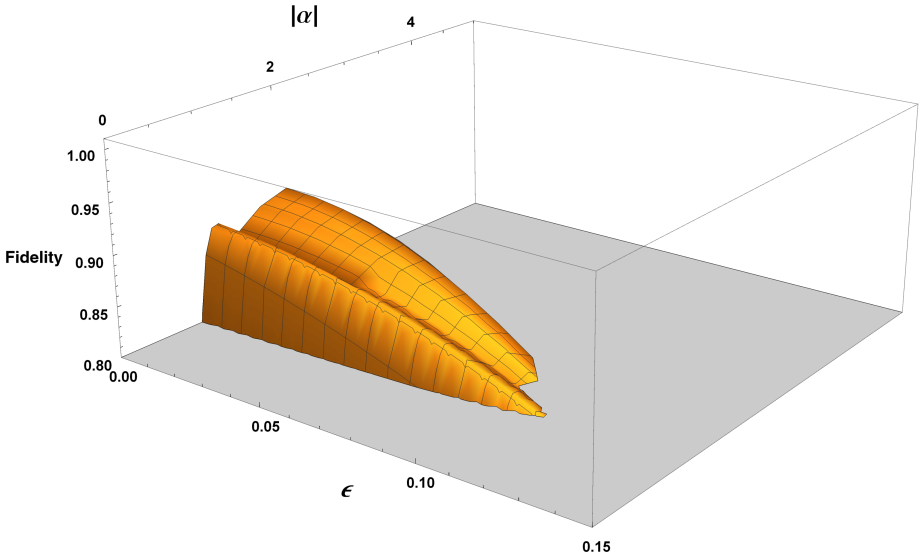

FIGURE 5.51: Fidelity against the $|\Phi^+(\alpha)\rangle = \frac{1}{\sqrt{2}}(|00\rangle\, e^{-\mathrm{i}|\alpha|^2} + |11\rangle\, e^{+\mathrm{i}|\alpha|^2})$ Bell state as a function of $|\alpha|$ and ϵ for the final state generated via our coherent state entanglement swapping protocol (Eq. 5.21), for no loss ($T = 1$) and $\Delta x = 0.25$, for non-ideal homodyne measurement outcome $x_{\frac{\pi}{4}} = \pm\sqrt{T}\,|\alpha| \mp \epsilon$.

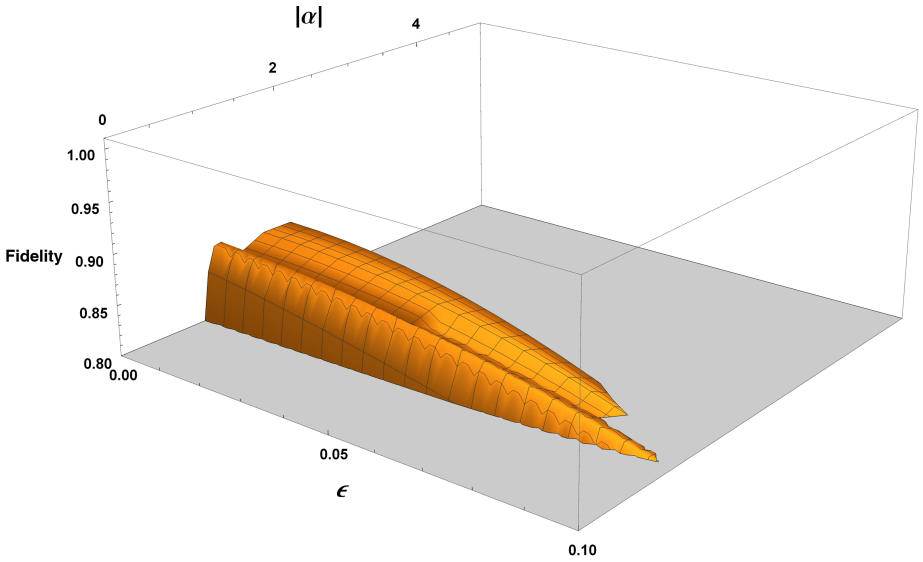

FIGURE 5.52: Fidelity against the $|\Phi^+(\alpha)\rangle = \frac{1}{\sqrt{2}}(|00\rangle\, e^{-\mathrm{i}|\alpha|^2} + |11\rangle\, e^{+\mathrm{i}|\alpha|^2})$ Bell state as a function of $|\alpha|$ and ϵ for the final state generated via our coherent state entanglement swapping protocol (Eq. 5.21), for $T = 0.99$ and $\Delta x = 0.25$, for non-ideal homodyne measurement outcome $x_{\frac{\pi}{4}} = \pm\sqrt{T}\,|\alpha| \mp \epsilon$.

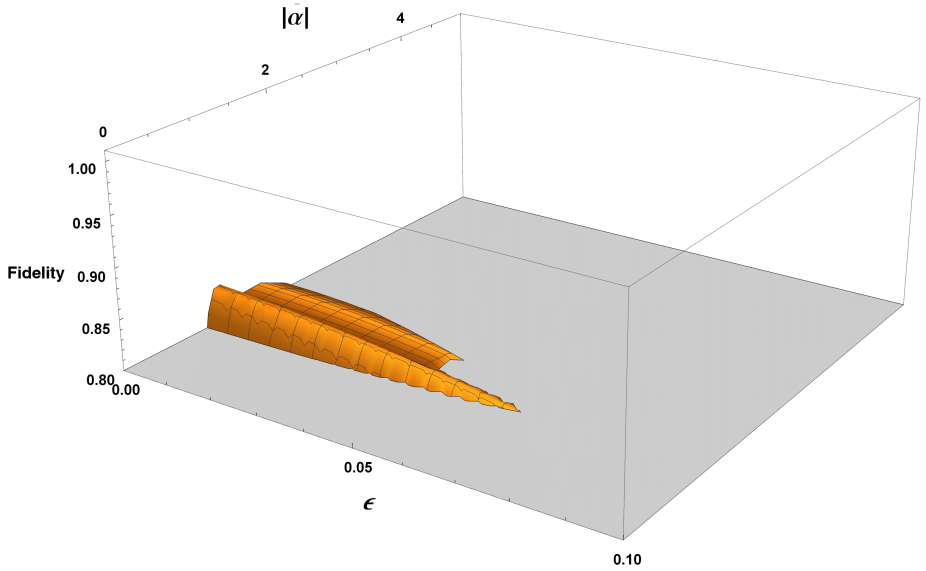

FIGURE 5.53: Fidelity against the $|\Phi^+(\alpha)\rangle = \frac{1}{\sqrt{2}}(|00\rangle\, e^{-\mathrm{i}|\alpha|^2} + |11\rangle\, e^{+\mathrm{i}|\alpha|^2})$ Bell state as a function of $|\alpha|$ and ϵ for the final state generated via our coherent state entanglement swapping protocol (Eq. 5.21), for $T = 0.97$ and $\Delta x = 0.25$, for non-ideal homodyne measurement outcome $x_{\frac{\pi}{4}} = \pm\sqrt{T}\,|\alpha| \mp \epsilon$.

Expectedly, when considering the non-ideal homodyne measurement outcome of $x_{\frac{\pi}{4}} = \pm\sqrt{T}\,|\alpha| \mp \epsilon$, the results, as displayed above, are far less tolerant as a function of ϵ as the circumstance in which the outcome is $x_{\frac{\pi}{4}} = \pm\sqrt{T}\,|\alpha| \pm \epsilon$. Already we knew this to be the case, as shown in the previous results of this chapter (see the no loss comparison example of Fig. 5.25); analytically, this pattern can be easily elucidated and justified, and was discussed previously in Subsec. 5.3.3.

If we consider the no loss plot of Fig. 5.51, then evidently we are not able to accept non-ideal values of $\epsilon \geq 0.12$ if we desire to produce the $|\Phi^+(\alpha)\rangle$ Bell state with fidelity of $F \geq 0.80$. In addition to this, if we also remark on the extremal loss case of $T = 0.97$ (Fig. 5.53) then we cannot even tolerate non-ideal values of $\epsilon > 0.08$ if we wish to abide by this fidelity limit.

5.8 Summary

In this chapter we have introduced and parametrised two variables, ϵ and Δx, to assess non-ideal homodyne measurement outcomes and imperfect homodyne detection, respectively. By allowing for non-ideal homodyne measurements, in which the shift away from the ideal measurement (given as $x_{\frac{\pi}{2}} = 0$ for the coherent state ES protocol, and $x_{\frac{\pi}{4}} = \pm\sqrt{T}\,|\alpha|$ for the cat state ES protocol) is parametrised by ϵ, we have investigated the impact on both protocols for the realistic circumstance in which the homodyne measurement outcome is not what we ideally desire.

Furthermore, by allowing for a resolution bandwidth (Δx) about the ideal measurement outcome, we have assessed the impact to the resultant state produce via our proposed ES protocol, by incorporating uncertainties into the homodyne measurement. Lastly, we combined both non-ideal and imperfect homodyne detection,

to assess the practical circumstance in which we have a shift away from the ideal measurement outcome, and consider a bandwidth about this shifted outcome.

Within this chapter we found, for the coherent state case, that the incorporation of ϵ and Δx causes our final quantum state to no longer be the $|\Phi^+\rangle = \frac{1}{\sqrt{2}}(|00\rangle+|11\rangle)$ Bell state, but instead a Bell state which contains phases - as such, this caused all fidelity plots to exhibit oscillatory behaviour as a function of $|\alpha|$, as shown by Figs. 5.6 and 5.35, for no loss. We remind the reader here that when allowing for higher levels of loss, such as $T = 0.95$, this oscillatory behaviour is no longer present (see Figs. 5.8 and 5.36), due to the fact that there is now exponential dampening of the final density matrix coefficients as a function of T and $|\alpha|$.

Despite this, we still investigate and consider fidelity only against the $|\Phi^+\rangle$ Bell state, for the reason that if this protocol was to be applied to a real-life application, such that one would carry out this protocol to supply customers with an entangled pair of qubits, we would like to provide them with the Bell state they think they would be getting, namely the $|\Phi^+\rangle$ Bell state, but with a given fidelity, which we would notify them of. Were it to be the case that we instead told the customer exactly what the non-ideal homodyne outcome and resolution bandwidth values were then, of course, we could tell the customers *exactly* what state they have, containing the phases introduced by ϵ and Δx. However, this would likely be a tedious, and somewhat unnecessary, task in practice and so we consider only fidelity against the *ideal* Bell state outcome.

For the cat state ES protocol, similar trends as discussed above were also discovered. When introducing non-ideal homodyne measurement outcomes into the cat state protocol, the measurement outcomes then became $x_{\frac{\pi}{4}} = \pm\sqrt{T}\,|\alpha| \pm \epsilon$ and $x_{\frac{\pi}{4}} = \pm\sqrt{T}\,|\alpha| \mp \epsilon$ (in which the $x_{\frac{\pi}{4}} = +\sqrt{T}\,|\alpha| + \epsilon$ and $x_{\frac{\pi}{4}} = -\sqrt{T}\,|\alpha| - \epsilon$ outcomes gave the same protocol result, as did the $x_{\frac{\pi}{4}} = +\sqrt{T}\,|\alpha| - \epsilon$ and $x_{\frac{\pi}{4}} = -\sqrt{T}\,|\alpha| + \epsilon$ outcomes).

Interestingly, when introducing non-ideal homodyne outcomes into the cat state protocol, it was found that the entanglement negativity increased in the peak $|\alpha|$ region for the $x_{\frac{\pi}{4}} = \pm\sqrt{T}\,|\alpha| \mp \epsilon$ outcomes (for non-zero ϵ), yet the fidelity values in these regions decreased for the same non-ideal outcome - conversely, we also saw that the $x_{\frac{\pi}{4}} = \pm\sqrt{T}\,|\alpha| \pm \epsilon$ non-ideal outcome gave far better fidelity results for much higher ϵ than could be tolerated with the $x_{\frac{\pi}{4}} = \pm\sqrt{T}\,|\alpha| \mp \epsilon$ outcome results.

The reasons behind this were discussed and justified in Subsec. 5.3.3, in which it was concluded that introducing ϵ for the $x_{\frac{\pi}{4}} = \pm\sqrt{T}\,|\alpha| \mp \epsilon$ outcome in fact caused a different entangled state to be produced, than the $|\Phi^+(\alpha)\rangle$ Bell state we have desired to produce so far. Theoretically, one could then aim to make this alternate Bell state, for the occurrences in which the non-ideal outcome is $x_{\frac{\pi}{4}} = \pm\sqrt{T}\,|\alpha| \mp \epsilon$, however, as discussed above in the coherent state regime, this would be tedious in practice with the notion to provide a customer (or customers) with entangled pairs of photons - a customer must know what state they are going to be supplied with, for a given fidelity which can be determined through our protocol, to ensure that this entangled

state is indeed fit for their intended purposes once it has been generated.

Finally, owing to the phases present in our final cat state density matrix, which contained both ϵ and Δx, we witnessed oscillatory behaviour as a function of $|\alpha|$ in the no loss fidelity plots for imperfect homodyne detection (see Fig. 5.42). This oscillatory behaviour was complimented perfectly in the equivalent no loss entanglement negativity and linear entropy plots of Figs. 5.38 and 5.40, respectively.

To conclude this chapter, we now tabulate fidelity values, with the lower imperfect homodyne limit of $\Delta x = 0.10$ and the higher limit of $\Delta x = 0.25$, for the maximum values we can allow ϵ to be such that the fidelity value is either $F = 0.80$ and $F = 0.90$. Firstly, we present data for the coherent state regime, for the upper limit of $F = 0.90$ and the lower limit of $F = 0.80$ for fidelity against the $|\Phi^+\rangle$ Bell state, corresponding to Tabs. 5.1 and 5.2 respectively:

T	1.00	0.99	0.98	1.00
Δx	0.10	0.10	0.10	0.25
ϵ	0.07	0.05	0.01	0.02
Peak $\|\alpha\|$	1.37	1.39	1.39	1.38
Fidelity	0.90	0.90	0.90	0.90

TABLE 5.1: Tabulated fidelity results ($F = 0.90$) for coherent state ES, non-ideal and imperfect homodyne detection, at the peak $|\alpha|$ value, for various T and ϵ with $\Delta x = 0.10$ and $\Delta x = 0.25$.

T	1.00	0.99	0.98	0.97	0.96	0.95
Δx	0.10	0.10	0.10	0.10	0.10	0.10
ϵ	0.11	0.11	0.10	0.08	0.07	0.05
Peak $\|\alpha\|$	1.20	1.18	1.19	1.23	1.22	1.23
Fidelity	0.80	0.80	0.80	0.80	0.80	0.80

T	1.00	0.99	0.98	0.97	0.96	0.95
Δx	0.25	0.25	0.25	0.25	0.25	0.25
ϵ	0.10	0.09	0.07	0.06	0.03	N/A
Peak $\|\alpha\|$	1.19	1.20	1.22	1.21	1.22	N/A
Fidelity	0.80	0.80	0.80	0.80	0.80	N/A

TABLE 5.2: Tabulated fidelity results ($F = 0.80$) for coherent state ES, non-ideal and imperfect homodyne detection, at the peak $|\alpha|$ value, for various T and ϵ with $\Delta x = 0.10$ and $\Delta x = 0.25$.

Evidently, what should immediately be clear is that, if we wish to produce the $|\Phi^+\rangle$ Bell state with a very high fidelity of $F = 0.90$, then we cannot tolerate any levels of loss beyond $T = 0.98$, if we want to have a small Δx value of $\Delta x = 0.10$, and cannot tolerate any losses at all for $\Delta x = 0.25$. Despite this, if we consider only the equal loss (in modes B and D) results (see Appendix D, Tab. D.1), then we can

see that even in the limit of ideal and perfect homodyne detection we still cannot tolerate loss levels of greater than $T = 0.98$ if we desire to produce the $|\Phi^+\rangle$ Bell state with fidelity $F = 0.90$.

Encouragingly, if we instead allow for lower fidelity of $F = 0.80$ then we may tolerate losses of $T \geq 0.96$ even when allowing for relatively high homodyne resolution bandwidth of $\Delta x = 0.25$. Furthermore, for $T \geq 0.97$ we can see that the fidelity results are slightly more tolerant to higher values of ϵ, such that $\epsilon \geq 0.06$ for $\Delta x = 0.25$. We do note here, however, that the coherent state protocol is in fact highly sensitive to non-ideal measurement outcomes, even in the no loss regime.

Now, let us consider the cat state protocol. Initially, we present data for the coherent state regime, for the upper limit of $F = 0.90$ and the lower limit of $F = 0.80$ for fidelity against the $|\Phi^+(\alpha)\rangle$ Bell state, for non-ideal outcome $x_{\frac{\pi}{4}} = \pm\sqrt{T}\,|\alpha| \pm \epsilon$, corresponding to Tabs. 5.3 and 5.4 respectively:

T	1.00	0.99	0.98	1.00
Δx	0.10	0.10	0.10	0.25
ϵ	0.11	0.07	0.01	0.05
Peak $\lvert\alpha\rvert$	1.09	1.14	2.00	1.16
Fidelity	0.90	0.90	0.90	0.90

TABLE 5.3: Tabulated fidelity results ($F = 0.90$) for cat state ES, non-ideal and imperfect homodyne detection, at the peak $|\alpha|$ value, for various T and ϵ with $\Delta x = 0.10$ and $\Delta x = 0.25$ and non-ideal homodyne outcome $x_{\frac{\pi}{4}} = \pm\sqrt{T}\,|\alpha| \pm \epsilon$.

T	1.00	0.99	0.98	0.97	0.96	0.95
Δx	0.10	0.10	0.10	0.10	0.10	0.10
ϵ	0.23	0.22	0.21	0.19	0.17	0.15
Peak $\lvert\alpha\rvert$	0.95	0.97	0.98	1.00	1.02	1.04
Fidelity	0.80	0.80	0.80	0.80	0.80	0.80

T	1.00	0.99	0.98	0.97	0.96	0.95
Δx	0.25	0.25	0.25	0.25	0.25	0.25
ϵ	0.22	0.21	0.19	0.17	0.15	0.12
Peak $\lvert\alpha\rvert$	0.97	0.98	1.00	1.02	1.04	1.08
Fidelity	0.80	0.80	0.80	0.80	0.80	0.80

TABLE 5.4: Tabulated fidelity results ($F = 0.80$) for cat state ES, non-ideal and imperfect homodyne detection, at the peak $|\alpha|$ value, for various T and ϵ with $\Delta x = 0.10$ and $\Delta x = 0.25$ and non-ideal homodyne outcome $x_{\frac{\pi}{4}} = \pm\sqrt{T}\,|\alpha| \pm \epsilon$.

Again, similarly to the coherent state $F = 0.90$ tabulated data of Tab. 5.1, we can conclude that in the cat state regime we cannot tolerate losses of $T < 0.98$ for

$\Delta x = 0.10$, and no losses at all for $\Delta x = 0.25$. In fact, this is also reflected in the equal loss (in modes B and D) results of Appendix D, Tab. D.2, for ideal and perfect homodyne detection. What is promising here, however, is that if we set our fidelity limit to $F = 0.80$, then the cat state ES protocol, for non-ideal outcome $x_{\frac{\pi}{4}} = \pm\sqrt{T}\,|\alpha| \pm \epsilon$, is far more resilient to larger ϵ. In fact, even in the bound of $\Delta x = 0.25$, we can suffer losses of $T \geq 0.95$ and still allow for non-ideal values of $\epsilon \leq 0.12$.

Despite these positive results, one must remember that this is for the more desirable non-ideal outcome of $x_{\frac{\pi}{4}} = \pm\sqrt{T}\,|\alpha| \pm \epsilon$. As such, we now tabulate the fidelity results for the cat state protocol, but for non-ideal outcome $x_{\frac{\pi}{4}} = \pm\sqrt{T}\,|\alpha| \mp \epsilon$, for fidelity results of $F = 0.90$ and $F = 0.80$ (Tabs. 5.5 and 5.6 respectively):

T	1.00	0.99	0.98	1.00
Δx	0.10	0.10	0.10	0.25
ϵ	0.07	0.05	0.01	0.02
Peak $\lvert\alpha\rvert$	1.99	2.01	2.01	2.00
Fidelity	0.90	0.90	0.90	0.90

TABLE 5.5: Tabulated fidelity results ($F = 0.90$) for cat state ES, non-ideal and imperfect homodyne detection, at the peak $|\alpha|$ value, for various T and ϵ with $\Delta x = 0.10$ and $\Delta x = 0.25$ and non-ideal homodyne outcome $x_{\frac{\pi}{4}} = \pm\sqrt{T}\,|\alpha| \mp \epsilon$.

T	1.00	0.99	0.98	0.97	0.96	0.95
Δx	0.10	0.10	0.10	0.10	0.10	0.10
ϵ	0.12	0.11	0.10	0.09	0.07	0.05
Peak $\lvert\alpha\rvert$	1.30	1.30	1.31	1.31	1.30	1.28
Fidelity	0.80	0.80	0.80	0.80	0.80	0.80

T	1.00	0.99	0.98	0.97	0.96	0.95
Δx	0.25	0.25	0.25	0.25	0.25	0.25
ϵ	0.11	0.10	0.08	0.07	0.05	0.02
Peak $\lvert\alpha\rvert$	1.29	1.29	1.28	1.28	1.26	1.23
Fidelity	0.80	0.80	0.80	0.80	0.80	0.80

TABLE 5.6: Tabulated fidelity results ($F = 0.80$) for cat state ES, non-ideal and imperfect homodyne detection, at the peak $|\alpha|$ value, for various T and ϵ with $\Delta x = 0.10$ and $\Delta x = 0.25$ and non-ideal homodyne outcome $x_{\frac{\pi}{4}} = \pm\sqrt{T}\,|\alpha| \mp \epsilon$.

Observing this data, we see from Tab. 5.5 that, once again, we cannot tolerate losses of $T < 0.98$ for $\Delta x = 0.10$, and no losses at all for $\Delta x = 0.25$ if we wish to produce the $|\Phi^+(\alpha)\rangle$ Bell state with fidelity of $F = 0.90$. Moreover, if we set our fidelity limit to the lower bound of $F = 0.80$, then we can indeed allow for losses of $T \geq 0.95$, however this comes at the cost of not being able to tolerate large shifts in non-ideal homodyne outcome. As a matter of fact, if we directly compare Tabs. 5.4

and 5.6 then we can note that, for non-ideal homodyne outcome of $x_{\frac{\pi}{4}} = \pm\sqrt{T}\,|\alpha| \pm \epsilon$, we can suffer ϵ values at least twice as large as for the $x_{\frac{\pi}{4}} = \pm\sqrt{T}\,|\alpha| \mp \epsilon$ outcome, for relatively large losses of $T = 0.95$.

Having discussed the impact that introducing non-ideal and imperfect homodyne measurements into our coherent state and cat state entanglement swapping protocols has on the fidelity of the ideal Bell state outcomes, we can see that both protocols are quite sensitive to this measurement.

We must vitally note here that, intrinsically, there are success probabilities associated with this homodyne measurement scheme, as previously mentioned in this chapter. This will be discussed in the following chapter (Chapter 6, Subsec. 6.1.2), in which we will show that even when allowing for a homodyne resolution bandwidth of up to $\Delta x = 0.50$, we still suffer a considerable drop in success probability of this measurement, in the region of $|\alpha|$ in which we are primarily concerned with, thus meaning that we have a trade-off of success probability of our protocol, against producing a highly entangled state through our proposed protocols.

Chapter 6

Protocol Optimisation

In this penultimate chapter to this work, we discuss optimisation of our proposed entanglement swapping protocol, with regards to success probabilities (Sec. 6.1) associated with the vacuum measurement and homodyne measurements (applied to modes B and D of our protocol respectively). We will also consider potential entanglement purification protocols (Sec. 6.2), with the aim to increase the fidelity of our final two qubit state produced via our protocol. Lastly, we then bring all investigations together (Sec. 6.3), regarding unequal losses in modes B and D (as presented in Chapter 4, and non-ideal and imperfect homodyne measurements (as discussed in Chapter 5, to give some realistic, practical limits in which one could perform this protocol to produce a given Bell state with a pre-determined fidelity.

6.1 Success Probabilities

In this section, we will discuss in further detail the success probabilities associated with performing the integral vacuum measurement and homodyne detection aspects of our proposed entanglement swapping protocol, when allowing for averaged unequal losses between modes B and D (as introduced in Chapter 4, Subsec. 4.2.1).

6.1.1 Vacuum Measurement Success Probability

Firstly, we discuss the success probability of the vacuum measurement we theoretically perform on mode B of our entanglement swapping protocol. This was first discussed in the equal loss (between modes B and D) coherent state protocol, of Chapter 3, Subsec. 3.1.2.

Coherent State Protocol

As the general method of determining the success probability of a vacuum measurement in mode B was carried out in Chapter 3, Subsec. 3.1.2, we do not discuss this in detail here. However, we remind the reader of our equation for vacuum measurement success probability, for the coherent state entanglement swapping protocol,

and for equal losses (in modes B and D):

$$\mathcal{P}_0^{Coh.}(\%) = \frac{1 + e^{-2T|\alpha|^2}}{2} \times 100. \tag{6.1}$$

In the more realistic circumstance, in which we have unequal (averaged) losses between modes B and D (averaged unequal losses was discussed in detail throughout Chapter 4), we can determine the success probability of a vacuum measurement in mode B using the same method outlined in Chapter 3, Subsec. 3.1.2. This then gives us:

$$\mathcal{P}_0^{Coh.}(\%) = \int_0^{\infty} f(\upsilon, \Upsilon) \frac{1 + e^{-\frac{|\mathcal{T}^+\alpha|^2}{2}}}{2} \mathrm{d}\upsilon \times 100, \tag{6.2}$$

where, $\mathcal{T}^+ = \sqrt{T} + \sqrt{T - \upsilon}$, and $f(\upsilon, \Upsilon) = \sqrt{\frac{2}{\pi\Upsilon^2}}\, e^{\frac{-\upsilon^2}{2\Upsilon^2}}$ was defined in Chapter 4, Subsec. 4.2.1. Of course, it holds that in the limit of $\Upsilon \to 0$ we return to the equal loss vacuum measurement success probability equation of Eq. 6.1.

In Fig. 6.1, we plot the vacuum measurement success probability for the coherent state regime, for various levels of equal loss:

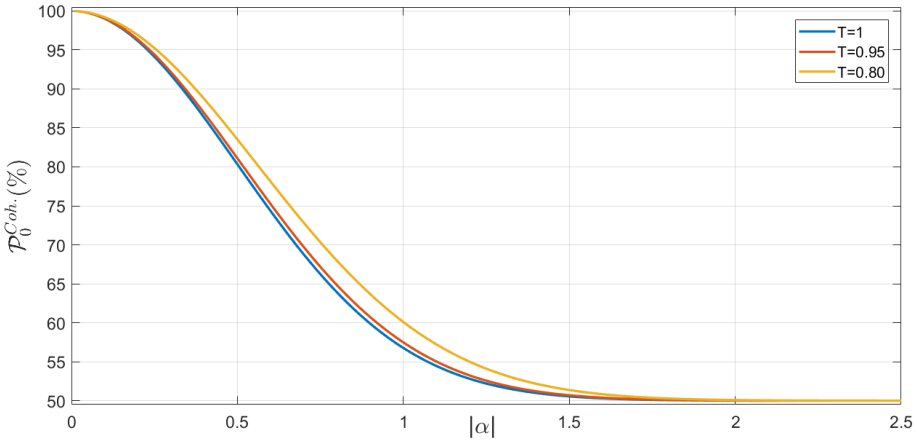

FIGURE 6.1: Success probability ($\mathcal{P}_0^{Coh.}(\%)$) of the vacuum measurement (Eq. 6.1), for the coherent state ES protocol, as a function of $|\alpha|$, for $T = 1$, $T = 0.95$ and the extremal limit of $T = 0.80$.

Note that we do not show results for unequal loss as these scale the same way in which the equal loss results do, however, the unequal loss equation (Eq. 6.2) is used to calculate success probability spot values for specific values of α, T and Υ at the end of this chapter, in Sec. 6.3.

Observing Fig. 6.1, clearly we can see, in the limit of $|\alpha| \geq 1.75$, that for $0.80 \leq T \leq 1$ the success probability plateaus at $\mathcal{P}_0^{Coh.}(\%) = 50\%$. In fact, we note here (although we do not see it for levels of loss calculated for in Fig. 6.1), that as the levels of equal losses in modes B and D increase, the success probability of the vacuum measurement also increases. Of course, this is entirely expected, as we already know that as we introduce loss into coherent states this causes the amplitude

to decrease. Hence, for very high levels of loss ($T \to 0$), the success probability of the vacuum measurement is then $\mathcal{P}_0^{Coh.}(\%) = 100\%$, as all we have are vacuum states (i.e coherent states of amplitude $\sqrt{T}\,|\alpha| = 0$). We point out that this is a useless region of losses, as we know from our results discussed throughout this thesis so far that we ideally would not consider losses greater than $T = 0.95$, as it causes the level of entanglement in our final state to decrease below what we desire.

Unfortunately, the limit in which the success probability plateaus at $\mathcal{P}_0^{Coh.}(\%) = 50\%$ is around the region of $|\alpha|$ we desire for our protocol outcome to yield the $|\Phi^+\rangle = \frac{1}{\sqrt{2}}(\,|00\rangle + |11\rangle)$ Bell state with high fidelity. This trade-off between entanglement and success probability is a common occurrence in quantum communication schemes, however, although success probability is undoubtedly significant when considering the practical implementation of our proposed entanglement swapping protocol, we argue that producing a Bell state of high fidelity is more important.

Cat State Protocol

We now move on to discuss the vacuum measurement success probability in the cat state entanglement swapping regime. As the general method for determining the vacuum measurement success probability was given in Chapter 3, Subsec. 3.1.2 (for the coherent state protocol), we do not discuss this derivation in detail here. However, the vacuum measurement success probability for the cat state protocol was discussed in Chapter 3, Subsec. 3.4.1, and given in Eq. 3.52, and so following an equivalent derivation we can give this success probability, for equal losses in mode B and D as:

$$\mathcal{P}_0^{Cat}(\%) = \left(\frac{(N_\alpha^+)^2}{2\mathcal{N}'}\right)^2 \times 100 \tag{6.3}$$

where,

$$\mathcal{N}' = 1/\Big(4 + 8e^{-T|\alpha|^2} + 24e^{-2T|\alpha|^2} + 8e^{-3T|\alpha|^2} + 4e^{-4T|\alpha|^2} + 8e^{-(2+\mathrm{i})T|\alpha|^2} + 8e^{-(2-\mathrm{i})T|\alpha|^2}\Big)^{\frac{1}{2}}, \tag{6.4}$$

and $N_\alpha^+ = 1/\sqrt{2 + 2e^{-2T|\alpha|^2}}$ is the normalisation of an even cat state.

As before, we ideally wish to consider unequal (averaged) losses between modes B and D and so we can calculate the success probability of a vacuum measurement in mode B using the same method applied to determine Eq. 6.3, but evaluate for unequal losses in modes B and D (as discussed in detail in Chapter 4). This then gives us:

$$\mathcal{P}_0^{Cat}(\%)(\Upsilon) = \int_0^\infty f(\upsilon, \Upsilon)\left(\frac{(N_\alpha^+(\upsilon))^2}{2\mathcal{N}'(\upsilon)}\right)^2 \mathrm{d}\upsilon \times 100 \tag{6.5}$$

where, $\mathcal{T}^{+}=\sqrt{T}+\sqrt{T-\upsilon}$, $f(\upsilon,\Upsilon)=\sqrt{\frac{2}{\pi\Upsilon^{2}}}\,e^{\frac{-\upsilon^{2}}{2\Upsilon^{2}}}$ was defined in Chapter 4, Subsec. 4.2.1, $N_{\alpha}^{+}(\upsilon)=1/\sqrt{2+2e^{-\frac{|\mathcal{T}^{+}\alpha|^{2}}{2}}}$ and

$$\mathcal{N}'(\upsilon)=1/\Big(4+8e^{-\frac{|\mathcal{T}^{+}\alpha|^{2}}{4}}+24e^{-\frac{|\mathcal{T}^{+}\alpha|^{2}}{2}}+8e^{-\frac{|\mathcal{T}^{+}\alpha|^{2}}{4/3}}+4e^{-|\mathcal{T}^{+}\alpha|^{2}} \\ +8e^{-(2+\mathrm{i})|\mathcal{T}^{+}\alpha|^{2}}+8e^{-(2-\mathrm{i})|\mathcal{T}^{+}\alpha|^{2}}\Big)^{\frac{1}{2}}. \tag{6.6}$$

Of course, it again stands that in the limit of $\Upsilon\rightarrow 0$ we return to the equal loss vacuum measurement success probability equation of Eq. 6.3.

In Fig. 6.2, we plot the vacuum measurement success probability for the cat state entanglement swapping protocol for various levels of equal losses (again, we do not show the unequal loss results as these scale similarly to the equal loss ones):

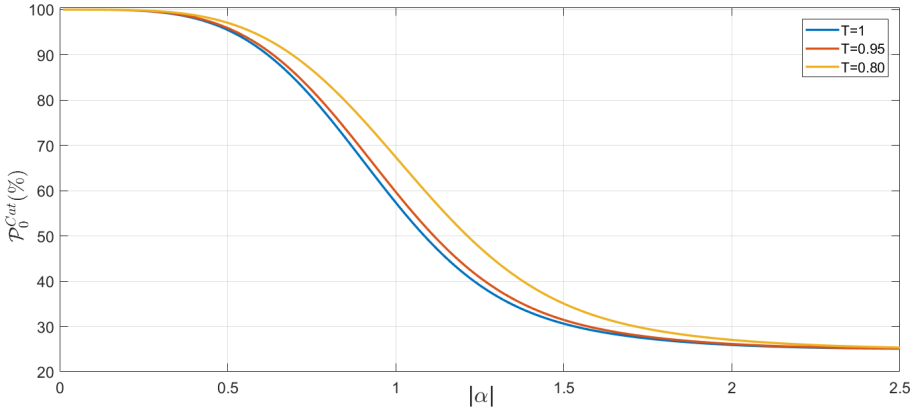

FIGURE 6.2: Success probability ($\mathcal{P}_0^{Cat}(\%)$) of the vacuum measurement (Eq. 6.3), for the cat state ES protocol, as a function of $|\alpha|$, for varying $T=1$, $T=0.95$ and the extremal limit of $T=0.80$.

As we saw in the coherent state vacuum measurement success probability plot of Fig. 6.1, the cat state success probability plot of Fig. 6.2 shows a similar trend that as the level of loss in our system increases, as does the success probability. We again note that in the limit of very large losses the success probability will remain at unity for all α. However, in the regions of loss we consider for our protocol (namely $0.95\leq T\leq 1$), we can see from Fig. 6.2 that as $|\alpha|\geq 2.5$ then the plots tend to $\mathcal{P}_0^{Cat}(\%)=25\%$. In fact, this is precisely half of the success probability value we see that the coherent state plot plateaus at, which is easily explained by recalling that the cat state protocol we propose has twice as many coherent states present, and as such this decreases the probability of a successful vacuum projection taking place.

Lastly, we note here that in the region of $|\alpha|$ which is useful in producing the $|\Phi^{+}(\alpha)\rangle=\frac{1}{\sqrt{2}}(\,|00\rangle\,e^{-i|\alpha|^{2}}+|11\rangle\,e^{+i|\alpha|^{2}})$ Bell state with high fidelity (around $1.0\leq|\alpha|\leq 2.0$), the success probability of the vacuum measurement will not be unity. However, as discussed previously in the coherent state vacuum measurement success probability results, this trade-off between fidelity and success probability

is something we must accept, and we argue that high fidelity is far more important to aim for as opposed to higher success probabilities; producing fewer pairs of higher fidelity quantum states is more useful for further quantum communication purposes, as opposed to producing more pairs of lower fidelity states.

6.1.2 Homodyne Measurement Success Probability

We now move on to investigate the success probability associated with the homodyne measurement we perform on mode D in our proposed entanglement swapping protocol. The homodyne measurement success probability was first mentioned when we considered imperfect homodyne detection, in Chapter 5, Sec. 5.4 - in this section we showed that increasing the bandwidth of the homodyne measurement, given by the projector defined in Eq. 5.9, the entanglement of the final state produced through our protocol is slightly lessened (for a relatively sharp bandwidth). However, we also mentioned that the success probability must also *increase* in the limit of this bandwidth increasing, as we are accepting more values for the homodyne measurement outcome. We therefore expect this pattern to be shown in the following results for the coherent state and cat state protocols.

Coherent State Protocol

Firstly, we consider the homodyne measurement success probability of the coherent state protocol. We determine this success probability by taking the modulus square of the normalised probability amplitudes (given by using the projector of Eq. 5.9 onto the coherent states present in mode D of the no loss equation of Eq. 3.16), to give us the probability distribution we integrate over, such that:

$$\begin{aligned}
&\left|{}_D\langle x_{\frac{\pi}{2}}|\Psi^{Coh.}\rangle_{ACD}\right|^2 = \\
&\mathcal{N}^2\Big|\Big({}_{AC}\langle 00|_D\ \langle\sqrt{2}\,|\alpha|| + {}_{AC}\langle 11|\ \langle -\sqrt{2}\,|\alpha|| \\
&\quad + e^{-|\alpha|^2}{}_{AC}\langle 01|_D\,|0\rangle + e^{-|\alpha|^2}{}_{AC}\langle 10|_D\,|0\rangle\Big)\,|x_{\frac{\pi}{2}}\rangle_D \\
&\qquad\qquad \times {}_D\langle x_{\frac{\pi}{2}}|\Big(|00\rangle_{AC}\ |\sqrt{2}\,|\alpha|\rangle_D + |11\rangle\ |-\sqrt{2}\,|\alpha|\rangle_D \\
&\qquad\qquad + e^{-|\alpha|^2}\,|01\rangle_{AC}\,|0\rangle_D + e^{-|\alpha|^2}\,|10\rangle_{AC}\,|0\rangle_D\Big)\Big|,
\end{aligned} \tag{6.7}$$

where $\mathcal{N} = \frac{1}{\sqrt{2}}$ is the normalisation.

This then gives the success probability of the homodyne measurement as:

$$\mathcal{P}^{Coh.}_{Hom.}(\%) = \mathcal{N}^2 \int_{-\frac{\Delta x}{2}}^{+\frac{\Delta x}{2}} \frac{2\sqrt{2}\,e^{-2(x_{\frac{\pi}{2}})^2}}{\sqrt{\pi}} \mathrm{d}x_{\frac{\pi}{2}} \times 100 = \int_{-\frac{\Delta x}{2}}^{+\frac{\Delta x}{2}} \frac{\sqrt{2}\,e^{-2(x_{\frac{\pi}{2}})^2}}{\sqrt{\pi}} \mathrm{d}x_{\frac{\pi}{2}} \times 100 \tag{6.8}$$

For the unequal (averaged) loss equivalent of Eq. 6.8, we simply apply the method used in Chapter 4, which in fact gives us the same expression as derived above in Eq. 6.8.

Finally, we also note that to establish non-ideal homodyne outcomes as well, the homodyne measurement success probability then simply becomes:

$$\mathcal{P}^{Coh.}_{Hom.}(\%) = \int_{\epsilon-\frac{\Delta x}{2}}^{\epsilon+\frac{\Delta x}{2}} \frac{\sqrt{2}\, e^{-2(x_{\frac{\pi}{2}})^2}}{\sqrt{\pi}} \mathrm{d}x_{\frac{\pi}{2}} \times 100 \tag{6.9}$$

We now plot the homodyne measurement success probability, for no loss, as a function of Δx with varying levels of non-ideal homodyne measurement outcome ϵ:

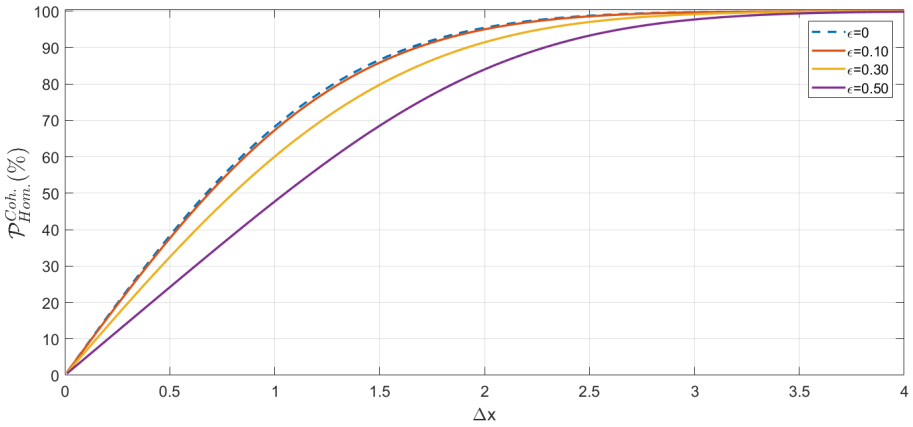

FIGURE 6.3: Success probability ($\mathcal{P}^{Coh.}_{Hom.}(\%)$) of the homodyne measurement (Eq. 6.9), for the coherent state ES protocol, as a function of Δx, for no loss, with varying non-ideal homodyne outcome ϵ.

Firstly, we can see in Fig. 6.3 that in the limit of $\Delta x \geq 3.0$ (for the case of $\epsilon = 0$) the success probability tends to $\mathcal{P}^{Coh.}_{Hom.}(\%) = 100\%$ - this is entirely expected, as in the limit of very large homodyne measurement bandwidth we of course anticipate that we accept far more homodyne measurement outcomes. Hence, for very large Δx, the success probability intrinsically approaches $\mathcal{P}^{Coh.}_{Hom.}(\%) = 100\%$. Contrastingly, in the limit of $\Delta x = 0$ (i.e. the "perfect", discrete outcome, homodyne measurement limit we assumed in the calculations in Chapters 3 and 4), we see from Fig. 6.3 that the success probability is always $\mathcal{P}^{Coh.}_{Hom.}(\%) = 0\%$. This again comes as no surprise, and in fact we have already discussed in the previous chapter (Chapter 5) that assuming we have a single, "perfect" homodyne measurement outcome (for example, $x_{\frac{\pi}{2}} = 0$ in the coherent state protocol) will inherently impact the success probability of that measurement.

Moreover, we also note here that increasing the value of ϵ also causes the homodyne measurement success probability to decrease (see Fig. 6.3). This can be justified by recalling that increasing ϵ causes the measurement outcome to shift along the measurement quadrature by a factor of ϵ (see the phase-space schematic of Fig. 5.1). It then follows that if we integrate between limits given by Δx, central around a shifted quadrature position (given by ϵ), then of course the integral has a lower

value than if we were to integrate between the same limits of Δx, but at the centre of the probability distribution peak.

Cat State Protocol

To determine the homodyne measurement success probability in the cat state protocol, we carry out the same process used in the coherent state regime, as per the previous section. However, we instead consider the states in mode D in which we project onto with the homodyne operator given by the no loss state of Eq. 3.51, such that:

$$\left|{}_D\left\langle x_{\frac{\pi}{4}}|\Psi^{Cat}\right\rangle_{ACD}\right|^2, \tag{6.10}$$

in which the amplitudes of the homodyne projection onto the states in mode D are calculated using Eq. 2.24. Note that we do not show the explicit expression for the probability distribution given in Eq. 6.10, as this is very lengthy, however we follow the exact same method used to derive the equivalent homodyne measurement success probability (of Eq. 6.8).

This then gives the homodyne measurement success probability as:

$$\mathcal{P}^{Cat}_{Hom.}(\%) = \mathcal{N}^2\left(\int_{|\alpha|-\frac{\Delta x}{2}}^{|\alpha|+\frac{\Delta x}{2}}\left|\left\langle x_{\frac{\pi}{4}}|\Psi^{Cat}\right\rangle\right|^2 \mathrm{d}x_{\frac{\pi}{4}} + \int_{-|\alpha|-\frac{\Delta x}{2}}^{-|\alpha|+\frac{\Delta x}{2}}\left|\left\langle x_{\frac{\pi}{4}}|\Psi^{Cat}\right\rangle\right|^2 \mathrm{d}x_{\frac{\pi}{4}}\right)\times 100 \tag{6.11}$$

where,

$$\mathcal{N} = 1/\Big(4 + 8e^{-|\alpha|^2} + 24e^{-2|\alpha|^2} + 8e^{-3|\alpha|^2} + 4e^{-4|\alpha|^2} + 8e^{-(2+\mathrm{i})|\alpha|^2} + 8e^{-(2-\mathrm{i})|\alpha|^2}\Big)^{\frac{1}{2}}, \tag{6.12}$$

is the normalisation.

For the unequal (averaged) loss equivalent of Eq. 6.11, we simply apply the method used in Chapter 4, and also allow for homodyne non-idealities (evaluated in the integral limits) to give us:

$$\mathcal{P}^{Cat}_{Hom.}(\%)(\Upsilon) = \tag{6.13}$$

$$\int_0^\infty f(\upsilon,\Upsilon)\mathcal{N}_\upsilon\left(\int_{\frac{\mathcal{T}^+}{2}|\alpha|+\epsilon-\frac{\Delta x}{2}}^{\frac{\mathcal{T}^+}{2}|\alpha|+\epsilon+\frac{\Delta x}{2}}\left|\left\langle x_{\frac{\pi}{4}}|\Psi^{Cat}\right\rangle\right|^2 \mathrm{d}x_{\frac{\pi}{4}} + \int_{-\frac{\mathcal{T}^+}{2}|\alpha|+\epsilon-\frac{\Delta x}{2}}^{-\frac{\mathcal{T}^+}{2}|\alpha|+\epsilon+\frac{\Delta x}{2}}\left|\left\langle x_{\frac{\pi}{4}}|\Psi^{Cat}\right\rangle\right|^2 \mathrm{d}x_{\frac{\pi}{4}}\right)\mathrm{d}\upsilon\times 100, \tag{6.14}$$

where, $\mathcal{T}^{+}=\sqrt{T}+\sqrt{T+v}$ and,

$$\mathcal{N}_v = 1/\Big(4+8e^{-\frac{|\mathcal{T}^{+}\alpha|^2}{4}}+24e^{-\frac{|\mathcal{T}^{+}\alpha|^2}{2}}+8e^{-\frac{|\mathcal{T}^{+}\alpha|^2}{4/3}}+4e^{-|\mathcal{T}^{+}\alpha|^2} \\ +8e^{-(2+\mathrm{i})|\mathcal{T}^{+}\alpha|^2}+8e^{-(2-\mathrm{i})|\mathcal{T}^{+}\alpha|^2}\Big)^{\frac{1}{2}}, \tag{6.15}$$

is the normalisation. We again note that we do not discuss any plots of the homodyne measurement success probability which includes losses and unequal losses, as these scale entirely as expected - however, the above equation (evaluated for averaged unequal losses and homodyne non-idealities) will be used in Sec. 6.3, in which we calculate spot values for the homodyne success probability.

We now plot the homodyne measurement success probability as a function of $|\alpha|$, for no loss, with varying homodyne measurement bandwidth Δx:

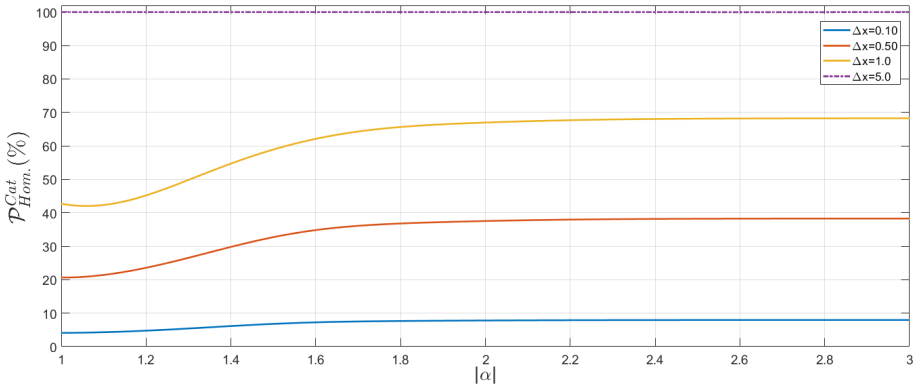

FIGURE 6.4: Success probability ($\mathcal{P}^{Cat}_{Hom.}(\%)$) of the homodyne measurement (Eq. 6.11), for the cat state ES protocol, as a function of $|\alpha|$, for varying homodyne measurement bandwidth Δx, $T=1$ and $\epsilon=0$.

What is instantly noticeable is that, with the exception of the plot for $\Delta x=5.0$, the success probability is lower at smaller values of $|\alpha|$. We do note that inherently the success probability in the case of $\Delta x=5.0$ will always be unity, for all $|\alpha|$, as this level of measurement bandwidth covers the entire range of the probability distribution. Although the success probability in this case is unity, we note that the fidelity against the desired Bell state is $F\leq 0.80$ in the limit of $\Delta x\geq 0.50$ (see Fig. 5.42) and so we would not look at values of homodyne measurement bandwidth beyond this limit.

To understand the homodyne measurement success probability plot of Fig. 6.4, we also plot the probability distribution of the cat state equation (given by Eq. 6.10), which we label $f(x_{\frac{\pi}{4}})$, as a function of $x_{\frac{\pi}{4}}$, for $|\alpha|=0$, $|\alpha|=1.0$ and $|\alpha|=2.0$ (for no loss):

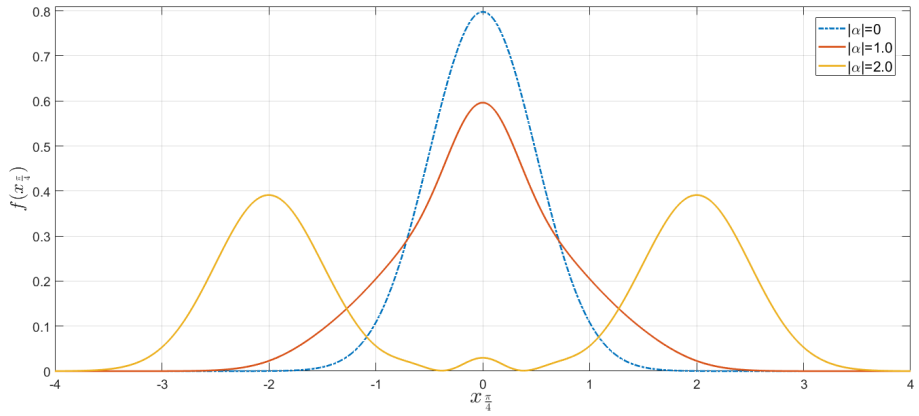

FIGURE 6.5: Probability distribution $f(x_{\frac{\pi}{4}})$ of the cat state equation (given by Eq. 6.10), as a function of $x_{\frac{\pi}{4}}$, for $|\alpha| = 0$, $|\alpha| = 1.0$ and $|\alpha| = 2.0$ (for no loss).

If we first consider the $|\alpha| = 0$ probability distribution plot in Fig. 6.5, then clearly the probability distribution peaks at $x_{\frac{\pi}{4}} = 0$ - this is entirely expected, as all coherent states which we are measuring via homodyne detection will be vacuum states. Conversely, once we go to $|\alpha| = 2.0$ in Fig. 6.5 then we can easily see that we now have two peaks present (with a small residual contribution around $x_{\frac{\pi}{4}} = 0$, due to the exponentially decaying terms which have not vanished at this amplitude yet). This is the ideal situation we would want for a successful homodyne measurement, in which we have two peaks associated with the outcome - one for the $x_{\frac{\pi}{4}} = +|\alpha|$ outcome and one for $x_{\frac{\pi}{4}} = -|\alpha|$ (see the phase-space diagram of Fig. 3.14).

However, the reason we see smaller success probabilities in Fig. 6.4 at lower amplitudes is explained in the probability distribution plot of $|\alpha| = 1.0$ in Fig. 6.5: for $|\alpha| = 1.0$ the two peaks present (for the two homodyne measurement outcomes) are still overlapping, however the width of the distribution is wider. In fact, if we consider the state which we are projecting onto with the homodyne measurement operator, given in Eq. 3.51, we can see that there are vacuum states present in mode D. Although these vacuum states are exponentially dampened by $e^{-|\alpha|^2}$, it is not until $|\alpha| \approx 2.0$ that we see the contribution of these vacuum states to the probability distribution decrease. Again, this is shown clearly in Fig. 6.5.

Regarding the homodyne measurement success probability plot of Fig. 6.4, we enforce homodyne outcomes around $x_{\frac{\pi}{4}} = \pm|\alpha|$, and so for $|\alpha| = 1.0$ we can see in the corresponding probability distribution that in this circumstance the peaks of interest to us ($x_{\frac{\pi}{4}} = \pm|\alpha|$) are not at the peak of the distribution. It is not until $|\alpha| > 2.0$ that these peaks are separated far enough (as the vacuum state is dampened) that the success probability plots plateau.

Importantly we must also note that for $|\alpha| = 1.0$ we tend to produce a pair of qubits with an acceptable fidelity against our desired Bell state, and so we again have a trade-off between fidelity and success probability - if we wish to aim for a higher success probability, by using amplitudes of $|\alpha| > 2.0$ then indeed we can see that the success probability of the plots in Fig. 6.4 increases (although this is only

really noticeable for $\Delta x = 0.50$ and $\Delta x = 1.0$ in this plot), however we know from previous discussion of results in this thesis that for the cat state protocol the peak $|\alpha|$ values we desire are around $1.0 \leq |\alpha| \leq 1.30$.

6.2 Entanglement Distillation

Entanglement distillation (also commonly referred to as entanglement purification or concentration) is a method used in the field of quantum information to overcome the degenerative effects of noisy quantum channels, such as the lossy channels we implement within this work [178]. Using only local operations and classical communications one can increase the level of entanglement shared between two arbitrarily separated qubits [179]. We stress here that, fundamentally, multiple pairs of qubits are required to distill off higher entanglement in one (or a few) qubit pairs.

In essence, if Alice and Bob share M pairs of *non-ideal* (less than perfect) entangled qubits, Alice and Bob could apply local (collective) operations to their respective halves of the qubit pairs. Using classical communications, Alice and Bob communicate the outcomes of their local operations back and forth, and as such can produce $N < M$ entangled states of higher quality [45] - although the fidelity of the resultant entangled pair against a Bell state can never reach unity. We clarify here that by "local operations" we refer to operations in which Alice and Bob may make on their half of the entangled state only, and by "classical communication" we of course mean any form of communication not reliant on quantum physics (such as a telephone call) [180].

The motivation for applying an entanglement distillation protocol to pairs of less entangled qubits should be clear by now, given the importance of the work carried out in this thesis, but we remind the reader here that for successful quantum communications (that rely on entanglement), one inherently needs highly entangled pairs of qubits. As all quantum channels (even optical fibres) are affected by noise, the quality of an entangled state degrades exponentially as a function of the channel length [181]. Note here that the consideration of a noisy quantum channel in our protocol is assessed in terms of photonic losses in modes B and D, although intrinsically there are still other potential forms of decoherence that would impact the successful transmission of our entangled states.

6.2.1 The General Method of Entanglement Distillation

The first entanglement distillation protocol for mixed states was produced in 1996 by C. H. Bennett and G. Brassard *et al.* in [43]. To present the general scheme of how entanglement distillation can be achieved, we now briefly discuss the method used in [43]:

Suppose Alice and Bob each share multiple less-than-perfectly entangled pair of qubits, given as M. The state M could be resultant from transmission of one or both modes of the $|\Psi^-\rangle_{AB} = \frac{1}{\sqrt{2}}(|01\rangle_{AB} - |10\rangle_{AB})$ Bell state, through a noisy

quantum channel, in which Alice is in control of mode A, and Bob has mode B. The quality of the non-pure state M can be assessed through fidelity against the maximally entangled Bell state $|\Psi^-\rangle_{AB}$, as:

$$F(M, |\Psi^-\rangle_{AB}) = {}_{AB}\langle\Psi^-| M |\Psi^-\rangle_{AB}. \tag{6.16}$$

To purify M, the following protocol is applied:

- Suppose Alice and Bob also share a second pair of qubits, in state M, across the same noisy channel. Alice and Bob apply a local random bilateral rotation to their halves of the states M, which then gives:

$$\begin{aligned} W_F =& F |\Psi^-\rangle_{AB}\langle\Psi^-| + \frac{1-F}{3} |\Psi^+\rangle_{AB}\langle\Psi^+| \\ &+ \frac{1-F}{3} |\Phi^+\rangle_{AB}\langle\Phi^+| + \frac{1-F}{3} |\Phi^-\rangle_{AB}\langle\Phi^-|, \end{aligned} \tag{6.17}$$

  in which F is equivalent to the fidelity defined in Eq. 6.16, and the states with coefficients $\frac{1-F}{3}$ in the state W_F are simply the three other Bell states, as defined in Eqs. 1.27 and 1.28. Also note that once applying this rotation to the states M we redefine it as the Werner State (W_F), as is commonly done [182]. In fact, we will refer to the state given in Eq. 6.17 as the Ψ^- Werner State, as it is comprised of the $|\Psi^-\rangle$ Bell State.

- Next, Alice and Bob then apply a unilateral Pauli rotation $\hat{\sigma}_y$ to their respective halves of the states W_F, in which $\hat{\sigma}_y$ maps $|\Psi^\pm\rangle \rightarrowtail |\Phi^\mp\rangle$. In doing so, this converts the mostly Ψ^- W_F states given in Eq. 6.17, to mostly Φ^+ Werner States (as the new state is comprised of mostly $|\Phi^+\rangle$).

- Alice and Bob then apply a bilateral XOR quantum logic gate [183] to their halves of the two mostly Φ^+ Werner States. A unilateral XOR gate is also referred to as a "controlled-NOT" (CNOT) gate, in which if Alice is in possession of two entangled qubits in the state $\frac{1}{\sqrt{2}}(|00\rangle_{12} + |11\rangle_{12})$ and performs an XOR operation on her state, the output is then $\frac{1}{\sqrt{2}}(|00\rangle_{12} + |10\rangle_{12})$ - clearly, this gate then works such that if the first *control* qubit is in state $|0\rangle$ then the second *target* qubit remains unchanged, however if the control qubit is in state $|1\rangle$ then the target qubit is switched to state $|0\rangle$. Hence, a bilateral XOR gate simply refers to the same process as just described, but instead having two parties present (and therefore four qubits overall), and as such two control qubits and two target qubits, as possessed by Alice and Bob in this protocol.

- After application of the bilateral XOR operation on the mostly Φ^+ Werner States, Alice and Bob then measure locally their respective *target* qubits. Classically communicating their results, they then keep their remaining shared (control) qubits if the measurement performed on their target qubit gave the same output (i.e. both outputs are $|0\rangle$ or both are $|1\rangle$), and discard their remaining qubits if the outputs differ.

- Finally, the probability of the resultant (control) entangled state to be found as $|\Phi^+\rangle$ is greater than $\frac{1}{4}$, with fidelity F_{ED} (in which the subscript ED refers to entanglement distillation) given as:

$$F_{ED} = \frac{F^2 + \frac{1}{9}(1-F)^2}{F^2 + \frac{2}{3}F(1-F) + \frac{5}{9}(1-F)}. \tag{6.18}$$

  Iteration of this protocol numerous times allows one to distill Φ^+ Werner states of arbitrarily high fidelity (but in the limit of $F_{ED} < 1$), using a supply of input M states, provided that $F > \frac{1}{2}$ in the initial states.

We note here that the original paper given in [43] was in fact written in terms of spins, however, in the above interpretation we have replaced the $|\uparrow\rangle$ and $|\downarrow\rangle$ states with $|0\rangle$ and $|1\rangle$ respectively, for consistency with the notation used throughout this thesis.

Following on from the introduction of the above entanglement distillation protocol, in 1996 D. Deutsch *et al.* [184] introduced their own distillation protocol, and improved the purification efficiency to that of [43]. Although these two protocols were absolutely ground-breaking with regards to introducing the possibility of improving the entanglement shared between two distant parties, these distillation protocols are nonetheless still difficult to implement to this day. At the time of the introduction of these entanglement distillation protocols, the CNOT gate was very challenging to perform experimentally, and so in 2001 J.-W. Pan *et al.* proposed a protocol that did not rely on these gates [185] - instead, they replaced the CNOT gate with polarisation beam-splitters, although this came at the sacrifice of lowering the success probability of their protocol.

In the protocols of [43, 184, 185] two noisy entangled states were required to produce one entangled pair of greater quality, however in 1996 N. Gisin also introduced an entanglement distillation protocol which required only one input noisy pair of qubits in each distillation round [186], and was successfully performed experimentally in 2001 by P. Kwiat *et al.* [187]. Also fundamental to the field of entanglement distillation was given by the Horodecki family in 1998 [188], in which they discussed the concepts of *free* entanglement (entangled states that can be distilled) and *bound* entanglement (states which cannot be distilled).

Following on from these fundamental entanglement distillation protocols, a plethora of further protocols were proposed, using a broad range of input states, such as the three-qubit W state [189], graph states [190], three-qubit GHZ states [191] and bipartite microwave photons [192]; we note here that evidently entanglement distillation is also possible with multipartite entangled states (as opposed to bipartite entangled states as discussed already in this section). Although we do not focus on this in the discussion of protocols here, as this is not relevant to the states which we would wish to increase the entanglement of within this thesis.

6.2.2 Distillation Considerations for our Entanglement Swapping Protocols

In this section, we briefly consider practical entanglement distillation methods which could be applied to the final (non-pure) entangled states produced throughout our coherent state and cat state entanglement swapping protocols. We note here that there are many entanglement distillation methods which would be suitable to act on the Bell state produced in our ES protocols, however in this section we review only a few.

Throughout this thesis we have focussed on levels of photon losses, and homodyne detector non-idealities and imperfections, that provide us with an entangled Bell state of fidelity $F \geq 0.80$. Therefore, we now wish to consider potential distillation protocols which could be applied to these states to increase our resultant distilled fidelity as high as possible - ideally, we would like a distilled fidelity of $F \geq 0.95$.

According to J.-W. Pan *et al.* [193], they found that they could produce typically one photon pair of fidelity $F = 0.92$, from two pairs each of fidelity $F = 0.75$. In fact, their proposed protocol does not rely on the CNOT gate which, as previously discussed in Subsec. 6.2.1, is a difficult logical gate to implement practically, as it requires non-linear optical elements. The protocol of [193] instead relies only on linear optics, and as such is a feasible, practical method in which one could vastly improve the fidelity of a pair of qubits (in any of the four Bell states) with a success probability of 25%. Of course, as already stated, we would ideally like to provide customers with a Bell state of fidelity $F \geq 0.95$, however, the protocol of [193] was tested on input states of fidelity $F = 0.75$, and so if the input states are of better quality (such as the $F = 0.80$ states we produce through our ES protocol) then the resultant distilled fidelity could indeed approach our target.

If we instead consider a protocol that does rely on non-linear optical elements, namely the controlled-controlled-NOT (CCNOT) gate, as per the method given by X.-L. Feng *et al.* [194]. The CCNOT gate acts similar to the two-qubit CNOT gate, however the CCNOT gate instead requires two control qubits, and one target - if the two control qubits are in state $|0\rangle$ then the target remains the same, however if the control qubits are in state $|1\rangle$ then the target qubits switches from $|0\rangle \leftrightarrow |1\rangle$. In this protocol, they found that by implementing this gate they could in fact distill a high fidelity Bell state of better quality than the original protocol proposed by C. H. Bennett *et al.* [43], with an improved success probability. By allowing for multiple iterations of their protocol. Feng *et al.* demonstrate the one could achieve a distilled fidelity of $F = 0.99$, from an input fidelity of $F = 0.90$, by iterating their protocol three times, with a success probability of 6%. If we consider an input fidelity of $F = 0.80$, then applying the entanglement distillation protocol of [194] could give us a resultant fidelity of $F \geq 0.95$ after just a few iterations. We do note, however, that the CCNOT gate is difficult to implement in reality, and as such explains why the success probability for this protocol is much lower.

More recently, in 2015 C. Chun *et al.* proposed a practical distillation protocol which does not rely on the CNOT or CCNOT gates [195]. In their work they rely only on polarisation beam-splitters (beam-splitters which split the input beam dependent on polarisation properties), which can easily be performed experimentally, as well as multiple input Bell states (i.e. more than two). In this work they show that one could produce a Bell state of fidelity $F \geq 0.95$ using their simple protocol with just three input Bell states of fidelity $F = 0.73$. This of course is suitable as a potential distillation scheme for our final Bell state of fidelity $F = 0.80$ produced via our ES protocol. Although the distilled fidelity is higher in this work, they also conclude that the success probability of performing their protocol is not as high as the original (similar) distillation scheme given by J.-W. Pan *et al.* in 2001 [185], which required only two input Bell states.

Soon after the protocol of [195] was published, an improved multi-copy entanglement distillation protocol was proposed by S.-S. Zhang *et al.* [196]. In this protocol they showed that they do not require an ideal entanglement source (as needed to successfully perform the protocols of [185] and [195]) - instead, they prove that by using a non-ideal entanglement source (in the form of spontaneous parametric down-conversion source, as discussed in Chapter 1, Subsec. 1.2.6) they can produce an even higher fidelity Bell state. In fact, they demonstrated that one could distill a Bell state of fidelity $F = 0.95$, from just two input Bell states of fidelity $F = 0.65$, which is a vast improvement over the other similar schemes of [185] and [195]. Moreover, if the two input states are of fidelity $F = 0.80$, then after just a single iteration of their protocol the resultant distilled fidelity is $F = 0.98$. However, the success probability of performing their protocol with just two input states of fidelity $F = 0.80$ is around 2%, and this success probability decreases as the number of required input copies increases. Hence, there is a clearly a trade-off between the desired distilled fidelity, which requires more copies of the input Bell states for higher resultant fidelity, and success probability.

Finally, we note here that although success probability has some significance, as it will relate to the delivered distilled entangled qubit rate, the fidelity is considered to be more important. This is because the fidelity will determine what can be done with the entangled qubits that are created, for further applications in quantum key distribution, quantum teleportation, or any other quantum communication/computation purposes.

By now, it should be clear that research into practical entanglement distillation schemes has improved such that the fidelity of a Bell state can be increased vastly through application of any of the aforementioned schemes in this section. As already stated there are of course many more potential distillation schemes we could apply to our protocol. However, we can easily conclude here that if we produce a Bell state of fidelity $F = 0.80$ then there will certainly be a suitable entanglement distillation protocol we could carry out on our final state to improve the fidelity to $0.95 \geq F < 1$.

6.3 Combining Unequal Losses with Non-Ideal and Imperfect Homodyning

In the final section of this chapter on protocol optimisation, we should importantly discuss the most realistic cases of our ES protocol, in which we have unequal losses (in modes B and D), as assessed in Chapter 4, as well as non-ideal and imperfect homodyne detection, as investigated in Chapter 5. In this section, we present possible fidelity results obtained through our protocol, for various values of loss and averaged unequal loss (given by T and Υ respectively), for an imperfect homodyne detection bandwidth of $\Delta x = 0.10$ and $\Delta x = 0.25$. We then increase the non-ideal homodyne measurement outcome, parametrised by ϵ, as high as possible whilst still giving a resultant fidelity of $F = 0.80$, at the peak $|\alpha|$ value. We also present associated vacuum measurement and homodyne measurement success probabilities (discussed in Subsecs. 6.1.1 and 6.1.2 respectively), calculated for the specific values of Δx, ϵ, T, Υ and $|\alpha|$.

Firstly, we will discuss the more simple coherent state protocol. The final density matrix, evaluated for unequal losses, and non-ideal and imperfect homodyne detection, is calculated as:

$$\bar{\rho}_{AC}^{Coh.}(\Upsilon, \Delta x, \epsilon) = \mathrm{Tr}_{\varepsilon_B, \varepsilon_D}\left[\int_{\epsilon-\frac{\Delta x}{2}}^{\epsilon+\frac{\Delta x}{2}} |\Psi_{\upsilon}^{Coh.}\rangle_{A\varepsilon_B C\varepsilon_D}\, \mathrm{d}x_{\frac{\pi}{2}} \int_{\epsilon-\frac{\Delta x}{2}}^{\epsilon+\frac{\Delta x}{2}} {}_{A\varepsilon_B C\varepsilon_D}\langle \Psi_{\upsilon}^{Coh.}|\, \mathrm{d}x_{\frac{\pi}{2}}\right], \tag{6.19}$$

where the state $|\Psi_{\upsilon}^{Coh.}\rangle_{A\varepsilon_B C\varepsilon_D}$ was defined in Eq. 4.9, and we have used the integration method (using the limits $\int_{\epsilon-\frac{\Delta x}{2}}^{\epsilon+\frac{\Delta x}{2}}$) as discussed in Chapter 5, Subsec. 5.7.1. We also note here that the notation of the bar over the final density matrix $\bar{\rho}_{AC}^{Coh.}(\upsilon, \Delta x, \epsilon)$ is used to denote that this matrix has been averaged over υ, as per the method given in Chapter 4, Subsec. 4.2.1.

Using the density matrix defined in Eq. 6.19, we now present tabulated fidelity data, against the $|\Phi^+\rangle = \frac{1}{\sqrt{2}}(|00\rangle + |11\rangle)$ Bell state. We fix the imperfect homodyne measurement bandwidth to $\Delta x = 0.10$ and $\Delta x = 0.25$, as these are the bandwidths evaluated for in Chapter 5, Subsec. 5.7.1, and investigate realistic values for loss (combined with averaged unequal loss), to see which level of homodyne non-ideality (parametrised by ϵ), we can tolerate for these combinations of variables. Finally, we present the peak $|\alpha|$ value which gives us the $|\Phi^+\rangle = \frac{1}{\sqrt{2}}(|00\rangle + |11\rangle)$ Bell state with fidelity of $F = 0.80$, along with associated vacuum and homodyne measurement success probabilities (denoted $\mathcal{P}_0$ (%) and $\mathcal{P}_{Hom.}$ (%), as defined in Eqs. 6.2 and 6.9 respectively):

T	0.98	0.98	0.97	0.99	0.98
Υ	0.05	0.10	0.05	0.05	0.05
Δx	0.10	0.10	0.10	0.25	0.25
ϵ	0.07	0.02	0.05	0.06	0.03
Peak $\|\alpha\|$	1.23	1.25	1.23	1.22	1.22
Fidelity	0.80	0.80	0.80	0.80	0.80
$\mathcal{P}_0^{Coh.}$(%)	52.7	52.7	52.8	52.8	52.7
$\mathcal{P}_{Hom.}^{Coh.}$(%)	7.9	8.0	7.9	19.6	19.7

TABLE 6.1: Tabulated fidelity results ($F = 0.80$) against the $|\Phi^+\rangle = \frac{1}{\sqrt{2}}(|00\rangle + |11\rangle)$ Bell state, for the final state generated through our coherent state entanglement swapping protocol (Eq. 6.19). The protocol has been evaluated for unequal (averaged) loss (Υ) and T, for imperfect homodyne as a measurement bandwidth (Δx), and homodyne non-idealities (ϵ), at the peak $|\alpha|$ value, along with associated vacuum and homodyne measurement success probabilities ($\mathcal{P}_0^{Coh.}$ (%) and $\mathcal{P}_{Hom.}^{Coh.}$ (%) respectively).

Of course, there are many other combinations of variables which could give an acceptable fidelity of $F = 0.80$, however we merely show a few. What is clearly noticeable in Tab. 6.1 is that as the success probability of the homodyne measurement increases (as we go from $\Delta x = 0.10$ to $\Delta x = 0.25$) the levels of loss we can tolerate, and the value of the non-ideal homodyne measurement, decreases. Of course we expect this, and this has been found in many results presented in this thesis. Evidently the vacuum measurement success probability barely changes, and in fact this is also anticipated - the peak $|\alpha|$ which gives us the $|\Phi^+\rangle = \frac{1}{\sqrt{2}}(|00\rangle + |11\rangle)$ Bell state with fidelity $F = 0.80$ remains effectively the same in all combinations of variables given in Tab. 6.1, and we already know, from the plot of Fig. 6.1, that the level of loss needs to increase far beyond the level we consider for this thesis to increase the vacuum measurement success probability.

This trade-off between the levels of imperfections and non-idealities in the homodyne measurement, as well as averaged unequal losses between modes B and D, versus the success probability of the measurements we perform on modes B and D is an important result in this work. Of course, one could theoretically improve these success probabilities by lowering $|\alpha|$ and increasing Δx however we know that this would cause the fidelity to decrease. Arguably, it is vital that we consider a protocol which would produce an entangled state with high enough fidelity such that it can be used for further purposes - the success probability is merely something one has to accept, and in fact, entanglement swapping experiments can be performed very quickly (provided the initial entangled state generation is relatively fast), and so we would simply need to perform this experiment more times to account for the lower success probability.

Let us now review the cat state regime. We first consider the circumstance in which we have the homodyne measurement outcome $x_{\frac{\pi}{4}} = \frac{\pm\mathcal{T}^{+}|\alpha|}{2} \pm \epsilon$:

$$\bar{\rho}^{Cat}_{AC}(\Upsilon, \Delta x, \pm\epsilon) = \text{Tr}_{\varepsilon_B,\varepsilon_D}\left[\int_{\frac{\pm\mathcal{T}^{+}|\alpha|}{2}\pm\epsilon-\frac{\Delta x}{2}}^{\frac{\pm\mathcal{T}^{+}|\alpha|}{2}\pm\epsilon+\frac{\Delta x}{2}} |\Psi^{Cat}_{\upsilon}\rangle_{A\varepsilon_B C\varepsilon_D}\, \mathrm{d}x_{\frac{\pi}{4}} \times \int_{\frac{\pm\mathcal{T}^{+}|\alpha|}{2}\pm\epsilon-\frac{\Delta x}{2}}^{\frac{\pm\mathcal{T}^{+}|\alpha|}{2}\pm\epsilon+\frac{\Delta x}{2}} {}_{A\varepsilon_B C\varepsilon_D}\langle\Psi^{Cat}_{\upsilon}|\, \mathrm{d}x_{\frac{\pi}{4}}\right], \tag{6.20}$$

where the state $|\Psi^{Cat}_{\upsilon}\rangle_{A\varepsilon_B C\varepsilon_D}$ was defined in Chapter 4, Subsec. 4.1.3, and we have used the integration method (using the limits $\int_{\frac{\pm\mathcal{T}^{+}|\alpha|}{2}\pm\epsilon-\frac{\Delta x}{2}}^{\frac{\pm\mathcal{T}^{+}|\alpha|}{2}\pm\epsilon+\frac{\Delta x}{2}}$) as discussed in Chapter 5, Subsec. 5.7.2, and also in Appendix C for the unequal loss ideal homodyne outcome. We also note here that, again, the notation of the bar over the final density matrix $\bar{\rho}^{Coh.}_{AC}(\upsilon, \Delta x, \epsilon)$ is used to denote that this matrix has been averaged over υ, as per the method given in Chapter 4, Subsec. 4.2.1.

Using the density matrix defined in Eq. 6.20, we now present the tabulated fidelity data for the cat state protocol against the $|\Phi^{+}(\alpha)\rangle = \frac{1}{\sqrt{2}}(\,|00\rangle\, e^{-\mathrm{i}|\alpha|^2} + |11\rangle\, e^{+\mathrm{i}|\alpha|^2})$ Bell state. Again, we fix the homodyne measurement bandwidth to $\Delta x = 0.10$ and $\Delta x = 0.25$, and consider various levels of loss, averaged unequal loss and non-ideal homodyne measurement non-idealities:

T	0.98	0.98	0.97	0.97	0.96	0.98	0.98	0.97	0.96
Υ	0.05	0.10	0.05	0.10	0.05	0.05	0.10	0.05	0.05
Δx	0.10	0.10	0.10	0.10	0.10	0.25	0.25	0.25	0.25
ϵ	0.17	0.12	0.15	0.09	0.13	0.15	0.08	0.12	0.07
Peak $\lvert\alpha\rvert$	1.03	1.08	1.05	1.12	1.07	1.05	1.12	1.08	1.13
Fidelity	0.80	0.80	0.80	0.80	0.80	0.80	0.80	0.80	0.80
$\mathcal{P}^{Cat}_{0}(\%)$	56.5	53.2	55.3	50.5	54.0	54.8	50.0	52.7	49.2
$\mathcal{P}^{Cat}_{Hom.}(\%)$	4.1	4.2	4.1	4.2	4.1	10.4	10.6	10.4	10.8

TABLE 6.2: Tabulated fidelity results ($F = 0.80$) against the $|\Phi^{+}(\alpha)\rangle = \frac{1}{\sqrt{2}}(\,|00\rangle\, e^{-\mathrm{i}|\alpha|^2} + |11\rangle\, e^{+\mathrm{i}|\alpha|^2})$ Bell state, for the final state generated through our cat state entanglement swapping protocol (Eq. 6.20), for non-ideal measurement outcome $x_{\frac{\pi}{4}} = \frac{\pm\mathcal{T}^{+}|\alpha|}{2} \pm \epsilon$. The protocol has been evaluated for unequal (averaged) loss (Υ) and T, for imperfect homodyne as a measurement bandwidth (Δx), and homodyne non-idealities (ϵ), at the peak $|\alpha|$ value, along with associated vacuum and homodyne measurement success probabilities ($\mathcal{P}^{Cat}_{0}$ (%) and $\mathcal{P}^{Cat}_{Hom.}$ (%) respectively).

What we can instantly see here is that, compared to the coherent state values presented in Tab. 6.1, we can tolerate higher levels of losses in the cat state regime, provided our homodyne measurement outcome is $x_{\frac{\pi}{4}} = \frac{\pm\mathcal{T}^{+}|\alpha|}{2} \pm \epsilon$. In fact, looking at Tab. 6.2, even when allowing for a homodyne measurement bandwidth of $\Delta x = 0.25$, we still see a peak $|\alpha|$ value which gives us a fidelity of $F = 0.80$, for higher levels of loss given as $T = 0.96$ with an averaged unequal loss value of $\Upsilon = 0.05$.

We note that there are no values of $|\alpha|$ in the coherent state regime in which we can tolerate homodyne measurement bandwidths of $\Delta x \geq 0.10$ whilst allowing for losses of $T < 0.97$ with any level of unequal loss, whilst still giving an acceptable fidelity of $F = 0.80$. This is a key point to this thesis: although the cat state protocol may be harder to implement than the simpler coherent state regime, and indeed the initial hybrid entangled states we require in the cat state protocol are more complicated to prepare (see Chap. 2, Sec. 2.2), the resultant fidelity is nonetheless better for higher levels of loss, and higher levels of homodyne measurement imperfections and non-idealities.

We also importantly point out that in Tab. 6.2 we again see the trade-off between success probability of the vacuum and homodyne measurement, against producing a Bell state of decent fidelity.

Evidently, the cat state protocol is more tolerant to photon losses, and homodyne measurement imperfections and non-idealities, compared to the coherent state protocol. However, we must also assess the cat state protocol for the other non-ideal homodyne measurement outcome $x_{\frac{\pi}{4}} = \frac{\pm\mathcal{T}^{+}|\alpha|}{2} \mp \epsilon$ - we know, from Chapter 5, that this homodyne measurement outcome is not preferred over the other potential homodyne outcome, as we are not producing the $|\Phi^{+}(\alpha)\rangle$ Bell state with as high a fidelity for the same values of losses and homodyne non-idealities and imperfections. In fact, for the homodyne outcome $x_{\frac{\pi}{4}} = \frac{\pm\mathcal{T}^{+}|\alpha|}{2} \mp \epsilon$ we have already seen that we are producing a Bell state of different phase - we discussed this in detail in Chapter 5, Subsec. 5.3.3, where we argued that although one could theoretically determine the phase of this "unknown" Bell state, this would become tedious when supplying a customer (or customers) with these entangled qubits, as we would have to determine the phase precisely each time, dependent on which homodyne measurement outcome we have.

Nevertheless, we can still assess the fidelity of our final state, against our desired $|\Phi^{+}(\alpha)\rangle$ Bell state, for the homodyne measurement outcome $x_{\frac{\pi}{4}} = \frac{\pm\mathcal{T}^{+}|\alpha|}{2} \mp \epsilon$, as we can still produce this Bell state with fidelity of $F = 0.80$ for small levels of loss and homodyne measurement non-idealities and imperfections. Firstly, we again determine the density matrix of our final state for this homodyne measurement outcome, calculated as:

$$\bar{\rho}_{AC}^{Cat}(\Upsilon, \Delta x, \mp\epsilon) = \mathrm{Tr}_{\varepsilon_B,\varepsilon_D}\left[\int_{\frac{\pm\mathcal{T}^{+}|\alpha|}{2}\mp\epsilon-\frac{\Delta x}{2}}^{\frac{\pm\mathcal{T}^{+}|\alpha|}{2}\mp\epsilon+\frac{\Delta x}{2}} |\Psi_{\upsilon}^{Cat}\rangle_{A\varepsilon_B C\varepsilon_D}\,\mathrm{d}x_{\frac{\pi}{4}} \times \int_{\frac{\pm\mathcal{T}^{+}|\alpha|}{2}\mp\epsilon-\frac{\Delta x}{2}}^{\frac{\pm\mathcal{T}^{+}|\alpha|}{2}\mp\epsilon+\frac{\Delta x}{2}} {}_{A\varepsilon_B C\varepsilon_D}\langle\Psi_{\upsilon}^{Cat}|\,\mathrm{d}x_{\frac{\pi}{4}}\right], \tag{6.21}$$

where the state $|\Psi_{\upsilon}^{Cat}\rangle_{A\varepsilon_B C\varepsilon_D}$ was defined in Chapter 4, Subsec. 4.1.3, and we have used the integration method (using the limits $\int_{\frac{\pm\mathcal{T}^{+}|\alpha|}{2}\mp\epsilon-\frac{\Delta x}{2}}^{\frac{\pm\mathcal{T}^{+}|\alpha|}{2}\mp\epsilon+\frac{\Delta x}{2}}$) as discussed in Chapter 5, Subsec. 5.7.2, and also in Appendix C for the unequal loss ideal homodyne outcome. Using the density matrix defined in Eq. 6.21, we now present tabulated

fidelity data, against the $|\Phi^+(\alpha)\rangle$ Bell state:

T	0.98	0.98	0.97	0.96	0.98	0.97
Υ	0.05	0.10	0.05	0.05	0.05	0.05
Δx	0.10	0.10	0.10	0.10	0.25	0.25
ϵ	0.07	0.03	0.06	0.03	0.05	0.02
Peak $\lvert\alpha\rvert$	1.28	1.27	1.29	1.29	1.28	1.26
Fidelity	0.80	0.80	0.80	0.80	0.80	0.80
$\mathcal{P}_0^{Cat}$(%)	38.9	40.2	38.7	39.1	38.9	40.3
$\mathcal{P}_{Hom.}^{Cat}$(%)	5.1	5.0	5.1	5.1	12.7	12.3

TABLE 6.3: Tabulated fidelity results ($F = 0.80$) against the $|\Phi^+(\alpha)\rangle = \frac{1}{\sqrt{2}}(|00\rangle e^{-i|\alpha|^2} + |11\rangle e^{+i|\alpha|^2})$ Bell state, for the final state generated through our cat state entanglement swapping protocol (Eq. 6.20), for non-ideal measurement outcome $x_{\frac{\pi}{4}} = \frac{\pm\mathcal{T}^+|\alpha|}{2} \mp \epsilon$. The protocol has been evaluated for unequal (averaged) loss (Υ) and T, for imperfect homodyne as a measurement bandwidth (Δx), and homodyne non-idealities (ϵ), at the peak $|\alpha|$ value, along with associated vacuum and homodyne measurement success probabilities ($\mathcal{P}_0^{Cat}$ (%) and $\mathcal{P}_{Hom.}^{Cat}$ (%) respectively).

Firstly, if we look at the non-ideal homodyne measurement outcome variable ϵ, we can see in Tab. 6.3 that ϵ has to be much lower to give a fidelity of $F = 0.80$, compared to the corresponding values in the other cat state homodyne outcome results (Tab. 6.2 - again, this has already been noticed and discussed in Chapter 5). Moreover, we can observe that we require higher values of $|\alpha|$ in the circumstance in which we have the $x_{\frac{\pi}{4}} = \frac{\pm\mathcal{T}^+|\alpha|}{2} \mp \epsilon$ homodyne measurement outcome - in fact, this is not entirely detrimental, as it means that the homodyne measurement success probabilities are slightly higher compared to the $x_{\frac{\pi}{4}} = \frac{\pm\mathcal{T}^+|\alpha|}{2} \mp \epsilon$ outcome case (compare Tabs. 6.2 and 6.3, and also the plot of Fig. 6.4). However, this does come at the expense of lower vacuum measurement success probabilities, because we already know that this particular success probability drops to $\mathcal{P}_0^{Cat} = 25\%$ for $|\alpha| > 2.0$. Actually, there is a roughly 10% drop in success probability going from $|\alpha| \approx 1.0$ (the peaks in the $x_{\frac{\pi}{4}} = \frac{\pm\mathcal{T}^+|\alpha|}{2} \pm \epsilon$ results in Tab. 6.2) to $|\alpha| \approx 1.18$ (the peaks in the $x_{\frac{\pi}{4}} = \frac{\pm\mathcal{T}^+|\alpha|}{2} \mp \epsilon$ results in Tab. 6.3).

Conclusively, although the cat state protocol is seemingly more tolerant to photon losses and homodyne measurement imperfections and non-idealities compared to the coherent state protocol, we must remember that this is only in the circumstance in which we have our preferred homodyne measurement outcome $x_{\frac{\pi}{4}} = \frac{\pm\mathcal{T}^+|\alpha|}{2} \pm \epsilon$. It is also of importance that the coherent state protocol gives considerably higher homodyne measurement success probabilities compared to either cat state protocol homodyne measurement outcome results, however the vacuum measurement success probability is best in the cat state regime when $x_{\frac{\pi}{4}} = \frac{\pm\mathcal{T}^+|\alpha|}{2} \pm \epsilon$.

6.4 Sensitivity Analysis of Protocol Variables

Within this section we present a brief so-called "sensitivity analysis" to analyse the trade-space of the protocol variables we have investigated throughout this thesis. Sensitivity analysis is vital, from an experimental perspective, as it can indicate the most optimal variable values one would use to perform this protocol [197, 198], in our case to produce a pair of qubits with the highest possible fidelity against a given Bell state. Although this sort of trade-space analysis has somewhat already been carried out throughout this thesis, particularly in the previous section (Chapter 6, Sec. 6.3), it is nonetheless useful to carry out sensitivity analysis in terms of a visual aid.

In this case, we investigate our protocol trade-space via a three-dimensional scatter plot; for simplicity, in this trade-space analysis we investigate only equal losses, homodyne measurement imperfections, and the peak $|\alpha|$ value which gives us the maximal possible fidelity value at these combinations of variable values. Arguably, these are the most important variables to consider in our protocol, as we showed in Chapter 4 that unequal losses scale almost identically to equal losses, and in terms of the homodyne measurement imperfections and non-idealities (as discussed throughout all of Chapter 5), the homodyne measurement imperfections are something which an experimentalist would somewhat be able to control, by using a more sensitive homodyne detection set-up. Nonetheless, future work within this research could be to carry out a full trade-space analysis.

Firstly, in Fig. 6.6 we present the sensitivity analysis plot for the coherent state ES protocol:

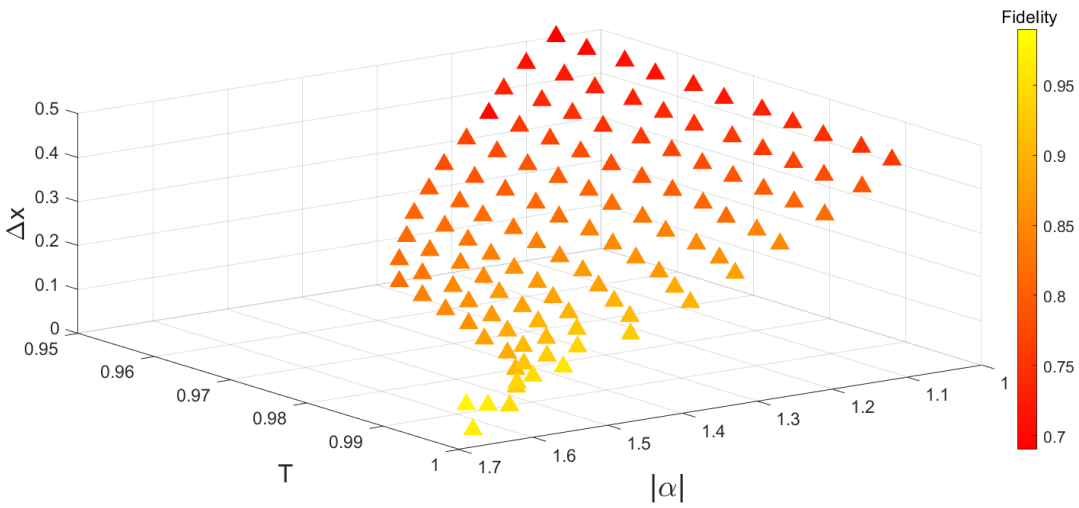

FIGURE 6.6: Sensitivity analysis plot for the coherent state ES protocol, analysing the trade-space of equal losses (T), homodyne measurement imperfections (Δx) and peak $|\alpha|$ values, with colour representing the fidelity value at these combinations of variable values.

What is instantly prominent in Fig. 6.6, is that there is a clear, precise trend to

give us the most optimal fidelity value. In the limits of large homodyne measurement imperfections ($\Delta x > 0.40$) all data points are dark red, thus indicating that the fidelity value is $F < 0.80$. Likewise, in the limits of $T = 0.95$, even for "perfect" homodyne detection (i.e. $\Delta x = 0$), we can see that the fidelity value is still represented as red (although we do note that this red is not as dark for the case in which $T = 0.95$ and $\Delta x \geq 0.25$).

Contrastingly, when considering the limit of very low losses ($T \geq 0.99$) and sharp homodyne measurement bandwidth ($\Delta x \leq 0.10$) we see that the fidelity values indeed approach unity (as represented by the data points turning yellow in Fig. 6.6). We also note the pattern which has been pointed out throughout this thesis: the peak $|\alpha|$ value shifts to larger $|\alpha|$ for lower losses.

We now present the sensitivity analysis plot for the cat state ES protocol in Fig. 6.7:

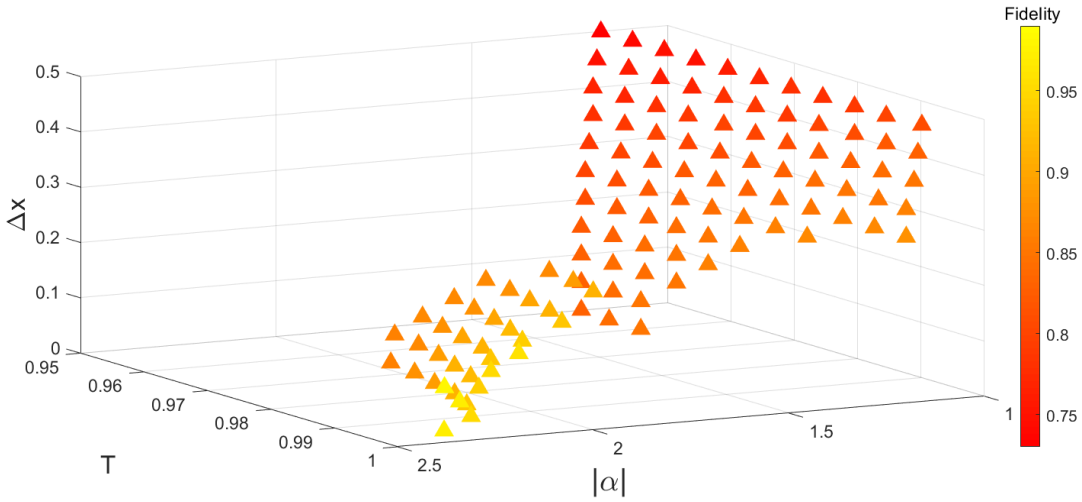

FIGURE 6.7: Sensitivity analysis plot for the cat state ES protocol, analysing the trade-space of equal losses (T), homodyne measurement imperfections (Δx) and peak $|\alpha|$ values, with colour representing the fidelity value at these combinations of variable values.

The trade-space plot of Fig. 6.7 shows a similar trend to that of the coherent state regime (Fig. 6.6). Firstly, we again note that in the limit of large homodyne measurement bandwidth ($\Delta x \geq 0.50$), all data points are represented as dark red, thus indicating that the fidelity is $F < 0.80$. However, we do also point out here that for $\Delta x = 0.40$, in the limit of low losses ($T \geq 0.98$) the data points are orange which indicates that this fidelity is acceptable (i.e. $F \geq 0.80$), which was not the case in Fig. 6.6 - this therefore supports our conclusion in Chapter 5 that the cat state regime is slightly more tolerant to homodyne measurement imperfections.

Furthermore, we note that in the case of low losses ($T \geq 0.97$) and relatively sharp homodyne measurement bandwidth ($\Delta x \leq 0.25$), there are no data points in Fig. 6.7 that are red. In fact, in this region we can see that the peak $|\alpha|$ value dramatically varies, and shifts to much higher values of $|\alpha|$ than in the limit of large homodyne measurement imperfections. This has in fact been noticed throughout

Chapter 5, in which we saw that the maximal fidelity value at characteristic "double-peak" we witness in most cat state plots, as a function of $|\alpha|$, varies; that is to say that for low homodyne measurement bandwidths ($\Delta x \leq 0.25$) and low losses ($T \geq 0.97$) the second peak in the cat state plot gives the highest fidelity value, and in the limit of larger homodyne bandwidths and greater losses, the first peak in the cat state plot gives the maximal fidelity. This behaviour is captured perfectly in the trade-space plot of Fig. 6.7.

To conclude, the variable sensitivity analysis conducted in this section is a graphical tool that would enable an experimentalist to explore different protocol parameters to produce a pair of qubits with a predicted fidelity, without necessarily needing to understand any of the specific underlying physics. We could extend the trade-space carried out in this section to cover all variables investigated in this thesis, however this would have to be done numerically (as opposed to graphically) due to the higher dimensions required to analyse all variables (i.e. including unequal averaged photons losses between modes B and D, and also non-ideal homodyne measurement outcomes). This however is out of the scope of the research carried out in this thesis, and so would make interesting future work.

Chapter 7

Conclusions

Throughout this thesis, we have proposed two entanglement swapping protocols, with the aim to produce a highly entangled pair of qubits. Both protocols require initial hybrid entanglement (between a discrete and continuous variable state), in which in one protocol our continuous variable half is a coherent state superposition, and in the second protocol this continuous variable is a cat state superposition. In the coherent state protocol we ideally produce the $|\Phi^+\rangle = \frac{1}{\sqrt{2}}(\,|00\rangle + |11\rangle)$ Bell state, and in the cat state case we aim to make the phase-rotated $|\Phi^+(\alpha)\rangle = \frac{1}{\sqrt{2}}(\,|00\rangle\, e^{-\mathrm{i}|\alpha|^2} + |11\rangle\, e^{+\mathrm{i}|\alpha|^2})$ Bell state.

We first allowed for small levels of photon losses subjected to two propagating modes (in which the continuous variable states travel through) in Chapter 3, before moving on to model the more realistic regime by investigating unequal (averaged) losses between these two propagating modes in Chapter 4. Next, in Chapter 5 we assessed imperfections and non-idealities in the homodyne measurement used to detect one mode of the propagating continuous variable states, before discussing success probabilities of the homodyne and vacuum measurement schemes, along with potential entanglement distillation methods in Chapter 6. Detailed discussions on all of this was given in the relevant chapters, and so we summarise here the key points discovered in this work:

- In the coherent state protocol, for perfect and ideal homodyne measurements, we can tolerate small levels of photon losses as well as small levels of unequal photon losses ($T \geq 0.96$ for $\Upsilon \geq 0.05$, see Appendix D, Tab. D.3), whilst still producing the $|\Phi^+\rangle$ Bell state with fidelity $F \geq 0.80$ with a peak amplitude $|\alpha|$ value of the coherent state.

- Also in the coherent state regime, we can tolerate smaller levels of photon losses, as well as smaller levels of unequal photon losses, provided that the homodyne measurement is performed with high resolution ($0.10 \leq \Delta x \leq 0.25$), and the non-ideal measurement outcome is $x_{\frac{\pi}{2}} \pm \epsilon$ for $\epsilon \approx \pm 0.05$ (see Chapter 6, Tab. 6.1), whilst still producing the $|\Phi^+\rangle$ Bell state with fidelity $F \geq 0.80$.

- In plots of fidelity as a function of $|\alpha|$, we witness a double-peak in most cat state plots (see the equal loss plot of Fig. 3.19 as an example). This is an advantage over the sharper single peak in coherent state regime, as we have a wider

range of accepted α values that give acceptable fidelity. This range of $|\alpha|$ is also practically feasible - see Chapter 2, Subsec. 1.2.8, in which we discussed that it is easier to experimentally generate lower amplitude ($|\alpha| \approx 1.0$) cat states.

- In the cat state protocol, for perfect and ideal homodyne measurement, we can tolerate higher levels of equal and unequal photon losses ($T \geq 0.95$ for $\Upsilon \geq 0.05$, see Appendix D, Tab. D.4), compared to the coherent state protocol, whilst still producing the $|\Phi^+(\alpha)\rangle$ Bell state with fidelity $F \geq 0.80$.

- Also in the cat state regime, if we allow for slightly smaller levels of photon losses, as well as smaller levels of unequal photon losses, provided that the homodyne measurement is performed with high resolution ($0.10 \leq \Delta x \leq 0.25$), and the non-ideal measurement outcome is $x_{\frac{\pi}{4}} = \frac{\pm\mathcal{T}^+|\alpha|}{2} \pm \epsilon$ for $\epsilon \approx 0.10$ (see Chapter 6, Tab. 6.2), we still produce the $|\Phi^+(\alpha)\rangle$ Bell state with fidelity $F \geq 0.80$.

- In the cat state protocol, if the non-ideal measurement outcome is $x_{\frac{\pi}{4}} = \frac{\pm\mathcal{T}^+|\alpha|}{2} \mp \epsilon$, then we cannot tolerate as large levels of photonic losses or homodyne measurement non-idealities compared to the $x_{\frac{\pi}{4}} = \frac{\pm\mathcal{T}^+|\alpha|}{2} \mp \epsilon$ outcome case (see Chapter 6, Tab. 6.3).

- In either the coherent state or cat state protocol there is a trade-off between the success probability of the vacuum and homodyne measurement schemes, at the expense of higher fidelity (see Tabs. 6.1, 6.2 and 6.3).

Given the summary above, we can conclude that it is indeed possible to produce a highly entangled pair of qubits, with high fidelity against a given Bell state. This is a significant result, as it is the basis for the research conducted as part of this thesis - there is a strong potential in the near future that quantum (as opposed to classical) communication schemes will be required, with the hope to avoid *undetectable* eavesdropping (see introductory discussion in Chapter 1) of information being transmitted between two (or more) parties. As such, there is a need for a secure communication channel that is likely to rely on entangled pairs of qubits to distribute keys of information (as per quantum key distribution, as discussed in the introductory section of Chapter 1).

Although we have, at the heart of quantum information, an elegant concept of quantum entanglement which allows us to detect the presence of an adversary in a quantum communication scheme, as well as performing measurements with correlations that are impossible in classical physics, it is nonetheless well known that entanglement is a very fragile resource and breaks down in the presence of environmental noise [41]. Therefore, investigations such as these carried out in this thesis are of vital importance - we recognise that our proposed entanglement swapping protocols are not particularly resilient to loss, and we do indeed require homodyne detection to be performed with great accuracy, however it is absolutely crucial that

the quantum information research community are aware of what can and cannot be done with regards to communication protocols.

Despite our protocol only being able to suffer relatively low levels of photon loss, we importantly remind the reader that there are a plethora of potential entanglement distillation protocols which could be applied to our final qubit state, as discussed in Chapter 6, Sec. 6.2. In fact, although the results for this are not explicitly discussed in this work, were we to allow for much greater photonic losses (in the region of $T \leq 0.90$), although the fidelity of our final qubit state against a given Bell state would drop dramatically, there are many entanglement distillation protocols which allow one to increase fidelity from $F \approx 0.50$ to $F \geq 0.90$. Although this does come at the expense of requiring many more pairs of lower fidelity qubits to perform this task (compared to applying an entanglement distillation protocol to a pair of qubits of fidelity $F \approx 0.80$), we do imperatively note that we could potentially consider far higher levels of photon loss.

Moreover, we also point out that quantum repeater networks (see introductory section of Chapter 1), that rely on relatively short-distance entanglement swapping experiments between "nodes" are a way in which quantum communications are able to compensate for continuous variable quantum states fragility to photon losses. Quantum repeater networks are a real possibility in the future for truly long-distance quantum communication schemes in distributing entanglement, and entanglement swapping protocols such as these proposed in this work are potential applicants for these schemes. We do also acknowledge there is indeed potential for entanglement swapping protocols to be used for quantum teleportation purposes for communication between *adjacent* (i.e. not far separated) quantum computing processors [199].

Nevertheless, the aim of this work is to provide a customer (or indeed customers) with a highly entangled pair of qubits, with a respectable fidelity against a given Bell state in which the customer are aware they are receiving. As already discussed, in the coherent state protocol we are producing a standard $|\Phi^+\rangle = \frac{1}{\sqrt{2}}(\,|00\rangle + |11\rangle)$ Bell state. Contrastingly, in the cat state regime we tend to produce a phase-rotated $|\Phi^+(\alpha)\rangle = \frac{1}{\sqrt{2}}(\,|00\rangle\, e^{-\mathrm{i}|\alpha|^2} + |11\rangle\, e^{+\mathrm{i}|\alpha|^2})$ Bell state. This phase is not of detriment to the usefulness of our cat state protocol, however in the practical implementation of this it would require one to inform a customer specifically the phase present each times (which is given by the amplitude of the coherent states used $|\alpha|$).

This does, however, become more complicated when we consider the realistic circumstance in which we allow for homodyne measurement non-idealities. In the cat state protocol, for the less desirable non-ideal outcome of $x_{\frac{\pi}{4}} = \pm|\alpha| \mp \epsilon$ we in fact are no longer tending towards the $|\Phi^+(\alpha)\rangle$ Bell state. We concluded in Chapter 5, Subsec. 5.3.3 that we nonetheless still provide this state to a customer but simply state the fidelity against the desired $|\Phi^+(\alpha)\rangle$ Bell state, however, we speculate here that we could potentially provide a better service to a customer: if an automatic phase compensation system could be implemented, which would take the actual non-ideal outcome (ϵ) of the homodyne measurement each time and automatically

apply a phase-correction shift to the outgoing Bell state, one could theoretically correct the phase to that for the ideal measurement result, such that we then would be sending a customer the $|\Phi^+(\alpha)\rangle$ Bell state with higher fidelity. Although this is in practice technologically demanding it is nevertheless possible, and could be investigated in detail as part of further work on this project.

Other possible further work on this project could be in actually theoretically performing an entanglement distillation protocol to our resultant state, to determine precisely the distilled fidelity that could be obtained, given our specific "pre-distillation" fidelities. We could also investigate other non-classical states of light as the propagating mode in our entanglement swapping protocol, such as squeezed coherent states (discussed briefly in Chapter 1, Subsec. 1.2.7), which are also extensively researched for potential candidates in quantum communication schemes [200–202]. Furthermore we could also apply other homodyne imperfections (as opposed to just the measurement resolution bandwidth as per this work), such as imperfections in the photon number detectors as part of the homodyne set-up (see the discussion of our homodyne set-up in Chapter 2, Sec. 2.6) to account for dark counts (the cases in which "clicks" were recorded despite there being no photon present), or even looking into noise that the homodyne local oscillator could be subjected to [152].

The field of quantum communications is no longer simply a theoretical possibility in its infancy, we are now at the stage of research in which we are approaching realisable communication systems which could be implemented in the relatively near future. Funding for this industry has flourished over the past few years: in 2014 the UK government invested £270 million towards quantum technology research funding, with the aim of commercialising these technologies [203], as well as the launch of the world's first quantum satellite (utilising entangled quantum states) by China in 2016 in the longest commercial quantum communications link established at the time of writing [204]. All of this substantial funding and effort is a global goal to realise one thing: provably secure, practical communication schemes to prevent eavesdropping and hacking of information. Entanglement distribution protocols, such as the ones investigated in this thesis, are therefore of paramount importance in realising the future of secure communications, for the safety and security of our own personal information and data.

Appendix A

The Completeness Relation of the Coherent State

We here present the completeness relation for coherent states, and in doing so show that they form an overcomplete basis. This derivation has been adapted from C. C. Gerry and P. L. Knight's *Introductory Quantum Optics*[80].

Firstly, we begin with an integral over the complex α plane:

$$\hat{I}_\alpha = \int |\alpha\rangle \langle\alpha| \, \mathrm{d}^2\alpha = \int e^{-|\alpha|^2} \sum_{n=0}^{\infty} \sum_{m=0}^{\infty} \frac{\alpha^n (\alpha^*)^m}{\sqrt{n!m!}} |n\rangle \langle m| \, \mathrm{d}^2\alpha, \tag{A.1}$$

where we have made use of the number state representation of the coherent states (see Eq. 1.7), and $\mathrm{d}^2\alpha = \mathrm{dRe}(\alpha)\mathrm{dIm}(\alpha)$. Transforming to polar coordinates this becomes:

$$\hat{I}_\alpha = \sum_{n=0}^{\infty} \sum_{m=0}^{\infty} \frac{|n\rangle \langle m|}{\sqrt{n!m!}} \int_0^\infty e^{-r^2} r^{n+m+1} \mathrm{d}r \int_0^{2\pi} e^{\mathrm{i}(n-m)\theta} \mathrm{d}\theta, \tag{A.2}$$

having set $\alpha = re^{\mathrm{i}\theta}$ and $\mathrm{d}^2\alpha = r\mathrm{d}r\mathrm{d}\theta$. It follows that:

$$\int_0^{2\pi} e^{\mathrm{i}(n-m)\theta} \mathrm{d}\theta = 2\pi\delta_{nm}, \tag{A.3}$$

where δ_{nm} is the Kronecker delta function, satisfying $\delta_{nm} = 0$ for $n \neq m$ and $\delta_{nm} = 1$ for $n = m$. Therefore:

$$\begin{aligned} \hat{I}_\alpha &= 2\pi \sum_{n=0}^{\infty} \frac{|n\rangle \langle n|}{n!} \int_0^\infty e^{-r^2} r^{n+m+1} \mathrm{d}r \\ &= \pi \sum_{n=0}^{\infty} \frac{|n\rangle \langle n|}{n!} \int_0^\infty e^{-y} y^n \mathrm{d}y, \end{aligned} \tag{A.4}$$

where we have set $r^2 = y$ and $2r\mathrm{d}r = \mathrm{d}y$. Finally, $\int_0^\infty e^{-y} y^n \mathrm{d}y = n!$, and so the proof finishes with:

$$\hat{I}_\alpha = \pi \sum_{n=0}^{\infty} |n\rangle \langle n| = \pi, \quad \text{since} \quad \sum_{n=0}^{\infty} |n\rangle \langle n| = \hat{I}. \tag{A.5}$$

Appendix B

Deriving the Homodyne Measurement Operator

We want to obtain the wavefunction $\psi_\alpha(x_\theta) = \langle x_\theta || \alpha | e^{\mathrm{i}\phi} \rangle$, as introduced in Eq. 1.13.

We can rewrite $||\alpha|e^{\mathrm{i}\phi}\rangle$ in terms of the displacement operator as

$$\psi_\alpha(x_\theta) = \langle x_\theta | \hat{D}(\alpha) |0\rangle , \tag{B.1}$$

where $\hat{D}(\alpha) = e^{\alpha\hat{a}^\dagger - \alpha^*\hat{a}}$ acts on the vacuum state $|0\rangle$ to give a coherent state (see Eq. 1.10). We then express the displacement operator in terms of $\hat{x}$ and $\hat{p}$ (given in Eq. 1.11), where:

$$\hat{x} = \frac{1}{2}(\hat{a}^\dagger + \hat{a}), \quad \hat{p} = \frac{\mathrm{i}}{2}(\hat{a}^\dagger - \hat{a}), \tag{B.2}$$

for $\hat{a} = \hat{x} + \mathrm{i}\hat{p}$ and $\hat{a}^\dagger = \hat{x} - \mathrm{i}\hat{p}$. The displacement operator is therefore:

$$\alpha\hat{a}^\dagger - \alpha^*\hat{a} = \hat{x}\,(\alpha - \alpha^*) - \mathrm{i}\hat{p}\,(\alpha + \alpha^*) , \tag{B.3}$$

$$\therefore \hat{D}(\alpha) = e^{\alpha\hat{a}^\dagger - \alpha^*\hat{a}} = \exp\left[\hat{x}\,(\alpha - \alpha^*)\right] \exp\left[-\mathrm{i}\hat{p}\,(\alpha + \alpha^*)\right] \exp\left[\frac{(\alpha^*)^2 - \alpha^2}{2}\right] \tag{B.4}$$

using the Baker-Campbell-Hausdorff Formula: $e^{A+B} = e^A e^B e^{-\frac{1}{2}[A,B]}$ [136]. Substituting Eq. B.4 into B.1 we have:

$$\psi_\alpha(x_\theta) = e^{\frac{(\alpha^*)^2 - \alpha^2}{2}} \langle x_\theta | e^{\hat{x}(\alpha - \alpha^*)} e^{-\mathrm{i}\hat{p}(\alpha + \alpha^*)} |0\rangle , \tag{B.5}$$

using, $\hat{x}\,|x_\theta\rangle = x_\theta\,|x_\theta\rangle$,

$$\psi_\alpha(x_\theta) = e^{\frac{(\alpha^*)^2 - \alpha^2}{2}} e^{x_\theta(\alpha - \alpha^*)} \langle x_\theta | e^{-\mathrm{i}\hat{p}(\alpha + \alpha^*)} |0\rangle . \tag{B.6}$$

We apply the translation operator $\hat{S}(\lambda) = e^{-\mathrm{i}\lambda\hat{p}}$ to $\langle x_\theta|$, using $\langle x_\theta| S(\lambda) = \langle x_\theta - \lambda|$. We now want to determine $\langle x_\theta| e^{-\mathrm{i}\hat{p}(\alpha+\alpha^*)}$, therefore $\lambda = \alpha + \alpha^*$,

$$\begin{aligned}\psi_\alpha(x_\theta) &= e^{\frac{(\alpha^*)^2-\alpha^2}{2}} e^{x_\theta(\alpha-\alpha^*)} \langle x_\theta - (\alpha+\alpha^*)|0\rangle \\ &= \pi^{-\frac{1}{4}} e^{-\frac{\left(\sqrt{2}\,x_\theta-(\alpha+\alpha^*)\right)^2}{2}} e^{\frac{(\alpha^*)^2-\alpha^2}{2}} e^{(\alpha-\alpha^*)x_\theta},\end{aligned} \tag{B.7}$$

where the factor $2^{\frac{1}{4}}\pi^{-\frac{1}{4}} e^{-\frac{\left(\sqrt{2}\,x_\theta-(\alpha+\alpha^*)\right)^2}{2}}$ comes from the wavefunction of the vacuum $\langle x_\theta - (\alpha+\alpha^*)|0\rangle$.

The next step is to write α and α^* in terms of the expectation values of the position and momentum operators, $\langle\hat{x}\rangle$ and $\langle\hat{p}\rangle$ respectively. To derive the "rotated" operators $\langle\hat{x}_\theta\rangle$ and $\langle\hat{p}_\theta\rangle$ from $\langle\hat{x}\rangle$ and $\langle\hat{p}\rangle$, we can use the rotation matrix as follows:

$$\begin{matrix}\langle\hat{x}\rangle \\ \langle\hat{p}\rangle\end{matrix}\begin{pmatrix}\cos\theta & \sin\theta \\ -\sin\theta & \cos\theta\end{pmatrix} \rightarrow \begin{cases}\langle\hat{x}_\theta\rangle = \alpha\left[\mathrm{Re}\left(e^{\mathrm{i}\phi}\right)\mathrm{Re}\left(e^{\mathrm{i}\theta}\right) + \mathrm{Im}\left(e^{\mathrm{i}\phi}\right)\mathrm{Im}\left(e^{\mathrm{i}\theta}\right)\right] \\ \langle\hat{p}_\theta\rangle = \alpha\left[-\mathrm{Re}\left(e^{\mathrm{i}\phi}\right)\mathrm{Im}\left(e^{\mathrm{i}\theta}\right) + \mathrm{Im}\left(e^{\mathrm{i}\phi}\right)\mathrm{Re}\left(e^{\mathrm{i}\theta}\right)\right],\end{cases} \tag{B.8}$$

where, $\cos\theta = \mathrm{Re}\left(e^{\mathrm{i}\theta}\right)$ and $\sin\theta = \mathrm{Im}\left(e^{\mathrm{i}\theta}\right)$, and also $\langle\hat{x}\rangle = \alpha\,\mathrm{Re}\left(e^{\mathrm{i}\phi}\right)$ and $\langle\hat{p}\rangle = \alpha\,\mathrm{Im}\left(e^{\mathrm{i}\phi}\right)$. Therefore,

$$\langle\hat{x}_\theta\rangle = \alpha\left[\cos\phi\cos\theta + \sin\phi\sin\theta\right] = \alpha\cos(\phi-\theta) = \alpha\,\mathrm{Re}\left(e^{\mathrm{i}(\phi-\theta)}\right), \tag{B.9}$$

$$\langle\hat{p}_\theta\rangle = \alpha\left[-\cos\phi\sin\theta + \sin\phi\cos\theta\right] = \alpha\sin(\phi-\theta) = \alpha\,\mathrm{Im}\left(e^{\mathrm{i}(\phi-\theta)}\right). \tag{B.10}$$

It follows that $\langle\hat{x}\rangle = \alpha_x$ and $\langle\hat{p}\rangle = \alpha_y$ (using $\alpha = \alpha_x + \mathrm{i}\alpha_y$ and $\alpha^* = \alpha_x - \mathrm{i}\alpha_y$), and the terms containing α and α^* in Eq. B.7 may be expressed as:

$$\frac{(\alpha+\alpha^*)}{2} = \frac{2\alpha_x}{2} = \alpha_x = \langle\hat{x}\rangle, \tag{B.11}$$

$$\frac{(\alpha-\alpha^*)}{2} = \frac{2\mathrm{i}\alpha_y}{2} = \mathrm{i}\alpha_y = \mathrm{i}\langle\hat{p}\rangle. \tag{B.12}$$

Bringing this altogether, the final equation for the derivation of the wavefunction $\psi_\alpha(x_\theta)$ is therefore given by:

$$\psi_\alpha(x_\theta) = \frac{2^{\frac{1}{4}}e^{\mathrm{i}\gamma}}{\pi^{\frac{1}{4}}}\exp\left[-\frac{1}{2}\left(\sqrt{2}\,x_\theta - 2\langle\hat{x}\rangle\right)^2 + 2\sqrt{2}\,\mathrm{i}\langle\hat{p}\rangle\,x_\theta\right], \tag{B.13}$$

where $e^{\mathrm{i}\gamma} = e^{\frac{(\alpha^*)^2-\alpha^2}{2}}$ is a global phase factor (and can therefore be omitted if need be). We can express B.13 in terms of the amplitude α of the coherent state $|\alpha\rangle$, and the homodyne measurement outcome x_θ, which gives:

$$\left\langle x_\theta\middle|\alpha e^{\mathrm{i}\varphi}\right\rangle = \frac{1}{2^{-\frac{1}{4}}\pi^{\frac{1}{4}}}\exp\left[-(x_\theta)^2 + 2e^{\mathrm{i}(\varphi-\theta)}\alpha x_\theta - \frac{1}{2}e^{2\mathrm{i}(\varphi-\theta)}\alpha^2 - \frac{1}{2}\alpha^2\right], \tag{B.14}$$

which is the exact form used in the calculations in this thesis (see Eq. 2.24).

Appendix C

Deriving the Homodyne Measurement Outcomes for Cat State ES

In this appendix we will briefly show why the measurement outcomes for the (no loss) cat state entanglement swapping protocol are $x_{\frac{\pi}{4}} = \pm|\alpha|$. Firstly, we begin this derivation with the state immediately after the vacuum projection has been applied (see Eq. 3.51), however this time we take the large $|\alpha|$ limit, so as to exponentially dampen the modes that decay as $|\alpha|$ increases, such that:

$$|\psi^{Cat}\rangle_{ACD} = \frac{1}{2}\Big[\,|00\rangle_{AC}\left(|\sqrt{2}\,|\alpha|\rangle_D + |-\sqrt{2}\,|\alpha|\rangle_D\right) + |11\rangle_{AC}\left(|\sqrt{2}\,\mathrm{i}|\alpha|\rangle_D + |-\sqrt{2}\,\mathrm{i}|\alpha|\rangle_D\right)\Big]. \tag{C.1}$$

(Note that this state is normalised for large $|\alpha|$). We now perform homodyne detection in mode D (see Sec. 2.24 for general case), which gives:

$$\begin{aligned}|\Psi^{Cat}\rangle_{AC} = \frac{1}{2}\frac{1}{2^{-\frac{1}{4}}\pi^{\frac{1}{4}}}\Bigg[\,&|00\rangle_{AC}\left(\exp\Big[-(x_{\frac{\pi}{4}})^2 + 2\sqrt{2}\,|\alpha|x_{\frac{\pi}{4}}e^{-\frac{\mathrm{i}\pi}{4}} - |\alpha|^2e^{-\frac{\mathrm{i}\pi}{2}} - |\alpha|^2\Big]\right.\\ &\left.+\exp\Big[-(x_{\frac{\pi}{4}})^2 + 2\sqrt{2}\,|\alpha|x_{\frac{\pi}{4}}e^{\frac{3\mathrm{i}\pi}{4}} - |\alpha|^2e^{\frac{3\mathrm{i}\pi}{2}} - |\alpha|^2\Big]\right)\\ &+|11\rangle_{AC}\left(\exp\Big[-(x_{\frac{\pi}{4}})^2 + 2\sqrt{2}\,|\alpha|x_{\frac{\pi}{4}}e^{\frac{\mathrm{i}\pi}{4}} - |\alpha|^2e^{\frac{\mathrm{i}\pi}{2}} - |\alpha|^2\Big]\right.\\ &\left.+\exp\Big[-(x_{\frac{\pi}{4}})^2 + 2\sqrt{2}\,|\alpha|x_{\frac{\pi}{4}}e^{-\frac{3\mathrm{i}\pi}{4}} - |\alpha|^2e^{-\frac{3\mathrm{i}\pi}{2}} - |\alpha|^2\Big]\right)\Bigg]\end{aligned} \tag{C.2}$$

$$= \frac{1}{2^{\frac{3}{4}}\pi^{\frac{1}{4}}}\Bigg[|00\rangle_{AC} \Bigg(\exp\Big[-(x_{\frac{\pi}{4}})^2 + (1-\mathrm{i})2|\alpha|x_{\frac{\pi}{4}} + \mathrm{i}|\alpha|^2 - |\alpha|^2\Big] + \exp\Big[-(x_{\frac{\pi}{4}})^2 - (1-\mathrm{i})2|\alpha|x_{\frac{\pi}{4}} + \mathrm{i}|\alpha|^2 - |\alpha|^2\Big]\Bigg) + |11\rangle_{AC} \Bigg(\exp\Big[-(x_{\frac{\pi}{4}})^2 + (1+\mathrm{i})2|\alpha|x_{\frac{\pi}{4}} - \mathrm{i}|\alpha|^2 - |\alpha|^2\Big] + \exp\Big[-(x_{\frac{\pi}{4}})^2 - (1+\mathrm{i})2|\alpha|x_{\frac{\pi}{4}} - \mathrm{i}|\alpha|^2 - |\alpha|^2\Big]\Bigg)\Bigg]. \tag{C.3}$$

Next, we then complete the square so that we can see analytically where the peaks in the distribution of the coherent states are:

$$|\Psi^{Cat}\rangle_{AC} = \frac{1}{2^{\frac{3}{4}}\pi^{\frac{1}{4}}}\Bigg[|00\rangle_{AC} \Bigg(\exp\Big[-(x_{\frac{\pi}{4}} - |\alpha|)^2 - \mathrm{i}2|\alpha|x_{\frac{\pi}{4}} + \mathrm{i}|\alpha|^2\Big] + \exp\Big[-(x_{\frac{\pi}{4}} + |\alpha|)^2 + \mathrm{i}2|\alpha|x_{\frac{\pi}{4}} + \mathrm{i}|\alpha|^2\Big]\Bigg) + |11\rangle_{AC} \Bigg(\exp\Big[-(x_{\frac{\pi}{4}} - |\alpha|)^2 + \mathrm{i}2|\alpha|x_{\frac{\pi}{4}} - \mathrm{i}|\alpha|^2\Big] + \exp\Big[-(x_{\frac{\pi}{4}} + |\alpha|)^2 - \mathrm{i}2|\alpha|x_{\frac{\pi}{4}} - \mathrm{i}|\alpha|^2\Big]\Bigg)\Bigg] \tag{C.4}$$

$$= \frac{1}{2^{-\frac{1}{4}}\pi^{\frac{1}{4}}}\Bigg[\frac{1}{\sqrt{2}}\Bigg(\frac{1}{\sqrt{2}}\Bigg(|00\rangle_{AC} \exp\Big[-\mathrm{i}2|\alpha|x_{\frac{\pi}{4}} + \mathrm{i}|\alpha|^2\Big] + |11\rangle_{AC} \exp\Big[\mathrm{i}2|\alpha|x_{\frac{\pi}{4}} - \mathrm{i}|\alpha|^2\Big]\Bigg) \times \exp\Big[-(x_{\frac{\pi}{4}} - |\alpha|)^2\Big] + \frac{1}{\sqrt{2}}\Bigg(|00\rangle_{AC} \exp\Big[\mathrm{i}2|\alpha|x_{\frac{\pi}{4}} + \mathrm{i}|\alpha|^2\Big] + |11\rangle_{AC} \exp\Big[-\mathrm{i}2|\alpha|x_{\frac{\pi}{4}} - \mathrm{i}|\alpha|^2\Big]\Bigg) \times \exp\Big[-(x_{\frac{\pi}{4}} + |\alpha|)^2\Big]\Bigg)\Bigg]. \tag{C.5}$$

This wavefunction describing the state immediately after the homodyne measurement (in the large α limit) clearly shows two possibilities of the homodyne measurement outcome for the cat state protocol: $x_{\frac{\pi}{4}} = \pm\alpha$. It then follows that the state we are producing is a maximally entangled Bell state that includes a phase:

$$\big|\psi^{Cat}_{Final}\big\rangle_{AC} = \frac{1}{\sqrt{2}}\Big(|00\rangle_{AC}\, e^{-\mathrm{i}|\alpha|^2} + |11\rangle_{AC}\, e^{+\mathrm{i}|\alpha|^2}\Big). \tag{C.6}$$

for both homodyne measurement outcomes.

Finally, note that when following the same derivation as detailed in this appendix, but instead considering losses, the homodyne measurement outcomes are then $x_{\frac{\pi}{4}} = \pm\sqrt{T}\,|\alpha|$, and for unequal losses (as detailed in Sec. 4) $x_{\frac{\pi}{4}} = \pm\frac{(\sqrt{T}+\sqrt{T-v})|\alpha|}{2}$.

Appendix D

Tabulated Fidelity Data

In this appendix we present tabulated data for the fidelity results at each peak $|\alpha|$ value present in the plots, for both equal and unequal photonic losses in modes B and D of our proposed protocols. The results displayed in **green** are the most acceptable values of fidelity for $F \geq 0.90$ and those highlighted in **amber** are for $F \geq 0.80$ and could be acceptable when combined with a suitable entanglement purification protocol.

T	1	0.99	0.98	0.97	0.96	0.95
Peak $\|\alpha\|$	$\geq$1.63	1.53	1.42	1.36	1.31	1.27
Fidelity	1.00	0.95	0.91	0.88	0.85	0.82

TABLE D.1: Tabulated fidelity results for coherent state ES, for equal loss, at the peak $|\alpha|$ value, for various T.

T	1	0.99	0.98	0.97	0.96	0.95
1st Peak $\|\alpha\|$	1.24	1.23	1.23	1.23	1.23	1.23
Fidelity	0.93	0.91	0.89	0.87	0.85	0.83
2nd Peak $\|\alpha\|$	$\geq$2.30	2.15	2.03	1.97	1.93	1.89
Fidelity	1.00	0.95	0.91	0.88	0.85	0.82

TABLE D.2: Tabulated fidelity results for cat state ES, for equal loss, at the two peak $|\alpha|$ values, for various T.

T	1	1	1	1	0.99	0.99	0.99	0.99
Υ	0	0.01	0.05	0.1	0	0.01	0.05	0.1
Peak $\|\alpha\|$	$\geq$1.63	1.67	1.44	1.34	1.53	1.48	1.37	1.30
Fidelity	1.00	0.97	0.91	0.86	0.95	0.93	0.88	0.83

T	0.98	0.98	0.98	0.98	0.97	0.97	0.97	0.97
Υ	0	0.01	0.05	0.1	0	0.01	0.05	0.1
Peak $\|\alpha\|$	1.42	1.39	1.32	1.26	1.36	1.34	1.28	1.23
Fidelity	0.91	0.90	0.85	0.81	0.88	0.86	0.83	0.79

T	0.96	0.96	0.96	0.96	0.95	0.95	0.95	0.95
Υ	0	0.01	0.05	0.1	0	0.01	0.05	0.1
Peak $\|\alpha\|$	1.31	1.30	1.25	1.21	1.27	1.26	1.22	1.19
Fidelity	0.85	0.84	0.80	0.77	0.82	0.81	0.78	0.75

TABLE D.3: Tabulated fidelity results for coherent state ES, unequal loss, at the peak $|\alpha|$ value, for various T and Υ.

T	1	1	1	1	0.99	0.99	0.99	0.99
Υ	0	0.01	0.05	0.1	0	0.01	0.05	0.1
1st Peak $\|\alpha\|$	1.24	1.23	1.23	1.23	1.23	1.23	1.23	1.23
Fidelity	0.93	0.92	0.89	0.85	0.91	0.90	0.87	0.83
2nd Peak $\|\alpha\|$	$\geq$2.30	2.36	2.05	1.96	2.15	2.09	1.98	1.92
Fidelity	1.00	0.97	0.91	0.86	0.95	0.93	0.88	0.83

T	0.98	0.98	0.98	0.98	0.97	0.97	0.97	0.97
Υ	0	0.01	0.05	0.1	0	0.01	0.05	0.1
1st Peak $\|\alpha\|$	1.23	1.23	1.23	1.23	1.23	1.23	1.23	1.23
Fidelity	0.89	0.88	0.85	0.82	0.87	0.86	0.83	0.80
2nd Peak $\|\alpha\|$	2.03	2.01	1.93	1.88	1.97	1.95	1.90	1.85
Fidelity	0.91	0.89	0.85	0.80	0.88	0.86	0.82	0.78

T	0.96	0.96	0.96	0.96	0.95	0.95	0.95	0.95
Υ	0	0.01	0.05	0.1	0	0.01	0.05	0.1
1st Peak $\|\alpha\|$	1.23	1.23	1.23	1.23	1.23	1.23	1.23	1.23
Fidelity	0.85	0.84	0.82	0.78	0.83	0.83	0.80	0.77
2nd Peak $\|\alpha\|$	1.93	1.91	1.86	1.81	1.89	1.87	1.83	1.77
Fidelity	0.85	0.84	0.80	0.76	0.82	0.81	0.78	0.74

TABLE D.4: Tabulated fidelity results for cat state ES, for unequal loss, at the two peak $|\alpha|$ values, for various T.

Appendix E

Examples of Code

In this appendix we present examples of the code used to generate the plots for entanglement negativity, fidelity and linear entropy throughout this thesis. We used Mathematica 11.3 [205] to perform calculations, having written the code manually ourselves. We reference the use of the "QDENSITY" Package, given in the reference [206], to perform the partial transpose operation ("PartialTranspose1" in code below) on our final density matrix, as part of the entanglement negativity calculation.

Firstly, we present the code used to perform the entanglement negativity calculation on our final density matrices ("DensityMatrix" in our codes below), calculated using a loop ($k = k + 1$):

```
EntanglementLoop = Table[{0, 0}, {i, 1, 1000}];
For[k = 1,
  k ≤ 1000,
  k = k + 1,
  Alpha = N[k / 100];
  Eigen1 = 0;
  Eigen2 = 0;
  Eigen3 = 0;
  Eigen4 = 0;
  DensityMatrixEigenvalues =
   Eigenvalues[PartialTranspose1[{2},
     DensityMatrix /. {alpha → Alpha, xtheta → 0,
       T → 1}]];
  Eigen1 = DensityMatrixEigenvalues[[1]];
  Eigen2 = DensityMatrixEigenvalues[[2]];
  Eigen3 = DensityMatrixEigenvalues[[3]];
  Eigen4 = DensityMatrixEigenvalues[[4]];
  EntanglementLoop[[k]] =
   {Alpha, Simplify[((Abs[Eigen1] - Eigen1)
       + (Abs[Eigen2] - Eigen2) + (Abs[Eigen3] - Eigen3) +
       (Abs[Eigen4] - Eigen4))]};
 ];
```

In a similar fashion, we also calculate fidelity and linear entropy using a loop code:

```
Fidelity = Table[{0, 0}, {i, 1, 1000}];
For[k = 1,
  k ≤ 1000,
  k = k + 1,
  Alpha = N[k / 100];
  Fidelity[[k]] =
   {Alpha,
    Abs[Tr[MatrixPower[(MatrixPower[BellState, 1 / 2])
          .(DensityMatrix /. {alpha → Alpha, T → 1,
             xtheta → 0})
          .(MatrixPower[BellState, 1 / 2]), 1 / 2]]^2};
 ];
```

```
LinearEntropy = Table[{0, 0}, {i, 1, 1000}];
For[k = 1,
  k ≤ 1000,
  k = k + 1,
  Alpha = N[k / 100];
  LinearEntropy[[k]] = {Alpha,
    1 -
     Tr[MatrixPower[DensityMatrix /.
        {alpha → Alpha, xtheta → 0, T → 1}, 2]]};
 ];
```

In the fidelity code note that "BellState" is the density matrix representation of whichever Bell state we calculate fidelity against.

Note that in the above codes we are looping the value of $|\alpha|$ ("Alpha" in the above codes), as most of the graphs throughout this thesis are plotted as a function of $|\alpha|$. Also, the variables contained within our density matrix ("xtheta", corresponding to the homodyne measurement outcome x_θ, and "T" in the above codes) can be simply adjusted by changing their value. We also assess homodyne measurement non-idealities (ϵ) and averaged unequal losses in the same manner.

Appendix F

Cat State ES with Unequal Losses

For the case where we do not have equal losses in modes B and D (i.e. $T_B \neq T_D \rightarrow T_B = T$ and $T_D = T - \delta$). Starting from Eq. 1, we apply our (unequal) lossy beam-splitters to obtain (in which we set $\eta = 1 - T$):

$$
\begin{aligned}
|\Psi_{v}^{Cat}\rangle_{AB\varepsilon_B CD\varepsilon_D} = \mathcal{N}\Big[\, |00\rangle_{AC} \Big((\, |\sqrt{T}\,|\alpha|\rangle_B \, |\sqrt{\eta}\,|\alpha|\rangle_{\varepsilon_B} + |-\sqrt{T}\,|\alpha|\rangle_B \, |-\sqrt{\eta}\,|\alpha|\rangle_{\varepsilon_B}) \times \\
(\, |\sqrt{T-v}\,|\alpha|\rangle_D \, |\sqrt{\eta+v}\,|\alpha|\rangle_{\varepsilon_D} + |-\sqrt{T-v}\,|\alpha|\rangle_D \, |-\sqrt{\eta+v}\,|\alpha|\rangle_{\varepsilon_D}) \Big) \\
+ |01\rangle_{AC} \Big((\, |\sqrt{T}\,|\alpha|\rangle_B \, |\sqrt{\eta}\,|\alpha|\rangle_{\varepsilon_B} + |-\sqrt{T}\,|\alpha|\rangle_B \, |-\sqrt{\eta}\,|\alpha|\rangle_{\varepsilon_B}) \times \\
(\, |\sqrt{T-v}\,\mathrm{i}|\alpha|\rangle_D \, |\sqrt{\eta+v}\,\mathrm{i}|\alpha|\rangle_{\varepsilon_D} + |-\sqrt{T-v}\,\mathrm{i}|\alpha|\rangle_D \, |-\sqrt{\eta+v}\,\mathrm{i}|\alpha|\rangle_{\varepsilon_D}) \Big) \\
+ |10\rangle_{AC} \Big((\, |\sqrt{T}\,\mathrm{i}|\alpha|\rangle_B \, |\sqrt{\eta}\,\mathrm{i}|\alpha|\rangle_{\varepsilon_B} + |-\sqrt{T}\,\mathrm{i}|\alpha|\rangle_B \, |-\sqrt{\eta}\,\mathrm{i}|\alpha|\rangle_{\varepsilon_B}) \times \\
(\, |\sqrt{T-v}\,|\alpha|\rangle_D \, |\sqrt{\eta+v}\,|\alpha|\rangle_{\varepsilon_D} + |-\sqrt{T-v}\,|\alpha|\rangle_D \, |-\sqrt{\eta+v}\,|\alpha|\rangle_{\varepsilon_D}) \Big) \\
+ |11\rangle_{AC} \Big((\, |\sqrt{T}\,\mathrm{i}|\alpha|\rangle_B \, |\sqrt{\eta}\,\mathrm{i}|\alpha|\rangle_{\varepsilon_B} + |-\sqrt{T}\,\mathrm{i}|\alpha|\rangle_B \, |-\sqrt{\eta}\,\mathrm{i}|\alpha|\rangle_{\varepsilon_B}) \times \\
(\, |\sqrt{T-v}\,\mathrm{i}|\alpha|\rangle_D \, |\sqrt{\eta+v}\,\mathrm{i}|\alpha|\rangle_{\varepsilon_D} + |-\sqrt{T-v}\,\mathrm{i}|\alpha|\rangle_D \, |-\sqrt{\eta+v}\,\mathrm{i}|\alpha|\rangle_{\varepsilon_D}) \Big) \Big]. \qquad \text{(F.1)}
\end{aligned}
$$

After applying the 50:50 beam-splitter ($BS^{1/2}_{B,D}$), using the method given in Chapter 2, Sec. 2.4, we get:

$$
\begin{aligned}
\left|\Psi_{v}^{Cat}\right\rangle_{AB\varepsilon_B CD\varepsilon_D} = \mathcal{N}\Bigg(& |00\rangle_{AC} \left(\left|\frac{\mathcal{T}^{-}|\alpha|}{\sqrt{2}}\right\rangle_B \left|\frac{\mathcal{T}^{+}|\alpha|}{\sqrt{2}}\right\rangle_D |\sqrt{\eta}\,|\alpha|\rangle_{\varepsilon_B} \left|\sqrt{\eta+v}\,|\alpha|\right\rangle_{\varepsilon_D} + \right. \\
& \left|\frac{\mathcal{T}^{+}|\alpha|}{\sqrt{2}}\right\rangle_B \left|\frac{\mathcal{T}^{-}|\alpha|}{\sqrt{2}}\right\rangle_D |\sqrt{\eta}\,|\alpha|\rangle_{\varepsilon_B} \left|-\sqrt{\eta+v}\,|\alpha|\right\rangle_{\varepsilon_D} + \\
& \left|\frac{-\mathcal{T}^{+}|\alpha|}{\sqrt{2}}\right\rangle_B \left|\frac{-\mathcal{T}^{-}|\alpha|}{\sqrt{2}}\right\rangle_D |-\sqrt{\eta}\,|\alpha|\rangle_{\varepsilon_B} \left|\sqrt{\eta+v}\,|\alpha|\right\rangle_{\varepsilon_D} + \\
& \left.\left|\frac{-\mathcal{T}^{-}|\alpha|}{\sqrt{2}}\right\rangle_B \left|\frac{-\mathcal{T}^{+}|\alpha|}{\sqrt{2}}\right\rangle_D |-\sqrt{\eta}\,|\alpha|\rangle_{\varepsilon_B} \left|-\sqrt{\eta+v}\,|\alpha|\right\rangle_{\varepsilon_D} \right) \\
& + |01\rangle_{AC} \left(\left|\frac{\mathcal{T}^{-}_{\mathrm{i}\sqrt{T-v}}|\alpha|}{\sqrt{2}}\right\rangle_B \left|\frac{\mathcal{T}^{+}_{\mathrm{i}\sqrt{T-v}}|\alpha|}{\sqrt{2}}\right\rangle_D |\sqrt{\eta}\,|\alpha|\rangle_{\varepsilon_B} \left|\sqrt{\eta+v}\,\mathrm{i}|\alpha|\right\rangle_{\varepsilon_D} + \right. \\
& \left|\frac{\mathcal{T}^{+}_{\mathrm{i}\sqrt{T-v}}|\alpha|}{\sqrt{2}}\right\rangle_B \left|\frac{\mathcal{T}^{-}_{\mathrm{i}\sqrt{T-v}}|\alpha|}{\sqrt{2}}\right\rangle_D |\sqrt{\eta}\,|\alpha|\rangle_{\varepsilon_B} \left|-\sqrt{\eta+v}\,\mathrm{i}|\alpha|\right\rangle_{\varepsilon_D} + \\
& \left|\frac{-\mathcal{T}^{+}_{\mathrm{i}\sqrt{T-v}}|\alpha|}{\sqrt{2}}\right\rangle_B \left|\frac{-\mathcal{T}^{-}_{\mathrm{i}\sqrt{T-v}}|\alpha|}{\sqrt{2}}\right\rangle_D |-\sqrt{\eta}\,|\alpha|\rangle_{\varepsilon_B} \left|\mathrm{i}\sqrt{\eta+v}\,|\alpha|\right\rangle_{\varepsilon_D} + \\
& \left.\left|\frac{-\mathcal{T}^{-}_{\mathrm{i}\sqrt{T-v}}|\alpha|}{\sqrt{2}}\right\rangle_B \left|\frac{-\mathcal{T}^{+}_{\mathrm{i}\sqrt{T-v}}|\alpha|}{\sqrt{2}}\right\rangle_D |-\sqrt{\eta}\,|\alpha|\rangle_{\varepsilon_B} \left|-\sqrt{\eta+v}\,\mathrm{i}|\alpha|\right\rangle_{\varepsilon_D} \right) \\
& + |10\rangle_{AC} \left(\left|\frac{\mathcal{T}^{-}_{\mathrm{i}\sqrt{T}}|\alpha|}{\sqrt{2}}\right\rangle_B \left|\frac{\mathcal{T}^{+}_{\mathrm{i}\sqrt{T}}|\alpha|}{\sqrt{2}}\right\rangle_D |\sqrt{\eta}\,\mathrm{i}|\alpha|\rangle_{\varepsilon_B} \left|\sqrt{\eta+v}\,|\alpha|\right\rangle_{\varepsilon_D} + \right. \\
& \left|\frac{\mathcal{T}^{+}_{\mathrm{i}\sqrt{T}}|\alpha|}{\sqrt{2}}\right\rangle_B \left|\frac{\mathcal{T}^{-}_{\mathrm{i}\sqrt{T}}|\alpha|}{\sqrt{2}}\right\rangle_D |\sqrt{\eta}\,\mathrm{i}|\alpha|\rangle_{\varepsilon_B} \left|-\sqrt{\eta+v}\,|\alpha|\right\rangle_{\varepsilon_D} + \\
& \left|\frac{-\mathcal{T}^{+}_{\mathrm{i}\sqrt{T}}|\alpha|}{\sqrt{2}}\right\rangle_B \left|\frac{-\mathcal{T}^{-}_{\mathrm{i}\sqrt{T}}|\alpha|}{\sqrt{2}}\right\rangle_D |-\sqrt{\eta}\,\mathrm{i}|\alpha|\rangle_{\varepsilon_B} \left|\sqrt{\eta+v}\,|\alpha|\right\rangle_{\varepsilon_D} + \\
& \left.\left|\frac{-\mathcal{T}^{-}_{\mathrm{i}\sqrt{T}}|\alpha|}{\sqrt{2}}\right\rangle_B \left|\frac{-\mathcal{T}^{+}_{\mathrm{i}\sqrt{T}}|\alpha|}{\sqrt{2}}\right\rangle_D |-\sqrt{\eta}\,\mathrm{i}|\alpha|\rangle_{\varepsilon_B} \left|-\sqrt{\eta+v}\,|\alpha|\right\rangle_{\varepsilon_D} \right) \\
& + |11\rangle_{AC} \left(\left|\frac{\mathrm{i}\mathcal{T}^{-}|\alpha|}{\sqrt{2}}\right\rangle_B \left|\frac{\mathrm{i}\mathcal{T}^{+}|\alpha|}{\sqrt{2}}\right\rangle_D |\sqrt{\eta}\,\mathrm{i}|\alpha|\rangle_{\varepsilon_B} \left|\sqrt{\eta+v}\,\mathrm{i}|\alpha|\right\rangle_{\varepsilon_D} + \right. \\
& \left|\frac{\mathrm{i}\mathcal{T}^{+}|\alpha|}{\sqrt{2}}\right\rangle_B \left|\frac{\mathrm{i}\mathcal{T}^{-}|\alpha|}{\sqrt{2}}\right\rangle_D |\sqrt{\eta}\,\mathrm{i}|\alpha|\rangle_{\varepsilon_B} \left|-\sqrt{\eta+v}\,\mathrm{i}|\alpha|\right\rangle_{\varepsilon_D} + \\
& \left|\frac{-\mathrm{i}\mathcal{T}^{+}|\alpha|}{\sqrt{2}}\right\rangle_B \left|\frac{-\mathrm{i}\mathcal{T}^{-}|\alpha|}{\sqrt{2}}\right\rangle_D |-\sqrt{\eta}\,\mathrm{i}|\alpha|\rangle_{\varepsilon_B} \left|\sqrt{\eta+v}\,\mathrm{i}|\alpha|\right\rangle_{\varepsilon_D} + \\
& \left.\left|\frac{-\mathrm{i}\mathcal{T}^{-}|\alpha|}{\sqrt{2}}\right\rangle_B \left|\frac{-\mathrm{i}\mathcal{T}^{+}|\alpha|}{\sqrt{2}}\right\rangle_D |-\sqrt{\eta}\,\mathrm{i}|\alpha|\rangle_{\varepsilon_B} \left|-\sqrt{\eta+v}\,\mathrm{i}|\alpha|\right\rangle_{\varepsilon_D} \right)\Bigg),
\end{aligned}
\tag{F.2}
$$

in which we have used the notation $\sqrt{T}\pm\sqrt{T-v}=\mathcal{T}^{\pm}$, $\mathrm{i}(\sqrt{T}\pm\sqrt{T-v})=\mathrm{i}\mathcal{T}^{\pm}$, $\mathrm{i}\sqrt{T}\pm\sqrt{T-v}=\mathcal{T}^{\pm}_{\mathrm{i}\sqrt{T}}$ and $\sqrt{T}\pm\mathrm{i}\sqrt{T-v}=\mathcal{T}^{\pm}_{\mathrm{i}\sqrt{T-v}}$.

Next, we apply the vacuum projection operator to mode B (see Chapter 2, Sec. 2.5), where $\left\langle 0\middle|\frac{\mathcal{T}^{\pm}}{\sqrt{2}}\right\rangle = \exp\left[-\frac{1}{4}|\alpha|^2|\mathcal{T}^{\pm}|^2\right]$ etc.:

$$
\begin{aligned}
\left|\Psi_v^{Cat}\right\rangle_{A\varepsilon_B C\varepsilon_D} = \mathcal{N}\Bigg(& |00\rangle_{AC}\left(\exp\left[-\frac{1}{4}|\alpha|^2|\mathcal{T}^{-}|^2\right]\left|\frac{\mathcal{T}^{+}|\alpha|}{\sqrt{2}}\right\rangle_D|\sqrt{\eta}\,|\alpha|\rangle_{\varepsilon_B}\left|\sqrt{\eta+v}\,|\alpha|\right\rangle_{\varepsilon_D}+\right.\\
& \exp\left[-\frac{1}{4}|\alpha|^2|\mathcal{T}^{+}|^2\right]\left|\frac{\mathcal{T}^{-}|\alpha|}{\sqrt{2}}\right\rangle_D|\sqrt{\eta}\,|\alpha|\rangle_{\varepsilon_B}\left|-\sqrt{\eta+v}\,|\alpha|\right\rangle_{\varepsilon_D}+\\
& \exp\left[-\frac{1}{4}|\alpha|^2|\mathcal{T}^{+}|^2\right]\left|\frac{-\mathcal{T}^{-}|\alpha|}{\sqrt{2}}\right\rangle_D|-\sqrt{\eta}\,|\alpha|\rangle_{\varepsilon_B}\left|\sqrt{\eta+v}\,|\alpha|\right\rangle_{\varepsilon_D}+\\
& \left.\exp\left[-\frac{1}{4}|\alpha|^2|\mathcal{T}^{-}|^2\right]\left|\frac{-\mathcal{T}^{+}|\alpha|}{\sqrt{2}}\right\rangle_D|-\sqrt{\eta}\,|\alpha|\rangle_{\varepsilon_B}\left|-\sqrt{\eta+v}\,|\alpha|\right\rangle_{\varepsilon_D}\right)\\
& +|01\rangle_{AC}\left(\exp\left[-\frac{1}{4}|\alpha|^2\left|\mathcal{T}^{-}_{\mathrm{i}\sqrt{T-v}}\right|^2\right]\left|\frac{\mathcal{T}^{+}_{\mathrm{i}\sqrt{T-v}}|\alpha|}{\sqrt{2}}\right\rangle_D|\sqrt{\eta}\,|\alpha|\rangle_{\varepsilon_B}\left|\sqrt{\eta+v}\,\mathrm{i}|\alpha|\right\rangle_{\varepsilon_D}+\right.\\
& \exp\left[-\frac{1}{4}|\alpha|^2\left|\mathcal{T}^{+}_{\mathrm{i}\sqrt{T-v}}\right|^2\right]\left|\frac{\mathcal{T}^{-}_{\mathrm{i}\sqrt{T-v}}|\alpha|}{\sqrt{2}}\right\rangle_D|\sqrt{\eta}\,|\alpha|\rangle_{\varepsilon_B}\left|-\sqrt{\eta+v}\,\mathrm{i}|\alpha|\right\rangle_{\varepsilon_D}+\\
& \exp\left[-\frac{1}{4}|\alpha|^2\left|\mathcal{T}^{+}_{\mathrm{i}\sqrt{T-v}}\right|^2\right]\left|\frac{-\mathcal{T}^{-}_{\mathrm{i}\sqrt{T-v}}|\alpha|}{\sqrt{2}}\right\rangle_D|-\sqrt{\eta}\,|\alpha|\rangle_{\varepsilon_B}\left|\mathrm{i}\sqrt{\eta+v}\,|\alpha|\right\rangle_{\varepsilon_D}+\\
& \left.\exp\left[-\frac{1}{4}|\alpha|^2\left|\mathcal{T}^{-}_{\mathrm{i}\sqrt{T-v}}\right|^2\right]\left|\frac{-\mathcal{T}^{+}_{\mathrm{i}\sqrt{T-v}}|\alpha|}{\sqrt{2}}\right\rangle_D|-\sqrt{\eta}\,|\alpha|\rangle_{\varepsilon_B}\left|-\sqrt{\eta+v}\,\mathrm{i}|\alpha|\right\rangle_{\varepsilon_D}\right)\\
& +|10\rangle_{AC}\left(\exp\left[-\frac{1}{4}|\alpha|^2|\mathrm{i}\mathcal{T}^{-}|^2\right]\left|\frac{\mathcal{T}^{+}_{\mathrm{i}\sqrt{T}}|\alpha|}{\sqrt{2}}\right\rangle_D|\sqrt{\eta}\,\mathrm{i}|\alpha|\rangle_{\varepsilon_B}\left|\sqrt{\eta+v}\,|\alpha|\right\rangle_{\varepsilon_D}+\right.\\
& \exp\left[-\frac{1}{4}|\alpha|^2|\mathrm{i}\mathcal{T}^{+}|^2\right]\left|\frac{\mathcal{T}^{-}_{\mathrm{i}\sqrt{T}}|\alpha|}{\sqrt{2}}\right\rangle_D|\sqrt{\eta}\,\mathrm{i}|\alpha|\rangle_{\varepsilon_B}\left|-\sqrt{\eta+v}\,|\alpha|\right\rangle_{\varepsilon_D}+\\
& \exp\left[-\frac{1}{4}|\alpha|^2|\mathrm{i}\mathcal{T}^{+}|^2\right]\left|\frac{-\mathcal{T}^{-}_{\mathrm{i}\sqrt{T}}|\alpha|}{\sqrt{2}}\right\rangle_D|-\sqrt{\eta}\,\mathrm{i}|\alpha|\rangle_{\varepsilon_B}\left|\sqrt{\eta+v}\,|\alpha|\right\rangle_{\varepsilon_D}+\\
& \left.\exp\left[-\frac{1}{4}|\alpha|^2|\mathrm{i}\mathcal{T}^{-}|^2\right]\left|\frac{-\mathcal{T}^{+}_{\mathrm{i}\sqrt{T}}|\alpha|}{\sqrt{2}}\right\rangle_D|-\sqrt{\eta}\,\mathrm{i}|\alpha|\rangle_{\varepsilon_B}\left|-\sqrt{\eta+v}\,|\alpha|\right\rangle_{\varepsilon_D}\right)\\
& +|11\rangle_{AC}\left(\exp\left[-\frac{1}{4}|\alpha|^2|\mathcal{T}^{-}|^2\right]\left|\frac{\mathrm{i}\mathcal{T}^{+}|\alpha|}{\sqrt{2}}\right\rangle_D|\sqrt{\eta}\,\mathrm{i}|\alpha|\rangle_{\varepsilon_B}\left|\sqrt{\eta+v}\,\mathrm{i}|\alpha|\right\rangle_{\varepsilon_D}+\right.\\
& \exp\left[-\frac{1}{4}|\alpha|^2|\mathcal{T}^{+}|^2\right]\left|\frac{\mathrm{i}\mathcal{T}^{-}|\alpha|}{\sqrt{2}}\right\rangle_D|\sqrt{\eta}\,\mathrm{i}|\alpha|\rangle_{\varepsilon_B}\left|-\sqrt{\eta+v}\,\mathrm{i}|\alpha|\right\rangle_{\varepsilon_D}+\\
& \exp\left[-\frac{1}{4}|\alpha|^2|\mathcal{T}^{+}|^2\right]\left|\frac{-\mathrm{i}\mathcal{T}^{-}|\alpha|}{\sqrt{2}}\right\rangle_D|-\sqrt{\eta}\,\mathrm{i}|\alpha|\rangle_{\varepsilon_B}\left|\sqrt{\eta+v}\,\mathrm{i}|\alpha|\right\rangle_{\varepsilon_D}+\\
& \left.\left.\exp\left[-\frac{1}{4}|\alpha|^2|\mathcal{T}^{-}|^2\right]\left|\frac{-\mathrm{i}\mathcal{T}^{+}|\alpha|}{\sqrt{2}}\right\rangle_D|-\sqrt{\eta}\,\mathrm{i}|\alpha|\rangle_{\varepsilon_B}\left|-\sqrt{\eta+v}\,\mathrm{i}|\alpha|\right\rangle_{\varepsilon_D}\right)\right).
\end{aligned}
\tag{F.3}
$$

Next, we apply the homodyne measurement projector (see Chapter 1, Sec. 2.6), which gives the outputs

$$|x_{\frac{\pi}{4}}\rangle_D \ \langle x_{\frac{\pi}{4}}|\mathcal{T}^{\pm}\rangle_D = {}_D\langle x_{\frac{\pi}{4}}|0\rangle_D \exp\left[(1-\mathrm{i})\mathcal{T}^{\pm}|\alpha|x_{\frac{\pi}{4}} + \frac{\mathrm{i}}{4}(\mathcal{T}^{\pm}|\alpha|)^2 - \frac{1}{4}|\mathcal{T}^{\pm}|^2|\alpha|^2\right], \tag{F.4}$$

$$|x_{\frac{\pi}{4}}\rangle_D \ \langle x_{\frac{\pi}{4}}|\mathrm{i}\mathcal{T}^{\pm}\rangle_D = {}_D\langle x_{\frac{\pi}{4}}|0\rangle_D \exp\left[(1-\mathrm{i})\mathrm{i}\mathcal{T}^{\pm}|\alpha|x_{\frac{\pi}{4}} + \frac{\mathrm{i}}{4}(\mathrm{i}\mathcal{T}^{\pm}|\alpha|)^2 - \frac{1}{4}|\mathrm{i}\mathcal{T}^{\pm}|^2|\alpha|^2\right], \tag{F.5}$$

$$|x_{\frac{\pi}{4}}\rangle_D \ \langle x_{\frac{\pi}{4}}|\mathcal{T}^{\pm}_{\mathrm{i}\sqrt{T}}\rangle_D = {}_D\langle x_{\frac{\pi}{4}}|0\rangle_D \exp\left[(1-\mathrm{i})\mathcal{T}^{\pm}_{\mathrm{i}\sqrt{T}}|\alpha|x_{\frac{\pi}{4}} + \frac{\mathrm{i}}{4}(\mathcal{T}^{\pm}_{\mathrm{i}\sqrt{T}}|\alpha|)^2 - \frac{1}{4}|\mathcal{T}^{\pm}_{\mathrm{i}\sqrt{T}}|^2|\alpha|^2\right], \tag{F.6}$$

$$|x_{\frac{\pi}{4}}\rangle_D \ \langle x_{\frac{\pi}{4}}|\mathcal{T}^{\pm}_{\mathrm{i}\sqrt{T-\upsilon}}\rangle_D = {}_D\langle x_{\frac{\pi}{4}}|0\rangle_D \exp\left[(1-\mathrm{i})\mathcal{T}^{\pm}_{\mathrm{i}\sqrt{T-\upsilon}}|\alpha|x_{\frac{\pi}{4}} + \frac{\mathrm{i}}{4}(\mathcal{T}^{\pm}_{\mathrm{i}\sqrt{T-\upsilon}}|\alpha|)^2 - \frac{1}{4}|\mathcal{T}^{\pm}_{\mathrm{i}\sqrt{T-\upsilon}}|^2|\alpha|^2\right]. \tag{F.7}$$

Note that we do not show the explicit form of the quantum state $\left|\Psi^{Cat}_{\upsilon}\right\rangle_{A\varepsilon_B C\varepsilon_D}$ here due to this containing many terms. Following the homodyne measurement of mode D, we then trace out the lossy modes, using the method outlined in Chapter 3, Subsec. 3.2.4, thus giving our final density matrix for the unequal loss cat state scenario as:

$$\rho^{Cat}_{AC}(\upsilon) = \mathrm{Tr}_{\varepsilon_B,\varepsilon_D}\left[|\Psi^{Cat}_{\upsilon}\rangle_{A\varepsilon_B C\varepsilon_D} \ \langle\Psi^{Cat.}_{\upsilon}|\right]. \tag{F.8}$$

The density matrix $\rho^{Cat}_{AC}(\upsilon)$ is then averaged over υ using the method detailed in Chapter 4, Subsec. 4.2.1, to give an averaged density matrix given as $\bar{\rho}^{Cat.}_{AC}(\Upsilon)$, which is then used to calculate fidelity from in Chapter 4, Sec. 4.4.

List of Abbreviations

BS	**B**eam-**S**plitter
CSS	**C**oherent **S**uperposition **S**tate
CV	**C**ontinuous **V**ariable
DV	**D**iscrete **V**ariable
ES	**E**ntanglement **S**wapping
HE	**H**ybrid **E**ntangled
MDI	**M**easurement **D**evice **I**ndependent
QKD	**Q**uantum **K**ey **D**istribution
QST	**Q**uantum **S**tate **T**omography
SPDC	**S**pontaneous **P**arametric **D**own **C**onversion

Eq.	Equation
Fig.	Figure
Tab.	Table
Sec.	Section
Subsec.	Subsection

List of Symbols

α	amplitude (of coherent state $\|\alpha\rangle$)
T	transmission coefficient
R	reflection coefficient
ρ	density matrix
$\hat{I}$	identity matrix
$\hat{a}$	annihilation operator
$\hat{a}^\dagger$	creation operator
$\hat{x}$	position operator
$\hat{p}$	momentum operator
θ	phase angle of homodyne measurement
$\hat{D}(\alpha)$	displacement operator (of coherent state $\|\alpha\rangle$)
υ	loss mismatch value
Υ	ensemble average loss mismatch value
x_θ	homodyne measurement outcome (of phase angle θ)
ϵ	non-ideal homodyne measurement outcome value
Δx	bandwidth of homodyne measurement
$\mathcal{P}_0$	vacuum measurement success probability
$\mathcal{P}_{Hom.}$	homodyne measurement success probability
$\mathcal{N}(\rho)$	entanglement negativity (of density matrix ρ)
F	fidelity
S_L	linear entropy
Tr	trace operation
$\mathcal{N}$	normalisation (in general)
$*$	complex conjugate

Throughout this work hats (ˆ) are used to denote mathematical operators.

References

[1] R. C. Parker et al. “Hybrid photonic loss resilient entanglement swapping”. *Journal of Optics* **19**, 10 (2017), p. 104004.

[2] M. A. Nielsen and I. L. Chuang. *Quantum computation and quantum information*. Nielsen201. Cambridge University Press, 2011.

[3] R. L. Rivest, A. Shamir, and L. Adleman. “A method for obtaining digital signatures and public-key cryptosystems”. *Communications of the ACM* **21**, 2 (1978), pp. 120–126.

[4] *Recently it was exposed that GCHQ in fact discovered this protocol 4 years before the authors of RSA: https://www.gchq.gov.uk/file/cesgresearchreportno3006pdf-0*.

[5] A. Salomaa. *Public-Key Cryptography*. Springer Berlin Heidelberg, 1996.

[6] A. M. Odlyzko. “Public Key Cryptography”. *AT&T Technical Journal* **73**, 5 (1994), pp. 17–23.

[7] V. Mavroeidis et al. “The Impact of Quantum Computing on Present Cryptography”. *International Journal of Advanced Computer Science and Applications* **9**, 3 (2018).

[8] P. Shor. “Algorithms for quantum computation: discrete logarithms and factoring”. *Proceedings 35th Annual Symposium on Foundations of Computer Science*. IEEE Comput. Soc. Press, 1994, pp. 124–134.

[9] E. Diamanti et al. “Practical challenges in quantum key distribution”. *npj Quantum Information* **2**, 1 (2016), p. 16025.

[10] R. Horodecki et al. “Quantum entanglement”. *Reviews of Modern Physics* **81**, 2 (2009), pp. 865–942.

[11] C. H. Bennett and G. Brassard. “Quantum cryptography: Public key distribution and coin tossing”. *Theoretical Computer Science* **560** (2014), pp. 7–11.

[12] A. K. Ekert. “Quantum cryptography based on Bell’s theorem”. *Physical Review Letters* **67**, 6 (1991), pp. 661–663.

[13] F.-G. Deng and G. L. Long. “Secure direct communication with a quantum one-time pad”. *Physical Review A* **69**, 5 (2004), p. 052319.

[14] H.-F. Li et al. “The Improvement of QKD Scheme Based on BB84 Protocol”. *2016 International Conference on Information System and Artificial Intelligence (ISAI)*. IEEE, 2016, pp. 314–317.

[15] E. Waks, A. Zeevi, and Y. Yamamoto. "Security of quantum key distribution with entangled photons against individual attacks". *Physical Review A* **65**, 5 (2002), p. 052310.

[16] N. Ilic. "The ekert protocol". *Journal of Phy334* **1** (2007), pp. 1–4.

[17] D. S. Naik et al. "Entangled State Quantum Cryptography: Eavesdropping on the Ekert Protocol". *Physical Review Letters* **84**, 20 (2000), pp. 4733–4736.

[18] J. S. Bell. "On the Einstein Podolsky Rosen paradox". *Physics* **1**, 3 (1964), pp. 195–200.

[19] N. Gisin et al. "Quantum cryptography". *Reviews of Modern Physics* **74**, 1 (2002), pp. 145–195.

[20] V. Scarani et al. "Quantum Cryptography Protocols Robust against Photon Number Splitting Attacks for Weak Laser Pulse Implementations". *Physical Review Letters* **92**, 5 (2004), p. 057901.

[21] C. H. Bennett. "Quantum cryptography using any two nonorthogonal states". *Physical Review Letters* **68**, 21 (1992), p. 3121.

[22] Y. Zhao et al. "Experimental Quantum Key Distribution with Decoy States". *Physical Review Letters* **96**, 7 (2006), p. 070502.

[23] H. Singh, D. Gupta, and A. Singh. "Quantum Key Distribution Protocols: A Review". *IOSR Journal of Computer Engineering* **16**, 2 (2014), pp. 01–09.

[24] B. Huttner et al. "Quantum cryptography with coherent states". *Physical Review A* **51**, 3 (1995), pp. 1863–1869.

[25] G. A. Barbosa et al. "Secure Communication Using Mesoscopic Coherent States". *Physical Review Letters* **90**, 22 (2003), p. 227901.

[26] D. Huang et al. "Long-distance continuous-variable quantum key distribution by controlling excess noise". *Scientific Reports* **6**, 1 (2016), p. 19201.

[27] A. Orieux and E. Diamanti. "Recent advances on integrated quantum communications". *Journal of Optics* **18**, 8 (2016), p. 083002.

[28] E. Diamanti and A. Leverrier. "Distributing Secret Keys with Quantum Continuous Variables: Principle, Security and Implementations". *Entropy* **17**, 12 (2015), pp. 6072–6092.

[29] H.-K. Lo, M. Curty, and B. Qi. "Measurement-Device-Independent Quantum Key Distribution". *Physical Review Letters* **108**, 13 (2012), p. 130503.

[30] S. Pirandola et al. "Reply to 'Discrete and continuous variables for measurement-device-independent quantum cryptography'". *Nature Photonics* **9**, 12 (2015), pp. 773–775.

[31] Feihu Xu et al. "Measurement-Device-Independent Quantum Cryptography". *IEEE Journal of Selected Topics in Quantum Electronics* **21**, 3 (2015), pp. 148–158.

[32] M. Żukowski et al. ""Event-ready-detectors" Bell experiment via entanglement swapping". *Physical Review Letters* **71**, 26 (1993), pp. 4287–4290.

[33] S. Giacomini et al. "Active teleportation of a quantum bit". *Physical Review A* **66**, 3 (2002), p. 030302.

[34] T. Jennewein et al. "Experimental Nonlocality Proof of Quantum Teleportation and Entanglement Swapping". *Physical Review Letters* **88**, 1 (2001), p. 017903.

[35] R. Kaltenbaek et al. "High-fidelity entanglement swapping with fully independent sources". *Physical Review A* **79**, 4 (2009), p. 040302.

[36] X. Jia et al. "Experimental Demonstration of Unconditional Entanglement Swapping for Continuous Variables". *Physical Review Letters* **93**, 25 (2004), p. 250503.

[37] N. Takei et al. "High-Fidelity Teleportation beyond the No-Cloning Limit and Entanglement Swapping for Continuous Variables". *Physical Review Letters* **94**, 22 (2005), p. 220502.

[38] H. Jeong et al. "Generation of hybrid entanglement of light". *Nature Photonics* **8**, 7 (2014), pp. 564–569.

[39] S. Takeda et al. "Entanglement Swapping between Discrete and Continuous Variables". *Physical Review Letters* **114**, 10 (2015), p. 100501.

[40] C. W.C. W. Gardiner and P. P. Zoller. *Quantum noise : a handbook of Markovian and non-Markovian quantum stochastic methods with applications to quantum optics*. Springer, 2004.

[41] A. Shaham et al. "Entanglement dynamics in the presence of controlled unital noise". *Scientific Reports* **5**, 1 (2015), p. 10796.

[42] N. L. Piparo, M. Razavi, and C. Panayi. "Measurement-Device-Independent Quantum Key Distribution With Ensemble-Based Memories". *IEEE Journal of Selected Topics in Quantum Electronics* **21**, 3 (2015), pp. 138–147.

[43] C. H. Bennett et al. "Purification of Noisy Entanglement and Faithful Teleportation via Noisy Channels". *Physical Review Letters* **76**, 5 (1996), pp. 722–725.

[44] J.-L. L. Gouët and S. Moiseev. "Quantum memory". *Journal of Physics B: Atomic, Molecular and Optical Physics* **45**, 12 (2012), p. 120201.

[45] M. Razavi. *An Introduction to Quantum Communications Networks Or, how shall we communicate in the quantum era?* IOP Publishing, 2018.

[46] J. Dias and T. C. Ralph. "Quantum repeaters using continuous-variable teleportation". *Physical Review A* **95**, 2 (2017), p. 022312.

[47] Y. Mao et al. "Integrating quantum key distribution with classical communications in backbone fiber network". *Optics Express* **26**, 5 (2018), p. 6010.

[48] K. Tsujikawa, K. Tajima, and J. Zhou. "Intrinsic loss of optical fibers". *Optical Fiber Technology* **11**, 4 (2005), pp. 319–331.

[49] A. I. M. Rae. *Quantum mechanics*. Rae2008: Taylor & Francis, 2008.

[50] D. P. Craig and T Thirunamachandran. *Molecular quantum electrodynamics : an introduction to radiation-molecule interactions*. Dover Publications, 1984.

[51] J. J. L. Morton et al. "Embracing the quantum limit in silicon computing". *Nature* **479**, 7373 (2011), pp. 345–353.

[52] J. J. Pla et al. "A single-atom electron spin qubit in silicon". *Nature* **489**, 7417 (2012), pp. 541–545.

[53] C. Navarrete-Benlloch. "Quantum information with continuous variables". *An Introduction to the Formalism of Quantum Information with Continuous Variables*. IOP Publishing, 2015.

[54] G. Kurizki et al. "Quantum technologies with hybrid systems". *Proceedings of the National Academy of Sciences* **112**, 13 (2015), pp. 3866–3873.

[55] R. Loudon. *The quantum theory of light*. Oxford Science Publications, 2000.

[56] S. Glancy and H. M. de Vasconcelos. "Methods for producing optical coherent state superpositions". *Journal of the Optical Society of America B* **25**, 5 (2008), p. 712.

[57] J. Greensite. *An Introduction to Quantum Theory*. IOP Publishing, 2017.

[58] E. Tiunov et al. "Towards interconversion between discrete- and continuous-variable encodings in quantum optics". *AIP Conference Proceedings*. AIP Publishing, 2018, p. 020017.

[59] S. Barnett and P. Radmore. *Methods in Theoretical Quantum Optics*. Oxford University Press, 2002.

[60] M. Namiki, H. Nakazato, and S. Pascazio. *Decoherence and Quantum Measurements*. World Scientific, 1998.

[61] M. D. Eisaman et al. "Invited Review Article: Single-photon sources and detectors". *Review of Scientific Instruments* **82**, 7 (2011), p. 071101.

[62] A. Schwagmann et al. "On-chip single photon emission from an integrated semiconductor quantum dot into a photonic crystal waveguide". *Applied Physics Letters* **99**, 26 (2011), p. 261108.

[63] S. Kalliakos et al. "In-plane emission of indistinguishable photons generated by an integrated quantum emitter". *Applied Physics Letters* **104**, 22 (2014), p. 221109.

[64] J. F. Clauser. "Experimental distinction between the quantum and classical field-theoretic predictions for the photoelectric effect". *Physical Review D* **9**, 4 (1974), pp. 853–860.

[65] P Grangier, G Roger, and A Aspect. "Experimental Evidence for a Photon Anticorrelation Effect on a Beam Splitter: A New Light on Single-Photon Interferences". *Europhysics Letters (EPL)* **1**, 4 (1986), pp. 173–179.

[66] C. Bennett et al. "Experimental quantum cryptography". *Journal of Cryptology* **5**, 1 (1992), pp. 3–28.

[67] P. Townsend, J. Rarity, and P. Tapster. "Single photon interference in 10 km long optical fibre interferometer". *Electronics Letters* **29**, 7 (1993), p. 634.

[68] G. Brassard et al. "Limitations on Practical Quantum Cryptography". *Physical Review Letters* **85**, 6 (2000), pp. 1330–1333.

[69] S. Walborn et al. "Spatial correlations in parametric down-conversion". *Physics Reports* **495**, 4-5 (2010), pp. 87–139.

[70] J. Schneeloch and J. C. Howell. "Introduction to the transverse spatial correlations in spontaneous parametric down-conversion through the biphoton birth zone". *Journal of Optics* **18**, 5 (2016), p. 053501.

[71] D. N. Klyshko, A. N. Penin, and B. F. Polkovnikov. "Parametric luminescence and light scattering by polaritons". *JETP Letters* **11**, 1 (1970), p. 5.

[72] C. K. Hong and L. Mandel. "Theory of parametric frequency down conversion of light". *Physical Review A* **31**, 4 (1985), pp. 2409–2418.

[73] C. K. Hong and L. Mandel. "Experimental realization of a localized one-photon state". *Physical Review Letters* **56**, 1 (1986), pp. 58–60.

[74] D. C. Burnham and D. L. Weinberg. "Observation of Simultaneity in Parametric Production of Optical Photon Pairs". *Physical Review Letters* **25**, 2 (1970), pp. 84–87.

[75] A. J. Shields. "Semiconductor quantum light sources". *Nature Photonics* **1**, 4 (2007), pp. 215–223.

[76] S. Takeuchi. "Recent progress in single-photon and entangled-photon generation and applications". *Japanese Journal of Applied Physics* **53**, 3 (2014), p. 030101.

[77] I. Aharonovich, D. Englund, and M. Toth. "Solid-state single-photon emitters". *Nature Photonics* **10**, 10 (2016), pp. 631–641.

[78] A. Hayat, P. Ginzburg, and M. Orenstein. "Observation of two-photon emission from semiconductors". *Nature Photonics* **2**, 4 (2008), pp. 238–241.

[79] P. Senellart, G. Solomon, and A. White. "High-performance semiconductor quantum-dot single-photon sources". *Nature Nanotechnology* **12**, 11 (2017), pp. 1026–1039.

[80] C. C. Gerry and P. L. Knight. *Introductory quantum optics*. Cambridge University Press, 2005.

[81] H.-P. Breuer and F. Petruccione. *The Theory of Open Quantum Systems*. Oxford University Press, 2007.

[82] M Arik. “Hilbert spaces of analytic functions and generalized coherent states”. *Journal of Mathematical Physics* **17**, 4 (1976), p. 524.

[83] E. Goldin. *Waves and Photons: An Introduction to Quantum Optics*. John Wiley and Sons, 1982.

[84] J. G. Webb, T. C. Ralph, and E. H. Huntington. “Homodyne measurement of the average photon number”. *Physical Review A* **73**, 3 (2006), p. 033808.

[85] A. I. Lvovsky. “Squeezed light”. *arXiv:1401.4118v2 [quant-ph]* (2016).

[86] S. Blackburn. *The Oxford Dictionary of Philosophy*. 2nd ed. Oxford University Press, 2008.

[87] V. Dodonov, I. Malkin, and V. Man’ko. “Even and odd coherent states and excitations of a singular oscillator”. *Physica* **72**, 3 (1974), pp. 597–615.

[88] B. Yurke and D. Stoler. “Generating quantum mechanical superpositions of macroscopically distinguishable states via amplitude dispersion”. *Physical Review Letters* **57**, 1 (1986), pp. 13–16.

[89] M. Mirrahimi et al. “Dynamically protected cat-qubits: a new paradigm for universal quantum computation”. *New Journal of Physics* **16**, 4 (2014), p. 045014.

[90] F. Grosshans and P. Grangier. “Continuous Variable Quantum Cryptography Using Coherent States”. *Physical Review Letters* **88**, 5 (2002), p. 057902.

[91] M. Brune et al. “Observing the Progressive Decoherence of the “Meter” in a Quantum Measurement”. *Physical Review Letters* **77**, 24 (1996), pp. 4887–4890.

[92] A. Auffeves et al. “Entanglement of a Mesoscopic Field with an Atom Induced by Photon Graininess in a Cavity”. *Physical Review Letters* **91**, 23 (2003), p. 230405.

[93] J. Kerr. “A new relation between electricity and light: Dielectrified media birefringent”. *The London, Edinburgh, and Dublin Philosophical Magazine and Journal of Science* **50**, 332 (1875), pp. 337–348.

[94] B. He, M. Nadeem, and J. A. Bergou. “Scheme for generating coherent state superpositions with realistic cross-Kerr nonlinearity”. *Physical Review A* **79**, 3 (2009), p. 035802.

[95] S. Puri, S. Boutin, and A. Blais. “Engineering the quantum states of light in a Kerr-nonlinear resonator by two-photon driving”. *npj Quantum Information* **3**, 1 (2017), p. 18.

[96] F. Shimizu. “Frequency Broadening in Liquids by a Short Light Pulse”. *Physical Review Letters* **19**, 19 (1967), pp. 1097–1100.

[97] R. W. Boyd. *Nonlinear optics*. Academic Press, 2003.

[98] V. Bužek, A. Vidiella-Barranco, and P. L. Knight. “Superpositions of coherent states: Squeezing and dissipation”. *Physical Review A* **45**, 9 (1992), pp. 6570–6585.

[99] M. Bartkowiak, L.-A. Wu, and A. Miranowicz. "Quantum circuits for amplification of Kerr nonlinearity via quadrature squeezing". *Journal of Physics B: Atomic, Molecular and Optical Physics* **47**, 14 (2014), p. 145501.

[100] A. P. Lund et al. "Conditional production of superpositions of coherent states with inefficient photon detection". *Physical Review A* **70**, 2 (2004), p. 020101.

[101] W. Asavanant et al. "Generation of highly pure Schrödinger's cat states and real-time quadrature measurements via optical filtering". *Optics Express* **25**, 26 (2017), p. 32227.

[102] J. S. Neergaard-Nielsen et al. "Generation of a Superposition of Odd Photon Number States for Quantum Information Networks". *Physical Review Letters* **97**, 8 (2006), p. 083604.

[103] M. C. Teich and B. E. A. Saleh. "Squeezed state of light". *Quantum Optics: Journal of the European Optical Society Part B* **1**, 2 (1989), pp. 153–191.

[104] M. Dakna et al. "Generating Schrödinger-cat-like states by means of conditional measurements on a beam splitter". *Physical Review A* **55**, 4 (1997), pp. 3184–3194.

[105] U. L. Andersen et al. "Hybrid discrete- and continuous-variable quantum information". *Nature Physics* **11**, 9 (2015), pp. 713–719.

[106] H. Takahashi et al. "Generation of Large-Amplitude Coherent-State Superposition via Ancilla-Assisted Photon Subtraction". *Physical Review Letters* **101**, 23 (2008), p. 233605.

[107] T. Gerrits et al. "Generation of optical coherent-state superpositions by number-resolved photon subtraction from the squeezed vacuum". *Physical Review A* **82**, 3 (2010), p. 031802.

[108] S. Song, C. M. Caves, and B. Yurke. "Generation of superpositions of classically distinguishable quantum states from optical back-action evasion". *Physical Review A* **41**, 9 (1990), pp. 5261–5264.

[109] M. S. Kim et al. "Entanglement by a beam splitter: Nonclassicality as a prerequisite for entanglement". *Physical Review A* **65**, 3 (2002), p. 032323.

[110] U. Leonhardt and H. Paul. "Measuring the quantum state of light". *Progress in Quantum Electronics* **19**, 2 (1995), pp. 89–130.

[111] S. D. Huver, C. F. Wildfeuer, and J. P. Dowling. "Entangled Fock states for robust quantum optical metrology, imaging, and sensing". *Physical Review A* **78**, 6 (2008), p. 063828.

[112] P. Kok et al. "Linear optical quantum computing with photonic qubits". *Reviews of Modern Physics* **79**, 1 (2007), pp. 135–174.

[113] A Zeilinger. "General properties of lossless beam splitters in interferometry". *American Journal of Physics* **49**, 9 (1981), pp. 882–883.

[114] H. Fearn and R. Loudon. "Quantum theory of the lossless beam splitter". *Optics Communications* **64**, 6 (1987), pp. 485–490.

[115] S. M. Barnett et al. "Quantum optics of lossy beam splitters". *Physical Review A* **57**, 3 (1998), pp. 2134–2145.

[116] S. Prasad, M. O. Scully, and W. Martienssen. "A quantum description of the beam splitter". *Optics Communications* **62**, 3 (1987), pp. 139–145.

[117] M. W. Hamilton. "Phase shifts in multilayer dielectric beam splitters". *American Journal of Physics* **68**, 2 (2000), pp. 186–191.

[118] J. Walleczek and G. Grössing. "Nonlocal Quantum Information Transfer Without Superluminal Signalling and Communication". *Foundations of Physics* **46**, 9 (2016), pp. 1208–1228.

[119] A. Einstein, B. Podolsky, and N. Rosen. "Can Quantum-Mechanical Description of Physical Reality Be Considered Complete?" *Physical Review* **47**, 10 (1935), pp. 777–780.

[120] J.-W. Pan et al. "Experimental Entanglement Swapping: Entangling Photons That Never Interacted". *Physical Review Letters* **80**, 18 (1998), pp. 3891–3894.

[121] E. Megidish et al. "Entanglement Swapping between Photons that have Never Coexisted". *Physical Review Letters* **110**, 21 (2013), p. 210403.

[122] C. H. Bennett et al. "Teleporting an unknown quantum state via dual classical and Einstein-Podolsky-Rosen channels". *Physical Review Letters* **70**, 13 (1993), pp. 1895–1899.

[123] S. L. Braunstein and H. J. Kimble. "Teleportation of Continuous Quantum Variables". *Physical Review Letters* **80**, 4 (1998), pp. 869–872.

[124] T. Herbst et al. "Teleportation of entanglement over 143 km." *Proceedings of the National Academy of Sciences of the United States of America* **112**, 46 (2015), pp. 14202–5.

[125] P. van Loock. "Optical hybrid approaches to quantum information". *Laser & Photonics Reviews* **5**, 2 (2011), pp. 167–200.

[126] O. Morin et al. "Remote creation of hybrid entanglement between particle-like and wave-like optical qubits". *Nature Photonics* **8**, 7 (2014), pp. 570–574.

[127] S. Li et al. "Experimentally feasible generation protocol for polarized hybrid entanglement". *Physical Review A* **98**, 2 (2018), p. 022334.

[128] C. C. Gerry. "Generation of optical macroscopic quantum superposition states via state reduction with a Mach-Zehnder interferometer containing a Kerr medium". *Physical Review A* **59**, 5 (1999), pp. 4095–4098.

[129] K. Nemoto and W. J. Munro. "Nearly Deterministic Linear Optical Controlled-NOT Gate". *Physical Review Letters* **93**, 25 (2004), p. 250502.

[130] H. Jeong. "Using weak nonlinearity under decoherence for macroscopic entanglement generation and quantum computation". *Physical Review A* **72**, 3 (2005), p. 034305.

[131] P. van Loock et al. "Hybrid Quantum Repeater Using Bright Coherent Light". *Physical Review Letters* **96**, 24 (2006), p. 240501.

[132] P. van Loock et al. "Quantum repeaters using coherent-state communication". *Physical Review A* **78**, 6 (2008), p. 062319.

[133] Y.-B. Sheng, L. Zhou, and G.-L. Long. "Hybrid entanglement purification for quantum repeaters". *Physical Review A* **88**, 2 (2013), p. 022302.

[134] T. D. Ladd et al. "Hybrid quantum repeater based on dispersive CQED interactions between matter qubits and bright coherent light". *New Journal of Physics* **8**, 9 (2006), p. 184.

[135] H. Kwon and H. Jeong. "Generation of hybrid entanglement between a single-photon polarization qubit and a coherent state". *Physical Review A* **91**, 1 (2015), p. 012340.

[136] C. Cohen-Tannoudji, B. Diu, and F. Laloe. *Quantum Mechanics - Volume 1*. Hermann and John Wiley & Sons Inc., 2006.

[137] D. Lv et al. "Reconstruction of the Jaynes-Cummings field state of ionic motion in a harmonic trap". *Physical Review A* **95**, 4 (2017), p. 043813.

[138] C. C. Gerry. "Heisenberg-limit interferometry with four-wave mixers operating in a nonlinear regime". *Physical Review A* **61**, 4 (2000), p. 043811.

[139] M. G. A. Paris. "Optical qubit by conditional interferometry". *Physical Review A* **62**, 3 (2000), p. 033813.

[140] I. Węgrzecka et al. "Design and Properties of Silicon Avalance Photodiodes". *Opto-Electronics Review* **12**, 1 (2004), pp. 95–104.

[141] S. D. Bartlett and B. C. Sanders. "Universal continuous-variable quantum computation: Requirement of optical nonlinearity for photon counting". *Physical Review A* **65**, 4 (2002), p. 042304.

[142] B. A. Fowler et al. "Method for estimating quantum efficiency for CMOS image sensors". *Proc. SPIE 3301, Solid State Sensor Arrays: Development and Applications II*. Ed. by M. M. Blouke. Vol. 3301. International Society for Optics and Photonics, 1998, p. 178.

[143] D. K. L. Oi, V. Potoček, and J. Jeffers. "Nondemolition Measurement of the Vacuum State or its Complement". *Physical Review Letters* **110**, 21 (2013), p. 210504.

[144] J. Joo, T. Rudolph, and B. C. Sanders. "A heralded two-qutrit entangled state". *Journal of Physics B: Atomic, Molecular and Optical Physics* **42**, 11 (2009), p. 114007.

[145] M. O.M. O. Scully and M. S. Zubairy. *Quantum optics*. Cambridge University Press, 1997.

[146] S. D. Barrett et al. “Symmetry analyzer for nondestructive Bell-state detection using weak nonlinearities”. *Physical Review A* **71**, 6 (2005), p. 060302.

[147] S. Suzuki et al. “Practical purification scheme for decohered coherent-state superpositions via partial homodyne detection”. *Physical Review A* **73**, 4 (2006), p. 042304.

[148] A. I. Lvovsky and M. G. Raymer. “Continuous-variable optical quantum-state tomography”. *Reviews of Modern Physics* **81**, 1 (2009), pp. 299–332.

[149] J. W. Noh, A. Fougères, and L. Mandel. “Measurement of the quantum phase by photon counting”. *Physical Review Letters* **67**, 11 (1991), pp. 1426–1429.

[150] D. T. Smithey et al. “Measurement of the Wigner distribution and the density matrix of a light mode using optical homodyne tomography: Application to squeezed states and the vacuum”. *Physical Review Letters* **70**, 9 (1993), pp. 1244–1247.

[151] D. T. Smithey et al. “Complete experimental characterization of the quantum state of a light mode via the Wigner function and the density matrix: application to quantum phase distributions of vacuum and squeezed-vacuum states”. *Physica Scripta* **T48** (1993), pp. 35–44.

[152] T. Lipfert, J. Sperling, and W. Vogel. “Homodyne detection with on-off detector systems”. *Physical Review A* **92**, 5 (2015), p. 053835.

[153] C. E. Shannon. “A Mathematical Theory of Communication”. *Bell System Technical Journal* **27**, 3 (1948), pp. 379–423.

[154] A. Wehrl. “General properties of entropy”. *Reviews of Modern Physics* **50**, 2 (1978), pp. 221–260.

[155] J. Von Neumann. *Mathematical foundations of quantum mechanics*. Princeton University Press, 1955.

[156] F. Buscemi, P. Bordone, and A. Bertoni. “Linear entropy as an entanglement measure in two-fermion systems”. *Physical Review A* **75**, 3 (2007), p. 032301.

[157] F. A. A. El-Orany. “Relationship between the linear entropy, the von Neumann entropy and the atomic Wehrl entropy for the Jaynes-Cummings model”. *arXiv:0705.4373v1 [quant-ph]* (2007).

[158] H. L. Royden, P. Fitzpatrick, and H. L. Royden. *Real analysis*. Prentice Hall, 2010.

[159] W. H. Zurek, S. Habib, and J. P. Paz. “Coherent states via decoherence”. *Physical Review Letters* **70**, 9 (1993), pp. 1187–1190.

[160] G. Manfredi and M. R. Feix. “Entropy and Wigner functions”. *Physical Review E* **62**, 4 (2000), pp. 4665–4674.

[161] N. A. Peters, T.-C. Wei, and P. G. Kwiat. “Mixed-state sensitivity of several quantum-information benchmarks”. *Physical Review A* **70**, 5 (2004), p. 052309.

[162] M. B. Plenio and S. Virmani. "An introduction to entanglement measures". *Quantum Information and Computation* **7**, 1 (2007), pp. 1–51.

[163] G. Vidal and R. F. Werner. "Computable measure of entanglement". *Physical Review A* **65**, 3 (2002), p. 032314.

[164] M. Horodecki, P. Horodecki, and R. Horodecki. "Limits for Entanglement Measures". *Physical Review Letters* **84**, 9 (2000), pp. 2014–2017.

[165] V. Vedral et al. "Quantifying Entanglement". *Physical Review Letters* **78**, 12 (1997), pp. 2275–2279.

[166] V. Vedral and M. B. Plenio. "Entanglement measures and purification procedures". *Physical Review A* **57**, 3 (1998), pp. 1619–1633.

[167] A. Peres. "Separability Criterion for Density Matrices". *Physical Review Letters* **77**, 8 (1996), pp. 1413–1415.

[168] M. Horodecki, P. Horodecki, and R. Horodecki. "Separability of mixed states: necessary and sufficient conditions". *Physics Letters A* **223**, 1 (1996), pp. 1–8.

[169] T.-C. Wei et al. "Maximal entanglement versus entropy for mixed quantum states". *Physical Review A* **67**, 2 (2003), p. 022110.

[170] G. B. Price. "Some Identities in the Theory of Determinants". *The American Mathematical Monthly* **54**, 2 (1947), p. 75.

[171] S. Kanno, J. P. Shock, and J. Soda. "Entanglement negativity in the multiverse". *Journal of Cosmology and Astroparticle Physics* **03** (2015), pp. 015–015.

[172] M. Rangamani and M. Rota. "Entanglement structures in qubit systems". *Journal of Physics A: Mathematical and Theoretical* **48**, 38 (2015), p. 385301.

[173] R. Jozsa and B. Schumacher. "A New Proof of the Quantum Noiseless Coding Theorem". *Journal of Modern Optics* **41**, 12 (1994), pp. 2343–2349.

[174] B. Schumacher. "Quantum coding". *Physical Review A* **51**, 4 (1995), pp. 2738–2747.

[175] R. Jozsa. "Fidelity for Mixed Quantum States". *Journal of Modern Optics* **41**, 12 (1994), pp. 2315–2323.

[176] E. N. Fokoua et al. "How to make the propagation time through an optical fiber fully insensitive to temperature variations". *Optica* **4**, 6 (2017), p. 659.

[177] A. Laghaout et al. "Amplification of realistic Schrödinger-cat-state-like states by homodyne heralding". *Physical Review A* **87**, 4 (2013), p. 043826.

[178] D. Bouwmeester, A. Ekert, and A. Zeilinger, eds. *The Physics of Quantum Information*. Berlin, Heidelberg: Springer Berlin Heidelberg, 2000.

[179] D. Bruß. "Entanglement Purification and Distillation". *Compendium of Quantum Physics*. Berlin, Heidelberg: Springer Berlin Heidelberg, 2009, pp. 202–205.

[180] C. H. Bennett et al. "Mixed-state entanglement and quantum error correction". *Physical Review A* **54**, 5 (1996), pp. 3824–3851.

[181] L.-M. Duan and G.-C. Guo. "Influence of noise on the fidelity and the entanglement fidelity of states". *Quantum and Semiclassical Optics: Journal of the European Optical Society Part B* **9**, 6 (1997), pp. 953–959.

[182] R. F. Werner. "Quantum states with Einstein-Podolsky-Rosen correlations admitting a hidden-variable model". *Physical Review A* **40**, 8 (1989), pp. 4277–4281.

[183] D. Deutsch. "Quantum Computational Networks". *Proceedings of the Royal Society A: Mathematical, Physical and Engineering Sciences* **425**, 1868 (1989), pp. 73–90.

[184] D. Deutsch et al. "Quantum Privacy Amplification and the Security of Quantum Cryptography over Noisy Channels". *Physical Review Letters* **77**, 13 (1996), pp. 2818–2821.

[185] J.-W. Pan et al. "Entanglement purification for quantum communication". *Nature* **410**, 6832 (2001), pp. 1067–1070.

[186] N. Gisin. "Hidden quantum nonlocality revealed by local filters". *Physics Letters A* **210**, 3 (1996), pp. 151–156.

[187] P. G. Kwiat et al. "Experimental entanglement distillation and 'hidden' nonlocality". *Nature* **409**, 6823 (2001), pp. 1014–1017.

[188] M. Horodecki, P. Horodecki, and R. Horodecki. "Mixed-State Entanglement and Distillation: Is there a "Bound" Entanglement in Nature?" *Physical Review Letters* **80**, 24 (1998), pp. 5239–5242.

[189] A. Miyake and H. J. Briegel. "Distillation of Multipartite Entanglement by Complementary Stabilizer Measurements". *Physical Review Letters* **95**, 22 (2005), p. 220501.

[190] W. Dür, H. Aschauer, and H.-J. Briegel. "Multiparticle Entanglement Purification for Graph States". *Physical Review Letters* **91**, 10 (2003), p. 107903.

[191] Y. W. Cheong et al. "Entanglement purification for high-dimensional multipartite systems". *Physical Review A* **76**, 4 (2007), p. 042314.

[192] H. Zhang et al. "Entanglement concentration and purification of two-mode squeezed microwave photons in circuit QED". *Annals of Physics* **391** (2018), pp. 112–119.

[193] J.-W. Pan et al. "Experimental entanglement purification of arbitrary unknown states". *Nature* **423**, 6938 (2003), pp. 417–422.

[194] X.-L. Feng, S.-Q. Gong, and Z.-Z. Xu. "Entanglement purification via controlled controlled NOT operations". *Physics Letters A* **271**, 1-2 (2000), pp. 44–47.

[195] C. Cai, L. Zhou, and Y.-B. Sheng. "Fast multi-copy entanglement purification with linear optics". *Chinese Physics B* **24**, 12 (2015), p. 120306.

[196] S.-S. Zhang et al. "Multi-copy entanglement purification with practical spontaneous parametric down conversion sources". *Chinese Physics B* **26**, 6 (2017), p. 060307.

[197] T. Simpson et al. "Visual Steering Commands and Test Problems to Support Research in Trade Space Exploration". *12th AIAA/ISSMO Multidisciplinary Analysis and Optimization Conference*. Reston, Virigina: American Institute of Aeronautics and Astronautics, 2008.

[198] M. J.d. C. Henshaw et al. "The challenges for Systems Engineers of non-classical quantum technologies". *arXiv:1710.05643v2 [quant-ph]* (2017).

[199] C. H. Bennett and D. P. DiVincenzo. "Quantum information and computation". *Nature* **404**, 6775 (2000), pp. 247–255.

[200] F. Hong-Yi and W. Hui. "Entanglement Swapping for Displaced Two-Mode Squeezed States". *Communications in Theoretical Physics* **36**, 4 (2001), pp. 455–458.

[201] H. Yonezawa and A. Furusawa. "Continuous-variable quantum information processing with squeezed states of light". *Optics and Spectroscopy* **108**, 2 (2010), pp. 288–296.

[202] X. Deng et al. "Disappearance and revival of squeezing in quantum communication with squeezed state over a noisy channel". *Applied Physics Letters* **108**, 8 (2016), p. 081105.

[203] *http://uknqt.epsrc.ac.uk/*.

[204] E. Gibney. "Chinese satellite is one giant step for the quantum internet". *Nature* **535**, 7613 (2016), pp. 478–479.

[205] W. R. Inc. *Mathematica*. Champaign, Illinois, 2018.

[206] B. Julia-Diaz and F. Tabakin. *QDENSITY: A Quantum Computer Simulation, version 4.0*. 2015.